DISSERTATION

submitted to the
Combined Faculties for the Natural Sciences and Mathematics
of the Ruperto-Carola University of Heidelberg, Germany
for the degree of

doctor rerum naturalium

presented by

Dipl.-Phys. Marc Deissenroth

born in Salzkotten, Germany

Oral examination: April 21$^{\text{st}}$, 2010

Software Alignment of
the LHC*b* Outer Tracker Chambers

Referees: Prof. Dr. Ulrich Uwer

Prof. Dr. Hans-Christian Schultz-Coulon

Abstract

This work presents an alignment algorithm that was developed to precisely determine the positions of the LHC*b* Outer Tracker detector elements. The algorithm is based on the reconstruction of tracks and exploits that misalignments of the detector change the residual between a measured hit and the reconstructed track. It considers different levels of granularities of the Outer Tracker geometry and fully accounts for correlations of all elements which are imposed by particle trajectories. In extensive tests, simulated shifts and rotations for different levels of the detector granularity have been used as input to the track reconstruction and alignment procedure. With about 260 000 tracks the misalignments are recovered with a statistical precision of $\mathcal{O}(10 - 100\,\mu\text{m})$ for the translational degrees of freedom and of $\mathcal{O}(10^{-2} - 10^{-1}\,\text{mrad})$ for rotations. A study has been performed to determine the impact of Outer Tracker misalignments on the performance of the track reconstruction algorithms. It shows that the achieved statistical precision does not decrease the track reconstruction performance in a significant way.

During the commissioning of the LHC*b* detector, cosmic ray muon events have been collected. The events have been analysed and used for the first alignment of the 216 Outer Tracker modules. The module positions have been determined within $\sim 90\,\mu\text{m}$.

The developed track based alignment algorithm has demonstrated its reliability and is one of the core algorithms which are used for the precise determination of the positions of the LHC*b* Outer Tracker elements.

Kurzfassung

In der vorliegenden Arbeit wird ein Algorithmus vorgestellt, der entwickelt wurde um die Positionen der äußeren Spurkammern des LHCb Detektors exakt zu bestimmen. Der Algorithmus basiert auf der Rekonstruktion von Spuren und nutzt die Tatsache, daß Verschiebungen der Spurkammern das Residuum zwischen einem Messpunkt und der rekonstruierten Spur verändern.

Der komplexe Aufbau der Spurkammern, bestehend aus verschiedenen Detektorkomponenten, wird berücksichtigt und die durch Spuren hervorgerufenen Korrelationen zwischen den Komponenten werden berechnet. Umfangreiche Studien haben gezeigt, daß simulierte Verschiebungen des Detektors mit einer statistischen Präzision von 10-100 μm für Translationen und 10^{-2}-10^{-1} mrad für Rotationen bestimmt werden können (260 000 Spuren).

Der Einfluss von Verschiebungen der äußeren Spurkammern auf die Qualität der Spurrekonstruktion wurde untersucht. Mit der erreichten statistischen Genauigkeit sind keine signifikanten Effekte auf die Qualität der Rekonstruktion zu erwarten.

Während der Inbetriebnahme des Detektors wurden Spuren von kosmischen Myonen aufgenommen. Die Daten wurden analysiert und zur Ausrichtung aller 216 Spurkammern verwendet. Die Positionen der Kammern konnten mit einer Genauigkeit von $\sim 90\,\mu$m bestimmt werden.

Der entwickelte spurbasierte Algorithmus ist einer der Hauptalgorithmen, die zur präzisen Bestimmung der Positionen der äußeren Spurkammern des LHCb Experimentes verwendet werden.

Contents

Introduction

The Standard Model of Particle Physics (SM), developed in the 1960's [1–3], entails the present understanding of the fundamental building blocks of matter and interactions between them. It describes successfully all results of collider experiments performed so far. Despite its huge success, the SM cannot explain nature's preference for matter over antimatter or the existence of Dark Matter in the universe. Moreover the SM does not explain the origin of the different particle flavors and the mass hierarchy that is observed. These open questions could potentially be answered by more fundamental theories which predict new phenomena, often referred to as New Physics (NP), at higher energy scales. In these theories the SM is regarded as a "low energy" approximation. New Physics phenomena can either be explored by searching directly for the production of new particles at highest energies, or by measuring precisely the effects of quantum loop corrections where NP could contribute via additional corrections.

A new energy frontier will be reached by the Large Hadron Collider (LHC) [4] at CERN in Geneva. Four LHC experiments will observe proton-proton collisions at a center of mass energy of up to $\sqrt{s} = 14\,\text{TeV}$. The LHC started colliding proton beams in a short commissioning run in November 2009 and will restart running at a center of mass energy of $\sqrt{s} = 7\,\text{TeV}$ in spring 2010.

The LHC*b* (Large Hadron Collider beauty) [5] experiment is one of the four LHC experiments. It is designed to study rare, loop-suppressed B meson decays with very high precision. One of the main focus of the LHC*b* experiment is the study of the particle-antiparticle asymmetry, so-called CP asymmetry, in the B meson sector. The CP transformation is a combined symmetry operation of the parity operator P (space inversion) and the charge conjugation operator C (charge conjugation). Although the precise study of CP violating effects in the B meson sector will not explain the origin of the matter dominance in the universe, it provides a powerful tool for indirect searches of NP [6, 7]. As these effects are a consequence of virtual particles that occur in loop processes, the measurement of CP asymmetries are especially sensitive to new heavy particles.

In one year of data taking at the nominal LHC luminosity foreseen for LHC*b*, about 10^{12} $B\overline{B}$ pairs are produced in the LHC*b* experiment. This gives access to CP violating B decay modes with very small branching fractions.

B mesons produced in the proton-proton collisions of the LHC fly on average about $7\,\text{mm}$ before they decay. The ability to precisely reconstruct the decay vertex is indispensable for a good proper-time resolution which is crucial to resolve the oscillations of neutral B mesons. Additionally, a good invariant mass resolution is necessary to reduce backgrounds: Besides the decay products of the B meson, about 50 other particles from

the underlying event are measured in the detector.
The up to five tracks originating from the B decay require a track reconstruction with high efficiency and a low rate of misidentified tracks.

All these requirements can only be accomplished with a well calibrated and spatially aligned detector. An accurate determination of the relative positions of the subdetectors to each other as well as an internal alignment of the subdetector components is of utmost importance.

Although during construction care was taken to install all detector elements at their nominal position, it is impossible to achieve absolute precisions of sub-mm over distances of many meters. Also, optical survey methods are limited in their significance. To achieve the required precision, the absolute positions of the detector elements have to be determined from the data itself. For this, dedicated alignment algorithms based on reconstructed tracks are necessary.

In the course of this thesis, a software alignment algorithm based on the program `Millepede` [8] has been developed. It allows to identify and correct for displacements of the LHC*b* Outer Tracker detector that is segmented into components of different granularities. The detector structure is considered by the algorithm and correlations between all detector elements imposed by particle trajectories are taken into account. The algorithm has been extensively tested on simulated data for the different granularities of the subdetector components.
It has been applied to tracks of cosmic ray events which have been collected during the LHC*b* commissioning phase. Within this thesis, the first spatial alignment of the LHC*b* Outer Tracker has been performed.

This thesis is divided into the following chapters:
In Chapter 1, an overview of the physics described by the Standard Model of Particle Physics is given. An emphasis is set to the introduction of the CP violation in the B meson system and to the decay channels of particular importance for the LHC*b* experiment. Further, the B meson production in proton-proton collisions is discussed. The LHC*b* experiment is presented in Chapter 2 where the main components of the detector and their functionalities are described. In Chapter 3, the impact of a misaligned Outer Tracker detector on the track reconstruction performance is discussed. The concept of a track based alignment algorithm is presented in Chapter 4 and the mathematics used in the algorithm that was developed is discussed. The general concept is adapted to the distinct needs of aligning the Outer Tracker detector elements. In the following Chapter 5, the developed algorithm is validated with simulated data and several misalignment scenarios. The results of the first spatial alignment of the Outer Tracker with measured data is presented in Chapter 6. Chapter 7 summarizes the results obtained with this alignment algorithm and an outlook is given on the detector alignment using data from proton-proton collisions.

Chapter 1

Theoretical background

1.1 The Standard Model

The aim of particle physics is to identify the fundamental building blocks of matter and the origin of interactions between them. The present understanding of this elementary question is given in a theory named the *Standard Model of Particle Physics* (SM) [9–11]. The SM basically describes two types of elementary particles: the fermions and bosons. They are elementary in the sense that they have no structure, at least down to the scale particle physics experiments could reach so far.

The fermions are spin $\frac{1}{2}$ particles and represent the matter units of the SM, they consist of leptons and quarks. The forces between particles are carried by the gauge bosons which are spin 1 particles. Four fundamental forces occur in nature, of which three are incorporated in the SM: electromagnetic, weak and strong force. The gravitation is the weakest of the forces and could not yet be integrated in the theory. Table 1.1 gives an overview of the forces and their relative strengths.

Leptons are arranged in three families, each family comprises one electrically charged and one neutral particle, the neutrino, as depicted in Table 1.2. Within the SM, neutrinos are massless[1]. The electron e forms a generation together with the electron neutrino ν_e. Accordingly, the muon μ and the tau τ lepton appear with the corresponding neutrinos. The muon and the tau differ from the electron only by means of their larger masses. In addition to the leptons, the quarks account for the other part of the SM fermions. Six different quark flavors are found that are again arranged in three families, each family comprises one up-type and one down-type quark. The up-type quarks carry the electric charge $+\frac{2}{3}q$, where q is the absolute value of the electron charge. The charge of the down-type quarks is $-\frac{1}{3}q$.

Additionally, quarks carry the so-called colour charge, a quantum number that is given in units of the colours red, green and blue and its corresponding anticolours antired, antigreen and antiblue. Colour, like electric charge, is always conserved and is responsible for the strong force which is described by the theory of Quantum Chromodynamics (QCD). The strong force is mediated by gluons, that also carry colour. A quark can change its colour when interacting with a gluon, hence gluons are in fact

---

[1] It has to be noted, that observations of neutrino oscillations provide evidence, that at least two neutrino flavors have non-zero masses [12]

Table 1.1: The four fundamental forces that occur in nature. Three of them, the strong, the electromagnetic and the weak force are incorporated in the Standard Model theory. Listed are the bosons which mediate the forces and the relative strengths of the forces. Note that the strength is an ambiguous notion in this case, as the strength of the force depends on the nature of the source and the distance with respect to it.

interaction	realtive strength	mediator	mass
strong	10	gluons	0
electromagnetic	10^{-2}	photon (γ)	0
weak	10^{-13}	$W^{\pm}$	$80\,\mathrm{GeV}/c^2$
		Z^0	$91\,\mathrm{GeV}/c^2$
gravitational	10^{-42}	graviton	?

"bicoloured" in order to preserve the colour quantum number. They carry colour and anticolour. On the macroscopic level, no colour charge is observed, i. e., all naturally occuring particles are colour neutral. This can only be achieved in states in which two or three quarks are bound (confinement). Baryons, for example, are composite structures of three quarks of which each has a different colour, resulting in a neutral particle. A bound state of a quark and an antiquark is called a meson which is neutral, as colour and anticolour are present. All these composed particles are denoted as hadrons.

About two orders of magnitude weaker than the strong force, the electromagnetic force interacts with all charged particles. The interaction is mediated by massless photons that are themselves electrically neutral bosons. The electromagnetic force is the dominant force between protons and electrons in an atom.

There is a little contribution to the proton-electron coupling by yet another neutral particle, namely the Z boson. Together with the charged W^+ and W^- bosons, it is a mediator of the weak force. Unlike the electromagnetic force, that couples only to charged particles and the strong force which only mediates between colour charged quarks and gluons, the weak force couples to all particles. The W^- boson of the weak force mediates for example the neutron decay: $n_{(udd)} \rightarrow p_{(uud)} + W^-(e^- + \bar{\nu_e})$. The underlying process of this decay is the flavor change $d \rightarrow u + W^-$ mediated by the W^-, see Figure 1.1 (b). In this process, both quark flavors are of the same family. But the weak force also mediates between quark families, e. g., $s \rightarrow u + W^-$, as depicted

Table 1.2: The matter particles of the Standard Model are leptons and quarks.They carry a half-integer spin and are arranged in three generations.

	charge q	1^{st} generation	2^{nd} generation	3^{rd} generation
Quarks	$+\frac{2}{3}$	u $(2\,\mathrm{MeV}/c^2)$	c $(1.25\,\mathrm{GeV}/c^2)$	t $(174\,\mathrm{GeV}/c^2)$
	$-\frac{1}{3}$	d $(5\,\mathrm{MeV}/c^2)$	s $(95\,\mathrm{MeV}/c^2)$	b $(4.2\,\mathrm{GeV}/c^2)$
Leptons	0	ν_e $(-)$	ν_μ $(-)$	ν_τ $(-)$
	-1	e $(511\,\mathrm{keV}/c^2)$	μ $(106\,\mathrm{MeV}/c^2)$	τ $(1.78\,\mathrm{GeV}/c^2)$

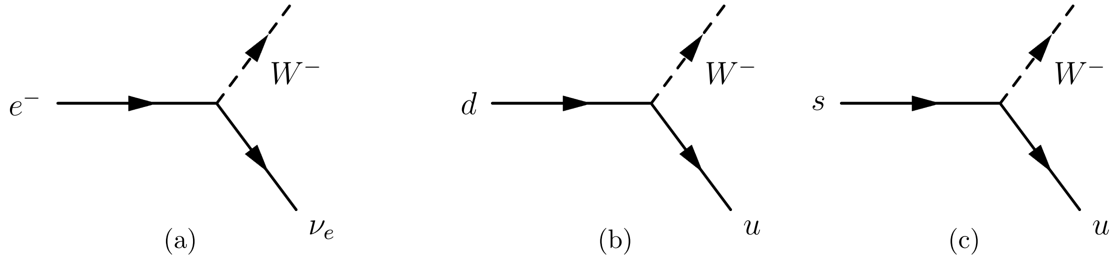

Figure 1.1: Feynman diagrams illustrating the coupling of the weak force to leptons and quarks. The time flows horizontally from left to right, this convention is used throughout this chapter. (a) The weak force couples only to leptons within the same generation. (b) Weak force coupling between the two quarks of the 1^{st} generation. (c) Cross-generational coupling of the W boson to the s quark of the 3^{rd} generation and the u of the 1^{st} generation.

in Figure 1.1 (c). This cross-generational coupling is much weaker compared to the previously mentioned. They may lead to CP violating effects, which will be discussed in detail in Section 1.1.1. In the SM, the electromagnetic and the weak forces are unified into one single elctroweak force.

Moreover, the SM not only describes the fundamental particles and forces, but also explains the origin of mass. This is achieved by the introduction of the so-called Higgs field into the theory. The quarks, leptons and also the massive Z and $W^\pm$ bosons acquire their mass after a spontaneous symmetry breaking (SSB) of the Higgs field. Additionally, the SSB introduces another new particle, which hasn't been observed yet: the Higgs boson. The discovery of the Higgs boson would manifest an important building block of the Standard Model. Therefore, the search for this particle is one of the main aspects for today's high energy physics experiments.

1.1.1 Quark mixing

The interaction between the charged weak force and leptons occures only between leptons within the same generation, as depicted for the first generation in Figure 1.1 (a). For quarks, the coupling within the same generation as well as the cross-generational coupling is possible. The feynman diagrams of these processes are given in Figure 1.1 (b) and (c), where the latter illustrates a coupling between quarks of the 2^{nd} and 1^{st} generations. The strength of the cross-generational coupling in figure (c) is much weaker than the strength of the process within the generation, although the same $W^\pm$ boson has coupled. The different coupling strengths are considered by so-called Cabibbo rotated states which transform the physical quarks d and s into the rotated states d' and s'. By using these weak interaction eigenstates, the correct coupling strength is obtained.

A general transformation from the physical quark state to the weak eigenstates is described by the Cabibbo-Kobayashi-Maskawa (CKM) quark mixing matrix as follows:

$$\begin{pmatrix} d' \\ s' \\ b' \end{pmatrix} = V_{CKM} \begin{pmatrix} d \\ s \\ b \end{pmatrix} . \tag{1.1}$$

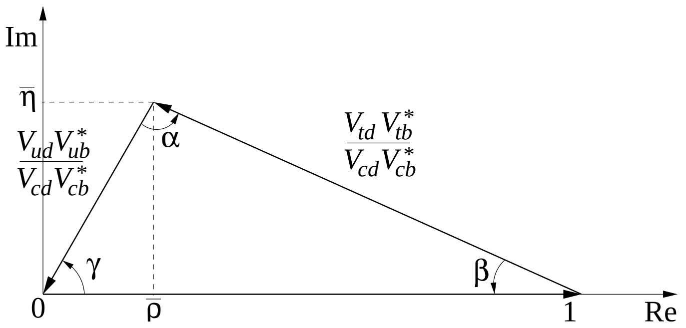

Figure 1.2: The unitarity triangle in the complex $\bar{\rho}, \bar{\eta}$ plane. (Figure from [14].)

The CKM matrix is a unitary matrix written as

$$V_{CKM} = \begin{pmatrix} V_{ud} & V_{us} & V_{ub} \\ V_{cd} & V_{cs} & V_{cb} \\ V_{td} & V_{ts} & V_{tb} \end{pmatrix} , \tag{1.2}$$

where V_{ud} specifies the coupling of u to d. A general complex 3×3 matrix represents in total 18 parameters. However, the unitarity relation $V_{CKM}^{\dagger} V_{CKM} = \mathbb{1}$ implies 9 constraints and another 5 phases can be absorbed by the redefintion of quark fields. This leaves 4 physical parameters which are represented by 3 rotation angles θ_{12}, θ_{13} and θ_{23} and one phase, resulting in the expression [13]

$$V_{CKM} = \begin{pmatrix} c_{12}c_{13} & s_{12}c_{13} & s_{13}e^{-i\delta} \\ -s_{12}c_{23} - c_{12}s_{23}s_{13}e^{i\delta} & c_{12}c_{23} - s_{12}s_{23}s_{13}e^{i\delta} & s_{23}c_{13} \\ s_{12}s_{23} - c_{12}c_{23}s_{13}e^{i\delta} & -c_{12}s_{23} - s_{12}c_{23}s_{13}e^{i\delta} & c_{23}c_{13} \end{pmatrix} , \tag{1.3}$$

where $s_{ij} = \sin\theta_{ij}$ and $c_{ij} = \cos\theta_{ij}$ and δ is the phase that is responsible for all CP violating effects in the Standard Model.

A convenient form of the CKM matrix is provided by the Wolfenstein parameterization that exhibits the experimentally known hierarchy $s_{13} \ll s_{23} \ll s_{12} \ll 1$. With the definitions

$$\begin{aligned} s_{12} &= \Lambda = \frac{|V_{us}|}{\sqrt{|V_{ud}^2| + |V_{us}|^2}} , \\ s_{23} &= A\Lambda^2 = \Lambda |\frac{V_{cb}}{V_{us}}| , \\ s_{13}e^{i\delta} &= V_{ub}^* = A\Lambda^3(\rho + i\eta) = \frac{A\Lambda^3(\bar{\rho} + i\bar{\eta})\sqrt{1 - A2\Lambda^4}}{\sqrt{1-\Lambda^2}[1 - A^2\Lambda^4(\bar{\rho} + i\bar{\eta})]} , \end{aligned} \tag{1.4}$$

the CKM matrix can be written in terms of Λ, A, $\bar{\rho}$ and $\bar{\eta}$ and fulfills the unitarity conditions in all orders of Λ:

$$V_{CKM} = \begin{pmatrix} 1 - \Lambda^2/2 & \Lambda & A\Lambda^3(\rho - i\eta) \\ -\Lambda & 1 - \Lambda^2/2 & A\Lambda^2 \\ A\Lambda^3(1 - \rho - i\eta) & -A\Lambda^2 & 1 \end{pmatrix} + \mathcal{O}(\Lambda^4) . \tag{1.5}$$

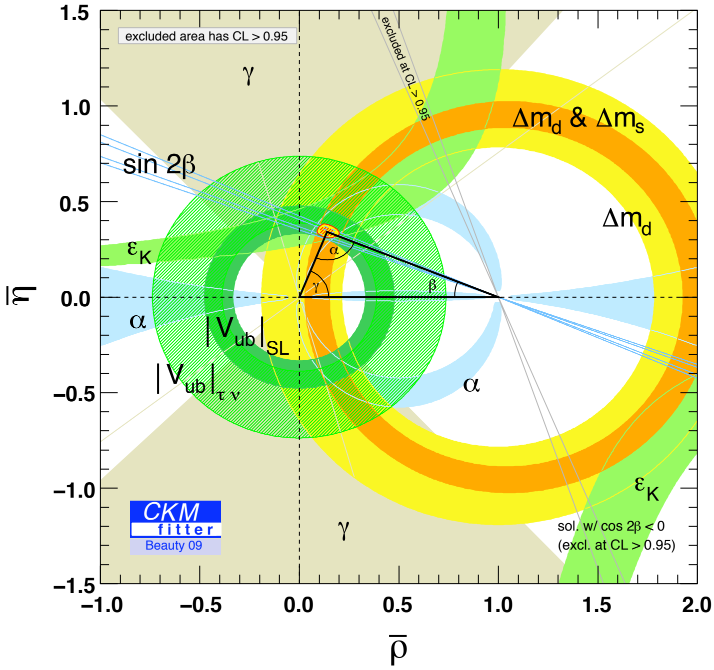

Figure 1.3: Constraints to the unitarity triangle from a global fit of all measurements contributing to the CKM matrix. The red hashed region of the global combination corresponds to 68 % confidence level. (Figure from [15].)

One of the constraints imposed by the unitarity condition can be expressed by the multiplication of the first column with the complex conjugates of the third column, resulting in

$$V_{ud}V_{ub}^* + V_{cd}V_{cb}^* + V_{td}V_{tb}^* = 0. \tag{1.6}$$

This relation can be expressed by a triangle in the complex plane by dividing each side by $V_{cd}V_{cb}^*$. The vertices of the triangle shown in Figure 1.2 are at $(0,0)$, $(1,0)$ and $(\bar{\rho},\bar{\eta})$ due to the definitions in Equation 1.4.

In total, six of the vanishing combinations like in Equation 1.6 can be described by such triangles. Of these triangles, only two have sides of the same order, whereas the others are squashed. However, the area within each triangle is the same for a all six triangles and is a direct measure of the amount of CP violation in the Standard Model [16].

The angles of the triangle in Figure 1.2 are given by

$$\alpha = \arg\left(-\frac{V_{td}V_{tb}^*}{V_{ud}V_{ub}^*}\right)\ ,\ \beta = \arg\left(-\frac{V_{cd}V_{cb}^*}{V_{td}V_{tb}^*}\right)\ ,\ \gamma = \arg\left(-\frac{V_{ud}V_{ub}^*}{V_{cd}V_{cb}^*}\right)\ . \tag{1.7}$$

In the B meson sector, the CP violating phase β_S is found in the almost degenerate $b-s$ unitary triangle obtained from the relation

$$V_{us}V_{ub}^* + V_{cs}V_{cb}^* + V_{ts}V_{tb}^* = 0. \tag{1.8}$$

Here, β_S is defined as the (positive) smaller angle given by

$$\beta_S = \arg\left(-\frac{V_{ts}V_{tb}^*}{V_{cs}V_{cb}^*}\right)\ . \tag{1.9}$$

An important goal of flavor physics is to find out if the CKM theory describes all flavor changing interactions. The CKM matrix elements are not calculable by the Standard Model, thus many measurements have been performed to overconstrain the matrix. The combination of all measurements performed on the matrix elements allows to check the unitarity of the CKM matrix. Figure 1.3 summarizes the current experimental status. Up to now, all measurements confirm that the flavor changing interactions are described by the CKM mechanism. The sum of the three angles, $\alpha + \beta + \gamma = (186^{+31}_{-32})^\circ$ [13] is consistent with the Standard Model expectation. However, the large uncertainty on this value is dominated by the uncertainty of the angle γ (as illustrated by the large brown band in the figure), for which a signifianct constraint from a direct measurement is missing up to now. One of the central goals of the LHC*b* experiment will be the precise measurement of this angle.

Moreover, many extensions of the Standard Model predict new effects in flavor physics which may be observable by measuring (CP-violating) decays in the B meson sector. Hence, an accurate measurement of the CKM matrix might give evidence to New Physics.

1.2 B meson sector

The LHC*b* experiment is dedicated to precision measurements in the B meson sector. This section introduces the phenomenon of B meson mixing and dicusses CP-violation in the B sector. The focus is put to the neutral B mesons, as they show large mixing amplitudes, which was first measured in 1987 by the ARGUS collaboration [17]. The quark content of the four neutral B mesons is as follows:

$$\begin{aligned} |B_d\rangle &= |\bar{b}d\rangle \quad , \quad |\overline{B}_d\rangle = |b\bar{d}\rangle \quad , \\ |B_s\rangle &= |\bar{b}s\rangle \quad , \quad |\overline{B}_s\rangle = |b\bar{s}\rangle \quad , \end{aligned} \tag{1.10}$$

which are the B flavor eigenstates. The B and $\overline{B}$ are antiparticles of each other and have the same mass and lifetime according to the CPT theorem. Throughout this section, the equations are written in terms of B and $\overline{B}$ which stands for either the B_d or B_s system.

A great advantage of studying these systems is the large mass of the b quark compared to the d or s, see Table 1.2. It enables to approximate effects due to the strong force, that cannot be calculated with perturbation theory. Thus, in a neutral B meson decay, the d and s quarks can be regarded as spectator quarks which allows a factorisation of the full process into a short-distant electroweak interaction and a long-distant strong interaction.

1.2.1 Mixing of B mesons

It is found that a B can evolve in time into a $\overline{B}$ and vice versa. This time evolution is described by the Schrödinger equation according to

$$i\frac{\mathrm{d}}{\mathrm{dt}} \begin{pmatrix} B \\ \overline{B} \end{pmatrix} = (M - \frac{i}{2}\Gamma) \begin{pmatrix} B \\ \overline{B} \end{pmatrix} \quad , \tag{1.11}$$

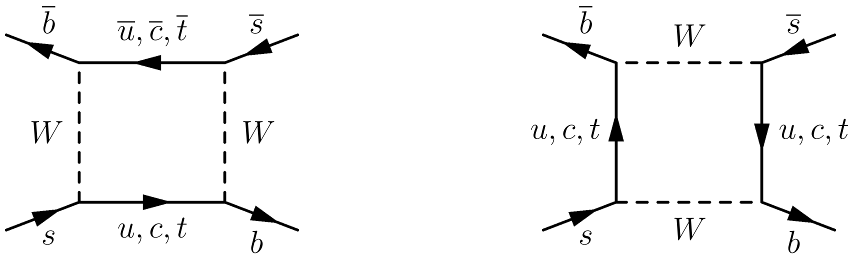

(a) (b)

Figure 1.4: The figure illustrates the B_s mixing through oscillation. One of the quarks u, c or t can "run" inside the loop. The dominant contribution arises from the t as its mass differs significantly from the u and c masses.

where M and Γ are two Hermitian 2×2 matrices. As follows from CPT symmetry, particle and antiparticle have the same mass and lifetime, hence $M_{11} = M_{22}$ and $\Gamma_{11} = \Gamma_{22}$. For the off-diagonal elements, the relation $M_{12} = M_{21}^*$ and $\Gamma_{12} = \Gamma_{21}^*$ holds. These elements are of importance for the discussion of two types of mixing, namely the mixing through decay and mixing through oscillation. The former mechanism corresponds to real, on-shell states from which Γ_{12} arises, whereas M_{12} arises from virtual intermediate states as depicted in Figure 1.4. The large B_s mixing follows from the top quark t contribution that dominates over u and c contributions in the loop due to the Glashow-Iliopoulus-Maiani (GIM) mechanism [18].

By diagonalizing the Hamiltonian $(M - i/2\Gamma)$, the mass eigenstates $|B_L\rangle$ and $|B_H\rangle$ of the neutral B mesons are obtained:

$$\begin{aligned} |B_L\rangle &= p|B\rangle + q|B\rangle \,, \\ |B_H\rangle &= p|B\rangle - q|B\rangle \,, \end{aligned} \tag{1.12}$$

with $|p|^2 + |q|^2 = 1$ and the time dependence given by

$$\begin{aligned} |B_L(t)\rangle &= |B_L\rangle e^{-\frac{\Gamma_L}{2}t} e^{-im_L t} \,, \\ |B_H(t)\rangle &= |B_H\rangle e^{-\frac{\Gamma_H}{2}t} e^{-im_H t} \,. \end{aligned} \tag{1.13}$$

$|B_L\rangle$ and $|B_H\rangle$ are the heavy and the light mass eigenstates, with $m_{L,H}$ and $\Gamma_{L,H}$ the corresponding masses and decay rates. The differences in mass and decay rates are defined as

$$\begin{aligned} \Delta m &= m_H - m_L \,, \\ \Delta\Gamma &= \Gamma_H - \Gamma_L \,, \end{aligned} \tag{1.14}$$

such that Δm is positive by definition, the sign of $\Delta\Gamma$ is determined experimentally. Additionally, the average mass and decay time are

$$\begin{aligned} m &= \frac{m_H + m_L}{2} \,, \\ \Gamma &= \frac{\Gamma_H + \Gamma_L}{2} \,. \end{aligned} \tag{1.15}$$

Solving Equation 1.11 gives the relation between ratio q/p and the off-diagonal elements M_{12} and Γ_{12}:

$$\left|\frac{q}{p}\right|^2 = \left|\frac{M_{12}^* - i\Gamma_{12}^*/2}{M_{12} - i\Gamma_{12}/2}\right| . \tag{1.16}$$

Together with the amplitudes of a decay to the final state f, that are given by $A_f = \langle f|B\rangle$ and $\overline{A}_f = \langle f|\overline{B}\rangle$, the weak mixing phase Φ is defined as

$$\Phi = -\arg\left(\frac{q}{p}\frac{\overline{A}_f}{A_f}\right) . \tag{1.17}$$

New Physics is expected to have almost no impact on Γ_{12}, but it can affect M_{12} considerably. This deviation can be parameterized by introducing the complex factor Δ_s [19]:

$$M_{12} = M_{12}^{SM} \cdot \Delta_s = M_{12}^{SM} \cdot |\Delta_s| e^{i\phi_s^\Delta} . \tag{1.18}$$

The mixing phase Φ is thus defined by the sum of its Standard Model value and the New Physics parameter ϕ_s^Δ:

$$\Phi = \Phi^{SM} + \phi_s^\Delta , \tag{1.19}$$

where Φ^{SM} is given by

$$\Phi^{SM} = 2\arg(V_{ts}^* V_{tb}) - 2\arg(V_{cb} V_{cs}^*) + \delta^{Penguin} , \tag{1.20}$$

and $\delta^{Penguin}$ is the contribution from the SM penguin decays. If this contribution is neglected,i.e. $\delta^{Penguin} = 0$, the weak SM mixing phase becomes

$$\Phi^{SM} = -2\beta_s , \tag{1.21}$$

with β_s as defined in Equation 1.9.

1.2.2 CP violation in the B meson system

The neutral B mesons are pseudoscalar particles which implies that a parity transformation P of the flavor eigenstates results in negative (odd) eigenvalues. The eigenvalue under charge conjugation C is +1 (even). Accordingly, the CP transformation of the B mesons gives

$$\begin{aligned} CP|B\rangle &= -|\overline{B}\rangle , \\ CP|\overline{B}\rangle &= -|B\rangle , \end{aligned} \tag{1.22}$$

which leads to the following (normalized) eigenstates of CP:

$$\begin{aligned} |B^{CP}\rangle_{even} &= \frac{1}{\sqrt{2}}(|B\rangle - |\overline{B}\rangle) , \\ |B^{CP}\rangle_{odd} &= \frac{1}{\sqrt{2}}(|B\rangle + |\overline{B}\rangle) . \end{aligned} \tag{1.23}$$

If CP conservation in the weak interactions is given, $|B^{CP}\rangle_{even}$ can only decay into a state with $CP = +1$ and $|B^{CP}\rangle_{odd}$ must go to a state with $CP = -1$. However, measurements of the K meson system revealed CP violation already in 1964 [20].

The following three types of CP violation must be distinguished:

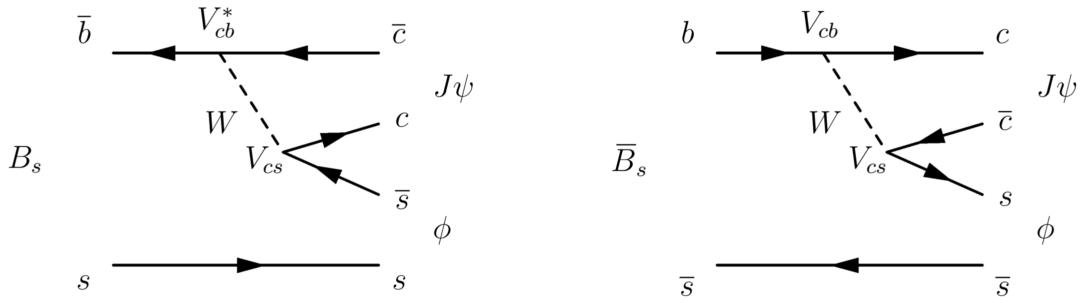

Figure 1.5: Feynman tree diagrams of the decays $B_s \to J\psi\phi$ and $\overline{B}_s \to J\psi\phi$.

- CP **violation in mixing** appears in case the oscillation probabilites of $B \to \overline{B}$ and $\overline{B} \to B$ are different. This implies that the CP eigenstates are not equal to the mass eigenstates, i. e., $|q/p \neq 1|$. In first order, CP violation in mixing is negligible in the B system ($< 10^{-2}$), however it is important in the Kaon system.

- CP **violation in decay** occurs when the amplitude of a B decay $A_f = \langle f|T|B\rangle$ and its CP conjugate process $\overline{A}_{\overline{f}} = \langle \overline{f}|T|\overline{B}\rangle$ have different magnitudes, hence if $|A_f| \neq |\overline{A}_{\overline{f}}|$. Here, T denotes the transition matrix element. CP violation in decay occurs in both charged and neutral systems. It has been measured by the Belle [21] and BaBar [22] experiments. This type of CP violation is caused by large interference between tree and penguin contributions in the decay.

- CP **violation in interference** connotes that the same final state can be reached directly via decay or through mixing and subsequent decay. This type of CP violation can be observed in case there is a relative phase between q/p from mixing and $\overline{A}_{\overline{f}}/A_f$ from decay. In the B_s and B_d system, CP violation in interference is a large effect.

In the following, the "golden" decay $B_s \to J/\psi\phi$ will be discussed which gives sensitivity to the CP violating phase Φ_s caused by interference between mixing and decay. Due to the domination of this single phase in the decay, the measured CP asymmetry can be interpreted in terms of purely electroweak parameters.

Decay to a CP eigenstate: $B_s \to J/\psi\phi$

The CP violation in the decay $B_s \to J/\psi\phi$ arises due to the interference between mixing and decay. Thus, the B_s can directly decay into the final states or oscillate into a $\overline{B}_s$ before decaying into the same final state. The feynman graphs for the particle and antiparticle decays are sketched in Figure 1.5. The final state in this decay consists of two vector mesons, whereas the B_s is a pseudo-scalar. Due to angular momentum conservation, the final state is a superposition of three possible states with relative orbital angular momentum $\ell = 0, 1, 2$ between the vector mesons. The CP eigenvalue depends on the relative angular momentum of the final state: The CP-odd final state is obtained for $\ell = 1$, the CP-even state for $\ell = 0, 2$. In order to statistically disentangle the CP-odd and CP-even components, an angular analysis of the decay is required.
Finally, an angular and time dependent analysis allows to extract the CP violating phase Φ_s, see Equation 1.17. In the Standard Model, this phase is predicted to be equal

to $-2\beta_s$ (Equation 1.21) with

$$-2\beta_s = -0.0360^{+0.0020}_{-0.0016}\,\text{rad}\ [13]\ . \tag{1.24}$$

The phase Φ_s is one of the CP observables with the smallest theoretical uncertainty in the Standard Model. As mentioned, New Physics can significantly modify the prediction of the phase which makes this B_s decay channel rather sensitive to contributions from physics beyond the Standard Model.
A detailed description of the LHC*b* analysis strategy for the decay $B_s \to J\psi\phi$ can be found in [23].

Currently, both experiments CDF and D∅ have presented results of the analysis of $B_s \to J\psi\phi$ decays [24–27]. It is expected that each of the two Tevatron experiments will have collected an integrated luminosity of $\mathcal{L}_{int} = 9\,\text{fb}^{-1}$ at the end of run 2. By scaling simply with $1/\sqrt{\mathcal{L}_{int}}$, the combined sensitivity to the weak phase Φ_s is estimated to be ~ 0.13 rad as illustrated by the black line in Figure 1.6. The figure reveals further that LHC*b* will measure the weak mixing phase Φ_s with a precision better than the magnitude of the Standard Model value with an integrated luminosity of about $2\,\text{fb}^{-1}$. Furthermore, the CDF and D∅ data have been analysed with respect to New Physics contributions to the measured phase Φ_s. The analysis has been performed in a model independent way (Equation 1.18), the result is presented in Figure 1.6. In the complex Δ_s plane, the obtained value shows a 1.9σ discrepancy with respect to the Standard

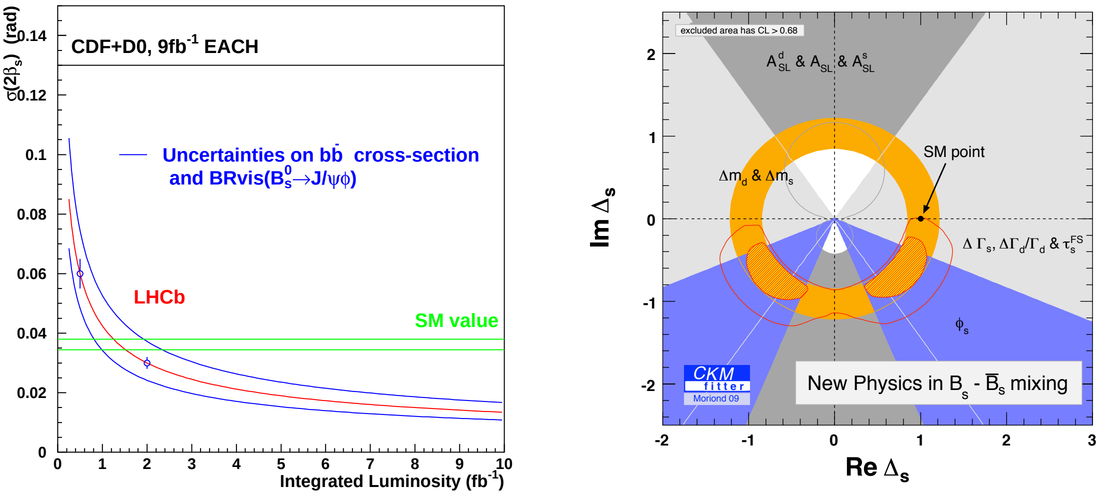

(a) (b)

Figure 1.6: (a) The red line shows LHC*b*'s sensitivity to the weak phase $\Phi_s = 2\beta_s$ versus the integrated luminosity. Blue band: Uncertainties due to the $b\bar{b}$ cross section and the visible branching ratio of $B_s \to J\psi(\mu^+\mu^-)\phi(KK)$. The black line shows the expected sensitivity from the Tevtron experiments. (Figure from [23].) (b) Constraints on New Physics in the $(Re\Delta_s, Im\Delta_s)$ plane, see Equation 1.18. The plot includes the current CDF and D∅ measurements. A 1.9σ deviation is obtained for the two dimensional Standard Model hypothesis $\Delta_s = 1$ $(Re\Delta_s = 1, Im\Delta_s = 0)$. (Figure from [15].)

Model value. It is one of the main goals of LHC*b* to determine whether the observed deviation is due to statistical fluctuations or a first sign of physics beyond the Standard Model.

Decay to a non-CP eigenstate: $B_s \to D_s^{\pm} K^{\pm}$

In the decay $B_s \to D_s^{\pm} K^{\pm}$, the final state is a non-CP eigenstate to which both the B and $\overline{B}$ can decay, the decay amplitudes differ for particle and antiparticle, respectively. The measurement of these decays allows to determine $\gamma + \Phi_s$, where Φ_s is the weak B_s mixing phase. The sensitivity of γ on tree level arises due to the interference between direct decay and decay after oscillation. In total, this process gives rise to four distinct, time dependent decay rates. The corresponding Feynman diagrams are drawn in Figure 1.7. The tree diagrams have different amplitudes due to different couplings: The process $\overline{B} \to D_s^- K^+$, for example, is "Cabibbo" suppressed due to the flavor change from the third to the first generation described by V_{ub}.

In principal, New Physics contribution could arise from charged Higgs bosons that mediate the decay rather than the $W^{\pm}$. However, given the large Higgs mass required to explain observed rates of processes like $b \to s\gamma$ [28], no significant contribution compared to the Standard Model expectation is anticipated.

At LHC*b*, the expected statistical uncertainty for an integrated luminosity of $2\,\mathrm{fb}^{-1}$ is $\sigma(\gamma + \Phi_s) = 10.3°$ [29]. The phase Φ_s originates from B_s mixing and can be measured directly using for example the decay $B_s \to J\psi\phi$. Combining the results of the weak angles from the two decays allows a clean way to extract γ. The current experimental result of γ is

$$\gamma = (77^{+30}_{-32})° \quad [13]\ . \tag{1.25}$$

The uncertainty on the parameter is expected to be reduced significantly at LHC*b*: Through the combination of the presented time dependent measurements of the decay

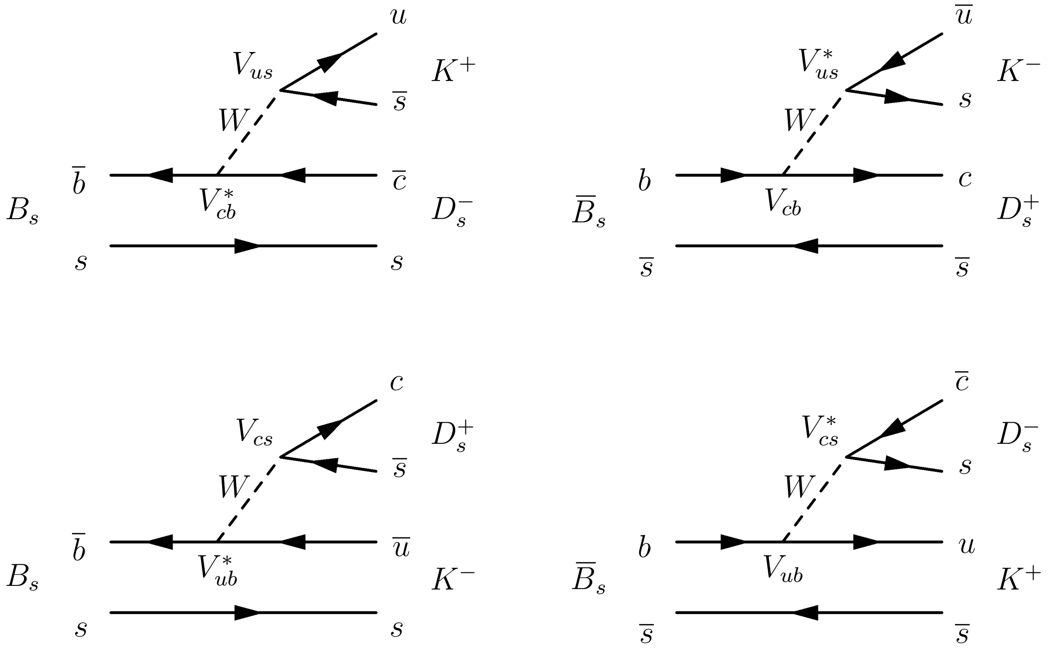

Figure 1.7: Feynman tree diagrams of the decays $B_s \to D_s^{\pm} K^{\pm}$ and $\overline{B}_s \to D_s^{\pm} K^{\pm}$.

$B_s \to D_s^{\pm} K^{\pm}$ with direct CP violation measurement of γ from the charged B meson decay $B^{\pm} \to D^0 K^{\pm}$, the estimated precision on γ will be $(4-5)^{\circ}$ after $2\,\mathrm{fb}^{-1}$ [29].

1.2.3 Rare decays

In the Standard Model flavor changing neutral currents (FCNC) are forbidden on the tree level. The lowest order contribution of FCNC in the Standard Model involve loops, for example weak penguin loops or weak box diagrams. The box diagram with two virtual W bosons is suppressed by a factor M_W^2/m_t^2 with respect to the penguin diagram. An example of a second order Standard Model contribution is presented in Figure 1.8 (a), which shows the Z-penguin diagram. The two outgoing muons are either both right handed or left handed, which leads to a helicity suppression proportional to m_μ/m_{B_s}. Furthermore, the electromagnetic penguin is forbidden because the B_s is a pseudo-scalar and the final state carries the momentum $\ell = 0$. The branching fraction expected from the Standard Model is

$$\mathcal{BR}(B_s \to \mu^+\mu^-) = (3.86 \pm 0.15) \times \frac{\tau_{B_s}}{1.527\,\mathrm{ps}} \frac{|V_{ts}|^2}{0.0408} \frac{f_{B_s}}{240\,\mathrm{MeV}} \times 10^{-9} \quad [31]\,, \qquad (1.26)$$

with the B_s meson lifetime τ_{B_s}, the decay constant f_{B_s} which has sizeable theoretical uncertainties and the CKM matrix element V_{ts} which is well measured.
Figure 1.9 (a) shows LHC*b*'s potential to exclude the $\mathcal{BR}$ at 90 % confidence level as a function of the integrated luminosity. Limits up to the Standard model prediction can be set with about $1\,\mathrm{fb}^{-1}$. Figure (b) shows the luminosity needed for a 3σ observation in case of presence of a signal. If the $\mathcal{BR}$ is equal with the Standard Model prediction, a 3σ observation is possible with an integrated luminosity of about $3\,\mathrm{fb}^{-1}$.
The Standard Model value of the branching ratio can be significantly enhanced in many New Physics models. The helicity suppression factor of m_μ/m_{B_s} makes the decay senstive to new scalar or pseudoscalar interactions. The decay $B_s \to \mu^+\mu^-$ can be used to probe models with an extended Higgs sector [33]. An example is the Minimal Supersymmetric Model (MSSM) which contains many new sources of flavor violation in

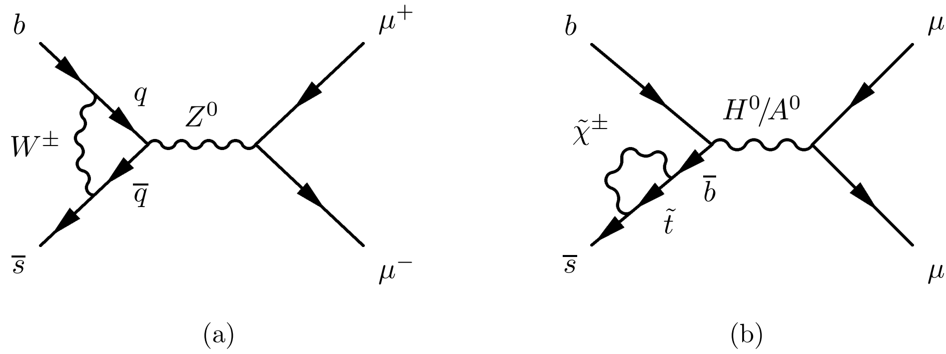

Figure 1.8: (a) Lowest order Standard Model diagram of the decay $B_s \to \mu^+\mu^-$. (b) The corresponding decay in the Minimal Supersymmetric Model (MSSM). New particles like the neutralino $\tilde{\chi}$ and heavy neutral Higgs bosons H^0 and A^0 can contribute to the process. (Figure from [30].)

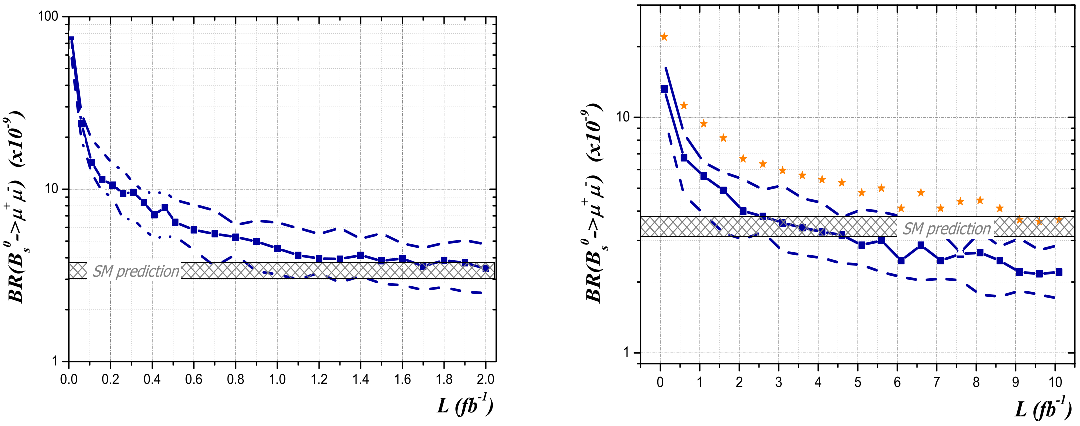

(a)

(b)

Figure 1.9: (a) LHCb's potential to exclude the branching ratio of the decay $B_s \to \mu^+\mu^-$ in case no signal is present. The blue line shows the exclusion at 90 % confidence level. (b) Luminosity needed for a observation of a signal with 3σ evidence (blue line). The orange stars indicate the luminosity needed for a 5σ discovery. The dashed lines define the 90 % probability region. (Figure from [32].)

addition to the Yukawa couplings. A feature of the MSSM are the two Higgs doublets which involve flavor changing neutral currents as depicted in Figure 1.8 (b). In this model, the branching ratio of $B_s \to \mu^+\mu^-$ can severely exceed the Standard Model value as it scales according to

$$\mathcal{BR}(B_s \to \mu^+\mu^-)_{MSSM} \propto \tan^6\beta \qquad [31]\ , \tag{1.27}$$

where $\tan\beta$ is the ratio of the vacuum expectation values of the Higgs doublets that couple to up-type and down-type particles, respectively [34].
Furthermore, the decay $B_d \to \mu^+\mu^-$ is well accessible by the LHCb experiment. However, its branching ratio is about an order of magnitude lower compared to $\mathcal{BR}(B_s \to \mu^+\mu^-)$ because of an additional CKM suppression $\sim V_{td}/V_{ts}$.

1.3 B meson production at the LHC

The Large Hadron Collider (LHC) will provide proton-proton collisions with a maximal center of mass energy of $\sqrt{s} = 14\,\text{TeV}$. The dominant production mechanism in the pp-collisions is the fusion process of gluons and partons as sketched in the leading order diagrams in Figure 1.10. The perturbative QCD cross section for heavy flavor production has been calculated to next-to-leading order [36].
The pp cross section are summarized in Figure 1.11 for different center of mass energies. It shows, that the expected total cross section at $\sqrt{s} = 14\,\text{TeV}$ is $\sigma_{tot} = 102.9\,\text{mb}$ and $698\,\mu\text{b}$ for the $b\bar{b}$ cross section [37].

The $b\bar{b}$ cross section is influenced by higher order diagrams where the $b\bar{b}$ pairs are created either through flavor excitation or gluon splitting. These higher order contributions are non-negligible and impose large uncertainties on the predicted cross sections. Therefore,

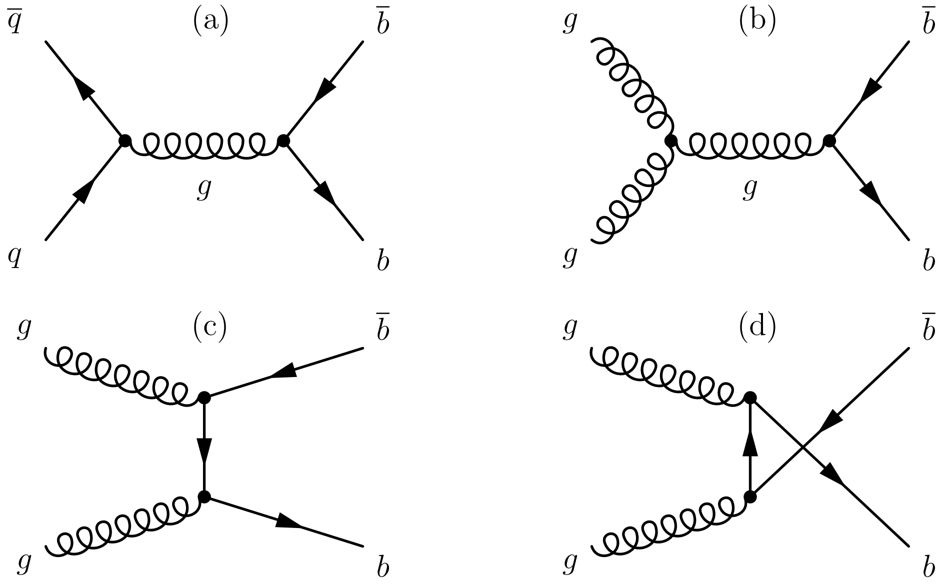

Figure 1.10: Leading order Feynman diagrams of $b\bar{b}$ production. (a) Pair creation through quark-antiquark annihilation. (b,c,d) $b\bar{b}$ creation through gluon fusion. (Reproduced from [35].)

the LHC*b* collaboration decided to use a conservative convention for the $b\bar{b}$ cross section to estimate event yields:

$$\sigma_{b\bar{b}} = 500\,\mu\text{b} \ . \tag{1.28}$$

The total cross section σ_{tot} is usually divided into two parts, namely the elastic and inelastic cross section. Elastic collisions leave the colliding protons intact and are rarely seen in the detector as the protons mainly escape through the beam pipe. The inelastic collisions, however, do emit particles that are measured in the detector. An important number for precision measurement of the CP asymmetry in the B meson sector is the ratio $\sigma_{b\bar{b}}/\sigma_{inel}$, with the inelastic cross section σ_{inel}. This ratio basically determines the ratio of signal over background. With an inelastic cross section of $\sigma_{inel} = 80\,\text{mb}$ expected for *pp*-collisions at $\sqrt{s} = 14\,\text{TeV}$ [38], about 1 in every 160 collisions produces a $b\bar{b}$ pair.

The total number of inelastic *pp*-collisions over a given time period equals

$$N_{pp} = \sigma_{inel} \int \mathcal{L}\text{d}t \ , \tag{1.29}$$

where σ_{inel} is the inelastic cross section and $\mathcal{L}$ the instantaneous luminosity. The nominal luminosity at the LHC*b* interaction point is $\mathcal{L} = 2 \times 10^{32}\,\text{cm}^{-2}\text{s}^{-1}$. Together with the $b\bar{b}$ cross section in Equation 1.28, one year ($10^7\,\text{s}$) of operation at nominal luminosity will yield about 10^{12} $b\bar{b}$ pairs. This b pair production yield makes the LHC an optimal facility to study the B sector as the branching fractions of the B decay channels used to measure CP violation are of order $10^{-4} - 10^{-6}$.

After a *pp*-collision, most of the B mesons created from the $b\bar{b}$ pairs are expected to be emitted in the same forward or backward cone, respectively. The reason for this boost are the different momenta of the interacting partons, that carry a momentum fraction

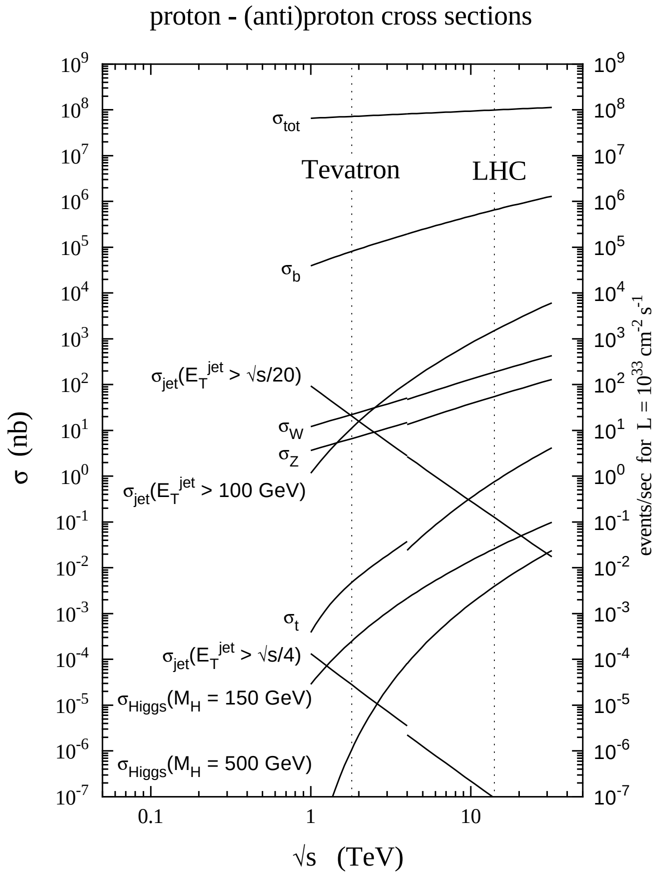

Figure 1.11: Cross section for hard scattering versus $\sqrt{s}$. The dashed lines indicate the center of mass energy of $p\bar{p}$ collisions at Tevatron and of pp collisions at $\sqrt{s} = 14\,\text{TeV}$ at the LHC, respectively. The expected cross section at $\sqrt{s} = 14\,\text{TeV}$ are $\sigma_{tot} = 102.9\,\text{mb}$ and $\sigma_{b\bar{b}} = 698\,\mu\text{b}$. (Figure from [37].)

x of the total proton momentum. As the center of mass energy of the pp-collisions rises, also the difference of the parton momenta increases which leads to a larger boost of the $b\bar{b}$ pair in the detector frame. Figure 1.12 shows a simulation result of the angular correlation of the produced b quark pairs. This correlation motivated the design of the LHCb detector as a single arm forward spectrometer. A common definition in particle physics is the pseudorapidity η given by

$$\eta = -\ln\left(\tan\frac{\theta}{2}\right) , \qquad (1.30)$$

where θ is the polar angle with respect to the beam axis. The LHCb detector covers a region of $2 < \eta < 5$ which implies that about one third of the produced $b\bar{b}$ pairs decay within the detector acceptance.

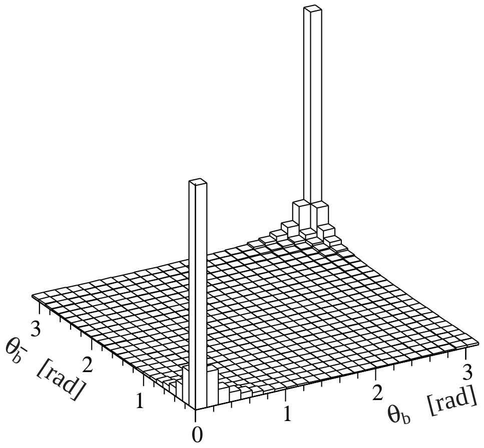

Figure 1.12: Correlation of the polar angles of the hadrons containing the b and $\bar{b}$ quark at $\sqrt{s} = 14\,\mathrm{TeV}$.

Chapter 2

The LHC*b* experiment

The LHC*b* experiment is dedicated to study B meson decays with very high precision. These B mesons are produced by inelastic proton-proton collisions that are provided by the LHC collider at CERN.
In the LHC*b* detector, the mean flight distance of the B mesons is expected to be about 11.8 mm. Hence a very good vertex resolution is requisite to separate the B decay vertex from the production vertex. This separation is decisive for the identification of fake background events, that typically come from primary *pp* collisions. The ability of a good vertex resolution is declined in case several inelastic *pp* collisions are within the same bunch crossing, so called pile-up events. In LHC*b*, these pile-up events are reduced to a minimum by operating with an average luminosity of $\mathcal{L} = 2 \times 10^{32}\,\mathrm{cm}^{-2}\mathrm{s}^{-1}$ [38]. Figure 2.1 (a) depicts the probability for single and multiple collisions for different luminosities. Clearly, the optimal luminosity has been chosen at a point where the probability of a single inelastic collision is significant larger than for multiple interactions.

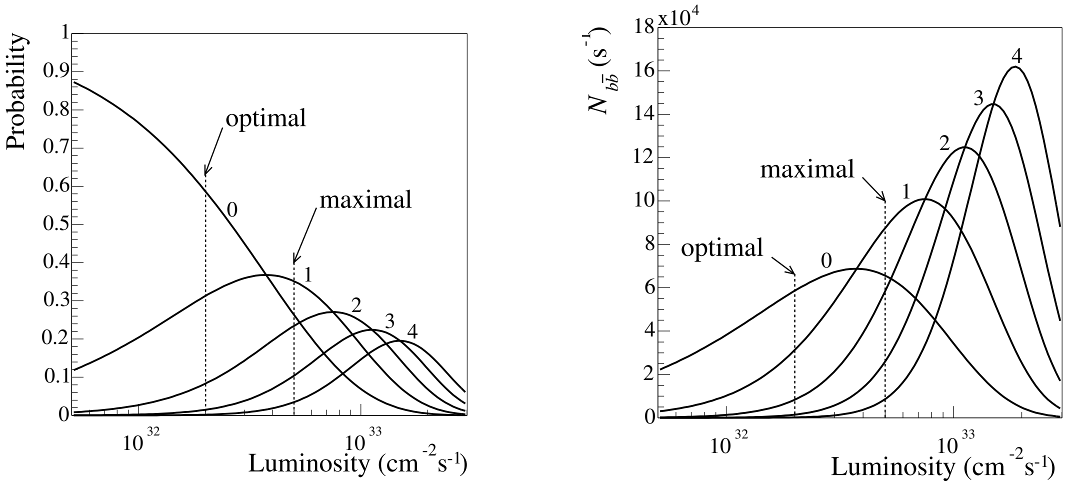

(a)

(b)

Figure 2.1: (a) Probability for $0, 1, 2, 3, 4$ inelastic bunch crossings versus luminosity. (b) Number of $b\bar{b}$ events per second for $0, 1, 2, 3, 4$ pile-up events with respect to the luminosity.

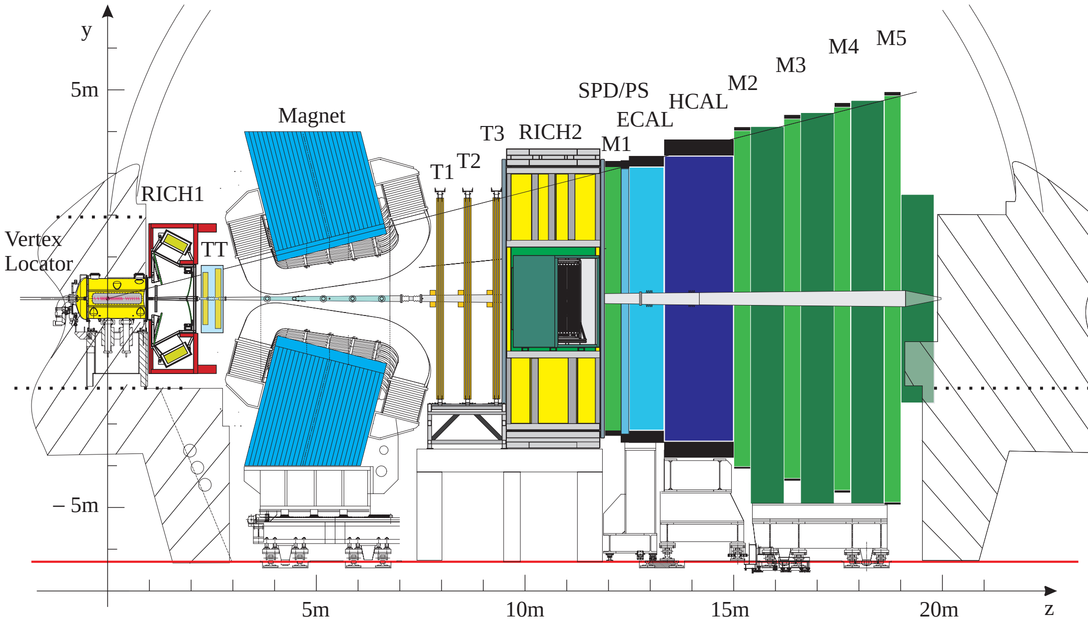

Figure 2.2: Side view of the LHC*b* detector. The interaction point in the Vertex Locator defines the origin of the coordinate system. Depicted are the two RICH detectors, the magnet and the tracking system composed of the Vertex Locator, Trigger Tracker (TT) and three tracking stations T1, T2 and T3. The calorimeter system with the Scintillating Pad Detector (SPD) and the Preshower Detector (PS), followed by the electromagnetic and hadronic calorimeters (ECal and HCal). The Muon stations are denoted M1-M5. (Figure from [5].)

At the optimal luminosity, the number of $b\bar{b}$ events per second without pile-up collisions is close to the maximum possible value, as shown in figure (b). Each subdetector is designed for an operation of a maximal luminosity of $\mathcal{L} = 5 \times 10^{32}\,\mathrm{cm}^{-2}\mathrm{s}^{-1}$, as indicated in the figure. This design leaves some freedom in the final choice of the optimal operation luminosity.

Running the detector at the moderate luminosity has several advantages: The detector occupancy is low which makes the reconstruction of particle trajectories easier and the radiation damage of the detector is reduced.

The optimal luminosity can already be obtained in the first year of LHC operation, when the collider runs at $\mathcal{L} = 10^{33}\,\mathrm{cm}^{-2}\mathrm{s}^{-1}$. One year of data taking (10^7 s) at nominal luminosity yields an integrated luminosity of $\mathcal{L} = 2\,\mathrm{fb}^{-1}$, which corresponds to about 10^{12} produced $b\bar{b}$ pairs [5].

As discussed in Section 1.3, the $b\bar{b}$ pairs are produced in forward or backward direction. Hence, the LHC*b* detector is designed as a single arm forward spectrometer as sketched in Figure 2.2, having a large acceptance for B events. Throughout this thesis, the coordinate system is defined as depicted in the figure:

- The origin of the system is the interaction point inside the vertex locator.
- The z axis points from the interaction point towards the LHC*b* detector and is aligned with the beam direction. It has to be noted, that due to construction

of the LHC collider, the beam line is inclined by 3.601 mrad with respect to the horizontal.

- The x axis is horizontal and perpendicular to the z axis. It points to the right when following the z axis, thus it points inside the paper in Figure 2.2.
- The y axis points upwards and is perpendicular to the x and z axis. The axis is inclined by 3.601 mrad with respect to the vertical.

The detector covers an acceptance of $10 - 300$ mrad in the x direction, the bending plane of the magnet, and $10 - 250$ mrad in the y direction (non-bending plane).
In the following sections, the subdetectors are described that can be categorized into tracking detectors and particle identification detectors:

- **Tracking detectors:** Vertex Locator (VELO), Trigger Tracker (TT), Inner Tracker (IT) and Outer Tracker (OT).
- **Particle identification detectors:** Cherenkov detectors (RICH 1 and RICH 2), electromagnetic and hadronic calorimeter (ECal and HCal) and the muon stations.

The introduction of the subdetectors is followed by the presentation of the LHC*b* trigger system and a brief introduction to the LHC*b* software framework.

2.1 Tracking system

Charged particles that traverse the detector are bend by the magnetic field of the main dipole magnet [39]. Their momenta are measured by the deflection of the trajectories. It is inversely proportional to the difference between the track slope in the Vertex Locator and the slope in the T stations, Figure 2.2.

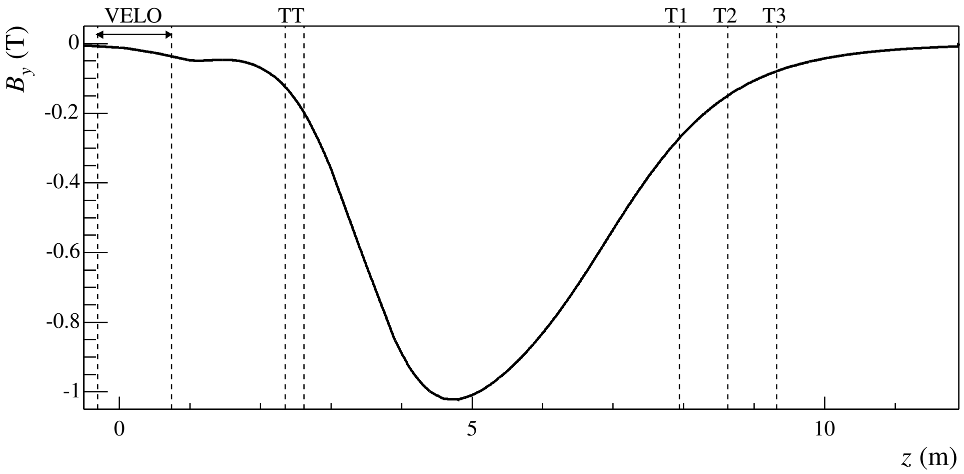

Figure 2.3: Main component of the magnetic field along the z direction. Indicated are the positions of the tracking stations.

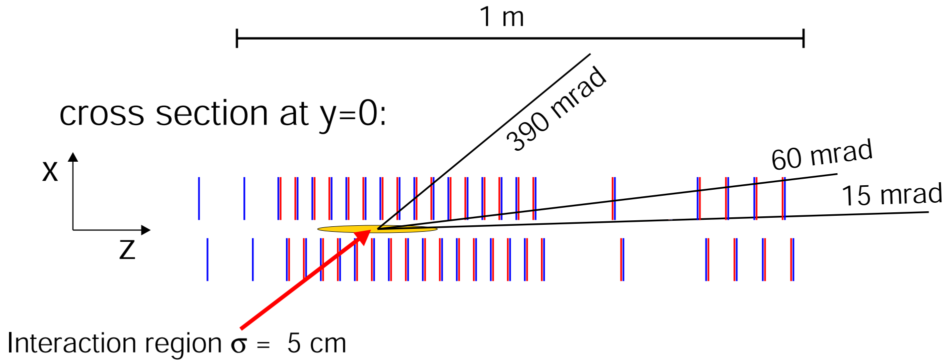

Figure 2.4: Top view of the arrangement of the Vertex Locator stations around the interaction point. (Reproduced from [5].)

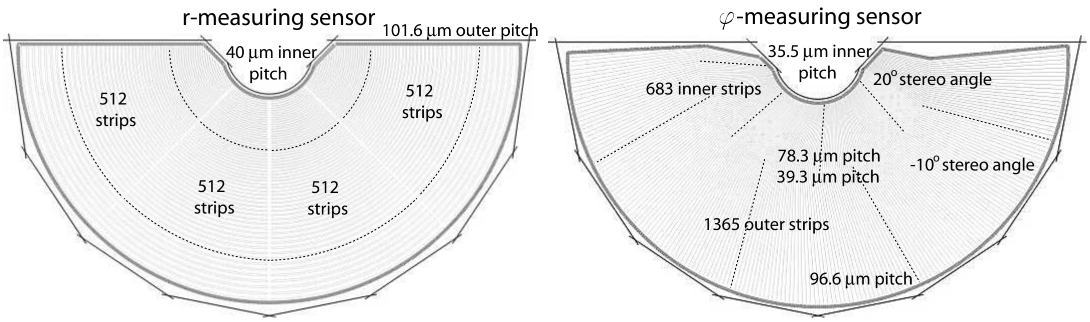

Figure 2.5: The two types of measuring sensors used in the Vertex Locator. (Figure from [5].)

The bending power of the magnetic is described by the integrated magnetic field following

$$\int Bdl = 4.2\,\mathrm{Tm}\ . \tag{2.1}$$

The magnetic field is orientated in the y direction, such that the bending of trajectories is maximal in the xz plane and almost negligible in yz. The strength of the y component of the field (B_y) along the z direction is sketched in Figure 2.3. The positions of the tracking detectors are indicated as well.

2.1.1 Vertex Locator

The Vertex Locator (VELO) [5, 40] comprises 21 stations that are positioned close to the interaction point. The stations are placed along and perpendicular to the z axis as sketched in Figure 2.4. The detector consists of two types of silicon sensors that are mounted back to back. One sensor is designed for position measurements in r direction, which is realized by circular strips mounted around the center, shown on the left of Figure 2.5. The second sensor is designed with radial, straight strips to measure the ϕ coordinate, depicted on the right of Figure 2.5.

With this $r - \phi$ geometry, a direct projection in the rz plane is possible by using only

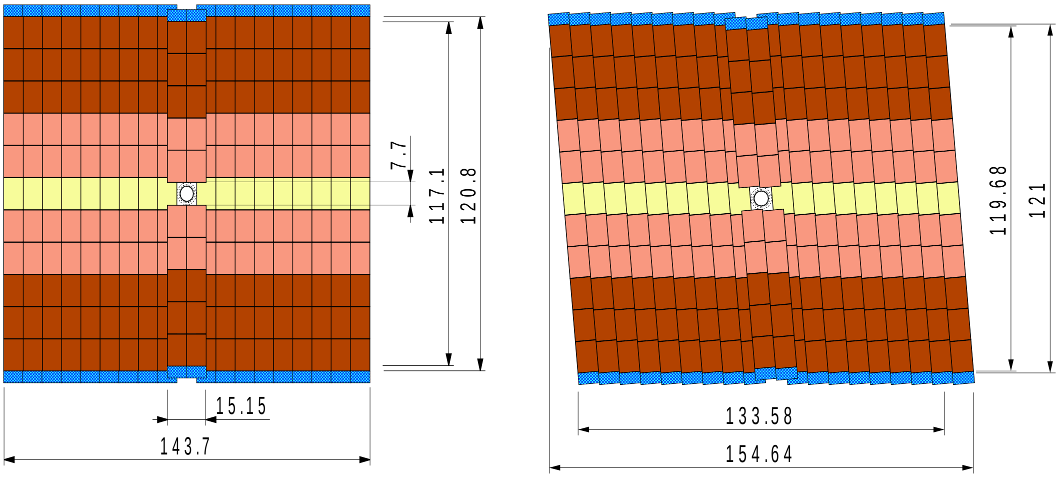

Figure 2.6: Two layers of the Trigger Tracker. The left panel shows a x layer, the right a stereo layer. The shading indicate strip connections, see text. (Figure taken from [5].)

r measurements. This way, forward going tracks with a high impact parameter[1] with respect to the production vertex are easily identified. This idea is extensively used by the trigger: It first reconstructs all tracks in the rz plane before reconstructing only the tracks with a large impact parameter in all three dimensions.
The $300\,\mu$m thick sensors are based on single-sided n-on-n technology. The particle flux is highest near the beam pipe, hence the pitch of the strips increases towards the outer sections of the sensors to provide a more homogeneous occupancy throughout the detector. For the ϕ sensors, the pitch increases from $35.5\,\mu$m to $96.6\,\mu$m on the outside, the pitch of the r strips increase from $40\,\mu$m to $101.6\,\mu$m. The average occupancy per channel is well below 1 %.
To reduce the uncertainty of impact parameter measurements because of track extrapolations to the interaction region, the sensitive area of the sensors starts at a radius of about 8 mm from the beam axis. To protect the sensors against severe radiation damage when the LHC is filled with protons, the VELO detector halves can be moved away from the beam in horizontal direction.
A thin aluminium foil (RF foil) separates the sensors from the beam vacuum in order to prevent out-gassing of the sensors into the this vacuum and to shield the electronics against RF pickup from the beams. In stable running condition, i. e., the VELO halves are closed, the distance between foil and beam line is 5 mm.

2.1.2 Trigger Tracker

The Trigger Tracker (TT) [5] sketched in Figure 2.6 is located just upstream the magnet (Figure 2.2). It consists of two stations that are separated by a distance of 27 cm. Each station has two layers of silicon strip detectors covering the full acceptance. The strips of the four layers are arranged as x, u and v, x layers, corresponding to angles with the y axis of $0°, -5°, +5°$ and $0°$. This stereo view allows the reconstruction of tracks in

---

[1] The impact parameter is defined as the distance of closest approach between the track and the primary vertex.

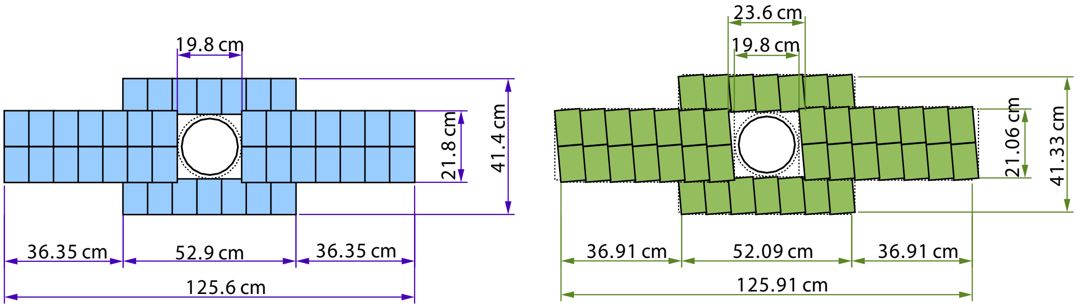

Figure 2.7: A x and stereo layer of the Inner Tracker. Depicted are the silicon sensors that are arranged around the beam pipe in a cross shape. (Figure from [14].)

three dimensions. The vertical orientation of the strips allows a good spatial resolution in the xz plane, the bending plane of the magnet.

A TT layer is build out of 9.44 cm × 9.64 cm sensors that cover in total an area of about $8.4\,\mathrm{m}^2$, see Figure 2.6. The thickness of a sensor is $500\,\mu$m, the pitch between the strips is $183\,\mu$m. Strips of three or four (depending on the distance from the horizontal plane) neighbouring sensors are connected, such that they share a single readout. Hence, a spatial resolution of about $50\,\mu$m [41] is reached.

2.1.3 Inner Tracker

The Inner Tracker (IT) [42] is part of the tracking detectors located downstream the magnet and covers the region of high particle flux close to the beam pipe. The IT consists of three stations that are composed of four boxes each, which are placed around the beam in a cross shape, as sketched in Figure 2.7. Though the detector covers only approximately 2 % of the 6 m × 5 m acceptance of the T stations, it measures about 20 % of the particle flux. Four layers of silicon strip detectors are installed inside every box, arranged in the x, u, v, x stereo view, similar to the TT. The used silicon sensors are based on the single-sided p^+-on-n technology and are of size 11 cm × 7.6 cm with a strip pitch of $198\,\mu$m. Single and double sensors are used which are of different thickness: $320\,\mu$m for the single and $410\,\mu$m for the double sensors. This choice of thicknesses ensures a sufficiently signal to noise ratio for each sensor type while minimising the material budget of the detector.

The resulting resolution is approximately $50\,\mu$m [5]. In the IT, the average hit occupancy is expected to be less than 2 %.

2.1.4 Outer Tracker

As part of the T stations behind the magnet, the Outer Tracker (OT) [43] covers the large area outside the acceptance of the Inner Tracker. The OT uses drift tube technology for the tracking of charged particles and the measurement of their momentum.

Like the IT, the Outer Tracker consists of three stations (T1, T2 and T3) of which each station has four detection layers in the x, u, v, x configuration. Table 2.1 lists the z positions of the layers. All layers are of equal size which is determined by the acceptance requirement of the last layer in T3. The detection surface of each layer is

Table 2.1: Positions of the Outer Tracker layers along the z direction.

T1		T2		T3	
layer	z_{min}[mm]	layer	z_{min}[mm]	layer	z_{min}[mm]
x	7838	x	8525	x	9215
u	7894	u	8581	u	9271
v	7951	v	8638	v	9328
x	8007	x	8694	x	9384

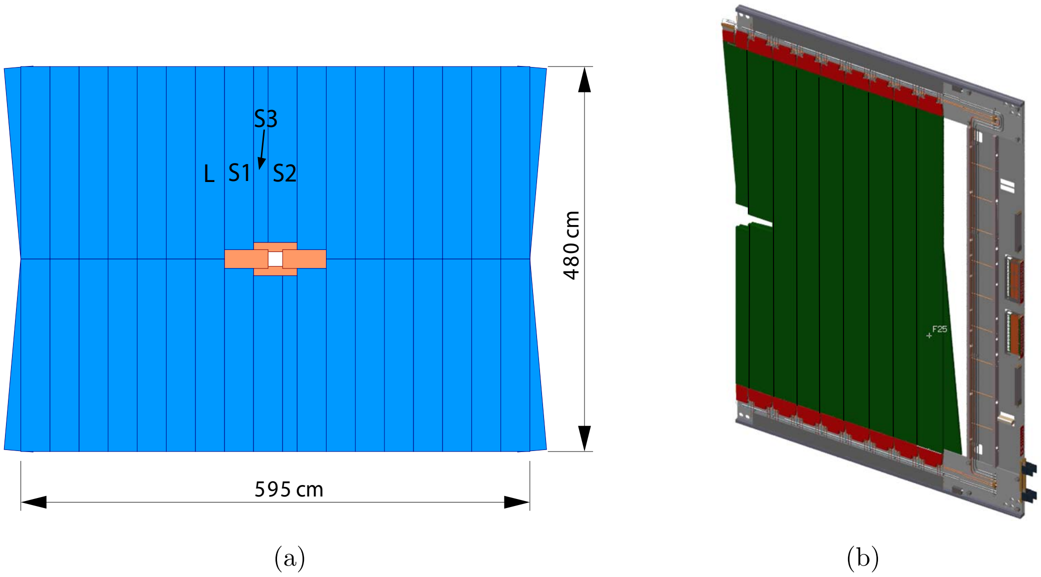

(a) (b)

Figure 2.8: (a) Front view of an Outer Tracker station. Depicted is a x layer with the Inner Tracker in the center. In addition, part of the outermost modules of the stereo layers are visible. (b) A C-frame, the supporting structure of the modules. One C-frame comprises one x and one stereo half layer.

5.95 m × 4.8 m, the front view of a layer is shown in Figure 2.8 (a). In the center of the picture the IT boxes are depicted that are placed around the clearance for the beam pipe. The inner boundaries of the OT acceptance are chosen such, that the occupancies do not exceed 10 % for nominal LHC*b* luminosity.

The modular design of the Outer Tracker is highlighted in the figure. Seven long modules (denoted L) are placed left and right of the Inner Tracker, respectively. Shorter modules are positioned above and below the silicon detector - named S1, S2, S3 in the figure. In total, the OT consists of 216 modules (the short modules above and below the the IT are physically connected to form four 4.8 m long modules).

The modules are mounted on aluminium support structures, the so called C-frames, an example is depicted in Figure 2.8 (b). Therefore every layer is laterally split into two halves. As visible in the figure, one x type and one stereo type half layer are mounted on the same frame. The C-frames are installed in a stainless steel structure and are movable along the x direction, as shown in Figure 2.9 (a). The supporting table and

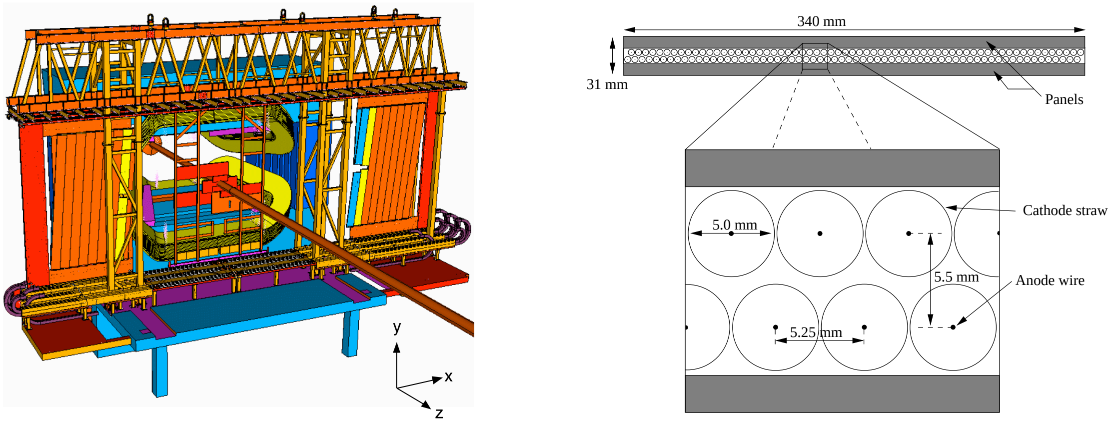

(a) (b)

Figure 2.9: (a) Supporting structure for the C-frames. Each frame is mounted on rails and can be moved along the x direction. (Figure from [5].) (b) The staggered layout of a module. A small region with a few modules is magnified. (Reproduced from [14].)

bridge are illustrated together with the magnet and the beam pipe. Moreover, the Inner Tracker is sketched around the beam pipe.

All modules contain 128 straw tubes that are arranged in two mono layers of 64 straws each, except for the S3 modules. These modules are of half width and thus comprise 32 straws per mono layer. Figure 2.9 (b) depicts the staggered layout of the module layers. The pitch between two straws of the same monolayer is 5.25 mm, a straw tube has a diameter of 5 mm. A 25.4 μm thick, gold coated tungsten wire is placed in the center of a straw and operates as the anode. Wire locaters are installed every 80 cm to guarantee the position of the wire. The cathode wall of the tube is composed of two foils: The inner foil is made of 40 μm carbon doped polyimide (Kapton-XC), the outer winding are of 25 μm polyimide and 12.5 μm aluminium to enhance the gas tightness and to ensure fast signal propagation and shielding, respectively.

The straw tube monolayers are glued between two panels of a 10 mm thick polymethacrylimide stiff foam (Rohacell) with a skin of 120 μm carbon fibre. This sandwich structure, together with the side walls, provides a stiff and gas tight box [44]. With the used materials, the total radiation length for the entire Outer Tracker is below 10 %.

The straws in the long L modules are not continuous from top to bottom, but are split in two halves to limit the occupancy of hits. Hence the readout electronic is installed at the top and bottom of the long modules, whereas for the short modules it is either on top or bottom. The electronic measures the time difference between measured signal and the bunch crossing (BX) time. The total time difference t_{tot} can be expressed by the following terms:

$$t_{tot} = t_{tof} + t_{drift} + t_{prop} + t_0 \, , \tag{2.2}$$

with t_{tof} is the time of flight of the particle, t_{drift} the drift time of the primary electrons in the straw tube, t_{prop} refers to the electronic signal propagation time in the wire and t_0 to an time offset. This time offset is caused by delays in the readout chain or in case of a phase shift between the readout electronic clock and the bunch crossing clock. The calibration of this offset is essential for the correct determination of the drift time.

The readout window of the OT is open for three consecutive bunch crossings (75 ns) in order to measure also maximum possible signal collection times. The average cell efficiency is 98 %, the spatial resolution is below 200 μm [45].

Optical Alignment and Monitoring

During installation of the OT, the C-frames positions are surveyed by optical triangulation measurements [46]. In order to identify displacements or even deformation of the frames, the points at which the modules are mounted to the frame are determined with respect to a well defined survey coordinate system. Selected points on the surface of the modules are surveyed additionally for the determination of possible deviations from a planar surface. The positions are measured with an accuracy of 500 μm.
The position of the C-frames are further monitored under running conditions. For that, the RASNIK [47] system has been developed. The basic idea is to project a reference picture through a lens onto a CCD camera. Thus, misalignments perpendicular to the measurement line are detected by a shift of the reference picture to the side. A change of the picture size indicates a shift along the measurement direction. The intrinsic resolution of the system is 10 μm and 150 μm perpendicular and along the measurement direction, respectively.

2.1.5 Tracking strategy

The LHC*b* track reconstruction is basically done in two steps: First, the pattern recognition or track finding algorithms are processed, which associate measurements to tracks. Second the found particle tracks are fitted.
Depending on the subdetectors that are traversed by a particle, different track types are defined. They are illustrated in Figure 2.10 and described in the following:

- **Long tracks** traverse the whole tracking system from the VELO to the T stations. The momentum resolution of *long tracks* is very precise, hence they are most useful for physics analyses.
- **VELO tracks** only traverse the VELO. Due to their typically large polar angle, they allow a precise determination of the primary vertex. Also backward tracks are solely measured in the VELO.
- **Upstream tracks** are measured only in the VELO and TT stations. They are bent out of the acceptance before reaching the T stations. Though their momentum resolution is reduced, they can be used in several B decay analyses.
- **Donwstream tracks** traverse the TT stations and are measured in addition in the T stations. They are used for the reconstruction of K_S^0 mesons that decay outside the VELO.
- **T tracks** are solely reconstructed in the T stations.

Several pattern recognition algorithms are used for the reconstruction of these tracks. The aim is to achieve a high track reconstruction efficiency while the rate of ghost

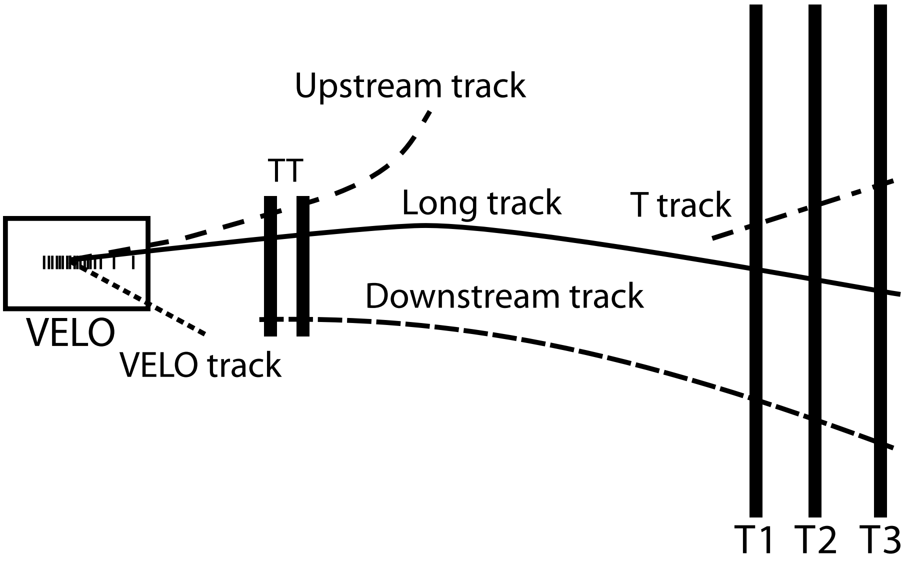

Figure 2.10: The different track types in the LHC*b* tracking system. (Figure from [5].)

tracks, i. e., tracks with a significant number of wrong hits, is kept to a minimum.
As mentioned, *long tracks* are most useful for physics and hence of particular interest. In Chapter 3, the impact of Outer Tracker misalignment on the reconstruction of *long tracks* will be discussed in detail. Hence, the algorithms used to find and reconstruct long tracks are described in the following:

- **VELO seeding:** The algorithm [48] combines $r - \phi$ clusters for a three dimensional reconstruction of the track. As the residual magnetic field in the VELO is negligible the tracks are reconstructed as straight lines. This VELO seeds are further used in the other track finding algorithms.

- **Forward tracking:** The aim of the forward tracking [49, 50] is to reconstruct *long tracks*. The track search starts with a VELO seed and searches for continuations in the T stations. The idea is that a single additional hit in either T1, T2 or T3 is sufficient to describe the trajectory. Hence, the track is parameterized as a polynomial of second order in y, and of third order in x direction. Remaining hits are collected inside a search window around the trajectory. Finally, a likelihood method is applied to the track candidate with the most confirming hits. This way, correctly reconstructed tracks are verified whereas ghost tracks are rejected. TT hits are added if they are close enough to the reconstructed track.

- **T seeding:** This algorithm [51] searches for track segments in the T stations. At first, it searches for measurement in the xz plane assuming a straight line track and considering only hits in the x layers. Second, the residual magnetic field is regarded and the found trajectory is parameterized as a parabola. The stereo layer hits are finally added for the confirmation of the two dimensional candidates. Again, a likelihood method is applied to consider inefficiencies and insensitive detector regions and to reject ghost tracks.

- **Track matching:** The combination of VELO seeds and T seeds to *long tracks* is called track matching [14]. The algorithm matches the two seed tracks at a plane located just behind the last VELO station. After a first momentum estimation for the T seeds, this momentum is used to propagated the track with a fifth order Runge-Kutta method from the T stations to the matching plane. The VELO seed is extrapolated to the plane by a straight line. Here, a χ^2 criterion[2] is applied to select the successfully matched tracks.

The performance of the presented track reconstruction algorithms is discussed in detail in Chapter 3. A description of the overall tracking strategy can be found in [52].

2.2 Particle identification system

Particle identification (PID) is required for many purposes at LHCb. Lepton identification is required for the muon trigger as well as for tagging applications. A π/K separation is essential for the selection of many B decay channels.
The sub detectors belonging to the PID system are described in the following sections.

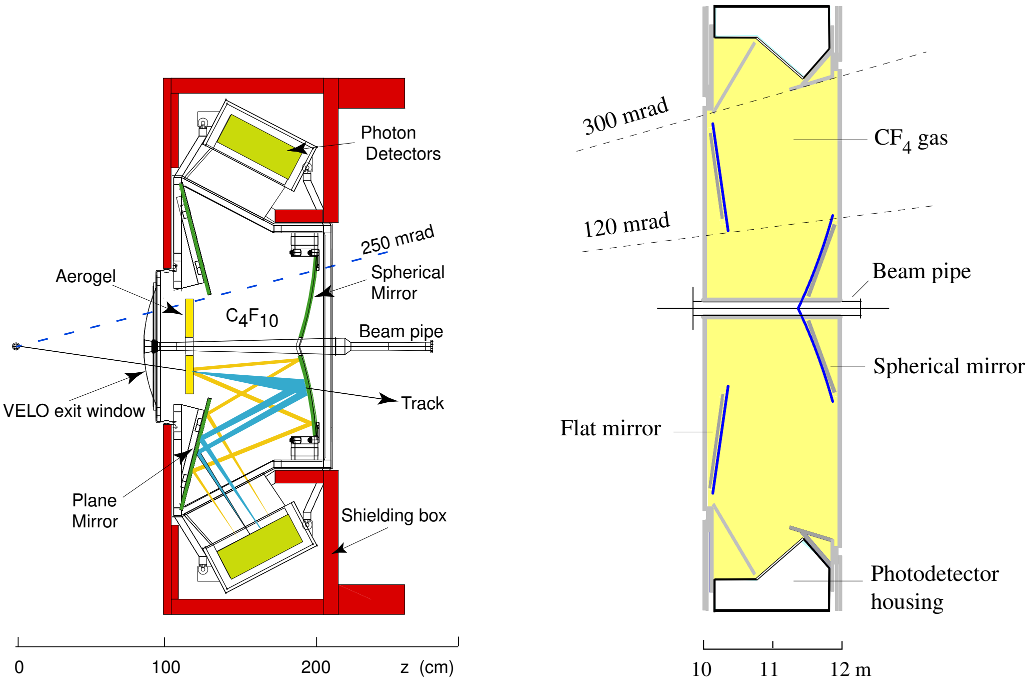

(a) (b)

Figure 2.11: (a) Side view of the RICH 1 detector. (b) Horizontal cross section of RICH 2. (Figures from [14].)

2.2.1 Rich Detectors

The Ring Imaging Cherenkov (RICH) detectors [5, 53] provide a π/K separation in the range of $2-100\,\text{GeV}$. The system consists of the RICH 1 and RICH 2 detectors that are placed between VELO and TT stations and just in front of the calorimeters, respectively.

The particle identification provided by the RICH detectors is based on the determination of the particle velocity: Once the velocity is determined and the momentum is known from the reconstructed track, the particle is identified by its mass.

The particle velocity relies on the measurement of Cherenkov light. This light is emitted by particles that traverse a medium with a velocity greater than the velocity of light in that same medium. The photons are emitted under an angle with respect to the particle trajectory, which is called the Cherenkov angle θ_c. This angle depends on the particle velocity $\beta = v/c$

$$\theta_c = \frac{1}{n\beta}\,, \tag{2.3}$$

with n being the refraction index of the radiator material. The use of different radiator media allows the velocity determination over a large momentum spectrum.

Two radiators are used in RICH 1 to cover a momentum spectrum between about $1-60\,\text{GeV}$. A 5 cm thick silica aerogel with an refraction index $n = 1.03$ serves as first radiator to identify particles with momenta up to 10 GeV. Second, particles traverse through a gas of C_4F_{10} along a 85 cm long path. This gas has an refraction index $n = 1.0014$ and is used for measurements in the momentum range $10-60\,\text{GeV}$.

Emitted photons are detected with Hybrid Photon Detectors (HPD) that project an image at the photocathode with a granularity of $2.5\,\text{mm} \times 2.5\,\text{mm}$. Figure 2.11 (a) depicts the RICH 1 detector which covers an acceptance of $25\,\text{mrad} - 300\,\text{mrad}$ in x direction and of $25\,\text{mrad} - 250\,\text{mrad}$ in y.

A horizontal cross section of RICH 2 is illustrated in figure (b). The detector is designed for the identification of particles with momenta from about 15 GeV up to 100 GeV and beyond for which CF_4 gas with a refraction index $n = 1.0005$ is utilized. The covered acceptance of RICH 2 is between 25 mrad and 120 mrad in the horizontal and up to 100 mrad in the vertical.

2.2.2 Calorimeter system

The Calorimeter system [54] is designed to identify hadrons, electrons and photons and to measure their energies and positions. This information is used in the trigger and has to be provided with sufficient selectivity in a very short time. Furthermore, the system allows an accurate photon detection which is essential for the reconstruction of many B decays.

Incident particles interact with the calorimeter material and produce a cascade of secondary particles which are finally absorbed. Induced ionisations excite atoms in the scintillator material that emit light when returning to the ground states. The total amount of measured light is proportional to the energy deposit of the shower in the calorimeter.

---

[2] The general definition of the χ^2 is given in Section 4.2.

Table 2.2: The physical dimension in z and the corresponding electromagnetic (X_0) and hadronic (Λ) interaction length for the different parts of the Calorimeter system. In addition, the segmentation of the detector layers is listed.

	depth along	interaction length	segmentation $[\mathrm{mm}^2]$		
	$z[\mathrm{mm}]$	X_0/Λ	inner part	middle part	outer part
SPD	180	2.0/0.1	40.4×40.4	60.6×60.6	121.2×121.2
PS			40.4×40.4	60.6×60.6	121.2×121.2
ECal	835	25/1.1	40.4×40.4	60.6×60.6	121.2×121.2
HCal	1650	$-/5.6$	131.3×131.3	-	262.6×262.6

The demanding requirements on the detector performance in terms of resolution and shower separation lead to a longitudinal segmentation of the system (Figure 2.2):

- **Scintillating Pad Detectors** (SPD) are installed right after Muon station M1 in order to distinguish between charged and neutral particles.
- The **Preshower Detector** (PS) just behind the SPD is used for the e/π separation.
- The **Electromagnetic calorimeter** (ECal) follows the PS detector and determines the energies of electrons and photons.
- The **Hadronic calorimeter** (HCal) is positioned downstream the ECal for the measurement of hadronic showers of pions, kaons and protons.

The acceptance of the Calorimeter system is 300 mrad horizontally and 250 mrad vertically.

The SPD and PS detectors are designed to improve the particle identification in the ECal. An incident particle first traverses the scintillator material of the SPD where charged particles will deposit energy while neutral particles will not interact with the material. Hence a separation between neutral and charged particles is possible. Between SPD and PS, a 12 mm thick lead wall is installed. Here, electromagnetic showers will be induced and detected in the PS, which provides information for the discrimination between electrons and hadrons.

The light of the scintillators is readout by wavelength shifting (WLS) fibres and that are coupled to multianode photomultipliers (MAPMT) by clear plastic fibres. For both the SPD and PS, the scintillator pad sizes differ from the inner to the outermost detector region in order to consider the high particle flux near the beam pipe. The lateral segmentation is realized by three sections of different granularity, as shown in Figure 2.12. The scintillator pad size is given in Table 2.2 for the corresponding sections. The SPD and PS segmentation is adopted by the ECal.

The ECal uses shashlik type modules which implies 66 alternating layers of 2 mm thick lead and 4 mm thick scintillator tiles. The resulting stack corresponds to 25 electromagnetic interaction length (X_0) and 1.1 hadronic interaction length (Λ). Shashlik technology has been chosen considering modest energy resolution, fast time response

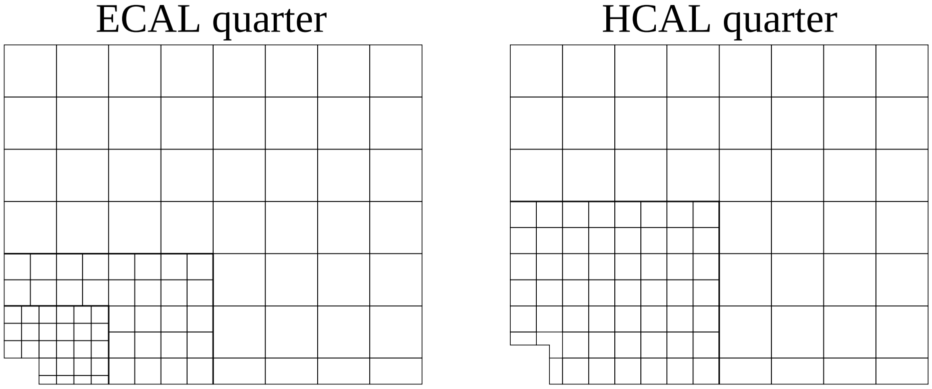

Figure 2.12: A quadrant of a layer of the electromagnetic and of the hadronic calorimeter. The segmentation ensures a constant occupancy over the whole detector layer. The dimensions of the pads are listed in Table 2.2. (Figure from [14].)

and eligible radiation resistance. The deposited energy E is measured with a resolution according to

$$\frac{\sigma(E)}{E} = \frac{10\,\%}{\sqrt{E}} \oplus 1\,\% \,, \tag{2.4}$$

where the energy is given in GeV and $\oplus$ means addition in quadrature.
The hadron calorimeter is a sampling device made from iron and scintillating tiles. The tile are interspaced with 1 cm thick iron in the lateral direction, whereas the longitudinal dimension of the tiles and iron spacers corresponds to the hadron interaction length in steel, which sums up to 5.6Λ for the whole HCal (Table 2.2). The orientation of the scintillator tiles is parallel to the beam axis. Hence, the WLS readout fibres are running along the detector towards the back side to the photomultipliers.
The segmentation of the HCal is depicted in the right panel of Figure 2.12. It shows the square cells of size $131.3\,\mathrm{mm}^2$ for the inner section and of size $262.6\,\mathrm{mm}^2$ for the outer section. By grouping together different sets of fibres onto one photomultiplier, readout cells of different sizes are defined resulting in the modest energy resolution of

$$\frac{\sigma(E)}{E} = \frac{80\,\%}{\sqrt{E}} \oplus 10\,\% \,, \tag{2.5}$$

where E is expressed in GeV.

2.2.3 Muon system

Many CP-sensitive B decays have muons in their final states. Hence, muon triggering and also offline reconstruction of muons is of great importance at LHC*b*. Therefore, five muons stations (M1-M5) [55] are installed that cover an acceptance of $20-306\,\mathrm{mrad}$ in the bending and $16-258\,\mathrm{mrad}$ in the non-bending plane. It is the acceptance of about 20 % for muons from inclusive b semileptonic decays.
The Muon system is sketched in Figure 2.13 (a) and shows the positioning of stations M2-M5 downstream the calorimeters that are interleaved with 80 cm thick iron absorbers. Station M1 is placed in front of the Calorimeter system to improve the momentum

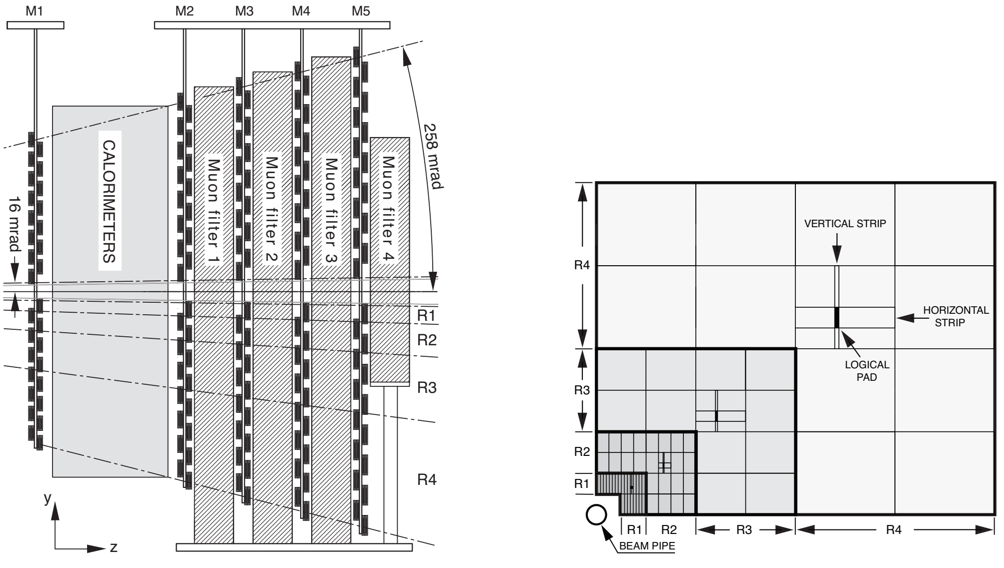

(a) (b)

Figure 2.13: (a) Side view of the five Muon stations that are interleaved with iron absorbers. (b) Front view of one quadrant of station M2, showing the four regions R1, R2, R3 and R4 of different size. A region is divided into sectors that contain crossing strips. The intersection of a horizontal and a vertical pad defines a logical pad. (Figure from [5].)

Table 2.3: Size of the logical pads (see Figure 2.13 (b)) in x and y for the four regions of every Muon station.

	M1	M2	M3	M4	M5
R1 [mm^2]	10 × 25	6.3 × 31	6.7 × 34	29 × 36	31 × 39
R2 [mm^2]	20 × 50	12.5 × 63	13.5 × 68	58 × 73	62 × 77
R3 [mm^2]	40 × 100	25 × 125	27 × 135	116 × 145	124 × 155
R4 [mm^2]	80 × 200	50 × 250	54 × 270	231 × 290	248 × 309

measurement of muons by minimizing uncertainties due to scattering in the calorimeter material. The minimum muon momentum required for the traverse of all five stations is about 6 GeV.

Each Muon station is laterally segmented into four regions R1-R4 with increasing pad granularity from inner to outer sections, see Figure 2.13 (b). The pad dimensions are listed in Table 2.3 for the four regions of each Muon station. With this geometry, the channel occupancy is expected to stay constant over the four regions of a station. Moreover, a more accurate momentum measurement in x direction is provided by the rectangle dimensions of the pads.

The detector is equipped with multiwire proportional chambers (MWPC) [56], which fulfill the trigger requirement to collect the signal within 20 ns as well as the required radiation hardness. Yet, in the innermost region of M1, triple-GEM detectors [57] are used due to the high particle flux.

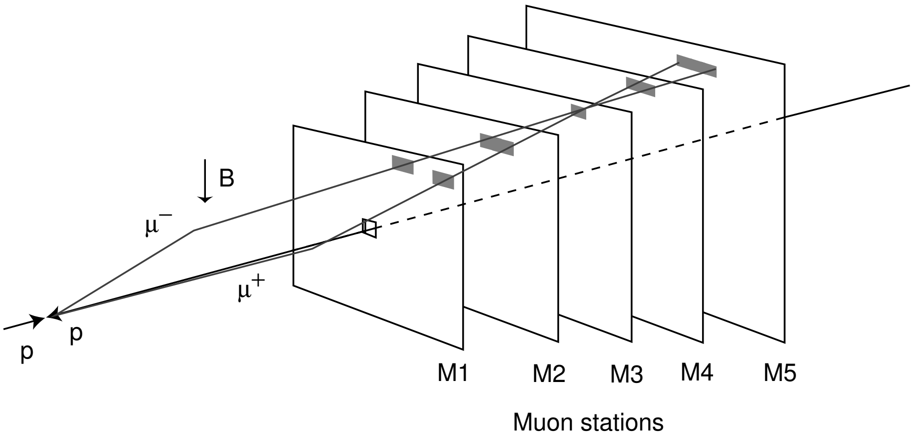

Figure 2.14: Tracking strategy for the muon trigger. The track search starts with hits in M3 and is continued in the region of interest in the other stations (highlighted). It is assumed, that the muon tracks originate form the interaction point. The deflection in the magnetic field is used ot estimate the transverse momentum p_T. (Figure from [58].)

2.3 Trigger system

LHC*b* plans to operate at a nominal luminosity of $\mathcal{L} = 2 \times 10^{32}\,\mathrm{cm}^{-2}\mathrm{s}^{-1}$. With a bunch crossing rate of 40 MHz provided by the LHC collider, the rate of events with at least one visible interaction[3] in the detector is 14 MHz. This rate has to be reduced by the trigger [58] to about 2 kHz at which rate the events can be written to storage for further offline analysis. For this purpose, the trigger performance is optimised to achieve highest efficiency for events selected in the offline analysis and to reject background events as strongly as possible at the same time.

The general trigger strategy is based on the hardware L0 trigger and the software High Level Trigger (HLT) that are described in the following.

2.3.1 L0 hardware trigger

The aim of the L0 trigger is to reduce the bunch crossing rate of 40 MHz down to a detector readout rate of 1.1 MHz. The trigger is divided into three subsystems, namely the muon trigger, the calorimeter trigger and the pile up system. With these systems, the hardware trigger attempts to reconstruct the hadron, electron and photon with the highest transversal energy E_T and muons with high transversal momentum p_T. The task of the different subsystems can be described as follows:

- The **Pile-Up** system is located upstream of the VELO and uses four VELO r-sensors. Its aim is to distinguish between bunch crossing with single and multiple visible interactions. Moreover it provides the positions of primary vertices along the beam line and a measure of the upstream track multiplicity. This allows to veto events with multiple primary vertices or which are particularly busy.

---

[3] An interaction is defined to be visible if at least five tracks are in the acceptance of the spectrometer.

- The **Calorimeter Trigger** searches for particles with high transverse energy E_T deposit in the electron and hadron calorimeters. A zone of two by two cells [54] is large enough to contain most of the energy of the candidates and small enough to avoid overlaps between various particles. In case of a hadronic shower, the energy measured in the ECal is added to the HCal candidate. A first particle hypothesis is given with the additional information of the Scintillating Pad Detector (SPD) and the Preshower detector (PS) in front of the ECal. For each particle type ($e^{\pm}, \gamma$ or hadron), only the candidate with the highest E_T is kept.

- The **Muon Trigger** is designed to select muons with a high transverse momentum p_T. These high p_T muons are found by a standalone fast track reconstruction algorithm that selects hits in all five stations. The momentum is estimated by the slope of the track between M1 and M2 assuming that the particle originated from the interaction point. The expected transverse momentum resolution is about 20 %. Figure 2.14 illustrates this tracking strategy.

The total latency of the L0 trigger is fixed to 4 μs. This implies the particle time of flight and delays in the cables and electronics that add up to 2 μs, which leaves another 2 μs for the processing of the data.

2.3.2 High Level Trigger

The High Level Trigger (HLT) is fully implemented in software and runs on the Event Filter Farm at the L0 output rate of 1.1 MHz. It reduces this input rate to the final 2 kHz output rate. The HLT is split in two consecutive running algorithms, the HLT 1 and HLT 2 algorithm.

HLT 1 reduces the hardware input rate by a factor ~ 30 by means of a partial event reconstruction. The idea is to use L0 objects as seeds to define a region of interest in which the reconstruction is performed. This way, the CPU time needed for decoding and pattern recognition is reduced to a minimum and a HLT 1 output rate of about 30 kHz is achieved.

Additional reduction of the data is reached by the full event reconstruction performed in HLT 2 following HLT 1. Several inclusive selections of B candidates allow to half the HLT 1 output rate to the final trigger output rate of 2 kHz.

Though the requirements for a fast processing prohibit a reconstruction as accurate as the offline reconstruction, both the tracking and the vertexing achieve a precision comparable to what is obtained offline. *Long tracks* which are fitted with a simplified fit in the trigger have a relative momentum resolution of $\sigma_p/p \approx 0.54\,\%$, whereas the corresponding offline precision is $\sigma_p/p \approx 0.50\,\%$ [59].

Table 2.4 summarizes the input and output rates of the different trigger levels.

2.4 LHC*b* software framework

The realization of a spectrometer as complex as the LHC*b* detector relies on intensive simulation studies concerning the overall performance of the detector. Track reconstruction studies, for example, provide valuable information about particle scattering

effects in the detector material, which in turn can lead to a redesign of certain detector components. Studies of the sensitivity to physics parameters have to be performed on simulated data for the determination of an optimal event selection. Later, the achieved selection criteria serve as a starting point for the analysis of real data.
All these studies, however, require an elaborate software framework that allows the simulation of the experiment as realistic as possible. In LHC*b*, this is achieved by the integration of the software within the object orientated framework of Gaudi [60]. The framework provides basic functionalities like job steering, data access and data analysis. Different applications that are implemented in this framework can exploit these services. The applications used for the simulation, reconstruction and analysis of an typical event in the LHC*b* detector are described below, followed by additional information of the software alignment application.

2.4.1 Framework applications

This section gives an overview over LHC*b*'s software applications within the Gaudi framework. The task of each application can be described as follows:

- **GAUSS:** The Gauss [61] application entails the event generation and detector simulation. For this purposes, it first delegates the simulation of the pp collision to the external program Pythia [62]. This program provides the four momentum vectors of the outgoing particles. However, the decay of the B mesons is reproduced by the program Evtgen [63].
  Finally, the propagation of the particle through the detector is simulated by the program package Geant4 [64]. The software considers the interaction of the particle with the detector material, the deflection in the magnetic field and the decay of the remaining unstable particles.

- **BOOLE:** The Boole [65] package simulates the detector response. Here, the interactions of particles with the sensitive area of the detector induce hits which are digitized into an electrical signal. For all subdetectors, this digitization simulation relies on the calibration from test beam data results.

- **MOORE:** The trigger application Moore [66] is processed in between the digitization and reconstruction step. As the trigger consists of the L0 hardware trigger and the HLT software trigger, this application can be seen as part of the digitization as well as part of the reconstruction.

Table 2.4: Input and output rates for the different trigger levels.

	input rate	output rate
L0	40 MHz	1.1 MHz
HLT 1	1.1 MHz	30 kHz
HLT 2	30 kHz	2 kHz

- **BRUNEL:** Once the measurements are provided by the detector electronics and the online system, they can be used as input for the reconstruction application BRUNEL [67]. The purpose of this software package is the track finding and the fit of the track.
  In addition, the software alignment application ESCHER [68] is implemented in this environment. The track based alignment algorithms benefit from the existing track reconstruction packages.
  The operation sequences of ESCHER are discussed in detail Section 5.1.
- **DAVINCI:** Finally, the event selection algorithms are processed by the physics analysis application DAVINCI [69].
- **PANORAMIX:** The visualization of the detector geometry and event objects is provided by the PANORAMIX [70] application. It can be run in parallel to any above mentioned application which makes it an important tool for the understanding of the detector and the data.

Another important service in the GAUDI framework is the detector description [71] that allows to handle detector information concerning geometry, materials, alignment and calibration. This essential service is used by all presented applications. The LHC*b* detector geometry and materials are described in files that are written in Extensible Markup Language (XML) [72] which are stored in a sqlite data base [73].

Description of the Outer Tracker geometry in the database

In the LHC*b* geometry data base, the Outer Tracker is described by four different detector elements, that are ordered in a hierarchical structure as illustrated in Figure 2.15. Smaller elements are placed inside the next larger element, which is called its parent. The largest of these elements represents an Outer Tracker station S, followed by layer L, quarter Q and a half module HM. The positions of half modules, for example, are given in the frame of the quarters. Shifts or rotations are applied to the geometrical center of the detector element, called pivot point and denoted P_i ($i = \mathrm{L,Q,HM}$) in the figure. Any misalignment applied in the data base are given with respect to the pivot point in the frame of the detector element parent.

A half module is part of a quarter with a length of 2.5 m, which matches the length of the straw tubes. This description is based on the readout structure of the detector (Section 2.1.4), but is in contrast to its physical construction.

Physically, the smallest individual detector unit is a $\sim 5\,\mathrm{m}$ long module that spans the whole acceptance of the Outer Tracker. The geometry information of the data base is modified for the detector alignment that determines the position of physical detector units. Thus, two 2.5 m long half modules are grouped to form one module. The geometrical center of the composed module is the pivot point to which any misalignments are applied.

Additionally, half layers are no generic elements in the data base. They are defined by grouping together half the modules of one layer, Figure 2.8. Again, the new pivot is defined by the geometrical center of the half layer that is composed of 9 modules.

With these definitions, the following detector elements can be aligned with the developed algorithm:

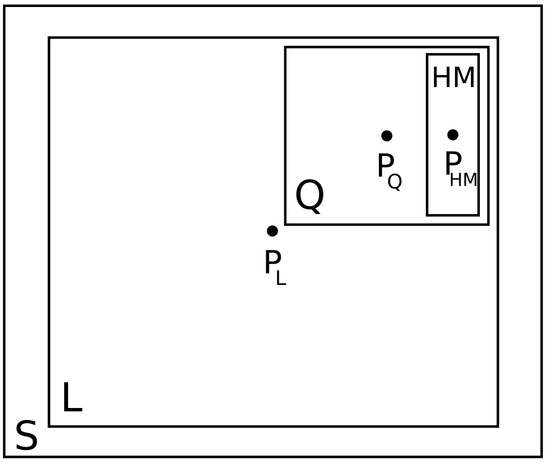

Figure 2.15: The hierarchical layout of detector elements for the Outer Tracker. Smaller elements are placed inside next larger elements. The layout is based on the readout structure of the detector and is modified for alignment purposes.

- **T Station**: The three stations of the Outer Tracker.
- **Layer**: The OT comprises four layers per T station, that are arranged in x, u, v, x configuration.
- **Half layer**: A layer of the detector is divided into two parts, left and right of the beam pipe. The 24 half layers are independently movable detector elements.
- **Module**: The 216 modules represent the smallest individual detector units and the smallest alignable detector elements of the OT.

For the validation of the alignment algorithm with simulated data, geometry databases containing misaligned detector positions have been generated. These misaligned geometries are applied to the Brunel application where the track reconstruction is processed. This procedure makes a time consuming reprocessing of event simulation and digitization obsolete and provides a simple and flexible way to simulate various misalignment scenarios, as will be discussed in Chapter 5.

Chapter 3

Impact of misalignments on the track reconstruction

The LHC*b* detector is designed to study B mesons with very high precision. Such precision measurements require excellent spatial resolution of the tracking system and therefore a well calibrated and aligned spectrometer. The alignment of the tracking stations is of utmost relevance, as misalignments can cause significant loss in both tracking and physics performance.

The impact of misalignments on the tracking is illustrated in Figure 3.1. Sketched are five detector modules in the xz measurement plane. The left figure shows displacements of the modules in x direction, which lead to a misinterpretation of the measured hit positions and thus to a wrongly reconstructed track. Only after the correction of the module positions the track can be reconstructed correctly, see right figure.

In this chapter, the effect of misalignments of the Outer Tracker layers on the tracking performance is studied in detail. The results of two analyses on simulated data are presented: One performed with nominal luminosity data, the other with high luminosity data.

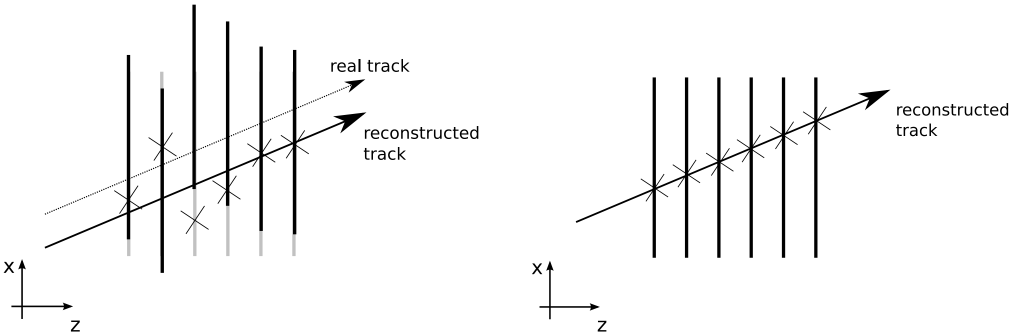

(a) (b)

Figure 3.1: Sketch of a track reconstruction on a misaligned (a) and aligned (b) detector. The light grey lines in figure (a) represent the nominal detector positions. (a) Under the assumption of no misalignments, the measured hit coordinates are given as illustrated by the crosses. This leads to a wrong track reconstruction. (b) The measured hits correspond to the reconstructed track for the aligned detector.

The aim of the study is to estimate the effect depending solely on the size of the applied misalignments.

3.1 Applied misalignments and data processing

Misalignments are simulated for the Outer Tracker layers following a Gaussian distribution with width σ. For that, the smallest misalignment scale is chosen to be roughly 1/4 of the hit resolution of the detector $\sigma_{hit} = 200\,\mu\text{m}$. This is the 1σ scale presented in Table 3.1. In order to study the impact of misalignments on the tracking performance, the following scenarios are discussed:

- 0σ or nominal scenario, for which the nominal detector positions are assumed.
- Misalignments of $1\sigma, 3\sigma, 5\sigma$ and 7σ according to Table 3.1, applied to the Outer Tracker layers.

In order to avoid statistical fluctuations that lead to harmless or catastrophic misalignments, five independent sets of misalignments have been produced for each of the five mentioned scenarios. Thus, in total 25 geometry data bases containing displaced layer positions are analysed.

The results given in this chapter represent the mean of the five results obtained for each misalignment case, the quoted uncertainty is given by the RMS of the five sets.

Data and data processing

The tracking performance of a misaligned OT is studied for nominal and high occupancy events. For that, the following data sets have been used:

- **Nominal luminosity**: As discussed in Chapter 2, a dedicated study [38] found the optimal luminosity for LHC*b* at $\mathcal{L} = 2 \cdot 10^{32}\,\text{cm}^{-2}\text{s}^{-1}$. The probability of a single inelastic *pp* collision is above 50 % at this luminosity, whereas the probability for multiple collisions is below 10 %. This is essential for a correct B decay vertex reconstruction, as it allows to discriminate signal events from prompt background events. Events of the decay $B_s \to J/\psi(\mu^+\mu^-)\phi(KK)$ ($E_{beam} = 5\,\text{TeV}$) are analysed with misaligned geometry. The number of inelastic collisions is $\nu = 1$ for this data.
- **High luminosity**: All subdetectors are designed to operate up to a maximal luminosity of $\mathcal{L} = 5 \cdot 10^{32}\,\text{cm}^{-2}\text{s}^{-1}$, for which the number of *pp* collisions per bunch

Table 3.1: Multiples of the given 1σ scale are used for the misalignment of the Outer Tracker layers.

Scenario	Translation [μm]			Rotation [mrad]		
	x	y	z	α	β	γ
1σ	50.0	50.0	100	0.15	0.15	0.05

crossing increases. A higher luminosity enhances the number of measured signal events, which is advantageous for physics analysis.
Therefore, the track reconstruction performance for events with $\nu = 3$ collisions per bunch crossing and misaligned geometry is studied additionally. For that purpose, high luminosity events of $B_s \to J/\psi(\mu^+\mu^-)\phi(KK)$ with a beam energy of $E_{beam} = 5$ TeV are used.

The used data have been produced by the LHC*b* Monte Carlo production in 2009 (MC09). They have been generated and digitized (see Chapter 2) using the nominal detector geometry. The misalignments are applied during the reconstruction (`Brunel`), when the pattern recognition and the track fit are performed.
For each of the 25 misalignment scenarios, 4 000 events of each data set are processed for the evaluation of the tracking performance.

3.2 Reconstruction performance indicators

The main focus of the study is put on the performance of the reconstruction of *long tracks*, which are used for many physics analysis.
A track is considered as long, in case it begins in the VELO and traverses the whole T stations. As discussed in Chapter 2, *long tracks* are reconstructed by two different algorithms, named forward tracking and track matching. The results of both algorithms are finally combined to determine the overall long track reconstruction performance. Therefore, the present study entails separate performance measurements for forward, matched and *long tracks*. The result of the algorithms are evaluated with respect to the track reconstruction efficiency, the ghost rate and the track clone rate. These quantities are introduced below.

3.2.1 Tracking efficiencies

The tracking efficiency is normalised to all reconstructable particles. A reconstructable particle is defined as follows:

- **VELO track**: The particle must have at least 3 r and 3 ϕ hits.
- **T track**: In each station T1-T3, the particle must have at least 1 hit in a x and 1 hit in a stereo layer.
- **Long tracks**: The particle must be reconstructible as VELO and as T track.

A track is successfully reconstructed, if at least 70 % of its associated hits belong to the same particle. Hence, the tracking efficiency is defined according to

$$\epsilon = \frac{N_{correct}}{N_{MC}} , \tag{3.1}$$

with $N_{correct}$ denoting the total number of reconstructed tracks that is associated to a reconstructible particle. N_{MC} is the number of all reconstructible particles. The error of the efficiency is given according to a binomial distribution by

$$\sigma_\epsilon = \sqrt{\frac{\epsilon(1-\epsilon)}{N_{MC}}} \,. \tag{3.2}$$

3.2.2 Ghost rate

In case a track is reconstructed with less than 70 % of its hits corresponding to the same Monte Carlo particle, the track is called a ghost track. Hence, the ghost rate is defined as

$$g = \frac{N_{ghost}}{N_{tot}} \,, \tag{3.3}$$

where N_{ghost} is the number of tracks that cannot be associated to a Monte Carlo particle. The total number of reconstructed tracks is N_{tot}. The uncertainty of the ghost rate is given by binomial statistics.

3.2.3 Track Clones

Two tracks, that share most of their hits, are called clones. In simulation studies like the one presented here, MC truth information is available, thus a clone is found if two tracks are associated to the same MC particle. The rate of track clones is defined as

$$c = \frac{N_{clones}}{N_{tot}} \,, \tag{3.4}$$

with the number of clones[1] N_{clones} and the total number of reconstructed tracks N_{tot}. As several algorithms are combined to reconstruct all possible tracks, it is likely that some find the same tracks. Hence, a dedicated clone killing algorithm is processed in the final reconstruction stage [74].

3.2.4 Event and track weighted quantities

The track reconstruction performance is different for normal and high occupancy events. For high occupancy events, the ghost rate tends to increase whereas the reconstruction efficiency degrades. The number of found tracks in these events is rather large, thus they have a significant weight on track averaged measurements. This distortion of track weighted quantities due to high occupancy events is avoided by the use of event averaged quantities. In this section, the ghost fraction is quoted event averaged:

$$g_{evt} = \frac{1}{N_{events}} \sum_{event\ i} \frac{N_{ghost,i}}{N_{tot,i}} \,, \tag{3.5}$$

where the sum is taken over all i events. If not noted otherwise, the track reconstruction efficiency and clone rate is given track averaged because high occupancy events have a minor effect on these quantities.

---

[1] The number of clones is counted once, i. e., for two tracks $N_{clones} = 1$.

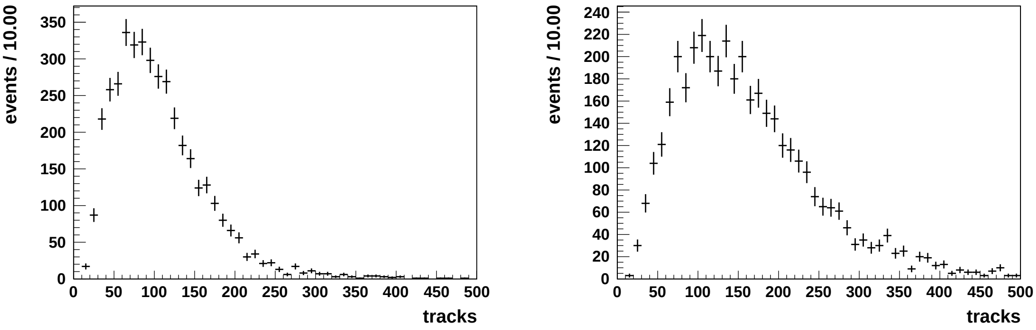

(a)

(b)

Figure 3.2: (a) The number of reconstructed tracks per event with one inelastic pp collision. (b) Track multiplicity for high luminosity events ($\nu = 3$).

3.3 Track reconstruction performance

The number of tracks in the detector acceptance are depicted in Figure 3.2 (a) and (b) for nominal and high luminosity events, respectively. Whereas an event with one inelastic pp collision (non empty) yields around 100 tracks on average, this number increases by about 50 % for the high luminosity scenario.

As mentioned above, signal data samples are used, which ensures that at least one B_s meson is created per event. This meson decays into a J/ψ and ϕ particle, that in turn decay and produce four signal tracks. The probability of a second B_s meson that decays the same way is on the per-mill level[2]. It is to assumed, that only about 4 tracks are assigned to a B decay. The reconstruction of all four tracks require a very efficient tracking. Already a decrease of about 1 % in efficiency due to potential misalignments results in a 4 % loss of B yield. For both data sets, the track reconstruction is performed with the default configuration that is based on nominal luminosity events. Furthermore, the same 25 misalignment sets are used for both studies.

First, the pattern recognition performance with respect to detector misalignments is presented. Afterwards, the impact on the track fit and the degradation of the momentum resolution are discussed.

All quoted results refer to *long tracks* with momentum $p > 5\,\text{GeV}$.

3.3.1 Forward tracking algorithm

For the forward tracking algorithm, the result for efficiency, the ghost rate and the clone rate are listed in Table 3.2 for the different misalignment scales and for the nominal and high luminosity events.

Forward tracking for nominal luminosity

The forward tracking efficiency for nominal geometry is $\epsilon = 92.5\,\%$, the ghost rate $g = 9.8\,\%$. These rates change only marginally up to the 3σ misalignment scenario. For

---

[2] The probability, that the remaining b quark forms, together with a strange quark, a B_s meson is about 10 %. In addition, the branching ratio for the same decay is about $9 \cdot 10^{-4}$ [13].

the 5σ scenario the efficiency decreases by almost 1 %. The ghost and clone stay rather constant for all misalignments, which implies that the track quality remains steady although less tracks are found.
The reason for this is found in the reconstruction strategy: The algorithm begins the track reconstruction in the VELO and searches for continuation in the T stations. As the VELO is not misaligned, the starting point to search for hits in the Outer Tracker is the same for all misalignment scenarios. If continuations are found for applied misalignments, the reconstructed track is most probably identical to the one found with nominal geometry. Hence, the ghost rate is constant. The probability to find a continuation is decreased by the misalignments.
This applies in particular for tracks with a large slope in the yz plane, as can be deduced from Figure 3.3 (b). The figure shows the efficiency versus the pseudo rapidity η for the nominal and misaligned cases. For nominal Outer Tracker geometry, the forward tracking efficiency is maximal in the region $\eta > 2.9$. In the maximally misaligned case, a plateau of highest efficiency is barely reached at all. It reflects the fact, that the track search in yz is significantly deteriorated by misalignments of the stereo layers.
The slight decrease in efficiency for the forward region $\eta > 5$ is due to enhanced particle scattering in the beampipe. This effect is considered for the definition of reconstructible particles, thus the denominator of the efficiency N_{MC} is adapted. Still, the edge effect of scattering slightly deteriorates the reconstruction on nominal geometry in this very forward region.

Table 3.2: The performance of forward tracking on nominal and high luminosity events, dependent of applied misalignments.

Scenario	Luminosity	Efficiency [%]	Ghost rate [%]	Clone rate [%]
nominal	nominal	92.5 ± 0.1	9.8 ± 0.1	1.0 ± 0.0
	(high)	(90.8 ± 0.0)	(15.0 ± 0.0)	(1.1 ± 0.0)
1σ	nominal	92.5 ± 0.0	9.8 ± 0.1	1.0 ± 0.0
	(high)	(90.7 ± 0.1)	(14.8 ± 0.1)	(1.1 ± 0.0)
3σ	nominal	92.1 ± 0.2	9.7 ± 0.1	1.0 ± 0.0
	(high)	(90.4 ± 0.2)	(14.9 ± 0.1)	(1.1 ± 0.0)
5σ	nominal	91.6 ± 0.6	9.8 ± 0.1	1.0 ± 0.0
	(high)	(89.9 ± 0.5)	(14.9 ± 0.1)	(1.1 ± 0.0)
7σ	nominal	90.0 ± 1.1	9.7 ± 0.2	1.0 ± 0.0
	(high)	(88.3 ± 1.1)	(15.0 ± 0.1)	(1.1 ± 0.0)

Forward tracking for high luminosity events

The high detector occupancy events decrease the forward tracking efficiency by 1.7 % compared to the efficiency of nominal luminosity events. At the same time, the ghost rate increases from 9.8 % to 15 %. It shows, that the hit to track association is significantly

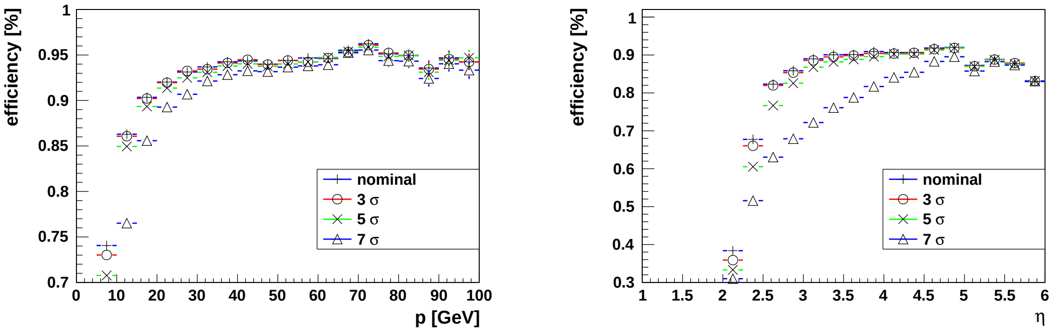

(a) (b)

Figure 3.3: Efficiency distributions for forward tracking on nominal luminosity.

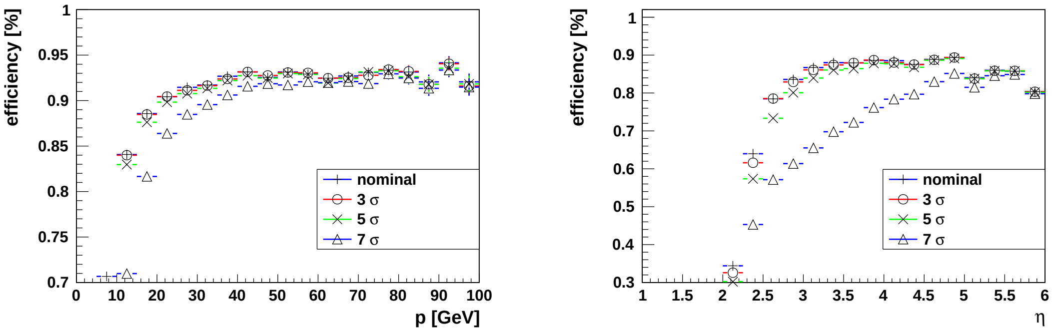

(a) (b)

Figure 3.4: Efficiency distributions for forward tracking on high luminosity.

deteriorated due to the high hit density. The rate of clone tracks, however, rises marginally to 1.1 %.
Though in general, the tracking performance is declined compared to $\nu = 1$ events, the impact of misalignments on the performance is similar: For the 5σ case, a decrease in efficiency of about 1 % is observed, ghost and clone rate stay steady.
The efficiency for different particle momenta and pseudorapidity regions is presented in Figure 3.4 (a) and (b). No qualitatively difference is observed compared to Figure 3.3.

3.3.2 Track matching algorithm

Track matching for nominal luminosity

The algorithm matches tracks from the VELO with tracks from T stations. The nominal matching efficiency is $\epsilon = 89.7\,\%$ with a ghost rate of $g = 7.3\,\%$, see Table 3.3. Due to the fact, that each VELO and T seed is only selected once, the clone rate is zero for all matched tracks. Compared to forward tracking, the change of efficiency and ghost rate in course of applied misalignments is more pronounced. For the 3σ misalignment scale, for example, the efficiency drops by more than 5 % and the ghost rate increases by 0.7 %. The performance is even more declined for scenarios of larger misalignments.
The reason for the increase of the ghost rate and the efficiency loss is twofold: Evidently,

Table 3.3: The performance of track matching on nominal and high luminosity events, dependent of applied misalignments.

Scenario	Luminosity	Efficiency [%]	Ghost rate [%]	Clone rate [%]
nominal	nominal	89.7 ± 0.1	7.3 ± 0.1	0.0 ± 0.0
	(high)	(86.6 ± 0.0)	(10.7 ± 0.0)	(0.0 ± 0.0)
1σ	nominal	89.5 ± 0.0	7.4 ± 0.1	0.0 ± 0.0
	(high)	(86.2 ± 0.1)	(10.7 ± 0.1)	(0.0 ± 0.0)
3σ	nominal	84.2 ± 2.1	8.0 ± 0.2	0.0 ± 0.0
	(high)	(79.9 ± 2.4)	(11.8 ± 0.4)	(0.0 ± 0.0)
5σ	nominal	81.5 ± 3.7	8.3 ± 0.4	0.0 ± 0.0
	(high)	(77.0 ± 3.8)	(12.2 ± 0.7)	(0.0 ± 0.0)
7σ	nominal	78.3 ± 2.6	8.5 ± 0.3	0.0 ± 0.0
	(high)	(73.7 ± 2.6)	(12.7 ± 0.4)	(0.0 ± 0.0)

less tracks are found in the T stations because of the misalignment and the worsened hit to track association. In addition, the matching between the reconstructed T and VELO tracks is deteriorated.

Figure 3.5 (a) shows the efficiency loss with respect to the momentum p of the particle, and figure (b) with respect to the pseudorapidity. The decrease of efficiency is evident over the whole momentum and η spectrum. Yet, for the 7σ case, the efficiency increases in the very forward region. This can be ascribed to the adaption of the efficiency denominator, as previously discussed.

Track matching for high luminosity events

For the ideal detector geometry, the track matching algorithm reconstructs tracks with an efficiency of $\epsilon = 86.6\,\%$ and a ghost rate of $g = 10.7\,\%$. Hence, the efficiency loss for matched tracks is about 3.7 % with a rise of the ghost rate by 3.4 % compared to nominal luminosity. The decrease in performance due to applied misalignments is more distinct than observed for normal luminosity events: Already for the 3σ case, the efficiency is reduced by more than 6 % and the ghost rate is increased by 1 %. Furthermore, a strong dependence between efficiency and particle momentum is observed for large misalignments, see Figure 3.6 (a). The distribution shows an explicit gradient towards low efficiency for momenta $p < 30\,\mathrm{GeV}$. The effect can be ascribed to a problematic track finding due to uncertainties of the track curvature and the high hit density.

3.3.3 Long track algorithm

Table 3.4 describes the overall performance of the long track reconstruction, i. e., after the combination of forward and matched tracks. Furthermore, the algorithm `TrackEventCloneKiller` [74] has been applied to the combined set of tracks, to reduce

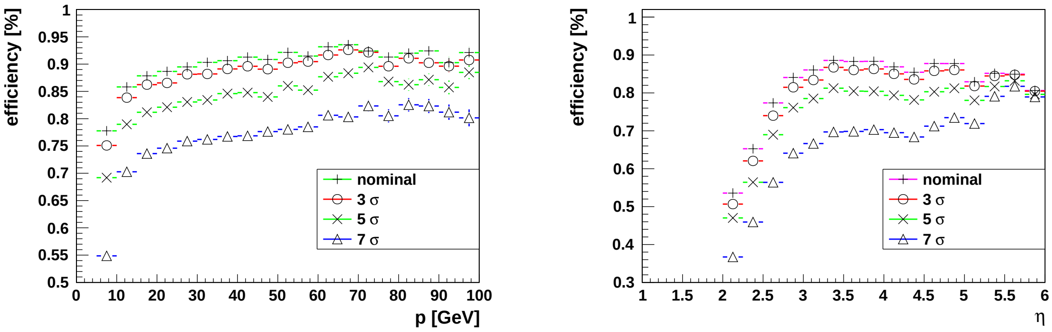

(a) (b)

Figure 3.5: Efficiency distributions for track matching on nominal luminosity.

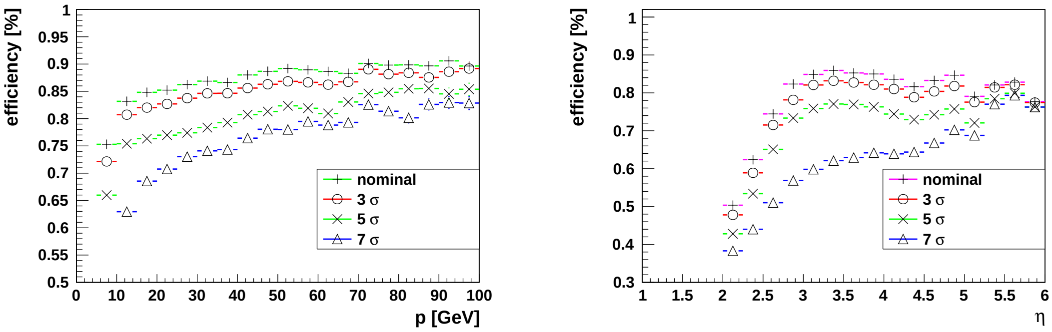

(a) (b)

Figure 3.6: Efficiency distributions for track matching on high luminosity.

the rate of clone tracks.

Long track algorithm for nominal luminosity events

For the ideal detector, the efficiency is $\epsilon = 94.6\,\%$. This efficiency is better than either of both previously discussed algorithms. It implies that the majority of tracks found by forward and track matching are identical, however a few per cent of the tracks differ. The same accounts for the ghost tracks: The ghost rate of $g = 11.9\,\%$ is higher than for forward or matched tracks. Additionally, the clone rate of 1.1 % for the forward tracking is reduced to 1.0 % for the final *long tracks*.
The impact of misaligned OT layers on the performance is significant for the 5σ case: Whereas the efficiency drops by 0.7 % and the ghost rate increases by 0.3 %, the clone rate rises to 1.6 %. A corresponding increase of the clone rate is neither observed for forward tracks nor for T tracks. This suggests, that the increase of the number of long track clones is due to a different combination of VELO and T tracks in the forward and matching algorithm, respectively. Hence, two different combinations are found to describe a trajectory which is created by the same particle. These *long tracks* are not identified as clones.

Finally, the effect of Outer Tracker misalignments on *long tracks* is depicted in

Table 3.4: The performance of long track reconstruction on nominal and high luminosity events, dependent of applied misalignments.

Scenario	Luminosity	Efficiency [%]	Ghost rate [%]	Clone rate [%]
nominal	nominal	94.6 ± 0.1	11.9 ± 0.1	1.0 ± 0.0
	(high)	(93.3 ± 0.0)	(17.6 ± 0.0)	(1.1 ± 0.0)
1σ	nominal	94.6 ± 0.1	11.9 ± 0.1	1.0 ± 0.0
	(high)	(93.3 ± 0.0)	(17.5 ± 0.0)	(1.1 ± 0.0)
3σ	nominal	94.3 ± 0.1	12.1 ± 0.2	1.3 ± 0.1
	(high)	(92.8 ± 0.2)	(18.0 ± 0.1)	(1.5 ± 0.1)
5σ	nominal	93.9 ± 0.4	12.2 ± 0.1	1.4 ± 0.1
	(high)	(92.4 ± 0.4)	(18.1 ± 0.2)	(1.6 ± 0.2)
7σ	nominal	92.8 ± 0.7	12.2 ± 0.2	1.5 ± 0.1
	(high)	(91.3 ± 0.7)	(18.2 ± 0.2)	(1.8 ± 0.1)

Figure 3.7. The distributions show basically the effect, which is expected from the results listed in Table 3.4.

Long track algorithm for high luminosity events

The final long track reconstruction efficiency for high luminosity events is $\epsilon = 93.3\,\%$. This is about $1.3\,\%$ smaller compared to the tracking on low luminosity events. The ghost rate is increased by more than $5.5\,\%$ to $g = 17.6\,\%$. Hence, already for the nominal detector geometry, the ghost tracks can severely affect the quality of tracks that are selected for physics analysis purposes.
For the 5σ scenario, the ghost rate is about $18\,\%$ and the efficiency is reduced by about $1\,\%$. Furthermore, the relative increase of the clone rate is $45\,\%$ for this misalignments scale.

Hence, the impact of misalignments on *long tracks* in high occupancy events is

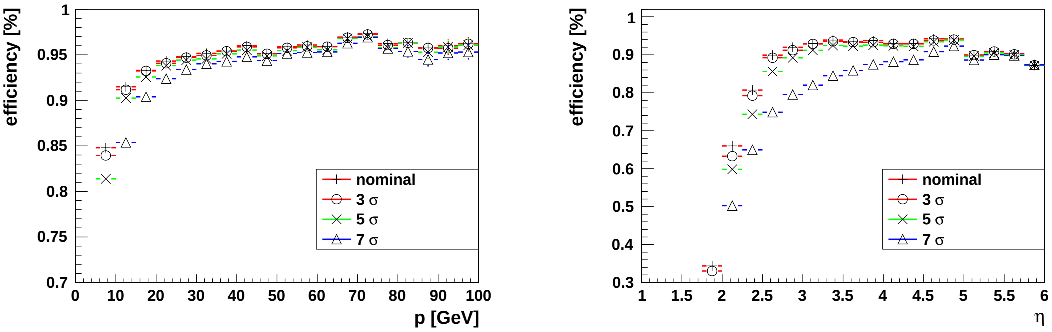

(a) (b)

Figure 3.7: Efficiency distributions for *long tracks* on nominal luminosity.

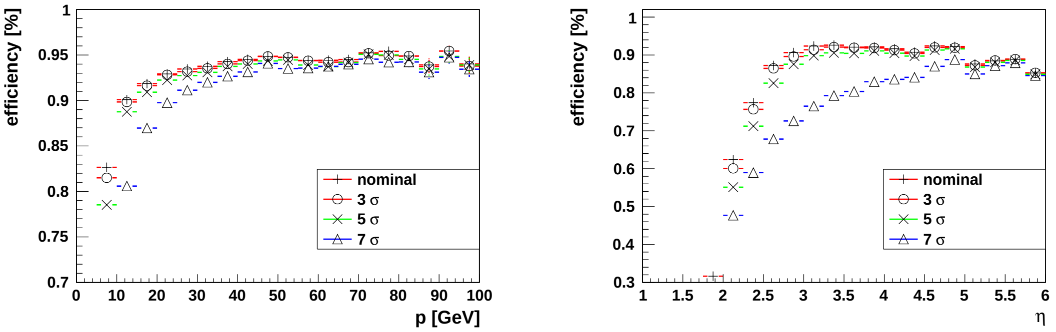

(a) (b)

Figure 3.8: Efficiency distributions for *long tracks* on high luminosity.

comparable to the impact for $\nu = 1$ events. Consequently, the efficiency distributions shown in Figure 3.8 are similar to the corresponding distributions in Figure 3.7.

3.3.4 Fit results

Nominal luminosity

The found tracks are fitted using a Kalman [75] filter fit, the default LHC*b* track fit [76]. The fit result for *long tracks* is presented in Figure 3.9 (a) and (b). It shows the reduced χ^2 and the χ^2 probability obtained with nominal (solid line) and misaligned (dashed line) geometry. Here, the effect of the 5σ misalignments are depicted, as these misalignments induce significant loss in the tracking efficiency. The mean value of the reduced χ^2 shows a relative increases of about 35 %. In addition, the $\chi^2_{probability}$ is no longer flat. For the physics analysis which select tracks based on track χ^2 cuts, this effect can deteriorate the analysis results.
Furthermore, the momentum resolution is studied. Figure 3.10 (a) shows the nominal average momentum resolution $\Delta p/p$ for *long tracks*. With a width of $\sigma_p \approx 0.33\,\%$ of the core Gaussian, long tracks have a good momentum resolution. The resolution

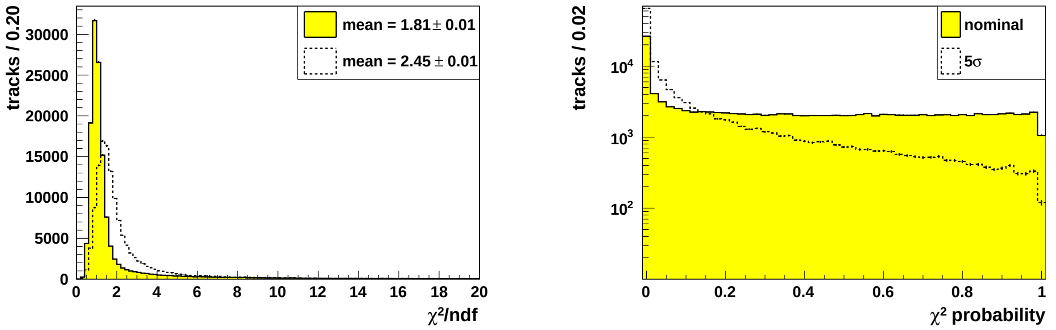

(a) (b)

Figure 3.9: (a) The reduced track χ^2 distribution for nominal (solid line) and misaligned geometry (dashed line). (b) The corresponding $\chi^2_{probability}$ distribution.

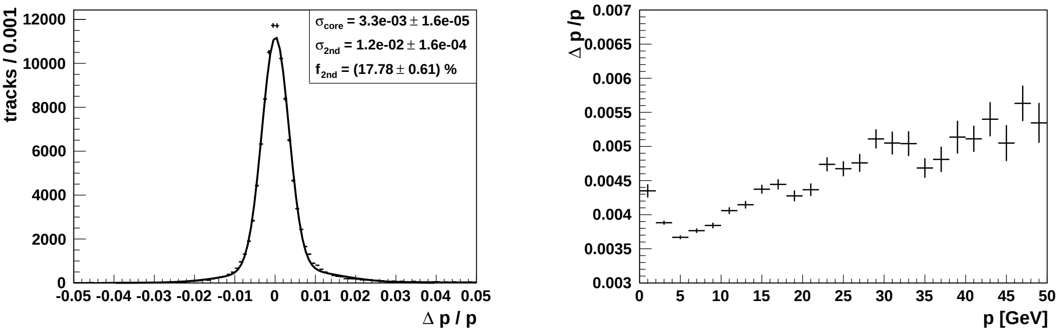

(a) (b)

Figure 3.10: (a) Average momentum resolution obtained with nominal Outer Tracker geometry. A double Gaussian is fitted to the distribution, the width of the core Gauss is determined to $\sigma_p \approx 0.33\,\%$. (b) The momentum resolution dependent on the particle momentum.

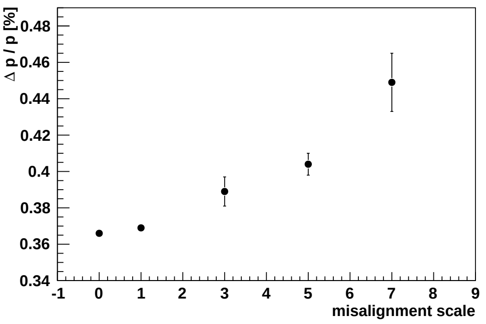

Figure 3.11: The impact of Outer Tracker layer misalignments on the momentum resolution for particle momenta of $p = 5\,\text{GeV}$. A relative resolution loss of about 10 % is observed for the 5σ scale.

dependence on the particle momentum is shown in figure (b). The rise of $\Delta p/p$ to very low momentum originates from the lower hit purity [14]. Whereas the larger resolution values at high momenta are due to the lower track curvature in this region.
For the study of the dependence of $\Delta p/p$ on the applied misalignments, the resolution at $p = 5\,\text{GeV}$ is compared for all misalignment scenarios. The result is depicted in Figure 3.11. The resolution is declined relative to its nominal value by about 10 % for the 5σ case, and by about 23 % for the 7σ case. A worsening of the resolution is expected as the momentum determination relies on tracks in the T stations.

High luminosity

The fit results for *long tracks* from high occupancy events are presented in Figure 3.12 (a) and (b). In both figures, the distributions are given for the 0σ and the 5σ case. As expected, the mean of the reduced χ^2 increases for misaligned Outer Tracker layers and the corresponding probability distribution shows a gradient. It has to be noted, however, that the $\frac{\chi^2}{ndf}$ distributions are significantly shifted towards higher values compared to the

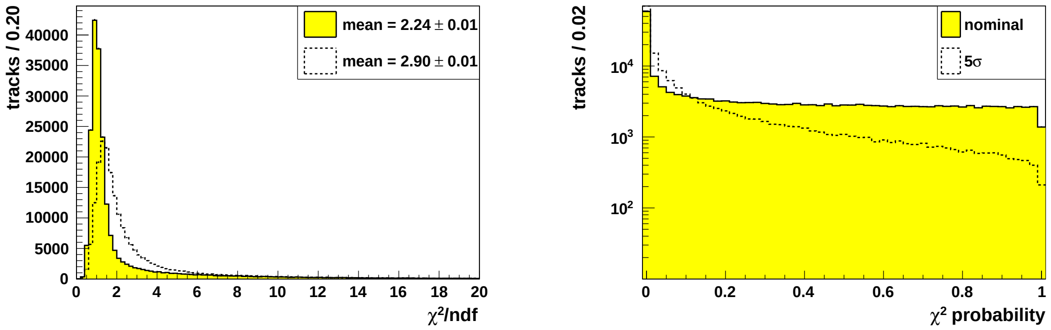

(a) (b)

Figure 3.12: (a) The reduced track χ^2 distribution of *long tracks* obtained on high luminosity events. Compared to the results of $\nu = 1$ events, the mean values are shifted towards larger values due to the higher hit density. (b) The corresponding $\chi^2_{probability}$ distribution.

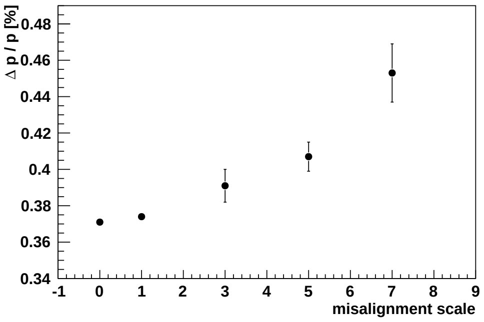

Figure 3.13: The impact of Outer Tracker layer misalignments on the momentum resolution for particle momenta of $p = 5\,\mathrm{GeV}$, measured for high luminosity events.

values observed for nominal occupancy. The shift reflects the declined hit purity[3] of the tracks for events with three inelastic proton-proton collisions. The momentum resolution determined for *long tracks* depending on the misalignments is depicted in Figure 3.13. The resolution decreases with the size of the applied OT layer displacements, as has been seen for nominal occupancy events. No additional worsening due to the high track density in the detector is observed.

3.4 Conclusion

As a B decay results in up to five tracks, a decrease in the tracking efficiency of already 1 % has significant impact on the B yield. The presented study reveals, that a 1 % efficiency loss is expected by Outer Tracker layer misalignments in the order of $\sigma_x = 5 \cdot 50\,\mu\mathrm{m}$ in the measurement direction.

---

[3] In the track reconstruction, it is unlikely that the hits which are associated to a track correspond all to the same particle. This fact is expressed by the hit purity $p_{hit} = N^{hit}_{correct}/N^{hit}_{tot}$. Here, $N^{hit}_{correct}$ refers to the number of hits, that are induced by the particle which produced the track. N^{hit}_{tot} is the total number of hits on the track.

In addition, not only the tracking efficiency, but also the track fit quality is degraded by misalignments, as the mean and width of the reduced track χ^2 distributions are significantly larger than 1.

Furthermore, the degradation of the momentum resolution is not negligible. Evidently, this affects the mass resolution of B mesons at the same time, because the invariant mass is determined by the momenta of the daughter particles. In physics analysis, the degradation of the invariant mass resolution significantly affects the background to signal (B/S) ratio. Especially in case the signal and background events have the same particles in the final state, e. g., for the hadronic decay $B_s^0 \to \pi^+K^-$ and the background $\bar{B}_d^0 \to \pi^+K^-$. In this case, the separation of the decays is not possible by particle identification, but relies on the invariant mass distributions. A dedicated study [35] analysed the effect of a worsened invariant mass resolution due to shifts and rotations of Outer Tracker stations T1 and T3 of 0.2 mm and 0.2 mrad, respectively. It has been shown, that in this case, the B/S ratio for $B_s^0 \to \pi^+K^-$ events already reaches a value of 1 compared to $B/S \approx 0.3$ for ideal detector positions.

Consequently, misalignments in the order of 250 μm along x and rotations of up to 0.75 mrad have to be avoided in order to prevent severe loss of the tracking performance and degradation of the track quality. To ensure the optimal performance of the track reconstruction for both, nominal and high luminosity events, the detector shifts should be known better than within 150 μm in measurement direction and rotations of the layer should be smaller then 0.45 mrad for α and β and below 0.15 mrad for γ.

In the following chapter, the alignment algorithm is presented which determines and corrects Outer Tracker misalignments with an accuracy even better than required by the presented study.

Chapter 4

Alignment - The principles

Detectors used in today's high energy physics experiments are of enormous size and complexity. They are composed of various sub-detectors, each with several hundred-thousands of readout channels. The calibration of the individual sub-detectors as well as the commissioning of the whole system are mandatory to allow measurements with highest precision. An efficient track reconstruction, for example, requires the accurate knowledge of the positions of all sub-detectors.

This chapter discusses a method which allows a precise determination of detector positions by the use of reconstructed tracks. After a brief introduction to the alignment problem, the general concept of this method will be presented in Sections 4.2, 4.3. In Section 4.4, the concept will be adapted to the needs of an accurate determination of the LHC*b* Outer Tracker detector position.

4.1 Introduction to the alignment

The impact of misaligned detector positions on the track reconstruction performance has been demonstrated in Chapter 3 on the basis of displaced LHC*b* Outer Tracker positions. It has been shown, that the OT detector positions should be known within an accuracy better than $\sigma_{acc} \approx 150\,\mu$m (OT hit resolution $\sigma_{hit} = 200\,\mu$m) to ensure optimal reconstruction performance.

This accurate knowledge of detector positions can only be achieved by analysing tracks that have been reconstructed with the detector. The method exploits the fact, that detector misalignments deteriorate the track residual, i. e., the distance between the reconstructed track and the associated hits, as depicted in Figure 4.1. The residuals of the reconstructed tracks contain information about the actual detector positions which can differ from the initially expected detector positions.

Dedicated algorithms use the information embedded in the residuals of several ten- or hundred-thousands of tracks to determine corrections to the assumed detector placement. As these algorithm are based on the track information, they are also referred to as *track based alignment algorithms*. They allow the determination of detector positions within $\mathcal{O}(10 - 100\,\mu\text{m})$, depending on the detector design and technology, e. g., silicon strip detectors or drift tube chambers.

Mathematically, the initially expected detector positions are described by the vector $\mathbf{a}$, that contains the assumed x, y, z positions of the detector in a Cartesian coordinate

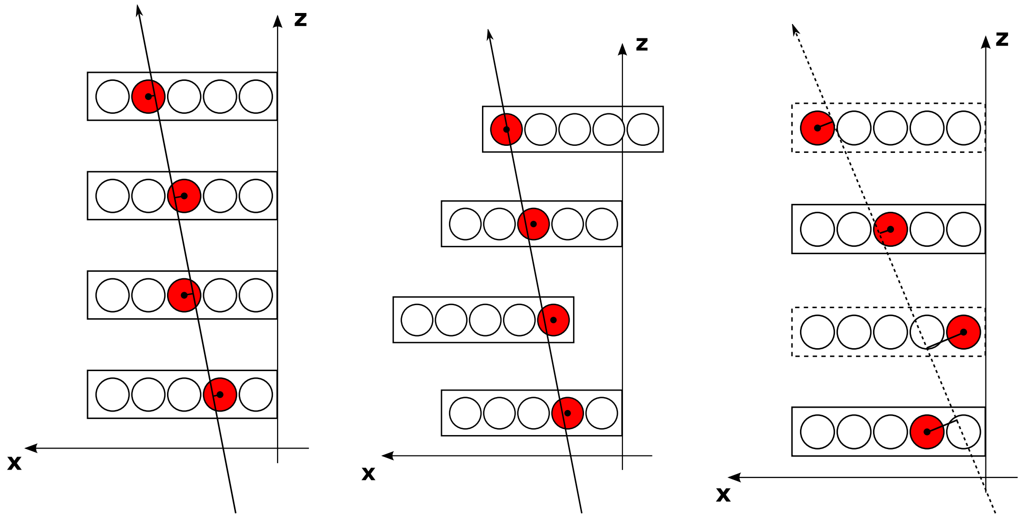

(a) ideal detector positions (b) misaligned detector positions and measured hits (c) initially expected detector positions and measured hits

Figure 4.1: The residual between reconstructed track and measured hit change due to misalignments of the detector elements, as can be seen in the figures from (a) to (c).

system and the rotations α, β, γ around these axes. By processing an alignment algorithm, corrections to the positions **a** are determined. These corrections are described by the *misalignment parameters* $\mathbf{\Delta a}$ that are given for the three translational and three rotational degrees of freedom:

$$\mathbf{\Delta a} = \begin{pmatrix} \Delta x \\ \Delta y \\ \Delta z \\ \Delta \alpha \\ \Delta \beta \\ \Delta \gamma \end{pmatrix} , \tag{4.1}$$

where Δx,Δy,Δz denote shifts and $\Delta\alpha$,$\Delta\beta$,$\Delta\gamma$ are the rotations of the detector around the x, y, z axis.

For the track based alignment procedure, the determination of the misalignment parameters $\mathbf{\Delta a}$ depends on the reconstructed particle trajectories. These trajectories are parameterized by a track model. Assuming the trajectory is reconstructed along the z direction and the track model takes into account the deflection of charged particles in a magnetic field in the xz plane of the detector. This results in the parameterization as follows:

$$\begin{aligned} x(z) &= a_x + b_x z + \kappa z^2 \ , \\ y(z) &= a_y + b_y z \ , \end{aligned} \tag{4.2}$$

with gradients $b_{x,y}$ and the curvature parameter κ that accounts for the bending in the magnetic field. Each point along the trajectory can be defined by a track state vector $\boldsymbol{\tau}$, that contains information about the (x, y) coordinates and the tangent to the trajectory at a given z position. Thus, the state vector (at a given z position) is

$$\boldsymbol{\tau}(z) = \begin{pmatrix} x \\ t_x \\ y \\ t_y \\ \kappa \end{pmatrix} \text{, with } t_x = \frac{\partial x}{\partial z} \text{ and } t_y = \frac{\partial y}{\partial z} \, , \tag{4.3}$$

with x and y from Equation 4.2.

The next section describes the mathematical method that is used to determine track parameters from measurements.

4.2 Introduction to the least squares method

The aim of the least squares fit method is to reconstruct a particle trajectory in the detector. A trajectory that is bent in the xz plane by a magnetic field can be parameterized by the following track model:

$$h(a, b, z) = a + bz + \kappa z^2 \, , \tag{4.4}$$

with the track parameters a, b and κ for a track along the z direction. Initially, the track parameters are unknown and have to be determined from measurement by the use of the least squares method.

For the discussion of the fit, it is convenient to introduce the track parameter vector $\boldsymbol{t}$, with $\boldsymbol{t} = \left(\begin{smallmatrix} a \\ b \\ \kappa \end{smallmatrix}\right)$ for the model of Equation 4.4. Furthermore, it is assumed, that the measurements are uncorrelated and that $h(\boldsymbol{t}, z)$ is linear in $\boldsymbol{t}$.

Assuming i measurements in the detector, the difference between measurement m_i at position z_i and the function value $h_i(\boldsymbol{t}) = h(\boldsymbol{t}, z_i)$ at this position is defined as residual,

$$r_i = m_i - h_i(\boldsymbol{t}) \, . \tag{4.5}$$

The square of the normalized residual, summed over all measurements i, is the χ^2:

$$\chi^2(\boldsymbol{t}) = \sum_i \left(\frac{r_i}{\sigma_i}\right)^2 = \sum_i \left(\frac{m_i - h_i(\boldsymbol{t})}{\sigma_i}\right)^2 \, , \tag{4.6}$$

where σ_i is the error of the i^{th} measurement. The track parameters $\boldsymbol{t}$ are determined by the minimization of the χ^2 (least squares). Equation 4.6 can be simplified by rewriting it in matrix notation, which will be used throughout this chapter. The vector $\mathbf{m}$ is defined as the vector of the measurements, vector $\mathbf{h}$ comprises the i function values $h_i(\boldsymbol{t})$ and is given by

$$\mathbf{h} = \boldsymbol{H}\boldsymbol{t} \, , \tag{4.7}$$

where $\boldsymbol{H}_{ij} = \frac{\partial h_i}{\partial t_j}$ contains the derivatives of $h_i(\boldsymbol{t})$ with respect to the parameters $\boldsymbol{t}$. Using this notation, the χ^2 is rewritten as

$$\chi^2(\boldsymbol{t}) = (\mathbf{m} - \boldsymbol{H}\boldsymbol{t})^T \boldsymbol{V}^{-1} (\mathbf{m} - \boldsymbol{H}\boldsymbol{t}) \, , \tag{4.8}$$

here V denotes the diagonal covariance matrix of the uncorrelated measurements, i. e., $\boldsymbol{V}_{ii} = \sigma_{ii}^2$. As the residual r depends on the track parameters $\boldsymbol{t}$, the minimum of the χ^2 has to be determined with respect to these parameters. The requirement for the minimum can be expressed as

$$0 \equiv \frac{\mathrm{d}\chi^2}{\mathrm{d}\boldsymbol{t}} = -2\boldsymbol{H}^T\boldsymbol{V}^{-1}(\mathbf{m} - \boldsymbol{H}\boldsymbol{t}) \; , \tag{4.9}$$

or in form of the normal equations

$$(\boldsymbol{H}^T\boldsymbol{V}^{-1}\boldsymbol{H})\boldsymbol{t} = (\boldsymbol{H}^T\boldsymbol{V}^{-1})\mathbf{m} \; . \tag{4.10}$$

The track parameters are obtained by solving Equation 4.10 for $\boldsymbol{t}$. With the substitution $\boldsymbol{\Lambda} = \boldsymbol{H}^T\boldsymbol{V}^{-1}\boldsymbol{H}$ and $\boldsymbol{\eta} = \boldsymbol{H}^T\boldsymbol{V}^{-1}\mathbf{m}$, the following simple relation is given for the parameters $\boldsymbol{t}$ and the modified measurements $\boldsymbol{\eta}$,

$$\boldsymbol{t} = \boldsymbol{\Lambda}^{-1}\boldsymbol{\eta} \; , \tag{4.11}$$

with the parameters covariance matrix $\boldsymbol{\Lambda}^{-1}$.

4.3 Determination of misalignment parameters

The aim of the track based alignment procedure is the determination of the misalignment parameters $\mathbf{\Delta a}$ that represent corrections to the nominal detector geometry parameters $\mathbf{a}$. The corrections are obtained by the minimization of the least squares function $\chi^2(\mathbf{a}, \mathbf{\Delta a}, \boldsymbol{t})$, which depends on the geometry parameters $\mathbf{a}$, the misalignment parameters $\mathbf{\Delta a}$ and the track parameters $\boldsymbol{t}$:

$$\chi^2(\mathbf{a}, \mathbf{\Delta a}, \boldsymbol{t}) = \sum_k \sum_i \left(\frac{m_{ik} - h_i(\mathbf{a}, \mathbf{\Delta a}, \boldsymbol{t}_k)}{\sigma_{ik}} \right)^2 \; , \tag{4.12}$$

where m_{ik} is the i^{th} measured value of the k^{th} track and $h_i(\mathbf{a}, \mathbf{\Delta a}, \boldsymbol{t}_k)$ the expectation value for the corresponding measurement, to which the uncertainty σ_{ik} is assigned. The measurements are assumed to be uncorrelated. An alignment process requires $\mathcal{O}(10\,000) - \mathcal{O}(1\,000\,000)$ tracks for the determination of $\mathbf{\Delta a}$. The actual number of used tracks depends on the specific task, e. g., the required accuracy of the detector positions or the degree of freedom for which geometry corrections are determined.
In high energy physics experiments, often two alignment methods are used for the determination of $\mathbf{\Delta a}$, namely *biased* and *unbiased* methods [77]:

- **Biased** alignment algorithms or *local* χ^2 methods treat the alignment parameters $\mathbf{\Delta a}$ independent from the track parameters. The track fit determines the track parameters without accounting for possible misalignments. Misalignment parameters are determined by studying the mean of the residuals between track and measurements. Residual distributions are visualized in histograms and deviations of the mean value from zero indicate the misalignment.
  In a second realization of this method, the derivatives of the residuals with respect to the alignment parameters are calculated to determine the displacements.

Analogue to the χ^2 minimization, a matrix Λ is filled for each measurement. In case three shifts and three rotations are to be determined the matrix is of size 6×6. For k tracks and i measurements per track, this method leads to $k \cdot i$ matrix equations of dimension six, for which the solution is simple and fast. As the track fit is done before the alignment procedure, the track parameters as well as the misalignment parameters are biased. This bias can be reduced by repeating the procedure many times, until the change of the results in subsequent iterations is below a given threshold that defines the convergence. The convergence can be rather slow, typically 20-100 iterations are needed. Correlations of the parameters have to be calculated explicitly.

- **Unbiased** algorithms or *global* χ^2 methods perform a simultaneous fit to the track and misalignment parameters. This implies the determination of a large number of unknown parameters, i. e., the misalignment parameters (possibly $\mathcal{O}(10^3)$ or more) and the track parameters of up to millions of tracks. The solution of the system of equation requires the inversion of a large matrix, for which enormous computing power is necessary[1]. This computing effort is reduced by partitioning the matrix into sub-matrices [78] which allows to easily obtain the inverse of the matrix. The method is exact, i. e., no approximations to the matrix elements are performed. Such a method is realized in the program `MILLEPEDE` [8]. This mathematical ansatz considers the strong correlation between alignment and track parameters.

In the next section, the unbiased method is presented in detail as this method is used to determine misalignment parameters $\mathbf{\Delta a}$ of the LHC*b* Outer Tracker (Section 4.4 and Chapters 5, 6).

4.3.1 Global χ^2 minimization

The parameters determination with the χ^2 minimization method requires a model which is linear in the parameters $\mathbf{\Delta a}$. The linearization of Equation 4.12 yields

$$\begin{aligned}\chi^2(\mathbf{a}, \mathbf{\Delta a}, \boldsymbol{t}) &= \sum_k \sum_i \left(\frac{m_{ik} - h_i(\mathbf{a}, \mathbf{\Delta a}, \boldsymbol{t}_k)}{\sigma_{ik}} \right)^2 \\ &\approx \sum_k \sum_i \frac{1}{\sigma_{ik}^2} \left(m_{ik} - h_i(\mathbf{a}, \boldsymbol{t}_k) + \left(\frac{\partial h_i}{\partial \mathbf{a}} \right)^T \mathbf{\Delta a} + \left(\frac{\partial h_i}{\partial \boldsymbol{t}_k} \right)^T \mathbf{\Delta} \boldsymbol{t}_k \right)^2 \end{aligned} \quad (4.13)$$

where $h_i(\mathbf{a}, \boldsymbol{t}_k) = h_i(\mathbf{a}, \mathbf{\Delta a} = 0, \boldsymbol{t}_k)$. $\mathbf{\Delta}\boldsymbol{t}_k$ are changes to the track parameters caused by correction to the detector positions $\mathbf{a}$.
Furthermore, the derivative of the measurement prediction $\frac{\partial h_i(\mathbf{a}, \boldsymbol{t})}{\partial \mathbf{a}}$ with respect to the geometrical degrees of freedom $\mathbf{a}$ is given. The derivative has to be calculated explicitly for the χ^2 minimization. As it is used to describe the change of the measurement

---

[1] Matrix inversion requires a CPU time proportional to $\propto n^3$ and a storage space $\propto n^2$. Additional, the computing accuracy should be double precision to avoid un-precise approximations. For example, on 64 bit machines, a $10^5 \times 10^5$ matrix in double precision would require a memory space of about 80 GByte.

prediction due to global shifts, it is called *global derivative.*
It is convenient to define the asymmetric derivative matrix $\boldsymbol{P}$, with $P_{dj} = \frac{\partial h^d}{\partial a_j}$. Here, h^d denotes the measurement prediction in direction d of the detector, with $d = x, y$. Furthermore, a_j with $j = 1, \ldots, 6$, represent the six degrees of freedom, in which the detector can be misaligned. A change of the measurement prediction is thus expressed by $\boldsymbol{\Delta h}_i = \boldsymbol{P \Delta}\mathbf{a}$, with

$$\boldsymbol{P} = \begin{pmatrix} -1 & 0 & t_x & yt_x & -xt_x & y \\ 0 & -1 & t_y & yt_y & -xt_y & -x \end{pmatrix} . \tag{4.14}$$

Here, x, y and t_x, t_y are the components of the track state vector $\boldsymbol{\tau}$ from Equation 5.11. Since the alignment corrections are small, the state trajectories can be linearly approximated by the state $\boldsymbol{\tau}$ in the vicinity of the measurement plane. The curvature is not needed to calculate the global derivatives. Furthermore, the linearization of the rotational contribution is entirely valid because the corrections to the angles are assumed to be of order of a mrad. Equation 4.14 is a general expression of the global derivatives for measurements in x and y direction, respectively. An expression for the direction of z perpendicular to the measurement plane is meaningless because the measurements are taken on the sensitive surface. A detailed calculation of $\boldsymbol{P}$ is presented in Appendix A.
The minimization of the χ^2 function from Equation 4.13 leads to a system of linear equations given by

$$\left(\begin{array}{c|ccc} \sum \boldsymbol{C}_k & \cdots & \boldsymbol{\mathcal{M}}_k & \cdots \\ \hline \vdots & \ddots & 0 & 0 \\ \boldsymbol{\mathcal{M}}_k^T & 0 & \boldsymbol{\Lambda}_k & 0 \\ \vdots & 0 & 0 & \ddots \end{array}\right) \left(\begin{array}{c} \Delta \mathbf{a} \\ \hline \vdots \\ \Delta \boldsymbol{t}_k \\ \vdots \end{array}\right) = \left(\begin{array}{c} \sum \mathbf{b}_k \\ \hline \vdots \\ \boldsymbol{\eta}_k \\ \vdots \end{array}\right) , \tag{4.15}$$

with the symmetric matrix $\boldsymbol{C}_k$ of size $N \times N$ (N is the number of misalignment parameters), that contains the global derivatives of each track k:

$$\boldsymbol{C}_k = \sum_i \frac{1}{\sigma_{ik}^2} \left(\frac{\partial h_i(\mathbf{a}, \boldsymbol{t}_k)}{\partial \mathbf{a}} \right) \left(\frac{\partial h_i(\mathbf{a}, \boldsymbol{t}_k)}{\partial \mathbf{a}} \right)^T , \tag{4.16}$$

where the sum is taken over the i measurements of the track. The matrices $\boldsymbol{C}_k$ are summed up for all tracks used to setup the matrix. The same accounts for the vector $\mathbf{b}_k$ which contains products of the global derivatives with the normalized residuals:

$$\mathbf{b}_k = \sum_i \left(\frac{m_{ik} - h_i(\mathbf{a}, \boldsymbol{t}_k)}{\sigma_{ik}} \right) \cdot \left(\frac{\partial h_i(\mathbf{a}, \boldsymbol{t}_k)}{\partial \mathbf{a}} \right) . \tag{4.17}$$

Λ_k is the modified derivative matrix for the k^{th} track, as given in Equation 4.11.
For j parameters per track, the rectangular $N \times j$ sub-matrix $\boldsymbol{\mathcal{M}}_k$ correlates the

parameters of track k with the misalignment parameters according to

$$\boldsymbol{\mathcal{M}}_k = \sum_i \frac{1}{\sigma_{ik}^2} \left(\frac{\partial h_i(\mathbf{a}, \boldsymbol{t}_k)}{\partial \mathbf{a}} \right) \left(\frac{\partial h_i(\mathbf{a}, \boldsymbol{t}_k)}{\partial \boldsymbol{t}_k} \right)^T , \tag{4.18}$$

by summing over i track measurements.
The total number of rows and columns of the symmetric matrix is $N + j \cdot n$ with n denoting the number of tracks. For millions of tracks and thousands of misalignment parameters, the matrix has several million rows and columns. The matrix cannot be solved directly because of its size.
The large system in Equation 4.15 can be reduced by considering that the aim of the fit is to determine the misalignment parameters $\boldsymbol{\Delta}\mathbf{a}$ and that corrections to the track parameters $\Delta \boldsymbol{t}_k$ are negligible. This allows to reduce the matrix system down to a $N \times N$ system, for which the large matrix is partitioned into symmetric sub-matrices [78]. This method is an exact method, without carrying out any approximations. It leads to the modified matrix $\boldsymbol{C}'$ and the modified vector $\mathbf{b}'$:

$$\begin{aligned} \boldsymbol{C}' &= \sum_k \boldsymbol{C}_k - \sum_k \boldsymbol{\mathcal{M}}_k \boldsymbol{\Lambda}_k^{-1} \boldsymbol{\mathcal{M}}_k^T , &(4.19) \\ \mathbf{b}' &= \sum_k \mathbf{b}_k - \sum_k \boldsymbol{\mathcal{M}}_k \boldsymbol{\Lambda}_k^{-1} \boldsymbol{\eta}_k . &(4.20) \end{aligned}$$

This results in the linear matrix equation with the misalignment parameters $\boldsymbol{\Delta}\mathbf{a}$ as the unknowns

$$\left(\quad \boldsymbol{C}' \quad \right) \left(\boldsymbol{\Delta}\mathbf{a} \right) = \left(\mathbf{b}' \right) , \tag{4.21}$$

that is solved for $\boldsymbol{\Delta}\mathbf{a}$ by inverting $\boldsymbol{C}'$. Equation 4.21 includes not only the global alignment information, but also the complete local track information for all tracks through the asymmetric $\boldsymbol{\mathcal{M}}_k$ matrices. The obtained $\boldsymbol{C}'^{-1}$ is the covariance matrix of the misalignment parameters including all correlations between the parameters.
With the method presented above, misalignment parameters are determined in one single step by inverting matrix $\boldsymbol{C}'$.
Iterations are necessary in the following cases:

- The problem is non-linear in the parameters $\boldsymbol{\Delta}\mathbf{a}$ which requires the linearization of the function $h(\mathbf{a}, \boldsymbol{\Delta}\mathbf{a})$. In each iteration step the correction δa_i to the previously determined parameter Δa_i is calculated.

- Measurements contain outliers, which have to be removed from the fit as they can have a large influence on the result, see Chapter 6.

- The measurement uncertainties are unknown and have to be determined after alignment.

4.3.2 Solution of large matrix equations

The solution of linear equations as Equation 4.21, can be achieved with several mathematical methods. This section gives an overview of different possible solutions, together with their advantages and disadvantages, concerning computing accuracy and time. The solution method used in the algorithm developed within this thesis is the inversion method.

Inversion method

The matrix inversion method, which is implemented in the `MILLEPEDE` program is based on the Gauss algorithm with a pivot point selection [78]. In every step of the inversion, an element on the diagonal of matrix $\boldsymbol{C}$ is selected, the so called pivot point. All matrix elements are then modified according to defined rules, e. g., the elements in the row and column of the selected pivot point are divided by this pivot element. In case the pivot point is very small or the matrix is singular (the pivot point is zero), the inversion will fail (a small value will give inaccurate results).

The inverted matrix $\boldsymbol{C}^{-1}$ contains all variances and covariances of the determined parameters. The *correlation coefficient* ρ_j [77] represents the total correlation of parameter j with all other parameters defined by

$$\rho_j = \sqrt{1 - \frac{1}{\boldsymbol{C}_{jj} \cdot \boldsymbol{C}^{-1}_{jj}}} \ , \tag{4.22}$$

where the range of ρ_j is $0 \leq \rho_j \leq 1$. In case of a diagonal matrix $\boldsymbol{C}$ representing completely uncorrelated parameters, the correlation coefficient is $\rho_j = 0$.

Matrix $\boldsymbol{C}'$ of Equation 4.19 is not diagonal and contains information of both misalignment and track parameters. Through inversion of the matrix, the correlation between all misalignment parameters induced by the tracks is obtained according to Equation 4.22. In case $\rho_j = 1$, constraints have to be applied to reduce the correlation. Using the matrix inversion method, this is achieved, e. g., by setting the row and column of the corresponding parameter j to zero, the parameter is denoted as *fixed*. Fixed parameters are used to constrain weakly defined degrees of freedom like overall shifts or shearings, as will be shown in Section 4.3.3.

For a matrix of size $n \times n$, the computation time is $\propto n^3$ and therefore not well suited for systems of equation exceeding 10 000 parameters.

Diagonalization

A linear equation can be solved by diagonalization of the matrix. This way, it is possible to analyze the eigenvectors and the eigenvalue spectrum of the matrix which allows to identify undefined degrees of freedom. The diagonalization of a matrix $\boldsymbol{C}$ is obtained by an orthogonal transformation of the matrix according to

$$\boldsymbol{C} = \boldsymbol{U}\boldsymbol{D}\boldsymbol{U}^T \ , \tag{4.23}$$

where $\boldsymbol{D}$ is the diagonal matrix and $\boldsymbol{U}\boldsymbol{U}^T = \boldsymbol{U}^T\boldsymbol{U} = \mathbb{1}$ for the orthogonal matrix $\boldsymbol{U}$. The eigenvalues are given by the elements $\boldsymbol{D}_{ii}$ and the corresponding eigenvectors are

the columns of $\boldsymbol{U}$. The inverse of matrix $\boldsymbol{C}$ is simply $\boldsymbol{C}^{-1} = \boldsymbol{U}\boldsymbol{D}^{-1}\boldsymbol{U}^T$.
Analogously, the eigenvalue matrix $\boldsymbol{D}'$ of the alignment matrix $\boldsymbol{C}'$ (Equation 4.19) and the covariance matrix $\boldsymbol{C}'^{-1}$ can be obtained by diagonalization. The covariance matrix follows from $\boldsymbol{D}'^{-1}$, which implies that small eigenvalues can lead to large variances of the parameters.
The eigenvectors associated to eigenvalues that are small or zero are often called *weak modes*. These weak modes occur in case the system of equations is underconstrained. In an alignment process, the weak modes represent transformations of the detector positions that leave the χ^2 invariant. Such transformations are, e. g., a shift or rotation of the whole detector. They are avoided by applying constraints to the system.
If a weak mode exists, the matrix is singular and the full solution cannot be obtained. In this case the linear equation can be solved by explicitly removing the weak modes of the matrix. However, the identification of weak modes with small eigenvalues is not trivial and requires further calculations [79].
The computing time needed to determine the diagonal matrix is about 10 times larger than for inversion because the diagonalization algorithms are iterative.

Minimal residual methods

For systems of linear equations with a very large and sparse matrix, it is useful to consider the properties of the matrix. Whereas the inversion method can not make use of the sparse structure, the minimal residual methods can. The `MINRES` [80] algorithm, for example, is developed to solve systems with indefinite symmetric matrices that are large and sparse. The solution requires only matrix-vector products which is clearly advantageous if most of the matrix elements are zero. An extension of this method to asymmetric matrices is given by the 'Generalized minimal residual method' (`GMRES`), for further details see [81].
The minimal residual methods can solve a problem much faster than the inversion method, especially for large matrices. For these methods, the errors of the parameters have to be calculated additionally and are not an automatic result of the procedure.

Many other solution methods are discussed in the literature, like the 'Cholesky decomposition' or the 'Singular value decomposition', see Reference [78].

4.3.3 Undefined degrees of freedom

The misalignment parameters $\mathbf{\Delta a}$ are determined by the minimization of the track χ^2 with respect to misalignment parameters. In the χ^2 minimization, linear transformations like a shift of the complete detector leave the residual unchanged. These linear transformations represent undefined degrees of freedom that have to be constrained, otherwise the alignment procedure has no unique solution.
Four undefined degrees of freedom are illustrated in Figure 4.2. The figure shows the xz view of five detector elements, the elements plotted in light grey define the nominal detector positions. Figure 4.2 (a) depicts a shift of the overall detector corresponding to a constant term added to the χ^2. In figure (b), a term $\epsilon_i = \theta z_i$ is added to each detector element. θ is the angle between the z axis and a line through the center of the shifted

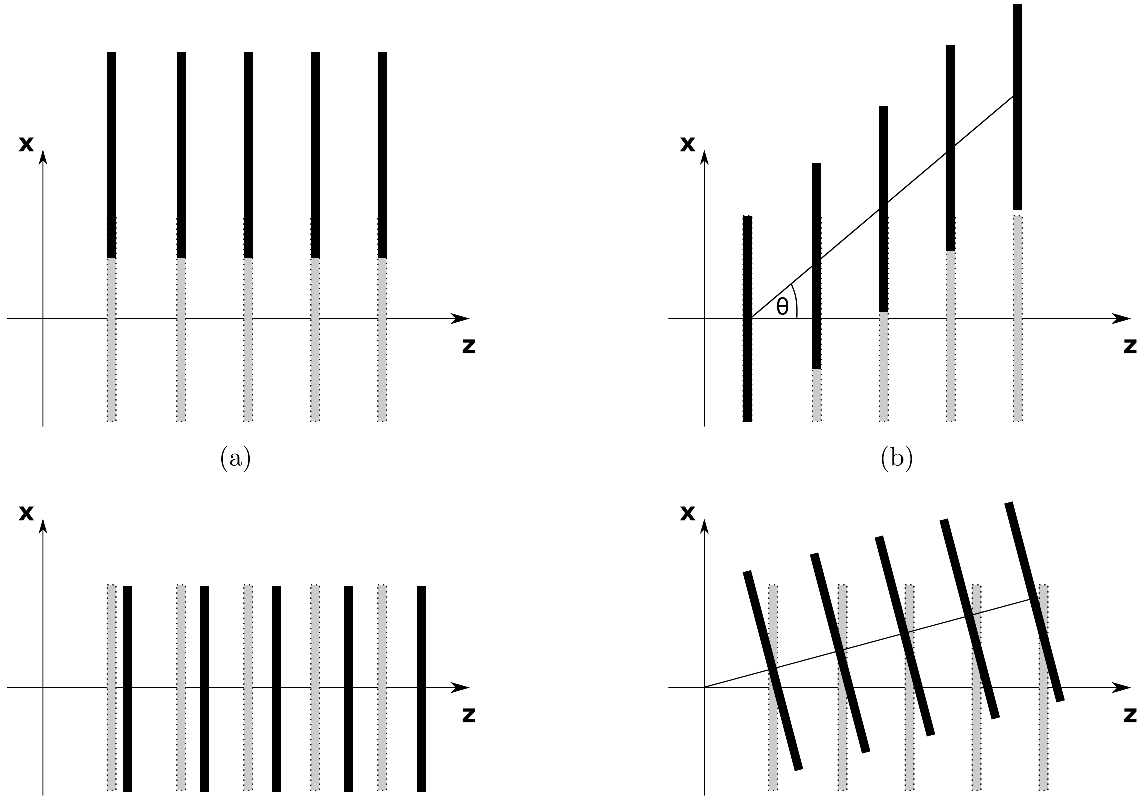

(a) (b)

(c) (d)

Figure 4.2: Example of undefined degrees of freedom that leave the corresponding track χ^2 invariant. (a) A shift D_x of the whole detector. (b) Shearing S_{xz} of the detector elements. (c) Scaling C_z along z direction and (d) an overall rotation R_y of the detector.

elements. This is called shearing S_{xz} in the xz plane. The transformation leaves the track residual unchanged, because the track slope it not known a priori. Additionally, a change of the scale as illustrated in figure (c) leaves the track residual invariant due to initially unknown track parameters. The same accounts for an overall rotation of the detector, depicted in figure (d).

The most general linear transformations in three dimensional space are described by twelve parameters:

- Three overall shifts D_x, D_y, D_z;
- Three scalings C_z, C_y, C_z;
- Three shearings S_{xz}, S_{yz}, S_{xy};
- Three rotations R_x, R_y, R_z.

4.3.4 Procedure to constrain undefined degrees of freedom

In order to obtain a unique solution for the track based alignment procedure, the undefined degrees of freedom discussed in the previous section have to be constrained. This section describes two methods with which a unique solution can be obtained.

Table 4.1: The minimum number of fixed detector elements n_{min} required to constrain the undefined degrees of freedoms: Shifts D, scalings C, shearings S and rotations R. The indices ν and μ stand for the three directions X, Y, Z, with $\nu \neq \mu$.

	D_ν	C_ν	$S_{\nu\mu}$	R_ν
n_{min}	1	2	2	1

Parameter fixation

As discussed in Section 4.3.1, the misalignment parameters are obtained by the solution of $\boldsymbol{C}'\boldsymbol{\Delta}\mathbf{a} = \mathbf{b}'$ (Equation 4.21) where the matrix $\boldsymbol{C}'$ contains all geometry and track information. If the system of equations is solved by matrix inversion, undefined degrees of freedom can be constrained by the *parameters fixation* method: A single detector element i is called *fixed*, in case the alignment procedure does not account for corrections to its geometry parameters $\mathbf{a}_i$. It implies, that the misalignment parameters $\boldsymbol{\Delta}\mathbf{a}_i$ of the corresponding element i are removed from the fit. This is achieved by setting the corresponding rows and columns in matrix $\boldsymbol{C}'$ to zero.
In order to constrain the linear transformations of detector elements as shown in Figure 4.2, a minimum number n_{min} of detector elements has to be fixed. To avoid an overall shift of the detector D_x in x direction as sketched in Figure 4.2 (a), it is necessary to fix one detector element to a defined x position. This way a common shift of the non-constrained elements is avoided, as it would increase the track residual.
It is necessary to fix the x position of a second detector element in order to avoid the shearing S_{xz} that is depicted in Figure 4.2 (b). Fixing the x position of two detector elements is the minimal constraint required to avoid an overall shift and shearing of the detector.

Figure 4.3 (a) illustrates a placement of 15 detector elements in the xz plane, the elements are distributed also along the x direction. This results in an additional degree

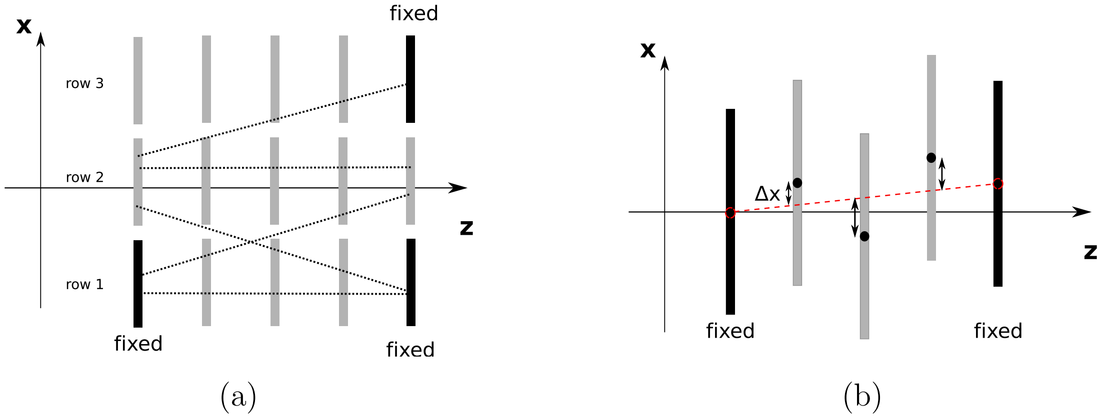

(a) (b)

Figure 4.3: (a) If several sub detectors are placed along x at the same z, the scale C_x is an additional degree of freedom. Constraints can be propagated by interconnecting tracks to all detector elements. (b) The determined misalignment parameters have to be interpreted in the alignment reference system which is defined by the applied constraints. Here, the fixed detector elements define the reference, illustrated by the dashed line.

of freedom, namely the scale C_x in x direction. For a track distribution as sketched in the figure, all 15 detector elements can be constrained by the fixation of three elements. The applied constraints are propagated by interconnecting tracks to all detector elements. A different track distribution might require to fix additional elments to constrain the system. This implies, that track slopes have to be as manifold as possible for the optimal propagation of constraints which results in the minimum number of fixed elements.
Table 4.1 shows the minimal number of detector elements n_{min} that have to be fixed to defined positions in order to avoid linear transformations of the detector.

The constraints imposed to the alignment process introduce a reference system in which the misalignment parameters have to be evaluated. The reference system is given by the positions to which the elements have been fixed. This fact is illustrated in Figure 4.3 (b) that shows the influence of the constraints on the determination of the misalignment parameter Δx. Depicted are five detector elements in the xz plane. The first and last detector elements are fixed to their actual (x, z) positions. The coordinates of these elements define the reference (dashed line) relative to which the misalignment parameters Δx are determined. As illustrated, the reference system is not necessary equal to the detector coordinate system given by the x and z axis in the figure. This has to be considered for the interpretation of the determined misalignment parameters.

Lagrange multiplier method

The second method to constrain undefined degrees of freedom is the Lagrange multiplier (LM) method [82]. In contrast to the parameter fixation method which *reduces* the size of matrix $\boldsymbol{C}'$ (Equation 4.21) by removing rows and columns, the LM method *extends* the matrix $\boldsymbol{C}'$. The LM method takes relations between misalignment parameters $\Delta \mathrm{a}_i$ ($= i^{th}$ entry of the vector $\mathbf{\Delta a}$) into account, expressed as

$$\mathbf{\Delta a}^T \boldsymbol{\varphi} = \varphi_0 \; . \tag{4.24}$$

The relation is applied to the linear least squares problem by adding a row and a column of $\boldsymbol{\varphi}$ to the matrix $\boldsymbol{C}'$, giving the equation

$$\left(\begin{array}{c|c} \boldsymbol{C}' & \boldsymbol{\varphi} \\ \hline \boldsymbol{\varphi}^T & \mathbf{0} \end{array}\right) \left(\begin{array}{c} \mathbf{\Delta a} \\ \hline \zeta \end{array}\right) = \left(\begin{array}{c} \mathbf{b}' \\ \hline \varphi_0 \end{array}\right) , \tag{4.25}$$

with the Lagrangian multiplier ζ, whereas each additional constraint introduces an extra multiplier.
The principle of the method is sketched in Figure 4.4. The figure shows five detector elements (grey) in the xz plane that are misaligned with respect to their ideal positions (dashed). Using the LM method to avoid an overall detector translation, the following relation between the shifts of all i detector elements is used: $\sum_i \Delta x_i = 0$, where the sum is taken over i detector elements. This constraint introduces a new reference system in which the misalignment parameters Δx_i are determined. In the figure, this reference is

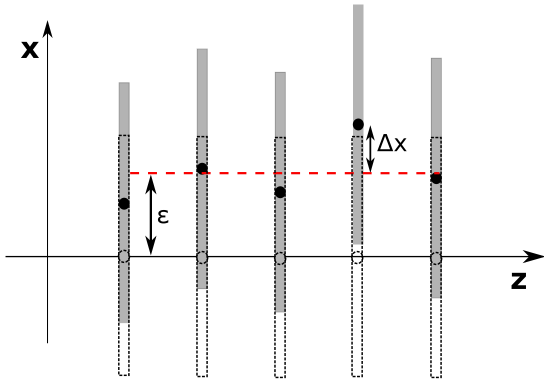

Figure 4.4: Example of the alignment reference system in case linear equality constraints are applied. In the plot, the constraint requires $\sum_i \Delta x_i = 0$, the reference is indicated by the dashed line relative to which the parameters are determined. ϵ can be calculated only if the misalignment are known, i. e., for simulated misalignment.

indicated by the red line that is displaced by $x = \epsilon$ with respect to the default detector reference at $x = 0$. Determined misalignment parameters Δx_i describe shifts with respect to the new reference.

4.4 Parameterization of the Outer Tracker alignment problem

Within this thesis, an algorithm for the determination of misalignment parameters $\mathbf{\Delta a}$ of the LHC*b* Outer Tracker detector has been developed. The general alignment procedure presented in Section 4.3 has been refined to the specific needs of an Outer Tracker alignment procedure.
In this section, first the definition of the misalignment parameters $\mathbf{\Delta a}$ of the Outer Tracker is given. Afterwards, the undefined degrees of freedom in the Outer Tracker alignment procedure are analysed and the two methods to constrain these degrees of freedom are compared.

4.4.1 Misalignment parameters of the Outer Tracker detector

As presented in Chapter 2, the Outer Tracker detector is a drift tube detector composed of 216 modules. The drift tube technology allows one dimensional measurements in direction perpendicular to the tubes. Measurements are given in the *local* coordinate system of a module that is defined by the Cartesian system shown in Figure 4.5. Shifts and rotations of a module affect these measurements. A determination of misalignment parameters in the local system of each module would imply 216 different coordinate system. As this is not feasible, misalignment parameters are determined in the LHC*b* coordinate system. This is the reference system for the position of all modules and is called the *global* coordinate system.
The transformation of measurements from the local to the global coordinates is described below.

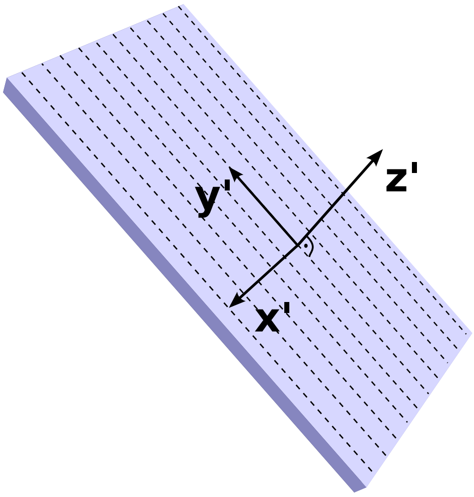

Figure 4.5: Definition of the local coordinate system of a detector element. Sketched is an element which is sensitive to measurements in x' direction, like it is realized for the Outer Tracker modules. Here, the y' axis is defined perpendicular to the measurement direction, the z' direction is equal to the normal.

Transformation between local and global coordinates

The local coordinate system of a module is depicted Figure 4.5, the point of origin lies in the center of the module. The dashed lines represent the straw tubes that are insensitive to information along the straw that defines the y' axis. Measurements are given along the local x' axis, the normal to the measurement plane is the z' axis. Any rotation of the module can be described as a rotation around one of the local coordinate axes. A traversing particle intersects with the measurement plane of the detector at point $\mathbf{x}' = (x', y', 0)$, where $z' = 0$ as the measurement is done on the sensitive surface. Thus, $\mathbf{x}'$ is transformed into the global coordinate $\mathbf{r}$ by

$$\mathbf{r} = \boldsymbol{\Omega}\mathbf{x}' + \mathbf{T} \,, \tag{4.26}$$

here, the rotation matrix $\boldsymbol{\Omega}$ describes the orientation and the vector $\mathbf{T}$ the position of the module in the global frame. The orientation is described by the matrix product of the three rotation matrices, i. e., $\boldsymbol{\Omega} = \boldsymbol{\Omega}_{y'}\boldsymbol{\Omega}_{x'}\boldsymbol{\Omega}_{z'}$ in this order[2], with

$$\boldsymbol{\Omega}_{x'} = \begin{pmatrix} 1 & 0 & 0 \\ 0 & \cos\alpha & -\sin\alpha \\ 0 & \sin\alpha & \cos\alpha \end{pmatrix}, \; \boldsymbol{\Omega}_{y'} = \begin{pmatrix} \cos\beta & 0 & \sin\beta \\ 0 & 1 & 0 \\ -\sin\beta & 0 & \cos\beta \end{pmatrix}, \; \boldsymbol{\Omega}_{z'} = \begin{pmatrix} \cos\gamma & -\sin\gamma & 0 \\ \sin\gamma & \cos\gamma & 0 \\ 0 & 0 & 1 \end{pmatrix}, \tag{4.27}$$

α, β, γ represent the rotations around the x', y', z' axis in the local frame. In the present case, the angle γ is the stereo angle of the Outer Tracker modules (see also Chapter 2).

Introducing misalignments

Misalignments are introduced by shifts and rotations of the module in its local frame. As possible misalignments in the rotational degrees of freedom are $\mathcal{O}(\,\text{mrad})$, the

---

[2] Matrix multiplication is non commutative and any other order leads to a different transformation.

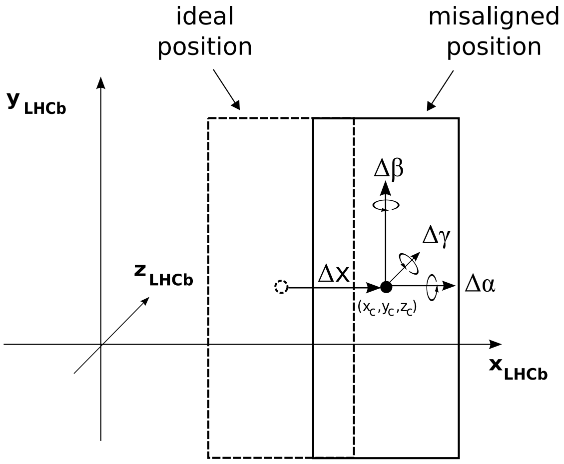

Figure 4.6: Sketched is the nominal (dashed line) and misaligned position of a detector element (solid line). Shifts and rotations with respect to the nominal position are defined relative to the geometrical center (x_C, y_C, z_C) of the element. Here, a shift in the measurement direction is depicted.

approximation $\sin a \to a$ and $\cos a \to 1$ are valid, leading to the following rotation matrix

$$\boldsymbol{\Delta\Omega}' = \begin{pmatrix} 1 & -\Delta\gamma' & \Delta\beta' \\ \Delta\gamma' & 1 & -\Delta\alpha' \\ -\Delta\beta' & \Delta\alpha' & 1 \end{pmatrix} . \qquad (4.28)$$

Together with the translation vector $\mathbf{\Delta T}'$, measurements in the misaligned local frame are transformed to the global frame by

$$\mathbf{\Delta r} = \boldsymbol{\Omega}(\boldsymbol{\Delta\Omega}'\mathbf{x}' + \mathbf{\Delta T}') + \mathbf{T} . \qquad (4.29)$$

The alignment procedure finally determines the misalignment parameters that represent shifts and rotations in the global LHCb coordinate system (Figure 4.6):

$$\mathbf{\Delta a} = \begin{pmatrix} \Delta x \\ \Delta z \\ \Delta\alpha \\ \Delta\beta \\ \Delta\gamma \end{pmatrix} . \qquad (4.30)$$

Here, $\Delta\alpha$,$\Delta\beta$,$\Delta\gamma$ are the rotations around the x, y, z axes and Δz represents shifts along z. The misalignment parameter Δx denotes shifts along the measurement direction, it is defined as

$$\Delta x = \delta x \cos\gamma + \delta y \sin\gamma , \qquad (4.31)$$

where δx and δy are shifts along the LHCb x and y axes. The angle γ describes the rotation of the module with respect to the y axis. Thus, $\gamma = 0°$ for modules of x layers, as shifts in y direction do not affect the measurement direction of these modules. For stereo modules, the angle is $\gamma = \pm 5°$. With this definition of Δx, the misalignment parameter $\mathbf{\Delta a}$ represents misalignments of x module as well as of stereo modules.

4.4.2 Undefined degrees of freedom in the Outer Tracker alignment procedure

In the track based alignment procedure, undefined degrees of freedom are represented by linear transformation of detector elements that leave the track residual unchanged (Section 4.3.3). The developed alignment algorithm determines misalignment parameters by using information contained in the residual of tracks that are solely reconstructed in the Outer Tracker stations. External track information from other subdetectors are not considered as possible misalignments of these detectors would influence the alignment procedure. This procedure is a so-called *internal* alignment procedure.

In order to constrain a linear transformation of the detector elements in the *internal* alignment process, the constraints must be imposed to the elements of the detector. The most general transformation are described by 3 scaling, 3 translation, 3 rotation and 3 shearing parameters. Some of these transformations become meaningless in the alignment procedure of the Outer Tracker because of the design of the detector:

- The pitch of the straw tubes constrains the scaling C_x in x direction.
- The detector is not segmented in y direction, hence a rescaling C_y in this direction is excluded.
- The shearing S_{xy} in the xy plane is impossible with a rigid module.

This leaves nine undefined degrees of freedom that have to be considered in the alignment procedure of the Outer Tracker.

It has been discussed in Section 4.3.2, that the linear transformations become evident in the eigenvalue spectrum of matrix $\boldsymbol{C}'$ (Equation 4.19): Small eigenvalues lead to large variances of the misalignment parameters which indicate a badly constrained system of equations. The corresponding eigenvectors are called weak modes. An analysis of the eigenvectors allows to identify the type of linear transformation that lead to the small eigenvalues. An example of an analysis of the eigenvalues and eigenvectors is presented in the following, where a track based alignment procedure is run for the twelve Outer

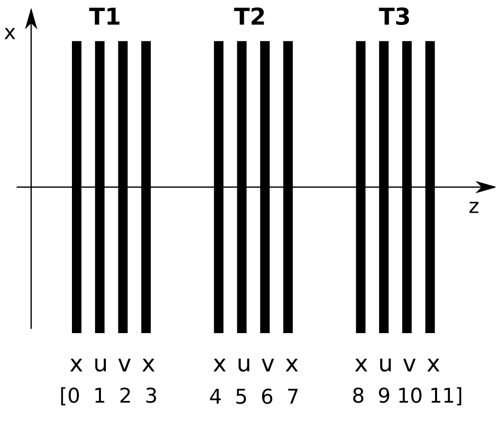

Figure 4.7: The *xuvx* arrangement of the Outer Tracker layers in the *xz* plane of the detector. The numbers correspond to the numbering of eigenvalues and the eigenvector entries in Figure 4.8 and Figure 4.9,

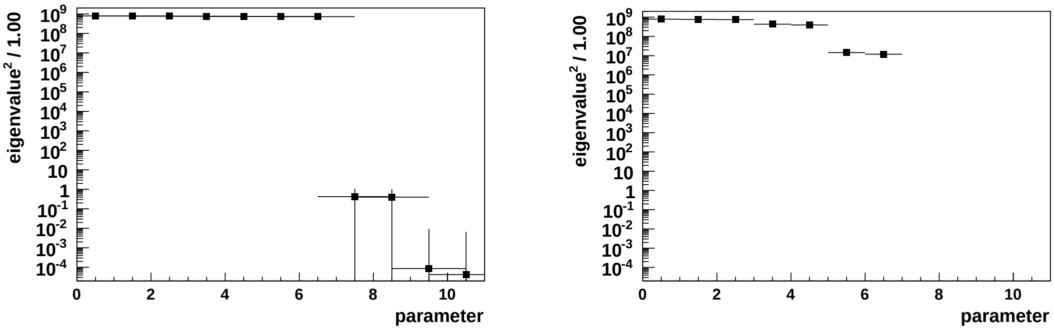

(a)

(b)

Figure 4.8: Squared eigenvalue spectrum obtained after diagonalization of matrix $\boldsymbol{C}'$ (Equation 4.19). The matrix is set up for the alignment procedure of the twelve Outer Tracker layers. (a) The last four values represent unconstrained external degrees of freedom. (b) The spectrum after constraining the external degrees of freedom.

Tracker layers without applying constraints to the problem.

The procedure is run within the LHC*b* software framework (Section 2.4) and exploits the detailed geometry description of the detector. Simulated data are used[3] in order to determine the misalignment parameters Δx_i ($i = 0 \ldots 11$) for all twelve layers. As the procedure is processed with ideal detector positions, the expected misalignment parameters are $\Delta x_i = 0\,\mathrm{mm}$ for each layer. The labelling of the layers as it is used below are sketched in Figure 4.7.

The eigenvalue spectrum of the determined alignment matrix $\boldsymbol{C}'$ (Equation 4.19) is presented in Figure 4.8 (a). It shows the eigenvalue[4] parameters obtained for each layer in case no constraints are applied to the problem. The last four eigenvalues are very close to zero and the ratio between the largest and smallest entry is $\kappa = 4\,336\,964$. This ratio is called the condition number of a matrix. In case $\kappa \gg 1$, the matrix is badly conditioned and the solution of the linear equations system is inaccurate, which can be seen in Table 4.2. Here, the twelve misalignment parameters Δx_i, their uncertainties σ_i and the correlation coefficients ρ_i that are obtained from the alignment procedure are shown. The parameters show an enormous arbitrary value which is in contrast to the expected $\Delta x_i = 0\,\mathrm{mm}$. Moreover, the parameter uncertainties are large and a 100 % correlation among the parameters is observed.

As mentioned above, this result is due to the four very small eigenvalues that represent linear transformation of the whole detector. The type of transformation is found in the corresponding eigenvectors, depicted in Figure 4.9. The vector entries $0 \ldots 11$ refer to the twelve layers and are marked according to the type of layer they refer to, i. e., x layer or stereo layer. The values of the vector in Figure 4.9 (a) constantly change from first to last entry for every layer type. This clearly indicates the shearing S_{xz} of the layers that is not constrained. From the stereo layers, additional information in y direction is obtained, thus they are affected also by a shearing S_{yz}, that is identified in

---

[3] The type of data are discussed in detail in Chapter 5.

[4] In fact the square of the eigenvalue is shown as some eigenvalues are negative but a logarithmic scale is requisite for the distinct presentation of the spectrum.

Table 4.2: Results for the alignment of the Outer Tracker layers. The alignment parameters Δx obtained for the unconstrained case show arbitrary offsets and complete correlation to each other. With constraints applied, the results are as expected.

		Unconstrained			Constrained		
	Layer	Δx [mm]	σ[mm]	ρ	Δx [mm]	σ[mm]	ρ
Station T1	X	5459	3471	1.00	-	-	-
	U	-337325	11008	1.00	-	-	-
	V	348202	10971	1.00	-0.0050	0.0140	0.72
	X	5458	3471	1.00	0.0040	0.0081	0.57
Station T2	X	5458	3471	1.00	-0.0003	0.0073	0.53
	U	-337326	11008	1.00	0.0002	0.0092	0.65
	V	-348202	10971	1.00	-0.0001	0.0093	0.66
	X	5458	3471	1.00	0.0025	0.0073	0.53
Station T3	X	5458	3471	1.00	-0.0064	0.0080	0.57
	U	-337327	11008	1.00	-0.0111	0.0139	0.71
	V	-348202	10971	1.00	-	-	-
	X	5457	3471	1.00	-	-	-

figure (b). Arbitrary shifts D_x and D_y are depicted in the lower figures (c) and (d). These undefined degrees of freedom have to be constrained to obtain meaningful solution of alignment procedure. One possibility is to remove the corresponding eigenvectors from the matrix, which is equivalent to a fixation of the layers to their actual, in this example ideal positions. The eigenvalue spectrum of this reduced matrix obtained with the alignment procedure is presented in Figure 4.8 (b). The matrix is well conditioned with $\kappa = 8.2$ and the misalignment parameters Δx_i are equal to zero within their uncertainties, listed in Table 4.2. Furthermore, the correlation ρ between the parameters is reduced significantly.

4.4.3 Comparison of two methods to constrain undefined degrees of freedom

The alignment algorithm developed within this thesis allows to constrain undefined degrees of freedom either with the Lagrange multipliers (LM) method or with the parameter fixation (PF) method. The methods have been discussed in Section 4.3.4 and it has been shown that the methods introduce new reference systems in which the misalignment parameters are determined. In this section, the equivalence of the two methods is discussed under consideration of the corresponding reference systems.

For this purpose, two alignment procedures are run, for which each run is performed with the same misaligned Outer Tracker geometry but a different constraining method. The displacement of the Outer Tracker is represented by shifts δx of the x layers (Figure 4.7) in measurement direction. The shifts are applied in the global LHCb coordinate system,

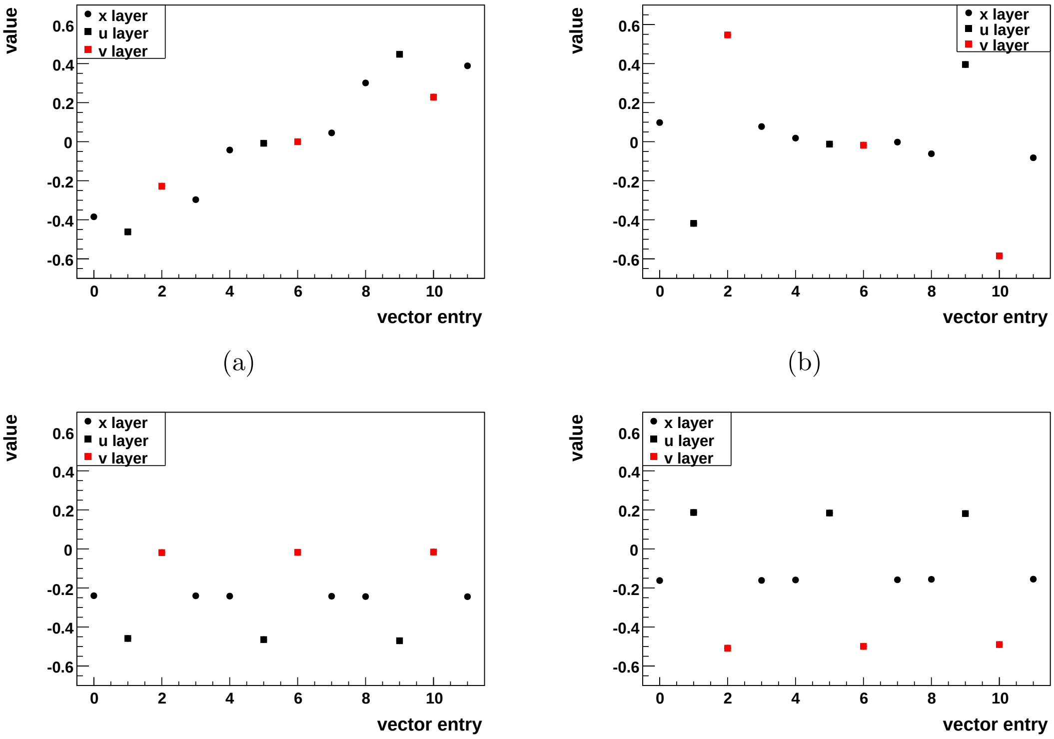

(a) (b)

(c) (d)

Figure 4.9: Eigenvectors of the last four eigenvalues from Figure 4.8 (a). The vectors reflect the unconstrained external degrees of freedom. Figures (a) and (b) indicate the shearing in the xz and yz plane respectively. (c) and (d) show an overall offset.

δx is listed in Table 4.3. Additionally, the table shows transformations of the shifts that are necessary in order to compare the simulated misalignments with the determined misalignment parameters:

- δx_{PF} are the simulated misalignments transformed in the reference system imposed by the constraints of the parameter fixation (PF) method.
- δx_{LM} denote the shifts in the reference system imposed by the Lagrange multiplier (LM) constraints.

For the sake of argument, the first layer T1X1 and the last layer T3X2 are not shifted. In this case, the shifts δx in the detector system are equal to shifts δx_{PF} in the system of the parameter fixation method.

For the Lagrange multiplier method, the shifts δx have to be transformed explicitly to the LM reference system. The transformation is given in detail in Appendix B. A net translation $\delta x - \delta x_{LM} \approx 200\,\mu$m becomes evident by comparing the numbers of the layers of station T2 in the table[5]. The relative difference of δx_{LM} of more than $400\,\mu$m for the first and last layer indicates the influence of a shearing term, see Appendix B. The two alignment runs are processed with simulated data, that are explained in detail in Chapter 5. Figure 4.10 (a) shows the result, which is obtained with the

---

[5] It is this net translation which is indicated by ϵ in Figure 4.4.

Table 4.3: The simulated misalignment used for the present comparison of the two constraining methods. The misalignment are applied to the Outer Tracker x layers in the LHCb coordinate system. To compare simulated misalignments with determined misalignment parameters, the shifts have to be transformed into the reference system imposed by the constraints. The transformed values are given by δx_{PF} and δx_{LM}.

reference system		T1X1	T1X2	T2X1	T2X2	T3X1	T3X2
detector	δx [mm]	0	0.53	-3.45	0.97	-0.68	0
PF	δx_{PF} [mm]	0	0.53	-3.45	0.97	-0.68	0
LM	δx_{LM} [mm]	-0.02	0.47	-3.66	0.72	-1.07	-0.44

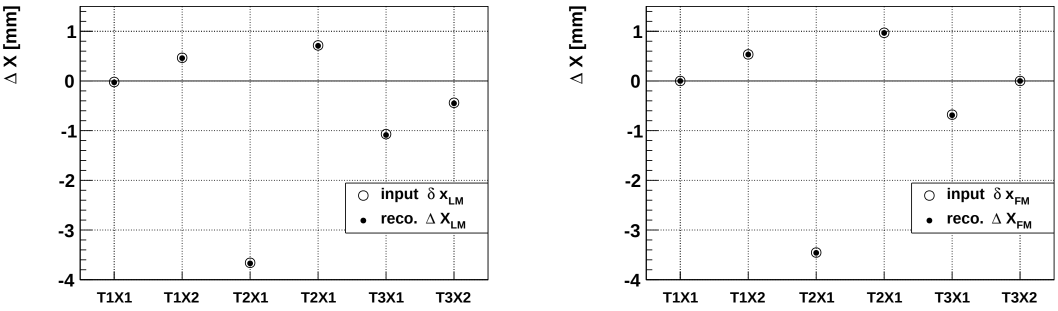

(a) Lagrange Multiplier

(b) Parameter Fixation

Figure 4.10: Comparison of simulated (circles) and reconstructed (points) misalignment of the x layers. (a) Results obtained with the Lagrange multipliers method that is used to constrain undefined degrees of freedom. (b) Using the parameters fixation method give the results shown in the right plot.

Lagrangian multiplier method. The transformed input misalignments (circles) and determined misalignment parameters (points) are depicted. It is evident, that in the LM reference system, the simulated misalignment are correctly determined with the alignment procedure.

The results for parameter fixation method are shown in Figure 4.10 (b). As mentioned, a transformation into a new reference system is gratuitous in this case. The figure shows, that the determined misalignment parameters are equal to the simulated input misalignments.

The equality of the two methods is shown by comparison of the track residuals and reduced χ^2 distribution, Figure 4.11. Figure (a) and (c) depict the track residual before and after alignment for both types of constraints. In addition, the corresponding reduced χ^2 distributions are given. The distributions obtained with the Lagrange multipliers constraints are identical to those achieved with the parameters fixation method.

For development and study of the alignment algorithm, the parameters fixation method is used as transformations into new reference systems can be avoided and simulated misalignments can be compared directly to determined misalignment parameters.

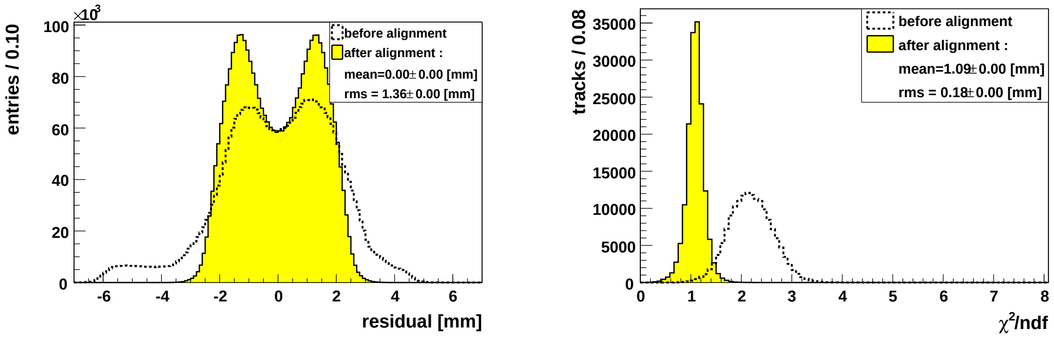

(a) Lagrange Multiplier

(b) Lagrange Multiplier

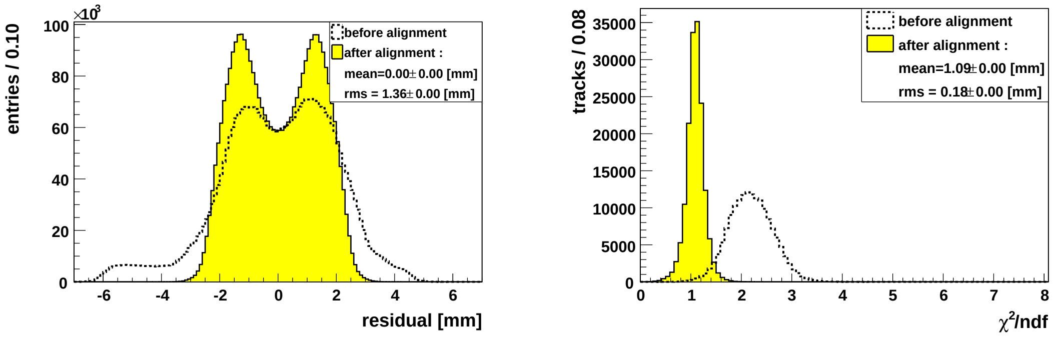

(c) Parameter Fixation

(d) Parameter Fixation

Figure 4.11: Comparison of track properties before and after alignment. The upper two figures are obtained by constraining undefined degrees of freedom with Lagrange multiplier. (a) Track residual before and after alignment. (b) Reduced χ^2 distribution for aligned and misaligned layers. The lower figures (c) and (d) depict the same distributions, gained with the fixed parameters method. All properties show the same distribution. The two constraining methods are equivalent.

Chapter 5

Validation of the LHC*b* Outer Tracker alignment procedure with simulated data

The LHC*b* Outer Tracker agnment algorithm developed within this thesis is validated by studies that are presented in this chapter. For the validation, simulated data and generated detector misalignments are used. The detector misalignments are applied during the reconstruction of the data when the pattern recognition algorithm and the track fit are processed. The reconstructed tracks are used in the alignment procedure to determine misalignment parameters that are then compared to the simulated shifts and rotations.
The validation procedure is discussed in Section 5.1 in which the used generated detector misalignment sets are presented and the simulated data are specified. The track fit used in the alignment procedure is presented in Section 5.2. The section is followed by results of the alignment procedures on the level of half layers (Section 5.3) and modules (Section 5.4) that are processed with straight line tracks. Section 5.5 gives an outlook on the alignmnet procedure with particle trajectories that are bent in the magnetic field of the detector.

5.1 Validation procedure

This section discusses the procedure for the validation of the developed algorithm. It entails the presentation of the misaligned geometries (Section 5.1.1) and the simulated data used for the validation (Section 5.1.2). The alignment procedure is explained in Section 5.1.3.

5.1.1 Misaligned Outer Tracker geometries

The developed algorithm is implemented in the software framework of the LHC*b* experiment and has access to the detailed geometry description of the detector. The Outer Tracker detector description in the database has been discussed in Chapter 2. It is based on a hierachical structure that reflects different segmentation levels of the

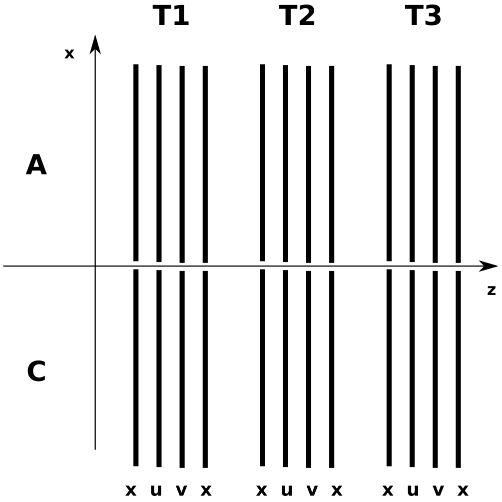

Figure 5.1: Sketch of the 24 Outer Tracker half layers. The half layers left and right of the z axis (beam axis) are denoted as A-side and C-side half layers, respectively.

detector and allows to align layers, half layers and modules. The validation of the algorithm is processed on the level of half layers and modules.

Simulated half layer misalignments

Figure 5.1 illustrates the arrangement of the 24 half layers in the xz plane of the detector. Each half layer is "mirrored" at the z axis that points along the beam direction.

Table 5.1 shows the seven geometry databases that have been generated to simulate different misalignments of the half layers[1]. For each of the databases $1-5$, the half layers are misaligned only in one degree of freedom. The remaining degrees of freedom are left

---

[1] Due to the layout of the geometry data base, shifts and rotations are applied to whole layers, instead of half layers. Thus, same shifts are applied to the half layers on the A-side and C-side. This has no influence on the results obtained with the alignment procedure.

Table 5.1: Generated geometry databases that contain misaligned half layer positions.

database	misaligned dof					misalignment
	x	z	α	β	γ	scale
1	×	-	-	-	-	$\sigma_x = 2\,\text{mm}$
2	-	×	-	-	-	$\sigma_z = 1\,\text{mm}$
3	-	-	×	-	-	$\sigma_\alpha = 1\,\text{mrad}$
4	-	-	-	×	-	$\sigma_\beta = 1\,\text{mrad}$
5	-	-	-	-	×	$\sigma_\gamma = 1\,\text{mrad}$
6	×	-	-	-	×	$\sigma_x = 1.5\,\text{mm}$, $\sigma_\gamma = 1\,\text{mrad}$
7	×	×	×	×	×	$\sigma_x = \sigma_z = 1\,\text{mm}$ $\sigma_\alpha = \sigma_\beta = \sigma_\gamma = 0.5\,\text{mrad}$

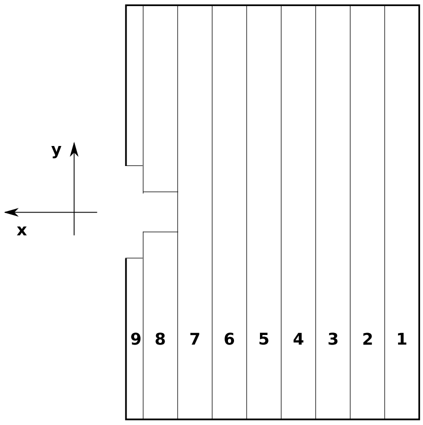

Figure 5.2: The numbering of modules in a half layer.

unchanged. Column three of the table indicates the scale of the applied misalignments which are randomly generated following a Gaussian distribution. The misalignment scales represent the width σ of the Gaussian distribution. For database 6, half layers are shifted in x direction and rotated around the z axis, database 7 represent misalignments in all degrees of freedom.

The mentioned misalignments are applied to 16 out of the 24 half layers. Excluded are the first four x, u half layers and the last four v, x half layers. This choice is based on the method used to constrain the undefined degrees of freedom: The parameter fixation (PF) method. As discussed in Section 4.3.4, with this method transformations of the simulated misalignments into a new reference system can be avoided and it is possible to directly compare the simulated misalignments with the determined misalignment parameters.

The first x, u and the last v, x half layers represent the minimum number of detector elements necessary to constrain the undefined degrees of freedom (Table 4.1):

- Linear transformations in x direction are constrained by the fixed x layers.
- The u and v layers constrain transformations in the y direction.

Simulated module misalignments

A half layer is composed of nine modules, as depicted in Figure 5.2 (the upper and lower part of modules 8 are connected with each other and count as one element, the same accounts for module 9). Modules are the smallest physical detector unit of the Outer Tracker which comprises in total 216 modules.

The databases that simulate misaligned module positions are listed in Table 5.2. A module rotation around the y axis is not simulated because it has no significant impact on the track residual and is thus not detectable. The reason for this is found in the short lever arm of 150 mm for a module width of 300 mm.

The modules in the first and the last two layers remain at their ideal positions. As undefined degrees of freedom are constrained by the parameter fixation method, this leaves some freedom in the final choice of the number modules that are fixed to the ideal positions.

Table 5.2: Misalignments of module positions are simulated with the listed geometry databases.

database	misaligned dof					misalignment
	x	z	α	β	γ	scale
1	×	-	-	-	-	$\sigma_x = 1\,\mathrm{mm}$
2	-	×	-	-	-	$\sigma_z = 1\,\mathrm{mm}$
3	-	-	×	-	-	$\sigma_\alpha = 1\,\mathrm{mrad}$
4	-	-	-	-	×	$\sigma_\gamma = 1\,\mathrm{mrad}$

5.1.2 Simulated data

Within this thesis, the main focus has been put on the development of an alignment algorithm that processes straight line tracks in order to determine misalignment parameters $\mathbf{\Delta a}$. Curved tracks impose one additional undefined degree of freedom to the alignment procedure that has to be constrained. In order to avoid the need of an additional constraint, alignment procedures are preferentially processed with straight tracks.
For the validation of the algorithm, data containing straight muon tracks have been simulated, the data is presented below (data set 1). A brief insight in the alignment procedure with curved tracks will be given in Section 5.5, for this purpose data set 2 is used.

Data set 1: This data set contains simulated “multi-muon” events. The energy of the simulated muons is $E_\mu > 100\,\mathrm{GeV}$ and the track density per event is below $20\frac{tracks}{evt}$. This results in negligible effects of multiple scattering in the detector material and a vanishing number of ghost and clone tracks (Chapter 3), that can influence the results of the alignment procedure.
The muon trajectories are straight lines that traverse the whole detector, beginning at the origin of the LHC*b* coordinate system. The generated track slopes are Gaussian distributed with the width $\sigma_{t_x} = \sigma_{t_y} = 0.14$ in x and y direction. The slope distribution

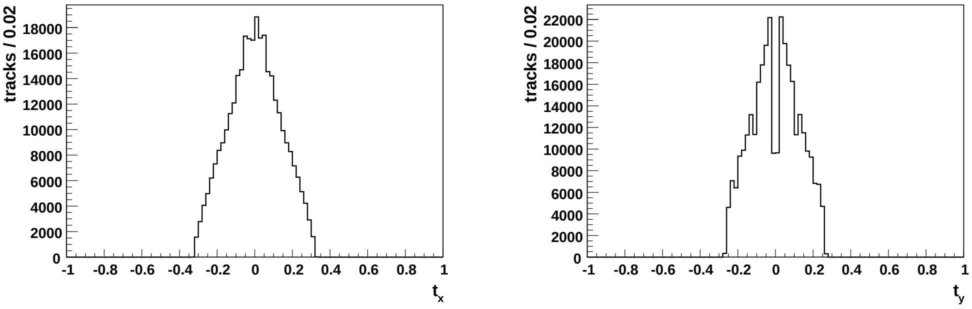

(a) (b)

Figure 5.3: Track slopes t_X and t_y in x and y direction for the generated data. The inefficient region of the Outer Tracker around $y = 0\,\mathrm{mm}$ is visibly in the t_y distribution.

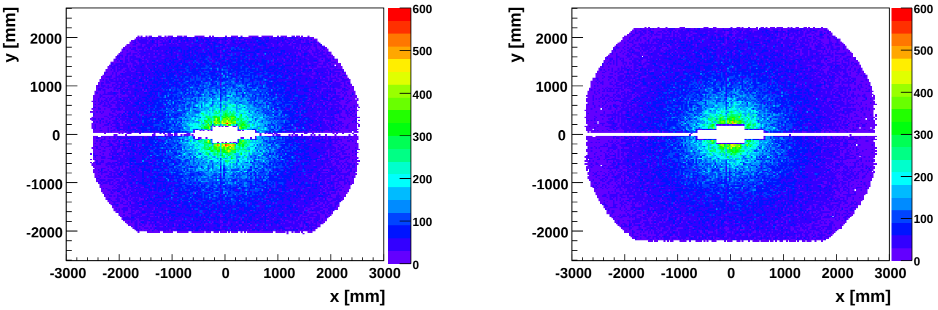

(a) T1: $z = 7838\,\mathrm{mm}$ (b) T2: $z = 8525\,\mathrm{mm}$

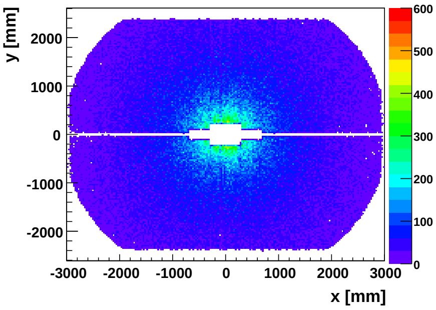

(c) T3: $z = 9215\,\mathrm{mm}$

Figure 5.4: Hit distribution of the generated muon data at $z = 0\,\mathrm{mm}$ and at the first layers of each T station. The cut of the distribution at the boundaries are due to the track selection criterion: at least 15 hits in the OT are required for a tracks to be accepted.

of the reconstructed tracks are depicted in Figure 5.3. The insensitive detector area around $y = 0\,\mathrm{mm}$ is visible in Figure (b).
Figure 5.4 (a)-(c) depict the resulting hit distribution in the first layer of each Outer Tracker station. The figure axes describe the acceptance of the detector, which is about $\pm 3000\,\mathrm{mm}$ in x and $\pm 2400\,\mathrm{mm}$ in y direction. Only tracks with at least 15 hits in the OT stations contribute to the presented distributions. The partial covering of the acceptance at stations T1 and T2 is due to this track selection criterion. This track distribution has to be considered for the alignment of modules and is discussed in Section 5.4.

Data set 2: In Section 5.5, the algorithm is tested with particle trajectories that are bent in the magnetic field of the detector. The muons from the simulated “multi-muon” events are too high energetic to be significantly deflected in the magnetic field. Therefore, a signal data sample of the decay $B_s \to J/\psi(\mu^+\mu^-)\phi(KK)$ is used for the validation in this section. The data will be explained in detail in Section 5.5.

5.1.3 Alignment procedure

The data presented in Section 5.1.2 have been generated and digitized (Section 2.4) with ideal detector positions. The generated misalignments are applied to the event reconstruction process where the pattern recognition and track fit algorithms are

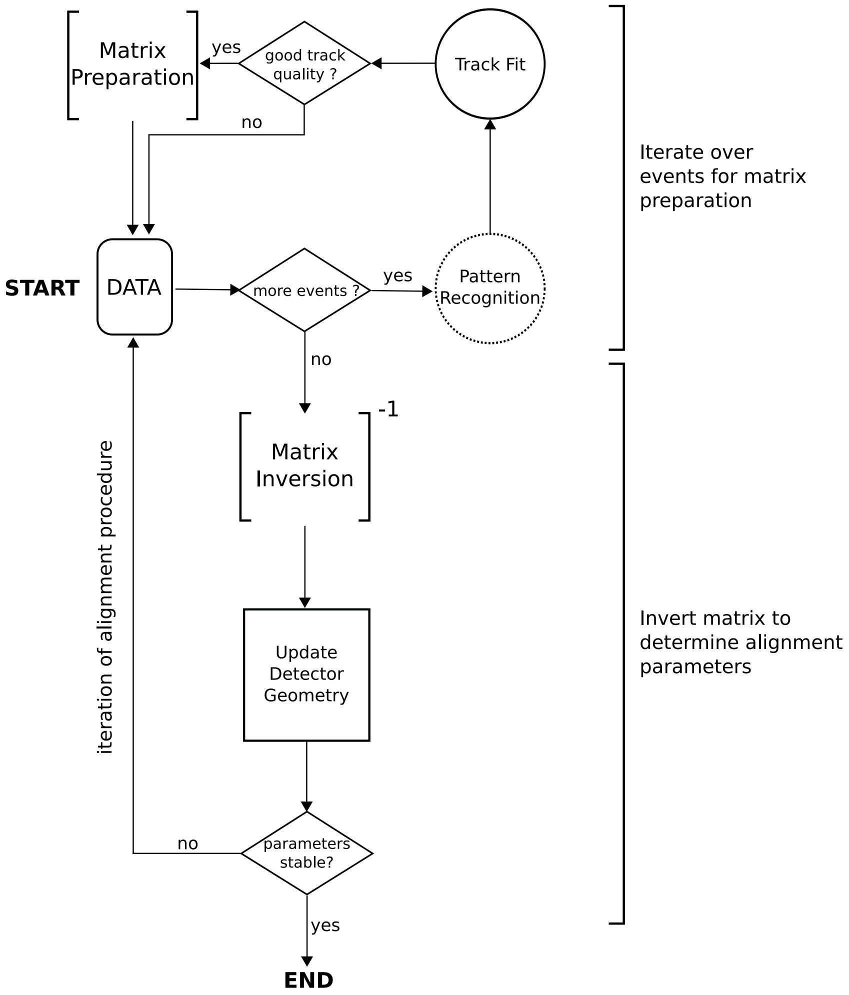

Figure 5.5: Flow chart of the alignment procedure. The scheme is divided into two main parts, that are characterized by operations on the alignment matrix $\boldsymbol{C}'$ from Equation 4.19, see text.

executed. The alignment procedure is embedded in this reconstruction process, as illustrated in Figure 5.5.

The procedure consists of two main parts, that are characterized by operations on the alignment matrix $\boldsymbol{C}'$ defined in Equation 4.19. The first part consists of the data evaluation that is used to fill matrix $\boldsymbol{C}'$. The data are read in event wise and the pattern recognition algorithm [83] is used to find track candidates[2]. A track candidate is fitted and the fit quality is evaluated. Either, the track is used for the preparation of the matrix, or it is rejected, for example if the reduced track χ^2 exceeds a certain threshold. In this case, either another track candidate is fitted, or the next event is analysed.

Once all data are read and the matrix has been prepared, the second part of the alignment procedure is entered. Here, the matrix is inverted in order to determine the misalignment parameters $\boldsymbol{\Delta}\mathbf{a}$ that represent corrections to the detector element positions. These corrections are passed to the geometry database for an update. Following, it is

---

[2] A detailed description of the pattern recognition is given in Chapter 6.

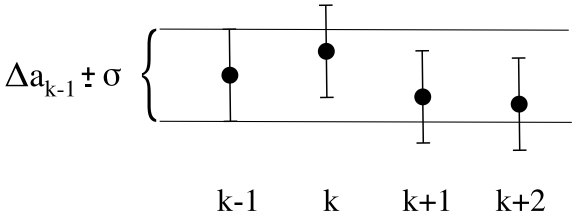

Figure 5.6: Sketch of the convergence criteria for alignment parameters. Convergence is reached, in case the parameters of three subsequent iterations are inside the interval $\mathbf{\Delta a}_{k-1} \pm \boldsymbol{\sigma}_{\mathbf{\Delta a}_{k-1}}$.

checked if the determined misalignment parameters have converged, the convergence criteria are discussed below. If convergence is reached, the misalignment parameters have finally been determined and the alignment procedure is finalized. Else, the data are evaluated again in a next alignment procedure, now using the updated geometry: The misalignment parameters are determined in an *iterative alignment process.*

The iterative alignment process

The iterative alignment process is necessary to consider non linearities in the mathematical formulation of the problem, Section 4.3.1 and to identify and remove outlier measurements that have a large influence on the result of the alignment procedure, as will be discussed in detail in Section 5.2.3.
The iterations imply a stepwise convergence of the determined misalignment parameters towards the final value $\mathbf{\Delta a}$. After each iteration k, the detector geometry is corrected and updated according to the misalignment parameters $\mathbf{\Delta a}_k$ determined in this iteration, Figure 5.5. The misalignment parameters $\mathbf{\Delta a}_{k+1}$ determined in iteration $k+1$ represent corrections to the geometry that has been updated in iteration k. The total determined misalignments $\mathbf{\Delta a}$ at the end of the iterative alignment procedure is given by

$$\mathbf{\Delta a} = \sum_k \mathbf{\Delta a}_k \ , \tag{5.1}$$

where the sum is taken over k iterations. The number of iterations necessary to determine the misalignment parameters $\mathbf{\Delta a}$ depends on the convergence of the parameters. Convergence is reached in case the following two criteria are fulfilled (see also Figure 5.6):

- The difference of the obtained misalignment parameters $\mathbf{\Delta a}_k$ and $\mathbf{\Delta a}_{k+1}$ for iteration k and $k+1$ is smaller than the uncertainties $\boldsymbol{\sigma}_{\mathbf{\Delta a}_k}$ of parameters $\mathbf{\Delta a}_k$,

$$|\mathbf{\Delta a}_{k+1} - \mathbf{\Delta a}_k| < \boldsymbol{\sigma}_{\mathbf{\Delta a}_k} \ . \tag{5.2}$$

- The values $\mathbf{\Delta a}_k, ..., \mathbf{\Delta a}_{k+2}$ of three subsequent iterations should be within the interval $\mathbf{\Delta a}_{k-1} \pm \boldsymbol{\sigma}_{\mathbf{\Delta a}_{k-1}}$.

During the iterations, any oscillation or even divergence of parameters indicate a severe problem of the algorithm and can have several origins. The most obvious ones are either a badly constraint minimization problem or an improper track sample, e. g., tracks with outlier hits or bad χ^2 are used for the alignment.

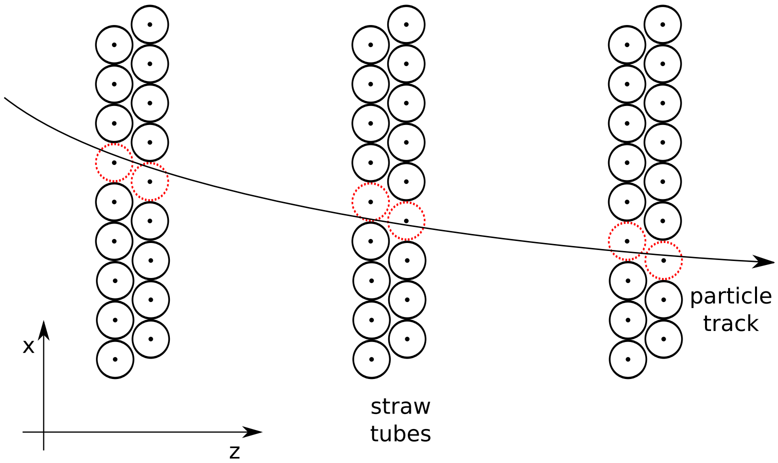

Figure 5.7: Sketch of straw tubes and a reconstructed particle trajectory in the xz plane. Traversed cells are indicated by dashed lines. The influence of the residual magnetic field is strongest at station T1 and decreases along z.

5.2 Track fit of the alignment procedure

As mentioned in the previous section, the pattern recognition provides track candidates that are fitted to evaluate the quality of the candidate (Figure 5.5) and to decide whether the track is considered in the alignment process. The track fit procedure has been developed in course of this thesis and is presented in this section.
Due to a total OT radiation length of less than 10 % [5], multiple scattering is negligible to first order and is not considered in the track fit. Considering these facts, a fast and robust standalone track fit is developed.

5.2.1 Track model and fit procedure

The used track model describes a parabola[3], that accounts for the residual magnetic field in the Outer Tracker. The residual field is strongest at station T1 and decreases along z (Figure 2.3). Figure 5.7 sketches a trajectory in the Outer Tracker. A parabola describes the bending in the xz plane in very good approximation [83]. Together with the assumption of a straight line trajectory in the yz plane the resulting track model becomes

$$\begin{aligned} x(z) &= a_x + b_x z + \kappa(z^2 + \epsilon z^3) \, , \\ y(z) &= a_y + b_y z \, , \end{aligned} \tag{5.3}$$

with the tangent to the trajectory given by $t_x = \frac{\partial x}{\partial z}$ and $t_y = \frac{\partial y}{\partial z}$ in the x and y direction and the curvature parameter κ. This parameter accounts for the magnetic field in the detector that bends particle tracks in x direction. The factor $\epsilon = -3.81831 \cdot 10^{-4}\mathrm{m}^{-1}$ in front of the cubic term improves the parabola fit and is determined by Monte Carlo studies [83].
The track parameters are determined from measurements by using the χ^2 minimization

---

[3] In fact, the parabola fit contains a contribution from a cubic term, but as it is rather small it is completely valid to call the fit parabolic.

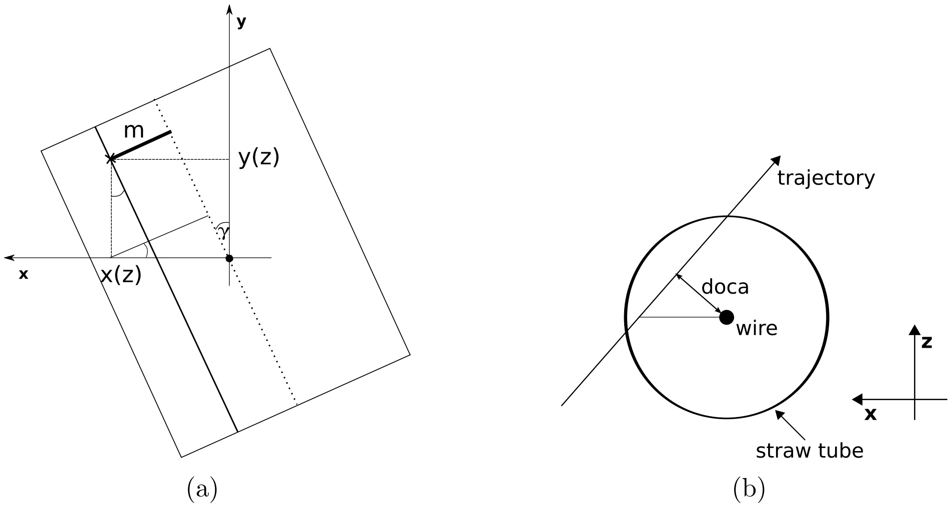

Figure 5.8: (a) Sketch of a stereo layer, that is rotated by $\gamma = 5^{\circ}$ with respect to the vertical. A traversing particle hits the straw (solid line) at $x(z), y(z)$. The resulting measurement m is taken perpendicular to the straw tube. (b) Definition of the distance of closest approach *doca* between wire and trajectory.

method as introduced in Section 4.2. The method is based on the determination of the residual between measurement m_i and the track coordinates (x, y) at the position z_i of the measurement. In the Outer Tracker, the straw tubes allow one dimensional measurements perpendicular to the tubes. As explained in Chapter 2, the track information in x direction is obtained by the vertical orientation of the straw tubes, the y information is gained by a stereo rotation with respect to the vertical. Figure 5.8 (a) illustrates the definition of a measurement m in a stereo layer: It is the shortest distance between the center of the module and the straw tube that gave a signal. With the track model defined in Equation 5.3, the measurement is described by the three dimensional model function $f(x, y, z)$ according to

$$f(x, y, z) = x(z)\cos\gamma + y(z)\sin\gamma\ , \tag{5.4}$$

where γ indicates the angle of the module with respect to the vertical, i. e., $\gamma = 0^{\circ}$ for a x module and $\gamma = \pm 5^{\circ}$ for the stereo angle of a v and u module, respectively. This allows to write down the χ^2 as

$$\chi^2 = \sum_i \frac{1}{\sigma_i^2}\left(\frac{m_i - f(x, y, z_i)}{\cos\varphi}\right)^2\ , \tag{5.5}$$

where the sum is taken over all measurements i along the trajectory. The uncertainty of the i^{th} measurement is given by σ_i, the factor $\cos\varphi = (1 + t_x^2)^{-1}$ determines the distance of closest approach (*doca*) between track and wire, see Figure 5.8 (b). Due to the tilt of the Outer Tracker layers with respect to the y axis (Chapter 2), the coordinate z_i changes along the y direction of a straw tube. Thus, the function value $f(z_i)$ is taken at $z_i(y_i)$. However, y_i is not known a priory and has to be determined from the fit. Therefore, the track fit is done iteratively, starting with positions z_i at $y_i = 0\,\text{mm}$ for

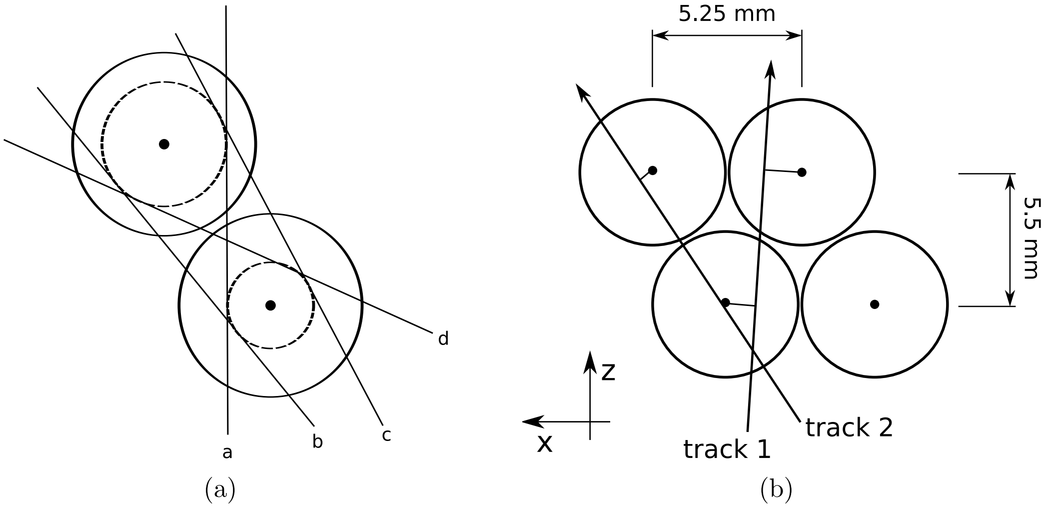

Figure 5.9: (a) Hit ambiguity: For the known drift radii in two cells, four possible particle trajectories are found. Misalignments significantly deteriorate the solution of the ambiguity. (b) Example of two tracks, that are reconstructed without drift time information. Track one enters the cell almost perpendicular the the x direction, which leads to a double peak in the track residual distribution. Due to the slope of track two, the resulting residual is single Gaussian distributed.

the first iteration. Subsequently, z_i is changed according to the determined y_i position. The iteration is stopped if the parameter change in consecutive iterations is smaller than

$$\begin{array}{rcll} |\Delta a_x| & < & 1\cdot 10^{-3}\,\text{mm} & |\Delta a_y| < 1\cdot 10^{-3}\,\text{mm} \\ |\Delta b_x| & < & 1\cdot 10^{-5} & |\Delta b_y| < 1\cdot 10^{-5} \\ |\Delta \kappa| & < & 1\cdot 10^{-9}\,\text{mm}^{-1}. & \end{array} \tag{5.6}$$

In case the fit has not converged after the tenth iteration, the current track is rejected and the next track is considered.

5.2.2 Validation of the track fit

The track fit used in the alignemnt procedure is done without drift time information. The reason for this is given in the following:

- **Robustness**: The hit resolution is $\sigma_{hit} = 200\,\mu$m if drift time information is used. Else, the resolution is defined by the acceptance of the straw tube. The single cell resolution is given by $\sigma = \frac{2R}{\sqrt{12}}$, with the tube radius $R = 2.5\,$mm. This larger hit uncertainty makes the track search and track fit more robust against misalignments.

- **Hit ambiguity**: In case a time calibration is performed and the drift radius is known, it still has to be determined whether the particle traverse the tube left or right of the wire, Figure 5.9 (a). This ambiguity can only be solved by correct association of the remaining hits to the track. Misalignments deteriorate

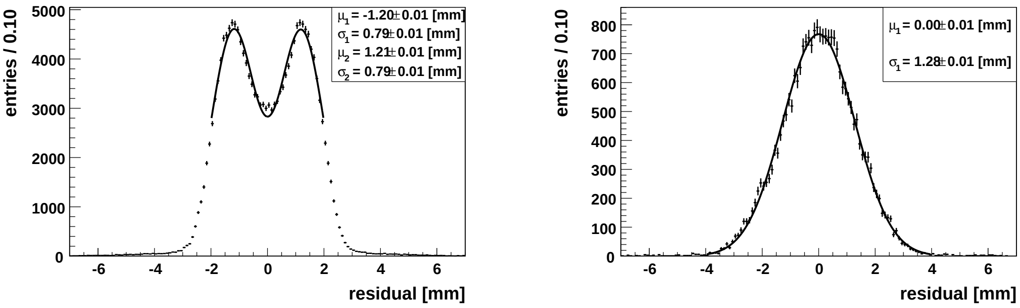

(a) $|t_x| < 0.2$ (b) $|t_x| > 0.5$

Figure 5.10: (a) Measured track residual for tracks with slope $|t_x| < 0.2$. The tracks enter the module surface almost perpendicular. (b) Track residual distribution for tracks with $|tx| > 0.5$, their trajectories run close to the wires.

the solution of the hit ambiguity and wrongly assigned hits can significantly bias the alignment (see Section 6.2.2). Without drift time information, the hit is unambiguously defined by the wire.

- **r-t calibration**: A drift chamber detector, like the Outer Tracker, measures the time difference between a trigger signal and a hit signal in a straw tube. The measured time t depends on the radius r between the straw tube wire and the particle trajectory, Figure 5.9 (a). It is necessary to calibrate the so-called $r - t$ relation which is a function of the operation parameters of the drift chambers [84]. Misalignments have influence on the calibration of the $r - t$ relation.

Furthermore, the uncertainties $\boldsymbol{\sigma_{\Delta a}}$ of the misalignment parameters depends both on the number of used tracks and the hit resolution. It is proportional to the inverse of the square root of the number of tracks, i. e., $\boldsymbol{\sigma_{\Delta a}} \propto \frac{1}{\sqrt{n}}$, with n denoting the number of tracks. In case the track sample is large enough, the hit resolution is of minor importance for an accurate parameter determination.
Without drift time information, the expected track residual $r = m - f(x, y, z)$, Equation 5.5, is not a single Gaussian distribution. As the quality of the track fit becomes apparent in the track residual and in the probability distribution for the track χ^2, it is of utmost importance to study these distributions. The fit is analysed using cosmic muon data, which are presented in detail in Chapter 6.

Without drift time information, the measurement used in the fit is represented by the wire position of the straw tube. The obtained distribution of the track residual describes the difference between the reconstructed trajectory and the wire position, as sketched in Figure 5.9 (b). The corresponding residual distributions are given in Figure 5.10. Figure (a) depicts the residual for tracks with slopes $|t_x| < 0.2$, i. e., tracks that enter the module surface almost perpendicularly (as the main measurement direction is x, slope t_y has a minor effect on the residual and is not considered in this example). The distribution shows a double peak, that is fitted with Gaussian functions to determine the mean and width of each peak. The obtained maxima are at $\mu_{1,2} \approx \pm 1.2\,\mathrm{mm}$ with a width of $\sigma_{1,2} \approx 0.79\,\mathrm{mm}$ for peak one and two, respectively. The double peak reflects the staggered layout of the straw tubes layers in the Outer

Tracker modules: As $|t_x| < 0.2$ and both hits (wire positions) are considered in the track fit with equal weights, the majority of reconstructed trajectories pass in between the hits. This situation is sketched in Figure 5.9 (b) by track 1. Due to the staggered layout, the minimal distance d between hits in consecutive monolayers is half the straw pitch, i.e. $d = 2.62\,\mathrm{mm}$, Figure 5.9 (b). The residual between hit and trajectory will peak at $\mu_1 = \frac{d}{2} = 1.31\,\mathrm{mm}$ and $\mu_2 = -1.31\,\mathrm{mm}$ for the first and second monolayer, respectively. The width of each peak is given by the distance between the two hits, i. e., $\sigma_{1,2} = \frac{d}{\sqrt{12}} = 0.76\,\mathrm{mm}$. For tracks with small slopes, this expectations match the observed distribution as presented in Figure 5.10 (a)[4].

The residual distribution for tracks with slopes $|t_x| > 0.5$ is presented in Figure 5.10 (b). This distribution is described by a single Gaussian function with a width of $\sigma \approx 1.3\,\mathrm{mm}$, which is about the expected single cell resolution without drift time information. Such a distribution is only observed for tracks, that run close to the two wires, as illustrated by track 2 in Figure 5.9 (b). Their slope is given by the wire distance dx and dz in x and z direction and is calculated according to $t_x^{crit} = \frac{dx}{dz} \approx 0.5$. Either they pass the straw tube wires on the same side, so that no double peak is observed, or the residual is too small to show a significant double peak. Trajectories with an even larger slope would cause a double peak residual distribution as discussed above. Only very few trajectories with such a large slope are measured for cosmic muons (Figure 6.4) and they do not contribute to the residual distributions.

The two examples show, that the observed track residual distributions are in agreement with the expectation based on the staggered module layout.

The reliability of the track fit is further confirmed by the χ^2 probability distributions[5], presented in Figure 5.11 (a) and (b). Figure (a) shows the χ^2 probability of tracks with small slopes t_x, i. e., tracks that contribute to a double peak distribution of the track residual. The non flat probability in figure (a) is expected, because the χ^2 probability is defined for Gaussian residuals [82, 85]. This is fulfilled only for tracks with $|t_x| > 0.5$, as shown in Figure 5.10 (b). The corresponding probability distribution is shown in Figure 5.11 (b). As expected, this distribution is flat and proves the correct implementation of the fit.

5.2.3 Ensuring the quality of tracks for the track based alignment

In the alignment procedure, the successful determination of the misalignment parameters depends on the quality of the used tracks. A track quality indicator is the reduced track χ^2, $\frac{\chi^2}{ndf}$, where $ndf = n - \nu$ is the number of degrees of freedom. n denotes the number of measurements associated to the track, ν is the number of track parameters, i. e., $\nu = 4$ for a straight line fit, $\nu = 5$ for a parabola fit in xz direction and a straight line fit in yz.

---

[4] The determination of $\mu_{1,2}$ depends on the assumption, that the tracks enter the straw perpendicularly and the cell tube is efficient over its whole area. In practice, however, the tracks enter the tube under a certain angle and the cell efficiency drops at the tube boundary [45].

[5] $\chi^2_{probability}$ represents the probability that the observed $\chi^2_{observed}$ value exceeds the theoretically calculated χ^2_{theo} value even for a correct model. The calculation of χ^2_{theo} is based on the gamma function $\Gamma(a, x)$ where $a = ndf$ and $x = \chi^2$ [85].

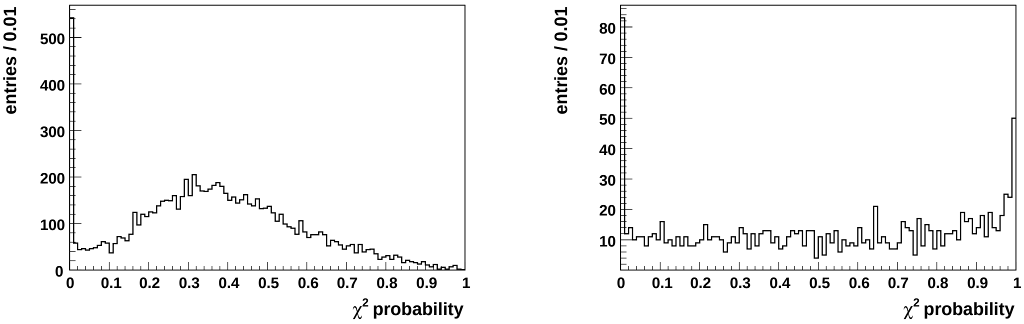

(a) $|t_x| < 0.2$

(b) $|t_x| > 0.5$

Figure 5.11: (a) χ^2 probability of tracks, for which the residual distribution shows a double peak. (b) Tracks contributing to a single Gauss residual distribution show a flat probability distribution.

The track quality can significantly be influenced by outliers. Outliers are measurements that are associated to a track but which ly significantly off the reconstructed trajectory such that the corresponding hit residual is large.
Outliers as well as large reduced track χ^2 values are expected due to initial misalignments of the detector. This has to be considered during the alignment procedure and imposes the need of an iterative alignment process:

- **Track** χ^2: Misalignments naturally increase the track χ^2 value. Thus, a large χ^2 does not represent a bad reconstructed track, but a misaligned detector. The tracks are therefore indispensable for the determination of misalignments and are considered in an iterative alignment procedure (Section 5.1.3): Initially, the misalignment parameters are determined with loose cuts on the track χ^2 value. The detector geometry is updated and in a subsequent alignment process, the misalignment parameters are determined with tightened cuts on the χ^2 value.

- **Outlier**: Depending on initial misalignments, it is possible that only a few hit residuals are significantly large. These outliers contain misalignment information. Thus, the maximum allowed hit residual value should be large for the first iterations of the alignment procedure. It is then reduced gradually to ensure the track quality.

Outliers are not solely caused by detector misalignments, but can have additional origins which are listed below:

- **Multiple scattering** in the detector material can cause outliers along the reconstructed trajectory that can have large impact on the determination of misalignment parameters. Low energetic particles are mostly affected by multiple scattering. A cut on the particle energy allows to reject bad tracks due to this effect.

- **Electronic noise** in the detector, like channel cross talk (Chapter 6), can cause false measurements. A false measurement can be associated to a track passing nearby this channel. As misalignment parameters of a detector element are determined by using the sum of all tracks through the corresponding element, the weight of this false measurement is negligible in the alignment procedure (for a homogeneous track distribution in the detector).

- **Adjacent tracks** can cause measurements in nearby channels. As the pattern recognition associates measurements to tracks, it has to be configured properly. The pattern recognition is discussed in detail in Chapter 6.

5.3 Determination of misalignment parameters for half layers without magnetic field

The Outer Tracker alignment procedure considers various levels of detector segmentation. This section discusses the determination of misalignment parameters $\mathbf{\Delta a}$ for half layers. For the validation of the alignment procedure, the geometry databases containing misaligned half layer position are applied to the alignment procedure (Section 5.1.3). The algorithm is validated in two steps.

The first step is presented in Section 5.3.1, in which the alignment procedure is tested for each of the five degrees of freedom *separately*: Five alignment processes are run, each with one of the misalignment databases 1-5 of Table 5.1. In this study, the determined misalignment parameters are not affected by correlations between different degrees of freedom.

In the second step, presented in Section 5.3.2, the alignment procedure is validated with simulated misalignments in all five degrees of freedom. The misaligned half layer geometry of database 7 is used. The *simultaneous* determination of the misalignment parameters for all degrees of freedom is discussed in more detail compared to step one.

5.3.1 Alignment procedure for a singular degree of freedom

This section discusses the results of five independently processed alignment procedures. The aim of each alignment process is to determine the misalignment parameters for a singular degree of freedom. About 160 000 generated muon tracks are used for each of the five alignment procedures (Data set 1, Section 5.1.2). The data are reconstructed with the geometry databases 1-5 of Table 5.1 in order to simulate misaligned half layers. The parameter fixation method (Chapter 4) is used to constrain the undefined degrees of freedom. Due to the stereo view of the layers, translations have to be constrained in x and y direction. For each of the two directions, two half layers are fixed to their nominal positions. The same constraints are applied for the rotational degrees of freedom. Thus, in total the first four and last four out of the 24 half layers are fixed.

The results of the five alignment procedures are presented in Figure 5.12. It shows both, the simulated misalignments on the abscissa and the determined misalignment parameters for the half layers on the ordinate. As the misalignments have been simulated for a whole layer, the half layers of the corresponding layers have identical input values. Each graph shows a dashed line with gradient $b = 1$ indicating equal values for simulated misalignments and determined parameters. For the successful alignment procedure, the graph entries are located along this line within their uncertainties. For comparison,

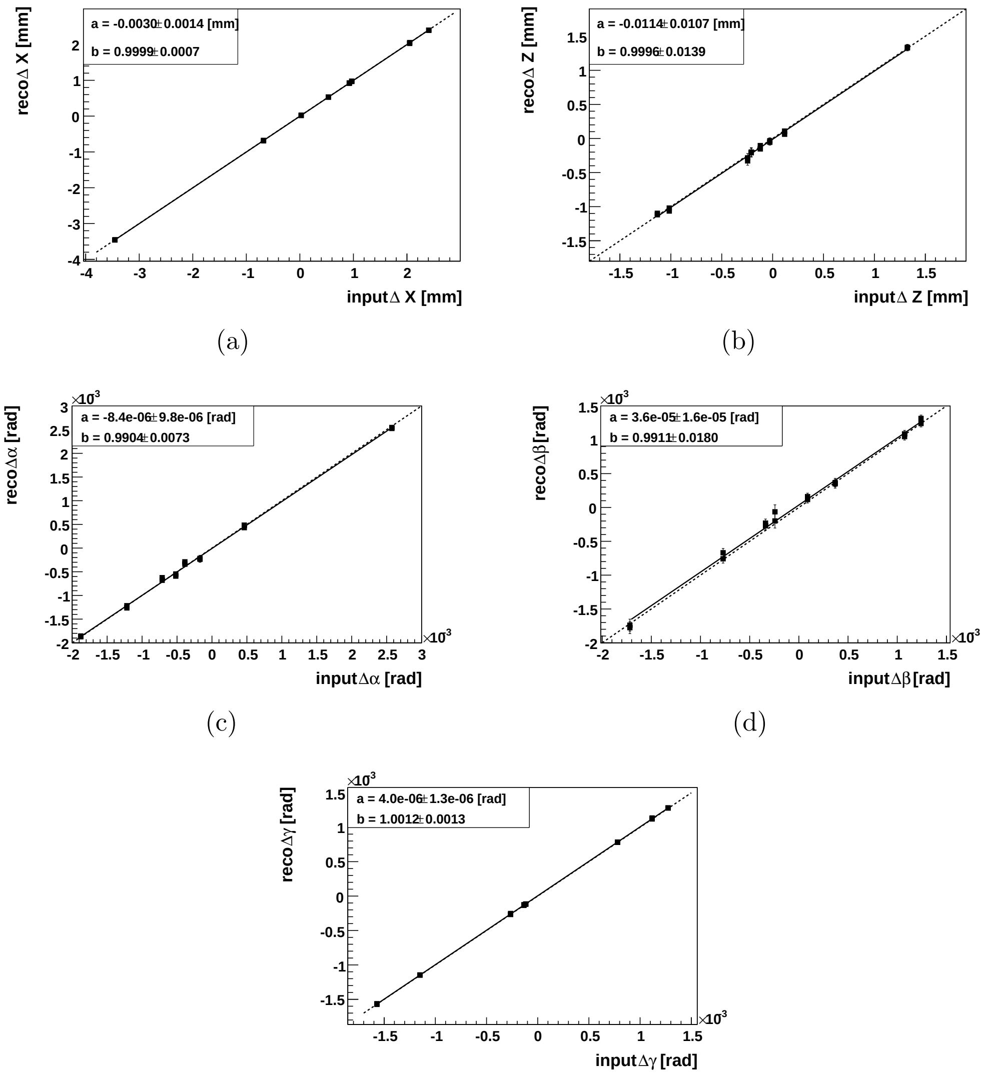

(a) (b)

(c) (d)

(e)

Figure 5.12: The figure shows the applied input misalignments together with the reconstructed alignment parameters for each degree of freedom. The dashed line indicates equal input and reconstructed values and is given as reference.

a straight line fit to the entries yields the offset a and gradient b, noted in the figure legends. The uncertainties of the determined misalignment parameters are given by the covariance matrix $\boldsymbol{C}'^{-1}$, Equation 4.19. They are to small to be visible in the graph. For all five degrees of freedom, the fit to the data points matches the dashed reference line. The simulated misalignments are resolved by the algorithm.

Figure 5.13 and Figure 5.14 depict the reduced track χ^2 distribution and the mean of the track residuals that are measured for each half layer. The two distributions are given for each degree of freedom before and after the alignment procedure.

Misalignments influence the width of track residual distributions only if they are in the order of the hit resolution. The mean of the residual distribution is affected even by misalignments smaller than $\mathcal{O}(\sigma_{hit})$. Except for displacements in x direction,

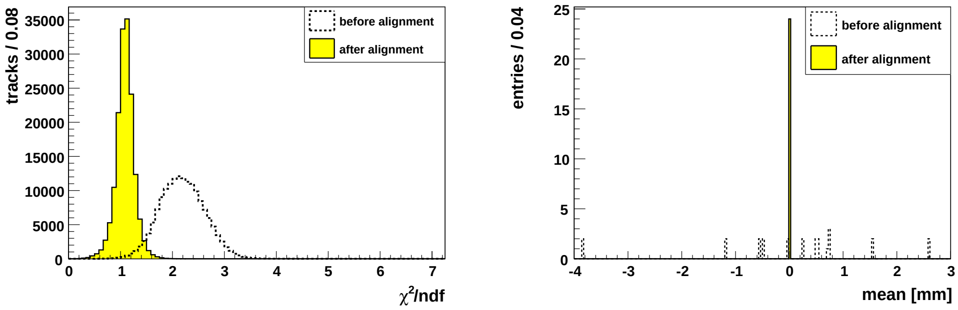

(a) misalignments in x (b) misalignments in x

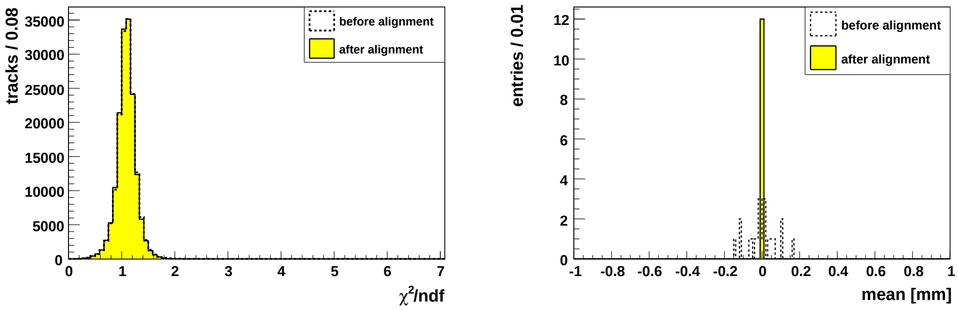

(c) misalignments in z (d) misalignments in z

Figure 5.13: Track χ^2 and residual mean for the translational degrees of freedom. For each degree of freedom, a separate alignment procedure has been proccesed using the geometry databases 1 and 2 (Section 5.1.1), respectively. The figures in the left column depict the track χ^2 before and after the correction of the half layers misalignments. The right column shows the corresponding mean of the track residuals that are measured for the 24 half layers.

the applied misalignments induce shifts that are several times smaller than the hit resolution $\sigma_{hit} = 1.44\,\mathrm{mm}^6$, as will be explained below.

For the discussion of the results, it is essential to recall the meaning of the global derivatives that have been introduced in Chapter 4: Misalignments of the detector are deduced from the residual between measured hit and reconstructed track, where the track is described by the track model function $h(\mathbf{a}, \mathbf{\Delta a}, \boldsymbol{t})$, Equation 4.12. Misalignments of detector elements change the expected track coordinates at the position of the element according to

$$\boldsymbol{\Delta h} = \boldsymbol{P}\mathbf{\Delta a}\ , \tag{5.7}$$

where $\mathbf{\Delta a}$ denotes the misalignments and matrix $\boldsymbol{P}$ (Equation 4.14) containes the global derivatives. Table 5.3 shows the global derivatives for all five degrees of freedom for x layers[7]. Equation 5.7 implies that the sensitivity of the algorithm to the misalignment depends on the scale of the change $\boldsymbol{\Delta h}$ and on the accuracy of the reconstructed track. The change $\boldsymbol{\Delta h}$ strongly depends on the misaligned degree of freedom.

Figure 5.13 (a) shows the track χ^2 measured for misalignments in x direction. The mean

---

[6] The track fit in the alignment procedure is done without drift time information.

[7] It is more convenient to consider only x layers, as this way, projections of measurements on the stereo layers are unnecessary. Certainly, the discussed consequences are the same for both layer types.

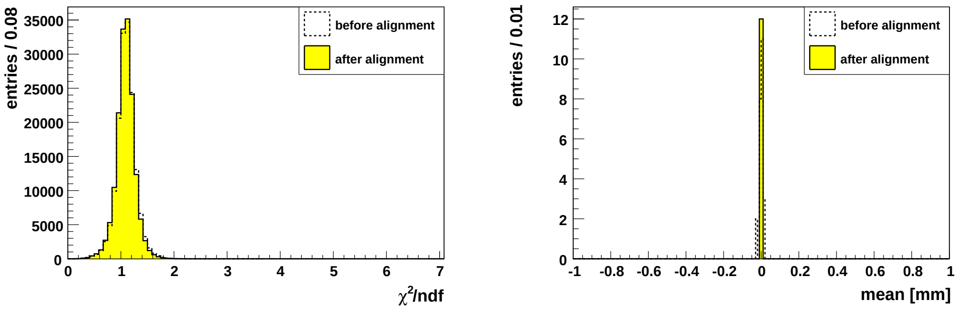

(a) misalignments in α (b) misalignments in α

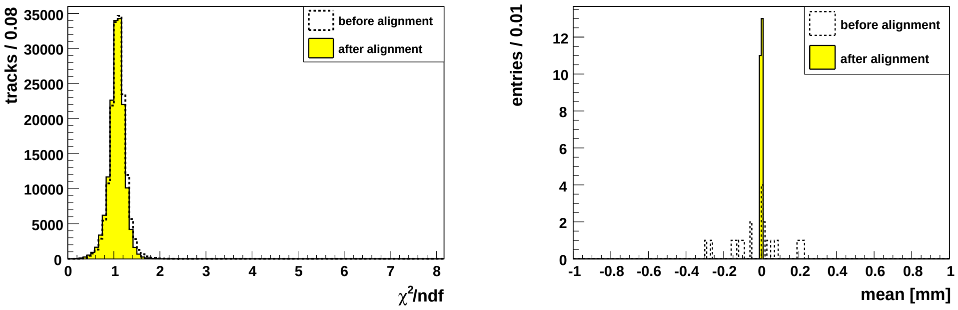

(c) misalignments in β (d) misalignments in β

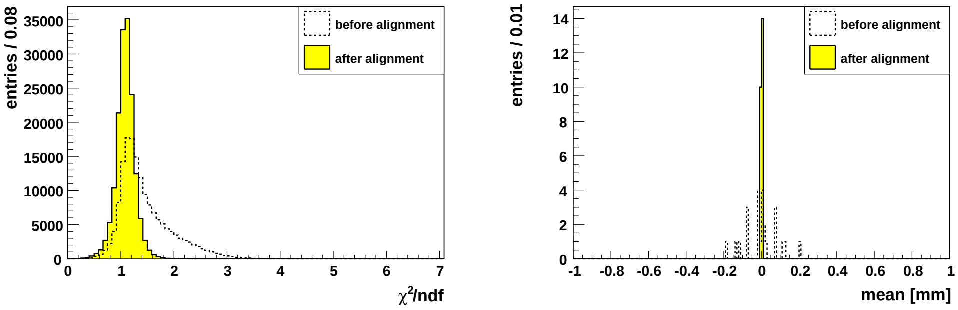

(e) misalignments in γ (f) misalignments in γ

Figure 5.14: The figures in the left column depict the track χ^2 before and after the correction of the half layers misalignments. For each degree of freedom, a separate alignment procedure has been proccesed using the geometry databases $3, 4$ and 5 (Section 5.1.1), respectively. The right column shows the corresponding mean of the track residuals that are measured for the 24 half layers.

of the reduced track χ^2 improves significantly from 2.19 before to 1.08 after alignment. It is evident, that the track χ^2 is very sensitive to shifts in the main measurement direction of the detector. The spread of the mean of the track residual, Figure (b), reduces to a peak at zero.

Contrary to this, the $\frac{\chi^2}{ndf}$ distribution for Δz before and after alignment are not distinguishable, Figure 5.13 (c). The mean of the track residuals scatter about ± 0.2 mm which indicate significant misalignments, Figure (d). These shifts are corrected after the alignment procedure, the mean are centered at zero. The reason for the unchanged reduced χ^2 is found in the global derivative of Δz: $P_{\Delta z} = t_x$. Thus, a detector shift in

Table 5.3: The global derivatives for measurements in x direction. The global derivatives are introduced in Section **??**, where also the derivatives for the y direction are presented.

dof	Δx	Δz	$\Delta\alpha$	$\Delta\beta$	$\Delta\gamma$
global derivative P	-1	t_x	yt_x	xt_x	$-y$

z direction changes the expected track position according to

$$\Delta h_{\Delta z} = t_x \cdot \Delta z \ . \tag{5.8}$$

The width of the track slope distribution for simulated muon tracks is $RMS \approx 0.14$, Figure 5.3 (a). With this slope distribution, it is evident from Equation 5.8, that misalignments Δz of $\mathcal{O}(\,\text{mm})$ change the measured hit coordinate only by $\mathcal{O}(\,\mu\text{m})$. Due to the hit residual $\sigma_{hit} = 1.44\,\text{mm}$, the impact on the track χ^2 is insignificant, but shifts of the mean of the residuals are observed.
Figure 5.14 (a) and (b) depict the results of the alignment of angle α. For both distributions, the difference before and after alignment is marginal. A rotation $\Delta\alpha$ around the x axis shifts the hit positions along y and z. According to the global derivative $P_{\Delta\alpha}$, $\Delta h_{\Delta\alpha}$ is

$$\Delta h_{\Delta\alpha} = y \cdot t_x \cdot \Delta\alpha \ , \tag{5.9}$$

with track slope t_x and the y position of the hit, predicted by the reconstructed track. As the track reconstruction in y depends on the stereo layers, the track uncertainty in this direction is about 100 times larger than in x. Thus, the y position has a rather large uncertainty. The product of $\Delta\alpha$ $\mathcal{O}(10^{-4})$, $y\,\mathcal{O}(10^3\,\text{mm})$ and t_x $\mathcal{O}(10^{-1})$ results in a change of $\Delta h_{\Delta\alpha}$ of $\mathcal{O}(10^{-2}\,\text{mm})$ and merely influences the track χ^2 and the mean of the track residual.
The χ^2 distribution of $\Delta\beta$ in Figure 5.14 (c) is similar to the one of $\Delta\alpha$ in Figure (a). The track residual mean depicted in figure (d) is apparently distributed between $\pm 0.4\,\text{mm}$ before alignment. After alignment, it is centered at zero, as expected. The difference between the mean distribution for $\Delta\beta$ and $\Delta\alpha$ is due to the factor x in the global derivative of $\Delta\beta$, Table 5.3: The track reconstruction in measurement direction is more accurate than in y direction, hence x has a small uncertainty. Thus, the applied misalignments are visible in a shifted mean of the track residual mean, but the width of the residual is still too small to significantly change the reduced χ^2.
Figure 5.14 (e) and (f) show the distributions obtained for the alignment of γ. Here, both, the reduced track χ^2 and residual mean improve considerably after alignment. The reason for this is the significant change of the measurement at large y, due to the rotation around the z axis. Tracks at large y contribute significantly to the tail of the χ^2 distribution. The mean of the residual distribution for each half layer is deduced from tracks over the whole y acceptance. Therefore, the shift of the mean is rather small with $\pm 0.2\,\text{mm}$, but still clearly visible in the distribution of Figure (f).

This study shows, that not only the track χ^2, but also the track residual mean distributions are indispensable for the alignment monitoring. Whereas, the track χ^2 is sensitive only to track residuals in the order of the hit precision σ_{hit}, the distributions

Table 5.4: The table shows the applied track quality cuts for each iteration. The number of rejected tracks is given, depending on the applied cut. Each iteration begins with the same 260 000 generated muon tracks.

iteration	1	2	3	4	5
max $\frac{\chi^2}{ndf}$	25	5	2.2	1.8	1.8
→ tracks rejected	0	0	0	64	64
max outlier r_{max}[mm]	12	6	3	3	3
→ tracks rejected	0	0	5194	5195	5194

of the mean of the residuals indicate misalignments even for track residuals smaller than $\mathcal{O}(\sigma_{hit})$.

5.3.2 Alignment procedure for all geometrical degrees of freedom

In this section, the simultaneous determination of the misalignment parameters of all five degrees of freedom is presented. For the validation of the algorithm about 260 000 generated muon tracks are used. The data are reconstructed with the geometry database 7 listed in Table 5.1 where half layers misalignments are simulated for all degrees of freedom.

Similar to the alignment process discussed in Section 5.3.1, the first four and last four half layers are fixed in order to apply constraints to the undefined degrees of freedom. This validation step is more complex compared to step one in Section 5.3.1, it requires an iterative alignment process to consider initial large track χ^2 values due to misalignments and the correlations between misalignment parameters of different degrees of freedom. The alignment procedure for the half layers presented in this section is processed in five iterations. The maximal allowed track $\frac{\chi^2}{ndf}$ and hit residual are listed in Table 5.4. It shows, that the $\frac{\chi^2}{ndf}$ value is reduced after each iteration by taking the square root of the preceding value. For the outlier treatment, the maximum allowed hit residual is halved after each iteration step. The minimum cut values at the end of the process are $\frac{\chi^2}{ndf} = 1.8$ and $r_{max} = 3\,\mathrm{mm}$. Initial cuts are very loose and no tracks are rejected in the first two alignment iterations. Even in subsequent steps, only about 2 % of the tracks exceed the threshold values.

Figure 5.15 (a) shows the reduced χ^2 distribution obtained in the first two iterations of the alignment process, in which all tracks in the data are considered. The dashed line represents the track χ^2 distribution obtained in the first iteration of the alignment procedure. The tracks are reconstructed on the misaligned geometry and the χ^2 distribution is rather broad with the mean $= 1.586 \pm 0.001$. The filled histogram is obtained after the first determination of the misalignment parameters and a correction of the detector geometry according to these parameters. The distribution improves significantly with mean $= 1.0680 \pm 0.0004$ and the width narrowed by a factor two. The sharp edge of the distribution at $\frac{\chi^2}{ndf} \approx 2.3$ indicates the well positioned detector already after the first iteration.

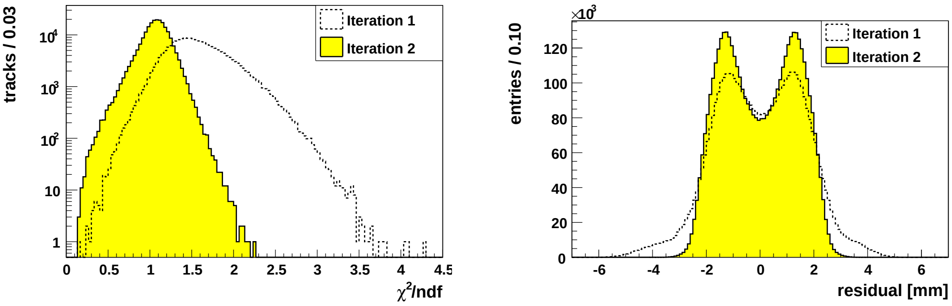

(a) (b)

Figure 5.15: Reduced track χ^2 and residual for the first two alignment iterations. The parameters of the first iteration are obtained with the misaligned geometry, as the track fit is done before the determination of the alignment parameters, see also Figure **??**. (a) The mean improves to 1.06. (b) After the first alignment, the gained residual $RMS = 1.35$ matches the expected width.

The excellent performance is further validated with Figure 5.15 (b). It shows the track residual distribution before and after the misalignment parameters have been determined. After the simulated misalignments have been corrected, the residual $RMS = 1.3480 \pm 0.0004\,\text{mm}$ matches the width that is expected for tracks which are reconstructed without drift time information.

The distribution shows that hit residuals $r > 3\,\text{mm}$ are expected for the track reconstruction without drift time information. The outlier cut with $r_{max} = 3\,\text{mm}$ that will be applied in the 3^{rd} iteration process will reject tracks from the tail of the distribution. However, the influence of this rejection on the determination of the misalignment parameters is negligible, as is evident from Figure 5.16 (a) and (b). The Figures show the misalignment parameters $\Delta x_1 - \Delta x_5$ and $\Delta\alpha_1 - \Delta\alpha_5$ that are determined in the five iterations of the alignment procedure. The uncertainties of the parameters Δx_i are too small to be visible in Figure (a). After determination of the misalignments parameter Δx_1 in the first iteration, the subsequently determined parameters $\Delta x_2 - \Delta x_5$ are equal to Δx_1 within their uncertainties.

The change of $\Delta\alpha_3$ in Figure (b) indicates the outlier cut with $r_{max} = 3\,\text{mm}$ in the 3^{rd} iteration. It is consistent with its uncertainty and therefore insignificant. The fast convergence underlines that the misalignment parameters are determined within the first iteration and the system of equations is set up properly.

For systematic studies, the iterative alignment procedure as discussed above is repeated three times. In each repetition, different tracks of the generated muon events are reconstructed with the same misaligned geometry (database 7, Table 5.1).

The result of the three iterative alignment procedures is shown in Figure 5.17 (a) - (e). Depicted is the difference $\boldsymbol{\delta}\mathbf{a}$ between simulated misalignments $\mathbf{\Delta a}^{true}$ and the determined misalignments $\mathbf{\Delta a}$:

$$\boldsymbol{\delta}\mathbf{a} = \mathbf{\Delta a}^{true} - \mathbf{\Delta a} \,, \tag{5.10}$$

where $\mathbf{\Delta a} = \sum_{k=1}^{5} \mathbf{\Delta a}_k$ is the sum of the misalignment parameters that are determined in the five iterations per alignment procedure, see also Equation 5.1. Due to the applied

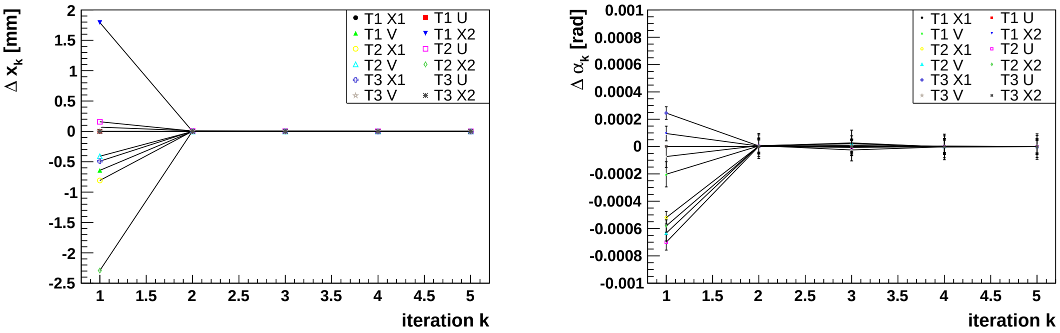

(a) (b)

Figure 5.16: Convergence behaviour of alignment parameters Δx and $\Delta\alpha$ for the half layer alignment. In the first iteration, the determined parameters are given with respect to the nominal geometry. In each iteration, the difference relative to the parameter of the previous iteration is determined.

constraints, 8 out of the 24 half layers are fixed to their positions. Thus, in each of the three repeated alignment procedures 16 misalignment parameters are determined per degree of freedom. This results in 48 entries per histogram in Figure 5.17. The distributions are fitted with a Gaussian function, the obtained mean μ and width σ of the function are given in the legend. The width of the Gauss function indicates the exactness of the alignment procedure. Systematic effects, e. g., from the track reconstruction are minimized with the simulated muon event sample as discussed in Section 5.1.2. Further systematic effects can be caused by deformations of the detector elements. However, deformations cannot be simulated with the software and are not considered in the generated geometry databases. The results for the obtained statistical precision for all degrees of freedom are summarized in Table 5.5. With already about 260 000 tracks, the exactness in measurement direction is a tenth of the measurement uncertainty of 200 μm[8]. The determination of rotations is as accurate as a tenth of a millirad and below. It has been shown in Chapter **??**, that the track reconstruction is not deteriorated with residual misalignments on the scale of the achieved exactness.

The distributions δz and $\delta\alpha$ in Figure 5.17 (c) and (d) show that about 20 % of the histogram entries are incompatible with the fitted Gauss function. Therefore, the

---

[8] Note, that these results are obtained without drift time information, thus the measurement error is about 1.44 mm. With drift time information, the alignment accuracy is expected to be even better with the same number of tracks.

Table 5.5: Statistical accuracy of the simultaneous half layer alignment. The values represent the width of the Gauss function, that is fitted to the distribution shown in Figure 5.17.

x [mm]	z [mm]	α [mrad]	β [mrad]	γ [mrad]]
0.022 ± 0.005	0.20 ± 0.07	0.067 ± 0.010	0.110 ± 0.018	0.016 ± 0.003

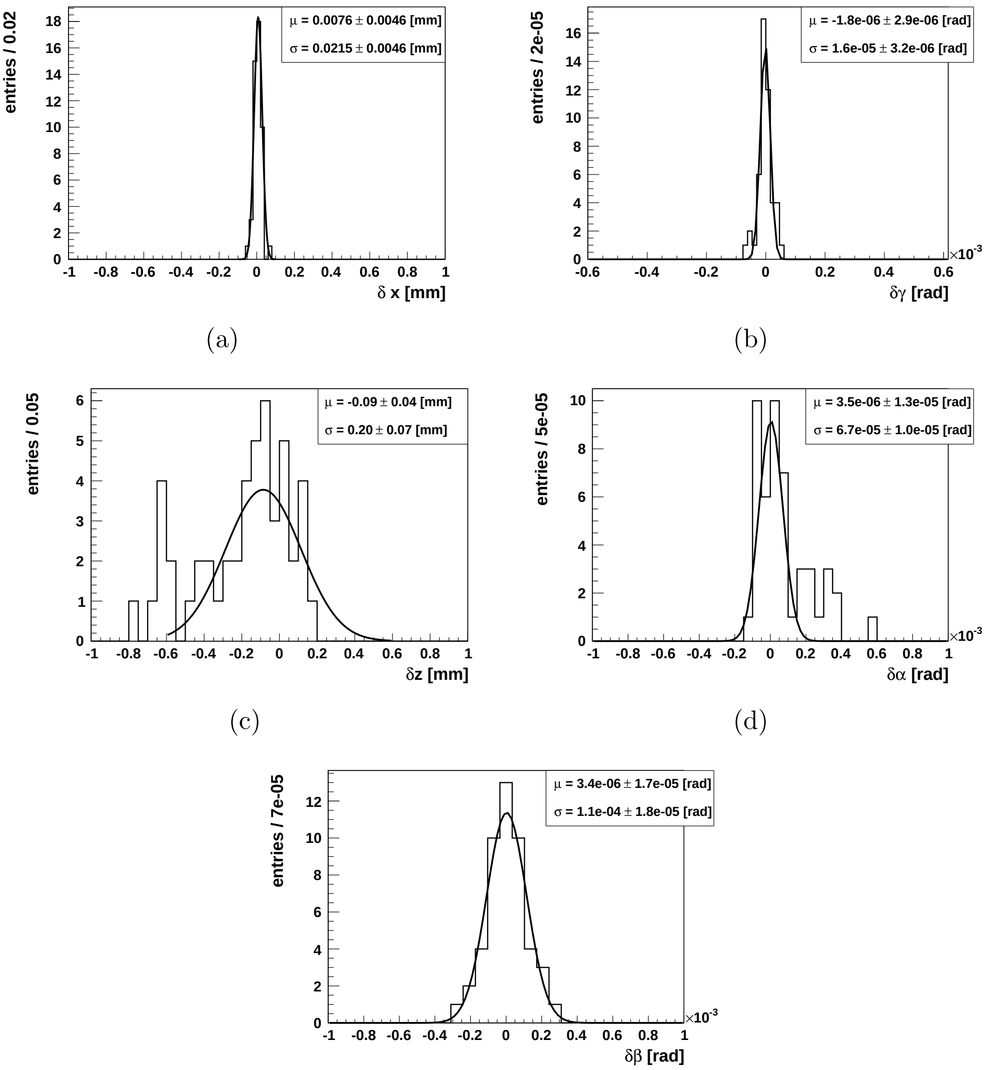

(a) (b)

(c) (d)

(e)

Figure 5.17: Difference $\boldsymbol{\delta}\mathbf{a}$ between simulated and determined misalignment parameters for all degrees of freedom. The width of the fitted Gauss indicates the alignment accuracy. The few outlier values in figure (c) and (d) are discussed in the text.

differences δz and $\delta\alpha$ between simulated misalignments and the determined misalignment parameters are studied in detail for Δz and $\Delta\alpha$.

Figure 5.18 (a) and (b) show for every half layer the number of standard deviations $n_\sigma = \frac{\delta z}{\sigma_{\Delta z}}$ and $n_\sigma = \frac{\delta\alpha}{\sigma_{\Delta\alpha}}$ between simulated and determined parameters. It is evident, that the u and v layers show deviations of $n_\sigma > 2.5$, whereas all x layers are below this value. Four u layers show badly reconstructed Δz parameters, $\Delta\alpha$ is poorly determined for four v layers. The differences δz and $\delta\alpha$ determined for these stereo layers deviate from the Gaussian distributions shown in Figure 5.17 (c) and (d).

No such deviations have been observed in Section 5.3.1, where the alignment procedure has been tested for each of the five degrees of freedom separately. The correlations between the different degrees of freedom lead to the observed effect of the stereo layers.

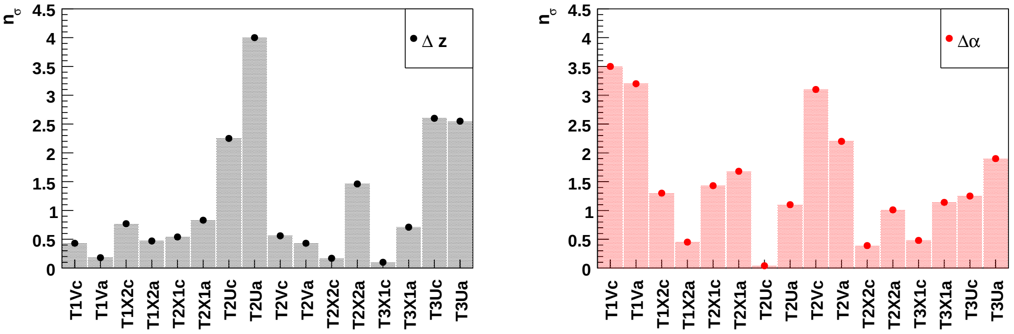

(a) (b)

Figure 5.18: The figures show the difference between input misalignment and reconstructed parameters for every aligned half layer. The difference is expressed in number of standard deviations $n_\sigma = \frac{\delta a}{\sigma_a}$. The half layers are named for example T1Vc and T1Va for the v layer of station 1 on the C-side and A-side, respectively. Only the stereo layer show deviations of more than 2.5σ.

Especially for Δz and $\Delta\alpha$, a rather strong correlation is expected as both degree of freedom change the detector in z direction. The reason for the observed strong dependence between degree of freedom and layer type is not yet understood.
However, the correlation between Δz and $\Delta\alpha$ has no impact on the quality of the reconstructed tracks, which is presented in the next section.

5.3.3 Track properties after the alignment procedure

The alignment procedure finalizes with the correction of the detector geometry that is stored in the geometry database. The quality of tracks, that are reconstructed with the corrected detector geometry is studied in the following. The track χ^2 and residual distributions that are obtained under ideal geometry conditions, are compared with the same distributions obtained with the corrected geometry.

Figure 5.19 (a) shows the reduced track χ^2 distributions. For both ideal and corrected geometry, the mean is found at $< \frac{\chi^2}{ndf} >= 1.06$. Beneath the histogram, the bin-wise difference between the distributions is drawn for better comparison. 5 258 more tracks are reconstructed with the nominal geometry compared to the corrected one. This is exactly the number of tracks that have been rejected during the iterative alignment process, Table 5.4. As no track quality cuts are applied during the reconstruction with nominal geometry, the found difference is expected. The track residuals are compared in Figure 5.19 (b). Both distribution are centered at zero with a width of $RMS \approx 1.35\,\text{mm}$. The difference plot beneath the residual distribution shows additional tails at $3\,\text{mm} < r < 3\,\text{mm}$. These tails are due to the track reconstruction for ideal geometry, where no quality cuts are applied. Again, the distributions are identical, except for the small difference in the number of used tracks.

As has been shown in Section 5.3.1, the mean of the residual is a good observable for the evaluation of the alignment procedure. Figure 5.20 depicts the mean of the track residuals, measured for the 24 half layers. The mean values obtained for the misaligned geometry (dashed lines) and for the corrected geometry (solid lines) are

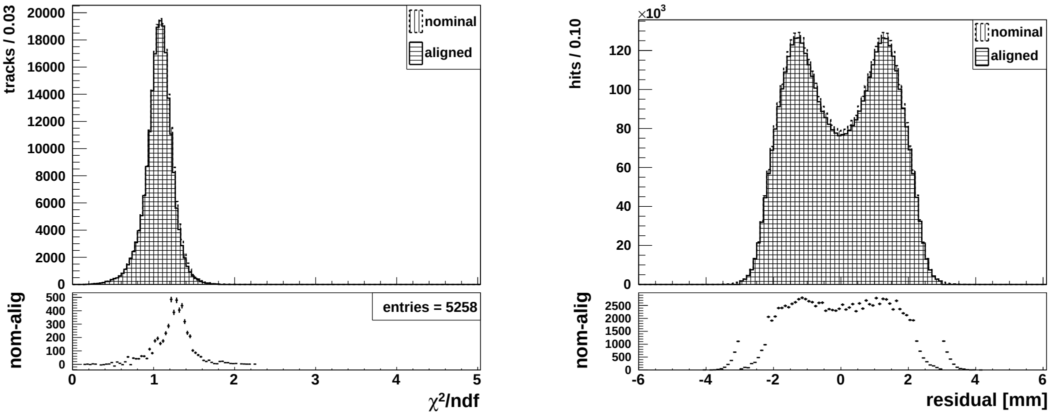

(a) (b)

Figure 5.19: Comparison of the reduced track χ^2 and residual distributions obtained on nominal and misaligned geometry. Below the histograms, the difference of the number of bin entries are depicted for clarification. The distributions are identical except for the number of tracks, that have been rejected in course of the alignment.

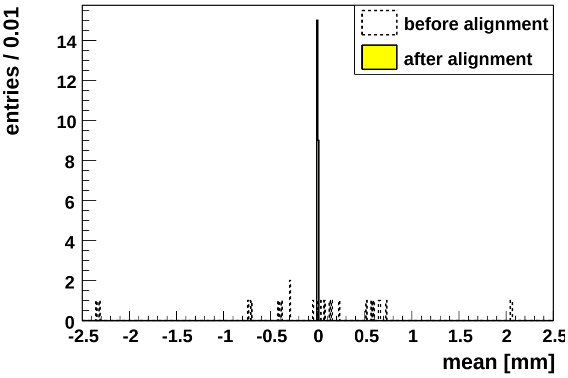

Figure 5.20: The track residual mean of the 24 half layers. The dashed line represents the residual mean before alignment. After alignment, the distribution peaks at zero, indicated by the solid line.

depicted. Misalignments induce shifts of the mean of more than 2 mm, after correcting the detector positions, the track residuals are perfectly centered at zero.
The presented results demonstrate, that the residual misalignments of Δz and $\Delta\alpha$, that have been observed for the stereo layers, are negligible. They have no impact on the quality of the track reconstruction, as the results obtained with ideal and aligned geometry are identical and the mean of the track residuals are centered at zero after the alignment procedure.

5.3.4 Statistical precision of misalignment parameters

The simulation allows to study the dependency of the statistical uncertainties of the misalignment parameters on the number of used tracks. The uncertainties of the misalignment parameters are given by the diagonal entries of the covariance matrix $\boldsymbol{C}'^{-1}$,

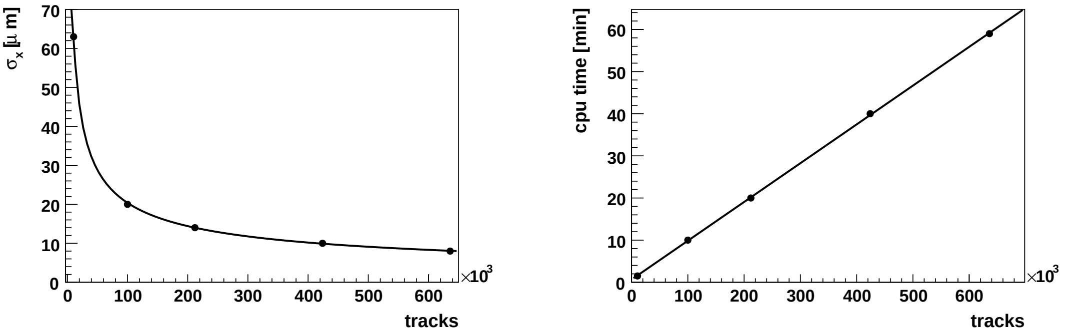

(a) misalignments in x (b) misalignments in z

Figure 5.21: (a) The uncertainty $\sigma_{\Delta x}$ of the alignment parameter Δx versus the number of tracks n used to align the Outer Tracker half layers. As expected, the statistical uncertainty is proportional to $1/\sqrt{n}$. (b) The computing time increases linearly with the number of tracks, that are used for alignment.

Equation 4.21. Figure 5.21 shows the uncertainty $\sigma_{\Delta x}$ of the misalignment parameter Δx as a function of the number n of used tracks. As expected, the size of the uncertainty is proportional to the inverse of $\sqrt{n}$. Theoretically, a statistical uncertainty down to an arbitrary small value can be achieved. In practice, the uncertainty of misalignment parameters is limited by unresolved weak degrees of freedom (Section 6.4.2), cross talk (Section 6.2.3), noise in the detector and measurement uncertainties. A compromise must be found between the number n of used tracks that affects the computing time and the desired statistical uncertainties.

Figure 5.21 (b) illustrates the computing time needed for the alignment procedure applied to the the Outer Tracker half layers. Depicted is the time for the simultaneous determination of misalignment parameters for all five degrees of freedom. The computing time increases linearly with the number of used tracks[9], as expected from Equation 4.15. The comparison with Figure (a) shows, that after ten minutes of computing time, the statistical uncertainty of misalignment parameter Δx is a tenth of the Outer Tracker hit resolution of 200 μm.

5.4 Alignment procedure for Outer Tracker modules without magnetic field

This section presents the determination of misalignment parameters $\mathbf{\Delta a}$ for the Outer Tracker modules. Due to the small lever arm for a rotation around the y axis (module width = 300 mm), the misalignment parameter $\Delta\beta$ is not considered in the alignment procedure (Section 5.1.1). The generated “multi-muon” events presented in Section 5.1.2 are used for the validation of the algorithm. Four independent alignment procedures are performed, each with about 430 000 muon tracks. The muon tracks are reconstructed with the geometry databases depicted in Table 5.2 that simulate misalignments in x

---

[9] The alignment process was performed on a computer with 1.25 times the speed of a 2.8 GHz Xeon computer.

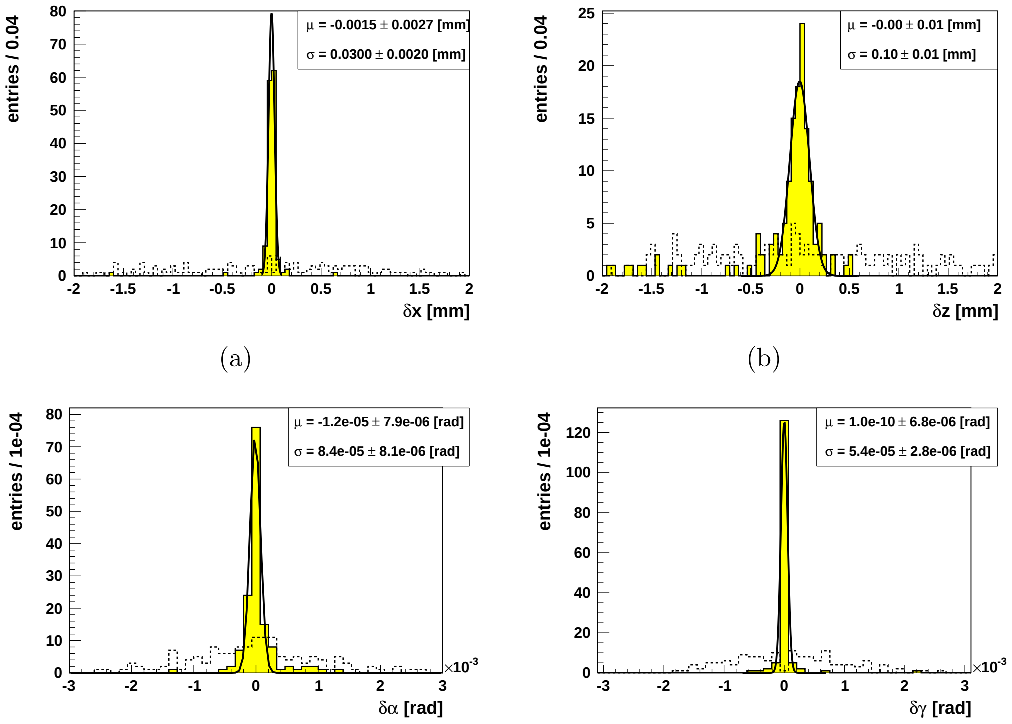

(a) (b)

(c) (d)

Figure 5.22: Depicted are the differences $\boldsymbol{\delta}\mathbf{a}$ between simulated and determined misalignment parameters for all modules and alignable degrees of freedom. A Gaussian function is fitted to the distributions to determine the alignment accuracy. The outliers in figure (b) and (c) are discussed in the text.

and z direction and around α and γ. The aim of each alignment procedure is the determination of misalignment parameters of one geometrical degrees of freedom.
Constraints are applied by the parameter fixation method (Section 4.3.4). All modules of the first and last two layers are fixed to their positions. Though tracks propagate constraints, as presented in Section 4.3.4, the module alignment cannot be processed with less fixed module positions: With the current track distribution of straight line tracks originating from one point, the propagation is not sufficient (compare Figure 4.3 (a)).
The results of the four alignment procedures are presented in Figure 5.22 (a)-(d). In each Figure, the dashed line represents the simulated misalignments $\boldsymbol{\Delta}\mathbf{a}^{true}$. The solid line indicates the difference $\boldsymbol{\delta}\mathbf{a} = \boldsymbol{\Delta}\mathbf{a}^{true} - \boldsymbol{\Delta}\mathbf{a}$ between simulatd misalignment and determined misalignment parameters for all aligned modules. The differences $\boldsymbol{\delta}\mathbf{a}$ peak at zero for all four degrees of freedom. A Gaussian distribution is fitted to the peaks in order to determine the achieved exactness of the alignment procedure. The procedure is exact to about 30 μm for the measurement direction and about 100 μm in z. For the rotations, the width of the Gauss function is about 0.08 mrad and 0.05 mrad for the alignment of α and γ, respectively.
Figure (b) and (c) show some entries, that are significantly off the Gauss function. These values are due to the track distribution as will be discussed in the following.

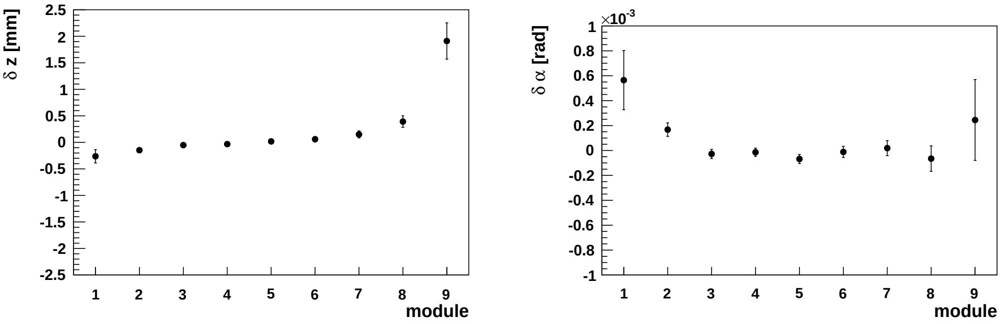

(a) (b)

Figure 5.23: Alignment exactness for Δz and $\Delta\alpha$ of the nine modules in layer one of station T2. The deviations from $\boldsymbol{\delta}\mathbf{a} = 0\,\mathrm{mm}$ are due to the track distribution in the detector, as explained in the text.

5.4.1 Impact of track distribution on the alignment procedure

As mentioned, the generated muon tracks presented in Section 5.1.2 are used in the alignment procedure. The simulated tracks start from a small region around the origin of the LHC*b* coordinate system. Their track slopes in x and y are presented in Figure 5.3. The numbering of the modules is sketched in Figure 5.2, module number 9 is close to the beam axis, module 1 is the outermost module of the half layer. As the trajectories are straight lines, track slopes and occupancies differ from the inner to the outer modules. Tracks, that traverse modules near the beam pipe have a much smaller slope t_x than those that pass the outermost modules. Furthermore, the innermost modules show full occupancy, whereas for modules 1 and 2 no hits are detected at the upper and lower y acceptance (about one third of the surface is not hit for module 1 at station T3, Figure 5.4 (c)). This track distribution has a direct impact on the determination of misalignments, as depicted in Figure 5.23 (a) and (b). The figure depictes the misalignment parameters Δz and $\Delta\alpha$ for the nine modules of layer one at station T2. This subset is representative for all modules and is chosen for convenience and clarity. The difference δz between simulated misalignment Δz^{true} and determined misalignment parameter Δz is shown in Figure (a). A significant difference $\delta z \approx 2\,\mathrm{mm}$ is visible for module 9 near the beam pipe. As discussed in Section 5.3.1, the determination of Δz depends on the slope of the track, see Equation 5.8. For tracks with small slopes, the determination of Δz is difficult. A more accurate determination of Δz at these positions requires additional and complementary data, like cosmic muon data, for example. They provide particle tracks with larger slopes at the inner modules. For all other modules, the figure shows that the positions are corrected according to the simulated displacements.

The determined misalignment parameters $\Delta\alpha$ are shown in Figure (b). It shows a deviation from $\delta\alpha = 0\,\mathrm{mm}$ for module 1 and 2 of about $2 - 3\sigma_{\Delta\alpha}$ and a large parameter uncertainty for module 9. The misalignment parameters of the remaining modules are correctly reconstructed within their uncertainties. The determination of $\Delta\alpha$ depends on the track slope as well as on the y position of the track at the corresponding detector element (Equation 5.9) The $2 - 3\sigma_{\Delta\alpha}$ deviation is due to the hit occupancy at the outermost modules: About one third of the module is not hit by tracks. Due to predominantly small values of y, the determination of misalignment parameter $\Delta\alpha$ is less accurate. The large uncertainty for module 9 is due to the small track slopes t_x at this position.

The simultaneous determination of the four misalignment parameters Δx,Δz,$\Delta\alpha$ and $\Delta\gamma$ for modules is presented in Chapter 6 on the basis of cosmic muon data. These data show a wide variety of track properties and thus are eligible for the alignment of modules.

5.5 Alignment procedure for half layers with magnetic field

This section presents results of the alignment procedure in case the dipole field in the detector is switched on and the particle trajectories are bent. The following discussion gives only a brief insight in the alignment with bent particle trajectories as the main focus of the present thesis is put on the alignment with cosmic muon data (Chapter 6), which have been taken without magnetic field.

5.5.1 Simulated data with magnetic field

The following study is performed with simulated data of the decay $B_s \rightarrow J/\Psi\Phi$, one of the key measurements of LHC*b* [23]. Due to the residual magnetic field in the Outer Tracker, as discussed in Chapter 2, particle trajectories are described by the parabola function given in Equation 5.3. The track parameters presented in Figure 5.24 are obtained for a reconstruction and fit of the tracks with ideal detector geometry. Figure (a) and (b) show the track slope parameter in x and y direction. Slope t_x is taken in station T1, slope t_y does not change along the track due to the straight line model in y direction. The broad distribution of t_x compared to t_y reflects the bending of tracks in the xz plane of the detector. The curvature κ is depicted in figure (c). Additional, the bending of the track is reflected in parameter τ, which describes the relative change of the trajectory tangent τ_1 at station T1 and tangent τ_3 at T3, i. e.,

$$\tau = \frac{\tau_3 - \tau_1}{\tau_1} \,. \tag{5.11}$$

The mean of the distribution is at $\tau \approx 0.06$, thus the slope of most of the tracks increase by 6 % from T1 to T3. About 7 % of the distribution is found at $\tau < 0$. These tracks describe trajectories, that are bend towards the beam pipe. Due to the geometry of the detector, only particles with a very high transverse momentum are bent like this. The majority of tracks is bent outwards of the detector, with $\tau > 0$.

5.5.2 Determination of mislignment parameters

For the validation of the alignment algorithm with tracks deflected in the magnetic field of the detector, 20 000 events of the $B_s \rightarrow J/\Psi\Phi$ data are processed resulting in

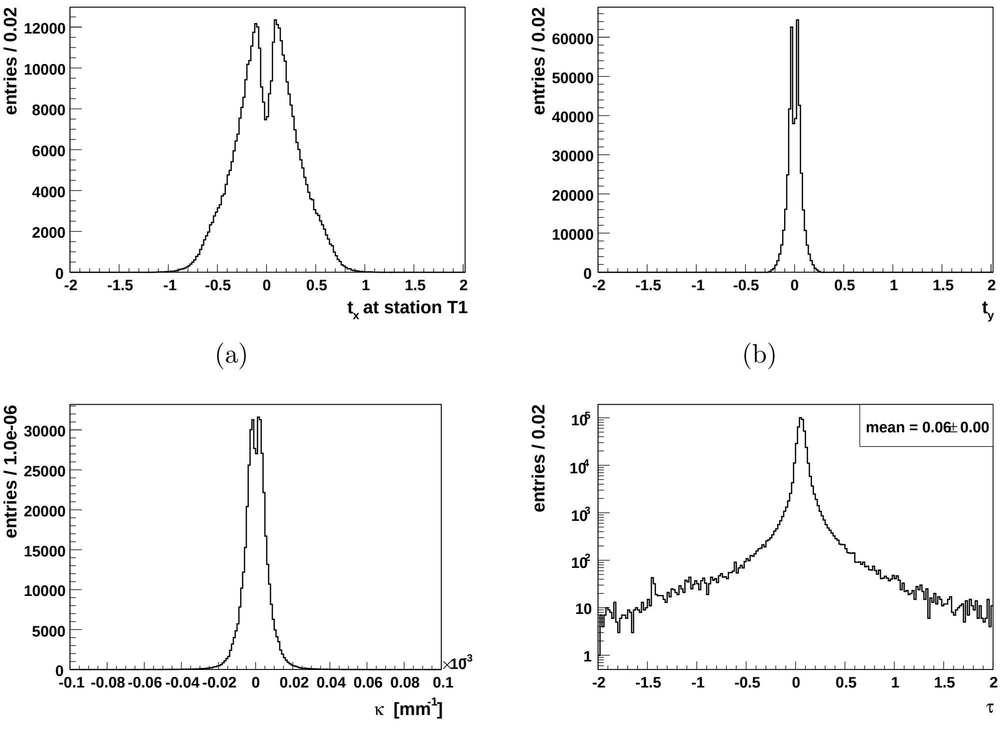

(a) (b)

(c) (d)

Figure 5.24: Track parameters, that describe particle trajectories in the residual magnetic field of the Outer Tracker. (a) The slope t_x at the first layer in station T1. The minimum around $t_x = 0$ shows, that the majority of tracks are bend towards the A-side and C-side. (b) The slope t_y for a straight line track model in y direction. (c) Curvature parameter κ, defined in Equation 5.3. (d) Relative change of the slope t_x measured at T1 and T3. The majority of tracks is bend outwards of the detector.

about 430 000 tracks that are used in the alignment procedure. The tracks have been reconstructed with the misaligned half layer geometry from database 6, Table 5.1, that describes shifts in the measurement direction and rotations around the z axis.

The bending of the tracks induces an additional degree of freedom that has to be constrained. Additionally to the 8 half layers that are fixed for straight line data, two more half layers (one on each side of the beam axis) are fixed for curved trajectories. The misalignment parameters Δx and $\Delta\gamma$ are simultaneously determined in the alignment procedure. The results are presented in Figure 5.25 (a) and (b), which shows the simulated misalignments versus the determined misalignment parameters. The parameters uncertainties are inside the drawn markers. A line fit to the distribution results in a line with slope $b \approx 1$ and a negligible offset a, that confirms the successful alignment procedure.

5.5.3 Improvement of track properties

The reduced track χ^2 before and after alignment is presented in Figure 5.26 (a). The maximum of the distribution reduces from 1.51 to 1.05. The improved mean of the track residual measured for the 24 half layers is shown in Figure 5.26 (b). The dashed

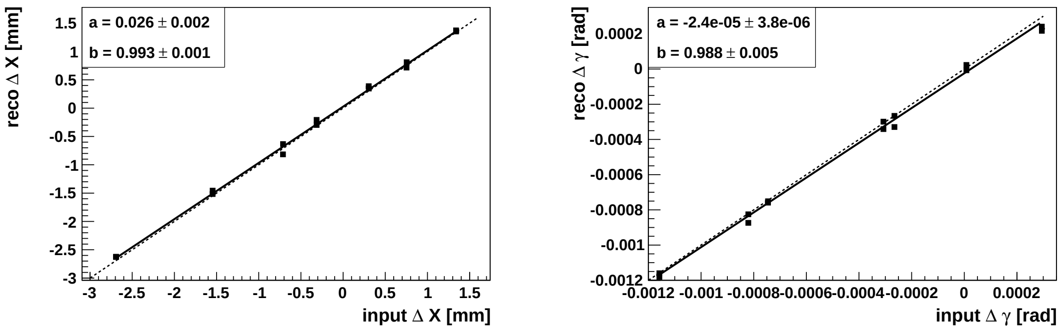

(a) (b)

Figure 5.25: Comparison of simulated misalignments with determined misalignment parameters Δx and $\Delta\gamma$. The dashed line with gradient one and offset line indicates equal values. The misalignments parameters are determined successfully.

Table 5.6: Efficiency and ghost rate before and after alignment with bend tracks. The nominal values of both quantities are gained after alignment.

	misaligned	aligned	nominal
efficiency[%]	84.7	94.5	94.5
ghost rate [%]	15.3	12.8	13.0

line represents the mean values that are widely spread due to misalignments. After the alignment procedure, the mean of the track residuals of all half layers peak at zero. The performances of the track reconstruction with misaligned and aligned detector geometry are compared. Table 5.6 shows the obtained efficiency and ghost rate for long tracks for misaligned, aligned and nominal detector geometries. The effect of the alignment is evident as the ghost rate decreases and the efficiency reaches its nominal value[10] of $\epsilon = 94.5\,\%$.

5.6 Conclusion

In this chapter, the developed alignment algortihm which allows to determine misalignment parameters $\mathbf{\Delta a}$ has been discussed. These parameters are obtained by a track base alignment procedure and represent corrections to a misaligned detector geometry. The developed algorithm considers different levels of detector sgementation. On the half layer level, the algorithm is validated in two steps. In the first step, the alignment procedure is processed for one singular degree of freedom at a time. Simulated misalignments are correctly determined by the procedure for all five degrees of freedom.

---

[10] The current study has been performed with data from the Data Challenge 2006 (“DC06”) and the corresponding track reconstruction algorithms. The optimization of the algorithms for the Monte Carlo 2009 Data (“MC09”) improved the efficiency and ghost rate. Thus, the numbers for the nominal geometry differ slightly from the numbers quoted in Table 3.4 in Chapter 3.

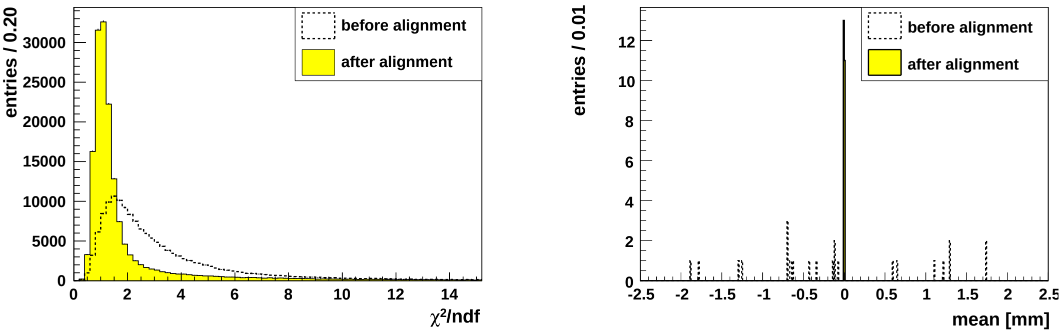

(a) (b)

Figure 5.26: (a) The reduced track χ^2 for long tracks improves clearly after alignment. (b) The residual mean before alignment is widely spread, dashed lines. After alignment, it peaks at zero, solid lines.

The success of the procedure is reflected in the track χ^2 and the mean of the track residual. Shifts of the mean of the track residual indicate misalignments of the detector even if these misalignments leave the track χ^2 nearly invariant. The mean of residuals is an important quantity for the evaluation of an alignment process.

The second validation step entails the simultaneous determination of misalignment parameters for all five degrees of freedom for applied detector translations and rotations. Misalignment parameters are determined in an iterative alignment procedure to consider initially large χ^2 values and correlations between the different degrees of freedom. The convergence of the parameters indicate a system of equations that is properly set up. The obtained statistical alignment accuracy is about $25\,\mu$m in measurement direction, $200\,\mu$m in z direction and $\mathcal{O}(10^{-2} - 10^{-1}\,\text{mrad})$ for the rotations. With this accuracy, the track reconstruction performance is not decreased in a significant way (Chapter 3).

On module level, the presented alignment procedure determines the misalignment parameters for each degree of freedom separately. A rotation around the y axis cannot be determined on this level because of the small lever arm of the narrow modules. Though tracks propagate constraints to all modules, the track distribution in the used data requires to fix the positions of all modules in the first and last two Outer Tracker layers. The number of modules used to constrain the undefined degrees of freedom could be reduced with other data, e. g., with cosmic muons tracks that show a homogeneous track distribution over the Outer Tracker acceptance.

A brief insight in the alignment procedure with curved tracks is given. Half layer misalignments are simulated in the measurement direction and around the stereo angle. The determined misalignment parameters are equal to the simulated displacements, the track properties improve significantly after the alignment procedure.

The developed alignment algorithm has been sucessfully validated with simulated data and is used for the first spatial alignment of the Outer Tracker modules with cosmic ray data, presented in the next section.

Chapter 6

LHC*b* Outer Tracker alignment with cosmic muons

This chapter demonstrates the performance of the developed alignment algorithm using tracks from cosmic ray muons.

After a short introduction of the origin of cosmic ray muons, the reconstruction of the muon tracks is presented. Following a detailed analysis of hit clusters is given since cosmic ray muons that enter the LHC*b* detector under steep angles lead to a increased number of clustered hits. A strategy to avoid a possible bias to the alignment procedure related to multi hit clusters is discussed and the results of the OT alignment on half layer and module level are given. The results represent the first complete spatial alignment of the Outer Tracker detector elements with measured data.

6.1 Cosmic muons in the LHC*b* detector

Cosmic rays which are created outside the earth's atmosphere consist of stable charged particles and nuclei synthesized by stars, e. g., electrons, protons, helium, carbon and other nuclei. By entering the atmosphere, these very high energetic particles collide with the atmosphere's particles producing nucleons and various mesons. Numerous charged mesons decay into muons in a height of about 15 km. At sea level, the muons have a mean energy of $E_\mu \approx 4\,\mathrm{GeV}$ and an integral intensity of $I \sim 1\,\mathrm{cm}^{-2}\,\mathrm{min}^{-1}$ (for horizontal detectors). The angular distribution of the muons at ground is $\propto \cos^2(\frac{\pi}{2} - \theta)$ with θ given with respect to the horizontal (this dependence is characteristic for muons with $E_\mu \sim 3\,\mathrm{GeV}$). Also the energy of the muons depends on θ, as can be seen in Figure 6.1. It shows the differential momentum spectrum at $\theta = 90^\circ$ and $\theta = 15^\circ$ in the range of $1\,\mathrm{GeV}/c < p_\mu < 1000\,\mathrm{GeV}/c$. The maximum of the measurements at large angles is shifted to higher momentum because low energy muons decay before reaching the surface and in addition high energy pions decay before interacting. Muons and neutrinos penetrate further into the earth where the muons loose their energy by means of ionization and radiative processes. In standard rock ($\rho = 2.65\,\mathrm{g\,cm}^{-3}$) the range for muons with $E_\mu \sim 100\,\mathrm{GeV}$ is 0.41 km-water-equivalent and even higher for higher energetic muons. Thus these cosmic particles can penetrate to depth of 100 m or more. This implies that cosmic muons can be detected with the LHC*b* detector that is

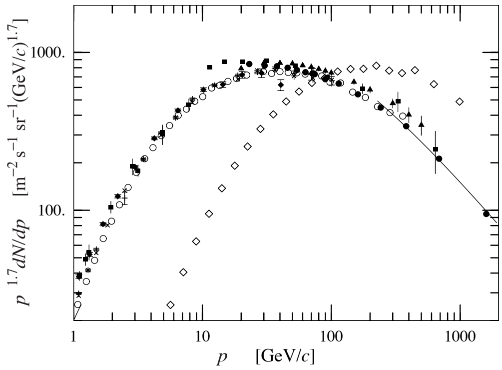

Figure 6.1: Momentum spectrum of muons with an incoming angle θ with respect to the horizontal of $\theta = 90°$ (filled markers) and $\theta = 15°$ (open diamonds). (Figure taken from [13].)

located about 100 m underground. The cosmic ray muons that enter the detector are triggerd by the Muon stations and the ECal. The large area of the detectors allows to collect numerous cosmic muon events although the horizontal orientation of the LHC*b* spectrometer is not suitable for the detection of the muons coming from the surface. The trigger decision is based on the measurement of hits in the muon stations and on energy deposit in the electromagnetic calorimeter.

Figure 6.2 shows a reconstructed cosmic muon event illustrated using the LHC*b* event display Panoramix [70]. Depicted is a three dimensional representation of the spectrometer with the following detector components visible from left to right: VELO, TT, magnet, Outer Tracker, calorimeters and Muon stations. The red bar visualizes the energy deposed in the calorimeter that triggered the event. Two tracks are shown, one is reconstructed with the hits in the Outer Tracker, the other from hits in the

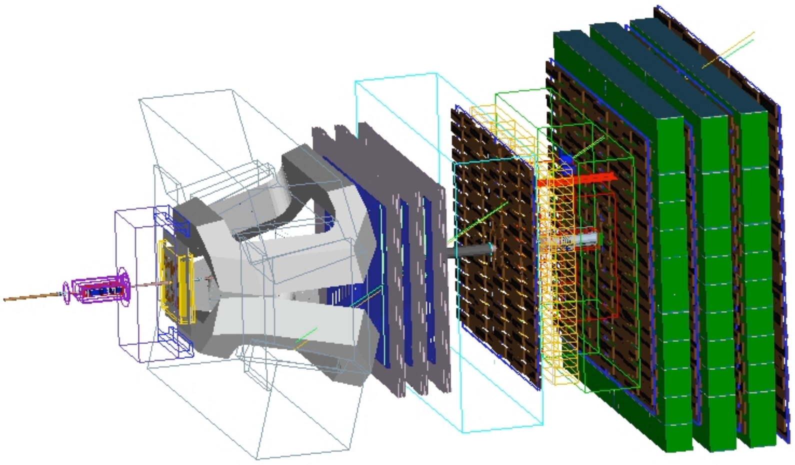

Figure 6.2: Three dimensional view of the spectrometer, generated with the LHC*b* event display. The trajectory of a cosmic muon is reconstructed, once in the Outer Tracker and also from hits in the Muon stations. The energy deposed in the ECal is depicted by the red bar.

Table 6.1: The cosmic particle runs from summer 2008 used for the Outer Tracker alignment. The abbreviation TAE stands for time alignment event. It denotes the number of readout intervals around the triggered event. Only very few cosmic muon tracks traverse the the silicon detectors as their sensitive surface are too small. The main purpose for adding them to the readout is to test their online performance.

Run	Evts	Date	Readout Configuration
31225	150k	27.08.2008	VELO,TT,OT,Calo,Muon; TAE±2
31557	180k	29.08.2008	VELO,TT,IT,OT,PRS,ECal,HCal,Muon; TAE ±2
34083	72k	20.09.2008	TT,IT,OT,PRS,ECal,HCal,Muon; TAE±3
34117	90k	20.09.2008	same as run 34083
34120	108k	21.09.2008	same as run 34083

Muon stations. The trajectories are almost identical and pass through the cluster found in the calorimeter.

Evidently, only muons entering the cavern under an incident angle $0° < \theta < 60°$ (upstream) and $120° < \theta < 180°$ (downstream) can be reconstructed, see Figure 6.3. Here, θ is the polar angle with respect to the z axis in the yz plane. The cosmic muon data is collected without magnetic field, so muons pass straight through the detector. Different detector readout configurations, listed in Table 6.1, are used for the commissioning and calibration of as many sub-detectors as possible.

For the first spatial alignment of the Outer Tracker about 600 000 cosmic ray events are reconstructed and analyzed. Many of these events have no tracks in the Outer Tracker as they are triggerd by the ECal and Muon stations. After quality cuts (Section 6.2.2) $\sim 20\,000$ tracks are used for the determination of the alignment parameters.

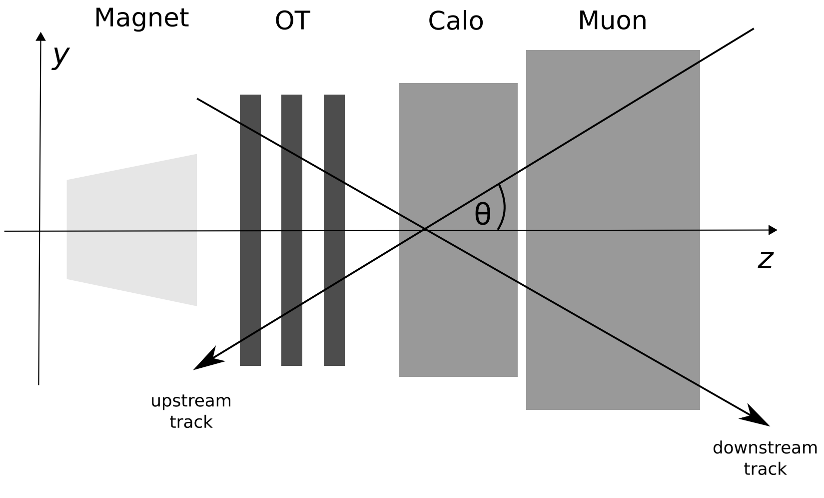

Figure 6.3: Sketch of part of the LHC*b* detector. The view in the yz plane shows the large area sub-detectors used for cosmic muon measurements. Cosmic muons enter the detector from above, muon tracks with a slope in y of $t_y < 0$ are referred to as *downstream*, tracks with $t_y > 0$ are called *upstream* tracks.

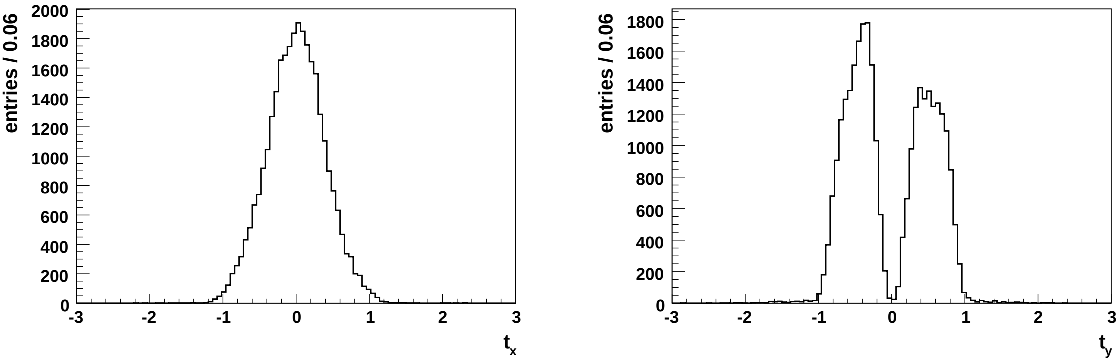

(a) (b)

Figure 6.4: The slopes in x and y directions of the measured cosmic tracks.

6.2 Cosmic ray muon track reconstruction in the Outer Tracker

In this section the reconstruction of the cosmic muon events is discussed. In Section 6.2.1 the pattern recognition algorithm is introduced briefly and results of the track reconstruction are given. An influence of the pattern recognition algorithm on the alignment procedure is discussed in Section 6.2.2, followed by Section 6.2.3 in which the origin of this influence is studied.

6.2.1 Pattern recognition and reconstructed cosmic ray muon tracks

Cosmic muon tracks are reconstructed using PatSeeding [83], a standalone pattern recognition algorithm for the T stations. Per default the algorithm is tuned to reconstruct tracks emerging from proton-proton collisions in the VELO and that are bent in the magnetic field of the detector. The pattern recognition algorithm configured for cosmic muon tracks is less complex compared to the default one because it accounts neither for a magnetic field nor for possible constraints imposed by production vertices. The track search strategy is briefly outlined in the following, a more detailed discussion is given in Appendix C.

The cosmic muon track search is done first in the xz plane. Two hits in the x layers of station T1 and T3 are selected and connected to a straight line, the remaining hits in the x layers lying inside a window around the line are counted. Every combination of two hits forming a line is tried and the combination giving the largest number of hits inside the window is taken as a track candidate.

The search in y direction begins with the projection of the stereo hits in the xz plane. Stereo layer hits are collected inside a window of the track candidate and are combined to pairs that define straight lines. A search window is defined around each line and further stereo hits inside the window are collected. The line of the pair with most associated hits is taken as the track candidate in y.

The track parameters of the candidates are determined by a χ^2 minimization method. The candidates are fitted in x and y direction to remove possible outlier hits and to

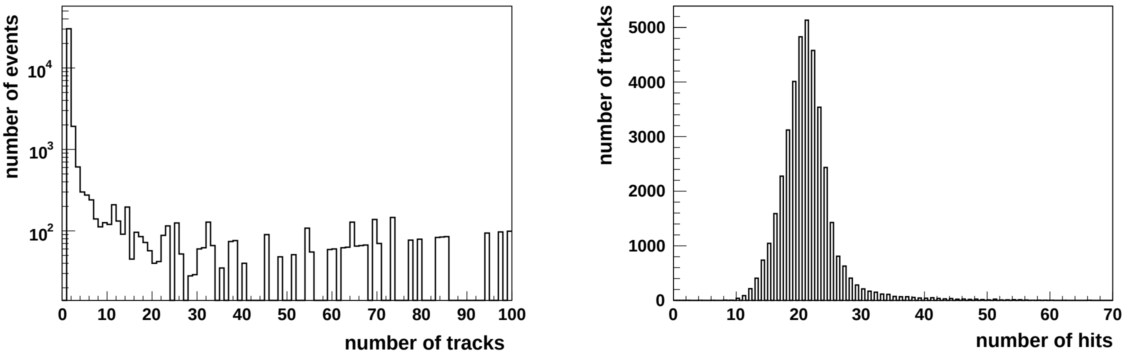

(a) (b)

Figure 6.5: (a) The number of tracks per cosmic muon event. More than 84 % of the events contain one or two tracks. (b) The number of hits associated to the track by the pattern recognition.

reject tracks with a χ^2 value greater than a predefined threshold.

The acceptance of the spectrometer for cosmic muons is restricted by the size of the ECal, Muon stations and T stations. The acceptance is clearly visible in the distribution of track slopes, shown in Figure 6.4. The slope t_x in x direction is symmetrical around zero with its maximum lying at $t_x = 0$. The two maxima of slope t_y in Figure 6.4 (b) represent *downstream* ($t_y < 0$) and *upstream* ($t_y > 0$) tracks, see also Figure 6.3. For both directions, the mean of the distribution is at $t_y \approx \pm 0.5$ which corresponds to polar angles θ with respect to the z axis of $\theta \approx \pm 30°$ and $\theta \approx \pm 150°$. These tracks are located, in good approximation, in the middle of the acceptance for *upstream* and *downstream* tracks, respectively. The different numbers of reconstructed *upstream* and *downstream* tracks reflects the fact that the majority of triggered cosmic ray muon events solely pass the ECal and Muon stations.
More than 84 % of the cosmic muon events contain one or two tracks, rather few compared to the ~ 100 tracks expected in proton-proton collision events (Figure 6.5 (a)). Multi track events most probably arise from cosmic ray showers.
The quality of a track strongly depends on the number of hits associated to it. A particle crossing the OT can interact with 24 sensitive detector planes, each plane giving one hit signal in the ideal case[1]. As can be seen in Figure 6.5 (b) the mean of associated hits is ~ 20, the same as from Monte Carlo simulations.

6.2.2 Influence of the pattern recognition algorithm on the alignment procedure

The pattern recognition selects appropriate hits in the Outer Tracker and assigns them to track candidates. The hits are measured in the straw tubes that are arranged in double layers in a module. Adjacent straw tubes that give a hit signal define a *hit cluster*. Due to the staggered layout of the straw tubes, the expected size of a hit cluster

---

[1] This means neglecting crosstalk effects and inefficiencies. Also multiple hit cluster due to high slopes are excluded here (see section Section 6.2.2).

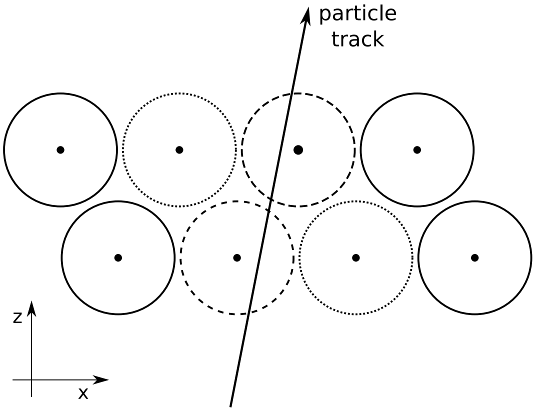

Figure 6.6: Sketch of a straw tube double layer in the xz plane. In an Outer Tracker module, a traversing particle leaves hits in the straw tubes of a double layer. The two tubes sketched with dashed lines represent an expected hit cluster of size $n = 2$. In case adjacent modules give a signal (dotted lines), the four tubes build a hit cluster of size $n = 4$.

is $n = 2$, Figure 6.6. Clusters of size $n > 2$ are called large clusters and can lead to an ambiguous association of the hits to a track candidate by the pattern recognition. These large clusters are observed at a rate of 8 % for events with a single reconstructed track. Their origin is discussed in Section 6.2.3. Such clusters have an impact on the iterative alignment procedure and the determination of the misalignment parameters as will be discussed in this section.

If the pattern recognition algorithm finds a hit cluster of size n, it will associates only a subset of n' of the hits to the track because of the search window size and possible outlier removals (Section 6.2.1). Assuming the first alignment iteration determines a set of parameters $\mathbf{\Delta a}_1$, for which the procedure used tracks with clusters of size n'. The parameters are passed to the geometry description which effectively shifts the modules and with them the hits of the clusters. A subsequent pattern recognition uses the new geometry and selects a different subset of hits from the n hit cluster: Some of the hits are shifted out of the search window, whereas other hits can be moved into the search region. This leads to new tracks with associated hits other than in the first reconstruction. The second alignment iteration then determines misalignment parameters $\mathbf{\Delta a}_2$ different from the parameters $\mathbf{\Delta a}_1$.
This effect is observed when processing the alignment algorithm using cosmic muon data. As an example, shifts in x direction are studied. Figure 6.7 shows the parameters Δx_k of the half layers on the C-side determined in the k^{th} alignment iteration. The shift in measurement direction is a linear degree of freedom in the alignment procedure and parameters of linear degrees of freedom are determined in one alignment iteration. Thus, it is expected that Δx stays constant after the first alignment iteration.
Figure 6.7 (a) shows the misalignment parameters Δx_k that are determined with tracks that comprise large clusters. The parameter Δx changes significantly up to the fourth alignment iteration. The subsequently parameters determined in the alignment iterations $4 - 10$ move inside an interval $\epsilon = \pm 0.03\,\mathrm{mm}$ around $\Delta x_k = 0\,\mathrm{mm}$. The observed effects are due to the pattern recognition influence on the alignment procedure.

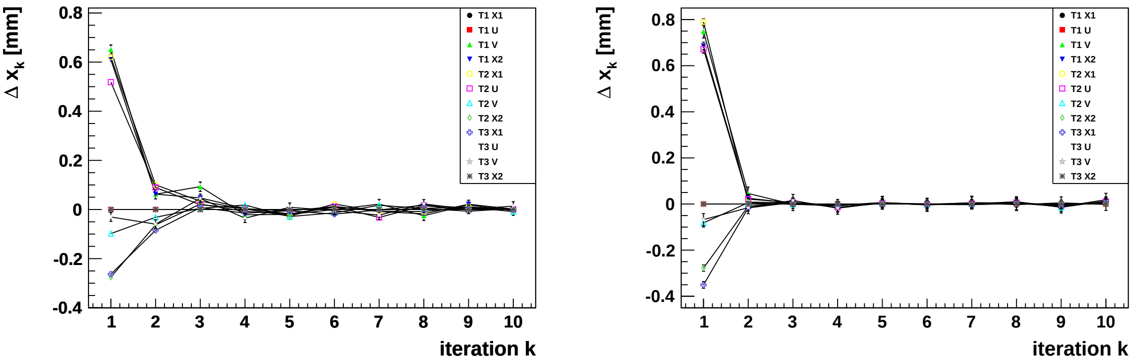

(a) Big cluster accepted (b) Big cluster rejected

Figure 6.7: Alignment constants Δx_k obtained in iteration k. Shown are the half layer constants for the translation in x, obtained on the C-side. (a) The slow convergence of the constants is due to the use of multi hit clusters in the pattern recognition. (b) Cuts on the maximum cluster size used in the pattern recognition lead to the determination of the constants in one step (linear degree of freedom).

Figure (b) depicts the convergence after having applied a cut on the size of clusters associated to the track. All used clusters are of size $n \leq 2$, which is the nominal cluster size in the modules. The results of the second alignment iteration reveal that parameter Δx is constant within its uncertainty after the first iteration, as expected. The changes of the parameters values in subsequent iterations are negligible.
The final misalignment parameters $\Delta x = \sum_k \Delta x_k$ (Equation 5.1) determined with the two approaches differ evidently. The parameters values for both approaches and the difference between them are listed in Table 6.2. Differences of more than $13\sigma_A$ are observed, where σ_A is the uncertainty of parameters that are determined with tracks comprising solely cluster of size $n \leq 2$.

The requirement of a hit cluster size $n \leq 2$ stabilizes the solution of the alignment procedure and all hits can unambiguously assigned to a track candidate by the pattern recognition[2]. The alignment of the half layers and modules presented in Sections 6.4, 6.5 are processed with tracks that fulfill this requirement.

6.2.3 The origin of multi hit clusters in the Outer Tracker

The cosmic ray muon tracks were the first tracks recorded with the assembled T stations and give valuable information of the performance of the Outer Tracker. Using the data for the understanding and calibration of the detector, their difference compared to data from proton-proton collisions must be considered: The muons are coming from the surface and enter the spectrometer under very steep angles (Figure 6.4). To exclude possible biases on the calibration and alignment due to these characteristics, a detailed study of the hit clusters is necessary. Especially the analysis of hit clusters with a size of $n > 2$ hits is important in order to understand the functionality of the detector. These

---

[2] This statement refers to the 84 % of the cosmic ray events that comprise one or two tracks, Figure 6.5 (a).

Table 6.2: The alignment parameters Δx for the half layers on the A-side and C-side. The values in column A are gained using tracks with a hit cluster size ≤ 2. Column B values are obtained by using also tracks with multi hit clusters for alignment. The difference of the values in A and B are of up to $13\,\sigma_A$, here σ_A is the error on the parameters in column A. No parameters are determined for layers 0,1,10 and 11 because they are used as constraints.

	A-side			C-side		
	Δx [mm]		$\frac{A-B}{\sigma_A}$	Δx [mm]		$\frac{A-B}{\sigma_A}$
Layer	$A \pm \sigma_A$	$B \pm \sigma_B$		$A \pm \sigma_A$	$B \pm \sigma_B$	
2	0.804 ± 0.028	0.776 ± 0.019	1.00	1.051 ± 0.029	1.010 ± 0.019	1.40
3	0.719 ± 0.016	0.716 ± 0.011	0.15	1.102 ± 0.017	1.147 ± 0.012	2.56
4	0.802 ± 0.014	0.748 ± 0.009	4.00	-0.491 ± 0.016	-0.284 ± 0.011	13.28
5	0.698 ± 0.017	0.621 ± 0.012	4.46	-0.381 ± 0.019	-0.125 ± 0.013	13.35
6	-0.069 ± 0.018	-0.126 ± 0.012	3.20	0.478 ± 0.020	0.521 ± 0.014	2.11
7	-0.28 ± 0.014	-0.334 ± 0.010	3.65	0.541 ± 0.015	0.670 ± 0.010	8.69
8	-0.363 ± 0.015	-0.358 ± 0.010	0.31	-0.102 ± 0.016	-0.050 ± 0.011	3.29
9	-0.075 ± 0.026	-0.061 ± 0.018	0.56	-0.163 ± 0.028	-0.079 ± 0.019	3.01

clusters could be caused by, e. g., cross talk[3] between adjacent straws in a monolayer or by faulty channels generating electronic noise in the detector.

Figure 6.5 reveals that only about 16 % of the cosmic particle events in the Outer Tracker contain more than two reconstructed tracks. These multi track events are either showers entering the detector or due to cosmic muons producing showers inside the detector. These kind of cosmic particle events are disregarded for the following study due to their complex structure and their statistical insignificance.

The study of the origin of multi hit clusters is done using about 30 000 events with a single reconstructed track. In order to understand the measured hit distribution, every measured hit must be taken into account during the track reconstruction. A bias because of cuts on the track χ^2 or outlier removal has to be prevented. Therefore the search window of the pattern recognition is set to a width of ±10 mm around the track candidate and the maximum allowed χ^2 is set to $\chi^2_{max} = 100$.

As can be seen in Figure 6.8, about 92 % of the track clusters are composed of $n \leq 2$ hits. These clusters are of the size expected in the OT modules. The remaining $\sim 8\,\%$ are multi hit clusters including $n \geq 3$ hits, the major fraction of these clusters ($\sim 70\,\%$) are of size $n = 3$. Due to this large fraction of three hit clusters the further detailed studies are solely performed with clusters of size $n = 3$.

First, it has been studied whether the multi hit clusters are caused by cross talk. A cross talk signal is measured with a negligible time difference with respect to the real hit signal. Therefore, the time difference between signals measured in two adjacent straw tubes in the same monolayer is determined. The time difference is histogrammed in Figure 6.9. On the abscissa, the unit is given in time to digital converter (TDC)

---

[3] The charge generated by an ionizing particle traversing a straw can cause a mirror charge in an adjacent straw. The signal produced by the mirror charge is termed cross talk.

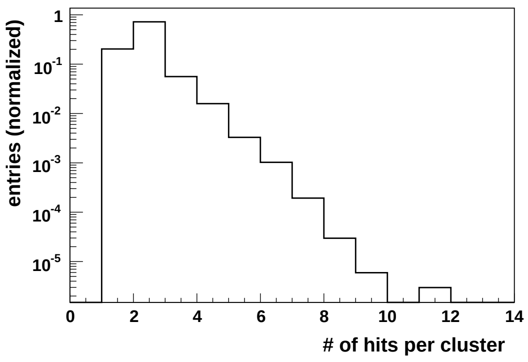

Figure 6.8: Several adjacent straws which gave a signal form a cluster. The size of the clusters found in events with a single reconstructed track is shown in this plot. About 92 % of the clusters are composed of ≤ 2 hits.

counts, one TDC count $\simeq 0.39$ ns. Cross talk signals would result in a sharp peak at $\Delta TDC \approx 0$ [45]. As can be seen, no such peak equivalent to large cross talk effects can be observed.

In the following it is studied, if the large clusters are a result of geometrical effects. For the staggered layout of the straw tubes, six different patterns of clusters with three hits are possible, as shown in Figure 6.10. Sketched is the double layer structure of a module in the xz sectional plane with the hit patterns highlighted. The rows a and b in the figure illustrate the appearance of double hits in monolayer a or b respectively. Given by the monolayer geometry, tracks with a slope $|t_x| \geq 0.48$ should contribute to pattern P_2 and P_3. The occurence of pattern P_1 is not yet understood, see below.

First, the track slope dependence of the patterns is verified by considering cluster pattern only in the x layer of the stations. This way additional geometrical effects on the patterns due to the stereo layer rotation are excluded. Figure 6.11 (a) depicts the high correlation between the track slope t_x and the appearance of pattern P_i, with $i = 1, 2, 3$. The ratio shown on the ordinate is given by the number of found pattern P_i with respect to all pattern with ≤ 3 hits, i. e., including normal clusters. For the sake of argument, only the pattern measured for track slopes $t_x \geq 0$ are depicted. The results for slopes $t_x \leq 0$ are equivalent. Pattern P_1 is maximal for tracks with slope $t_x \leq 0.4$, whereas P_2 and P_3 contribute with only a few per mill. As expected from the double layer design of the modules, clusters with pattern P_3 abruptly appear for $t_x \geq 0.48$ and their number increases with steeper slopes. The result confirms the expected geometrical effect on the occurrence of pattern P_2 and P_3.

A further analysis of pattern P_1 revealed a dependence of the pattern appearance

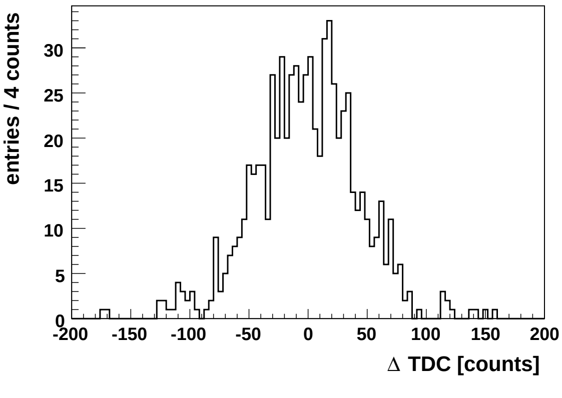

Figure 6.9: Time difference of the signals measured for two adjacent straws in the same monolayer, given in TDC counts (1 count $\eqsim 0.39$ ns). Since a cross talk would cause a peak at $\Delta TDC \approx 0$ it can be excluded as origin for a multi hit cluster.

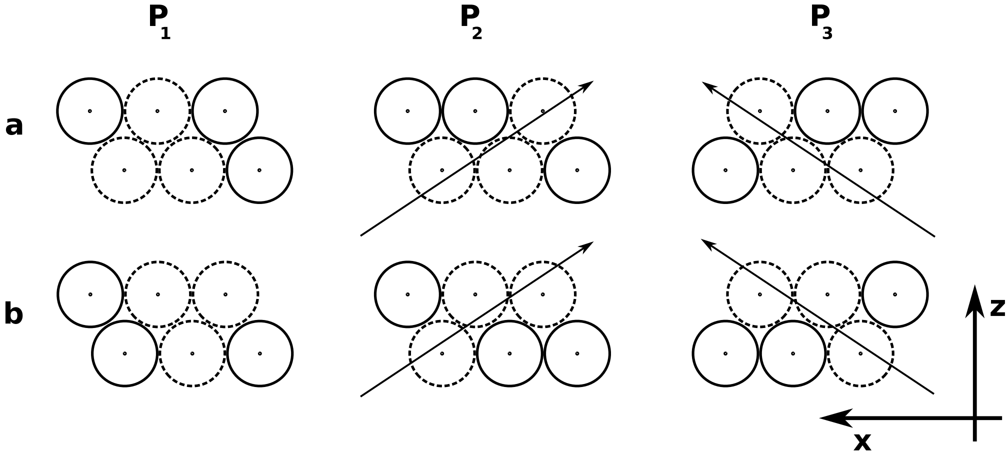

Figure 6.10: Six different patterns that can be found for module clusters with 3 hits. Sketched is the xz view of the staggered layout of the straw tubes in a module, the arrows indicate traversing particles. A signal measured in a straw is indicated by dashed lines. The first row shows the patterns with two hits in monolayer a, the same for monolayer b in the second row.

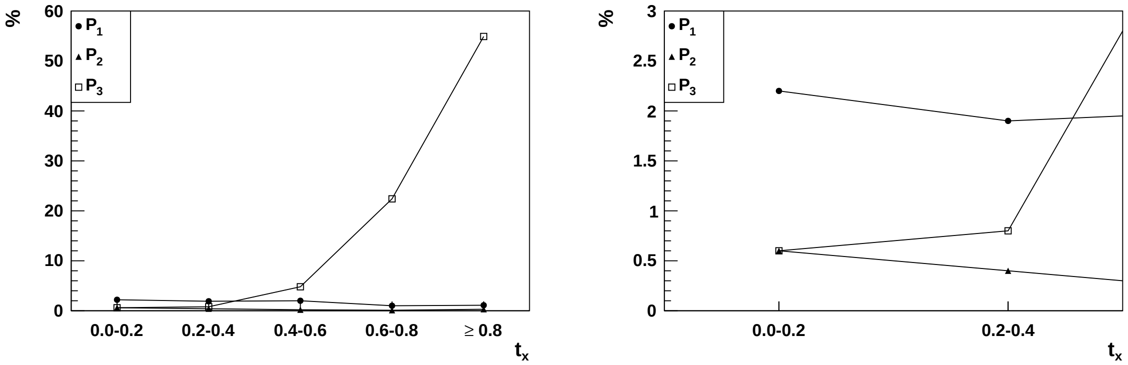

(a)

(b) Detail of (a)

Figure 6.11: (a) The figure shows the dependence of the occurrence of a pattern on the track slope t_x. The dependence is the same for tracks with $t_x > 0$ and with $t_x < 0$. (b) A detail of (a).

on the track slope t_y: The occurrence of P_1^a (adjacent hits in monolayer a) and P_1^b (adjacent hits in monolayer b) depends on whether the track is *upstream* ($t_y \geq 0$) or *downstream* ($t_y \leq 0$). In Figure 6.12, the asymmetry

$$\mathcal{A} = \frac{P_1^a - P_1^b}{P_1^a + P_1^b} \tag{6.1}$$

is plotted with respect to the track slope t_y. As can be seen, pattern P_1^a is found more often for *upstream* tracks, i. e., tracks first traversing monolayer b. The same effect is measured for pattern P_1^b in case of *downstream* tracks. The observed asymmetry for either *upstream* or *downstream* tracks is $\mathcal{A} \approx 17\,\% \pm 4\,\%$. The error is calculated assuming that P_1^a and P_1^b are uncorrelated and individually Poisson distributed.

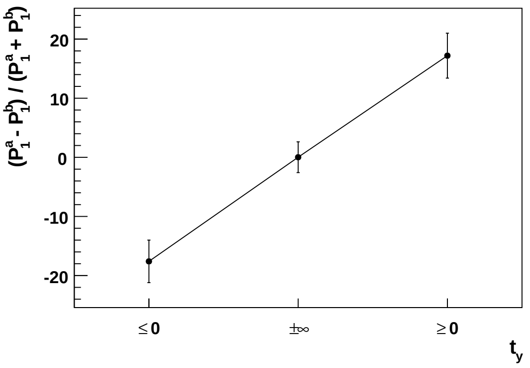

Figure 6.12: Asymmetry between the pattern of type P_1^a and P_1^b dependent on the track slope t_y. In case of *downstream* ($t_y < 0$) tracks the occurrence of P_1^b exceeds the one of P_1^a , i. e., double hits are found more often in monolayer b than in monolayer a. The same but reversed effect is found for *upstream* tracks.

This study rejects the assumption of detector noise as origin for the multi hit clusters: First, it can be assumed that noise is randomly spread in the detector and completely uncorrelated to the track slopes. Second, detector noise is expected to contribute at the per mill level [84] to the measured hits. The 2 % occurrence of pattern P_1 at $t_x < 0.4$ significantly exceeds this expectation.

Another possible explanation for pattern P_1 could be secondary particles. They could be produced by the interaction of muons with the detector, boosted in flight direction. The secondaries are found just locally in the Outer Tracker, because > 90 % of the tracks that comprise three hit clusters have exactly one big cluster associated. Therefore, the flight distance of secondaries is found to be in the range of a few mm. This implies that they are absorbed in the module in which they are produced. Since it is most likely that secondary particles are produced either in the material of the module wall or during the ionization in the straw tube gas, two candidates are considered:

- Photons from transition radiation emitted in the module wall that serves as radiator (the radiator material is *Rohacell*).
- δ electrons generated in the straw tube.

Transition radiation is emitted by particles traversing the radiator with a Lorentz factor of $\gamma \approx 1000$, which is reached by cosmic muons traversing the detector with an energy of $E_\mu \approx 100\,\mathrm{GeV}$ (Section **??**). The emission angle $\alpha \sim \frac{1}{\gamma}$ [86] is in the order of $\mathcal{O}(\,\mathrm{mrad})$ and the flight path of the emitted gamma is very close to the muon trajectory. The distance between the two trajectories will only be a few μm after a flight length of a few cm. Therefore it is unlikely that a secondary passes a straw tube other than the one passed by the primary. This excludes transition radiation as probable candidate for the cause of multi hit clusters.

δ electrons are produced by collisions of the incident particle with the gas in the straw tubes. Their kinetic energy is far higher than the mean excitation energy I of the concerning gas atom or molecule, i. e., $T_{kin} \gg I$. In case a δ electron is produced in the first monolayer, it is boosted in direction of the incident cosmic particle and therefore more likely to be detected in the second layer. Indeed, the production of δ electrons

is rather rare [13] and calculations show that the energy of the electrons produced in the straw tubes have too little energy to penetrate through the straw tube wall to an adjacent straw [87].
It has been shown that cross talk and noise can be excluded as origin of the multi hit clusters. The appearance of patterns P_2 and P_3 is the result of a geometrical effect. Possible explanations for pattern P_1 are discussed but none is capable to explain the 2 % occurrence of the pattern which can be a characteristic of the cosmic muon track topology. However, the 2 % occurence will not delimit the operation and performance of the Outer Tracker detector when collecting data from proton-proton collisions.

6.3 Alignment procedure

The collected cosmic muon data are the first data measured with the LHC*b* detector. Thus they provide the possibility to validate the alignment algorithm which is developed on simulated data.
First, the alignment of the 24 Outer Tracker half layers is processed. After validation of the reliability of the algorithm at this segmentation level of the detector, the position of the 216 Outer Tracker modules are aligned without prior knowledge of the half layer alignment results. Thus, the robustness of the alignment algorithm on the module level is tested.
The determined misalignment parameters of both approaches are then compared to each other for a cross check. As such a comparison is possible only if the results are given in the same reference system, identical constraints are applied in each case.

Constraints - Defining the alignment coordinate system

Technically, misalignment parameters are determined by solving a system of linear equations. Several possibilities to constrain this system are discussed in Section 4.3.3. The Outer Tracker alignment with cosmic muon data is performed by *fixing* certain degrees of freedom of a detector element. By fixing the same parameters for the half layer and module alignment, e. g., constraining the shift in x direction of one layer and thus of all modules of that layer, the results of both alignment approaches are obtained in the same coordinate system.

The minimum number of boundary conditions are defined by the Outer Tracker design and the used track sample. Interconnecting tracks introduce correlations between the detector elements that allow the propagation of constraints from one detector element to the other, see also Section 4.3.3. The correlation of the elements can be studied with the alignment covariance matrix $\boldsymbol{C}'^{-1}$ (Section 4.3.1 Equation 4.21). The correlation of two parameters a and b is given by $\eta = \frac{cov(a,b)}{\sigma_a \sigma_b}$, with σ as the error of the corresponding parameter and $cov(a, b)$ denoting the covariance matrix entry for row a and column b[4]. Figure 6.13 illustrates covariance matrix $\boldsymbol{C}'^{-1}$ obtained for the half layer alignment in x direction. The 12 parameters of the half layers on the C-side are plotted in bin number

---

[4] Note that the definition $\rho_j = \sqrt{1 - \frac{1}{\boldsymbol{C}_{jj} \cdot \boldsymbol{C}^{-1}_{jj}}}$ given in Chapter 4 indicates the correlation of parameter j with *all* other parameters, whereas η defines the correlation between *two* arbitrary parameters.

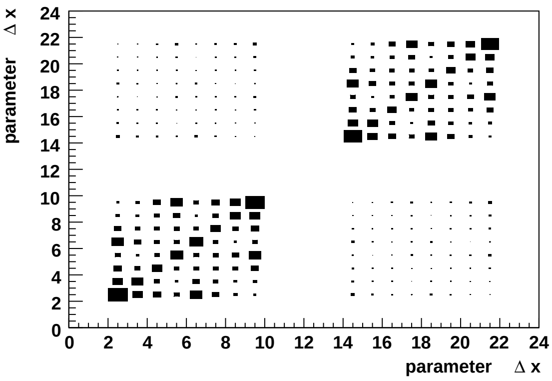

Figure 6.13: The covariance matrix C' which indicates the correlation between the alignment parameters. Here, the correlations of the 24 Δx parameters are shown. The layers on the C-side are numbered 0-11, on the A-side 12-23. The halves are essentially uncorrelated.

$0-11$, the A-side half layers in bin $12-23$. The rows and columns with no entry represent the constraints applied to the system of equation. The size of the entries reflects the matrix elements. Evidently, the sub-matrix in the lower left and upper right show the covariance values for each side. As the entries of the sub matrices in the upper left and the lower right are very close to zero, the correlation between the two halves is negligible. This reflects the fact that only few tracks traverse both halves. Both halves must therefore be constrained independently to fix the scaling C_X.
The applied constraints are shown in Table 6.3. For the discussed OT alignment, two x layers and two stereo layers per detector half are fixed to their nominal positions. The same constraints are applied to the rotational degrees of freedom. In the z direction, the boundary conditions are given by optical survey measurements that determined the frames of the corresponding half layers at $\Delta z = 0.0 \pm 0.5\,\mathrm{mm}$ [88].
Identical constraints are used for the module alignment, except for $\Delta\beta$ that is not determined on the module level. Due to the module size of $0.3\,\mathrm{m} \times 5\,\mathrm{m}$ (width × height), a rotation around the vertical axis cannot be determined.

6.4 Alignment of half layer positions

First, all degrees of freedom of the half layers position and rotation are determined. The shift in z and the three rotations are non linear degrees of freedom and are linearized to set up the linear system of equations according to Equation 4.15. Due to the linearization, the misalignment parameters must be determined in an iterative alignment procedure. During the iterations, any oscillations or even divergence of parameters indicate a severe problem of the algorithm and can have several origins. The most obvious ones are either a badly constraint minimization problem or an improper track sample containing tracks with outlier hits or bad χ^2 values. In case of convergence, the reliability of the determined misalignment parameters is controlled by a study of the track residual and χ^2 distributions.

Table 6.3: Fixed alignment parameters: Each cross indicates the layer that is not aligned in the corresponding degree of freedom. Identical constraints are applied to the A-side and C-side, therefore they are not explicitly listed in the table. The choice which layer to use as constraint is arbitrary, except for Δz. For this misalignment parameter the results from optical survey measurements are taken as reference.

Station	T1				T2				T3			
Layer	x	u	v	x	x	u	v	x	x	u	v	x
Δx	×	×	-	-	-	-	-	-	-	-	×	×
Δz	×	×	-	-	-	-	-	-	×	×	-	-
$\Delta\alpha$	×	×	-	-	-	-	-	-	-	-	×	×
$\Delta\beta$	×	×	-	-	-	-	-	-	-	-	×	×
$\Delta\gamma$	×	×	-	-	-	-	-	-	-	-	×	×

6.4.1 Convergence of alignment parameters and track selection

A first half layer alignment is done *without* track quality cuts and shows convergence for all degrees of freedom (the convergence criteria are defined in Section **??**). Figure 6.14 (a) and (b) depict the convergence behavior of a linear and a non-linear degree of freedom, i. e., the parameters Δx and $\Delta\beta$.

As expected, the linear parameter Δx is stable already after the first iteration, changes in following iterations are consistent with the uncertainty of the parameter.

Also for parameter $\Delta\beta$, the alignment procedure converges within one iteration. But in iterations $k = 2 - 10$, the determined parameter oscillates within an interval of $[+\sigma_{\Delta\beta}, -\sigma_{\Delta\beta}]$, where $\sigma_{\Delta\beta}$ is the uncertainty of the parameter.

To study the origin of the oscillations, a second half layer alignment is processed *with* a track selection based on the reduced track χ^2/ndf. The selection cuts are applied in each iteration of the alignment procedure. In case a track exceeds a given threshold value, the track is not considered for the determination of the misalignment parameters in this particular iteration (compare Figure 5.5). In a subsequent iteration of the alignment procedure, again all tracks are considered and new selection cuts are applied. The maximum allowed reduced χ^2 values are given in Table 6.4 together with the number of tracks that are used to determine the misalignment parameters. In total,

Table 6.4: Applied cuts on to the track χ^2/ndf for ten subsequent iterations of a half layer alignment run. Each track exceeding the maximum χ^2/ndf is not considered for alignment. In total, 19087 tracks are used.

Iteration	1	2	3	4	5	6	7	8	9	10
max χ^2/ndf	150	50	17	10	10	10	10	10	10	10
N_{tracks}	19087	19063	18985	18664	18667	18675	18670	18662	18676	18653

ten iterations are processed.
Considering only tracks with $\chi^2/ndf < 10$, less than 3 % of the tracks in the cosmic muon sample are rejected. The impact of the track selection on the alignment procedure is shown in Figure 6.14 (c) and (d) where the misalignment parameters Δx_k and $\Delta\beta_k$ obtained in the k^{th} iteration are depicted.
While the cuts have insignificant impact on the determination of Δx, the track selection is evident for $\Delta\beta$. The oscillations seen previously are completely prevented by rejecting about 400 tracks with $\chi^2/ndf > 10$. This result reflects that the selection of tracks with higher quality improves the convergence of non-linear degrees of freedom. The fast convergence suggests a well linearized and conditioned system of equations. Track selection criteria are used in the following for the determination of the misalignment parameters.

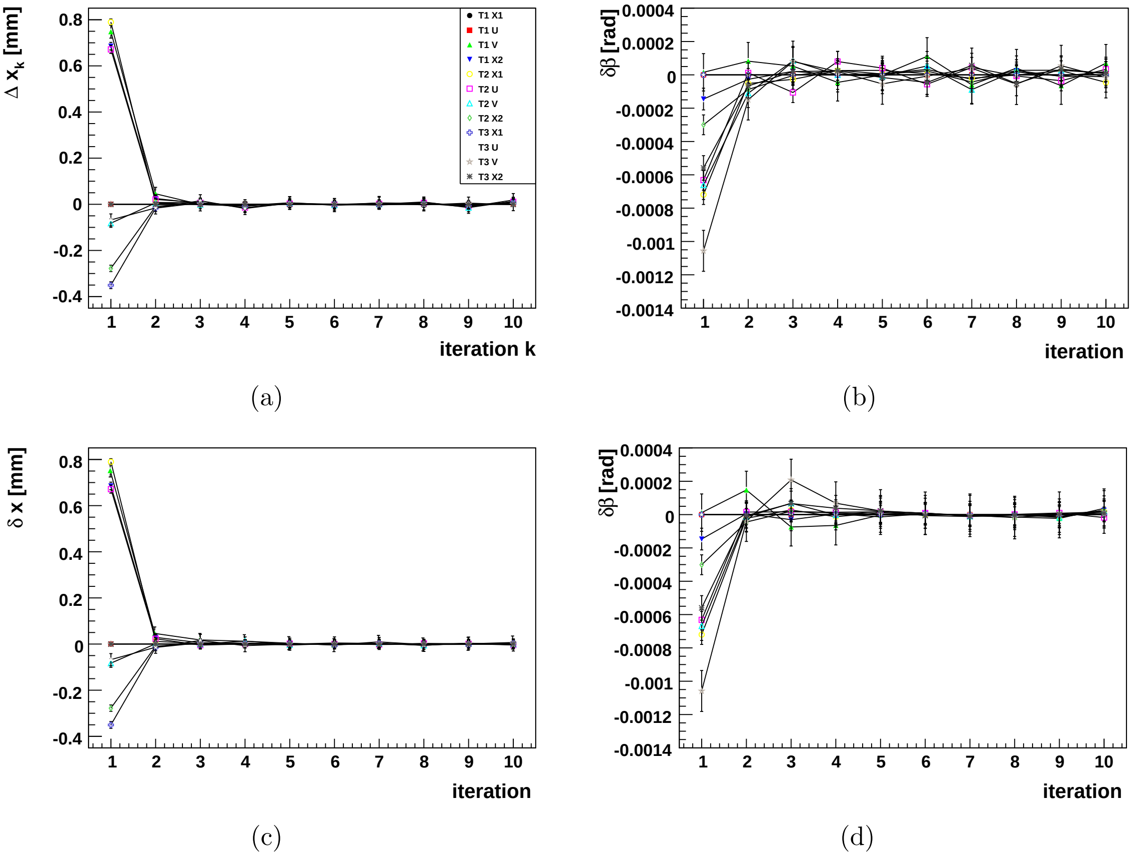

(a) (b)

(c) (d)

Figure 6.14: Convergence of the linear parameter Δx (a) + (c) and the non-linear $\Delta\beta$ (b) + (d). The alignment results shown in (a) and (b) are obtained without track quality cuts. Plots (c) and (d) show the convergence of the same parameters in case a track selection is applied. The effect of the track selection is negligible for Δx, but prevents the oscillation of $\Delta\beta$.

6.4.2 Misalignment parameters for half layers

The collected cosmic ray data allow the determination of the half layer misalignments in all degrees of freedom. The results for the translational degrees of freedom are presented in Figure 6.15 that depicts the determined misalignment parameters for the half layers on the A-side and C-side. In each plot, the parameters marked with a circle indicate the applied constraints.

The parameters Δx indicate shifts of up to $\sim 1\,\mathrm{mm}$ relative to the detector elements that are fixed to their nominal positions. Misalignments in this order are expected as the exact positioning of the large half layers ($\sim 15\,\mathrm{m}^2$ per half) during installation is not trivial.

The misalignment parameters Δx show equal shifts of neighbouring half layers. This is consistent with the expectation as neighbouring layers are mounted together on a mechanical unity, the C-frames.

The misalignment parameters Δz describe translation of up to $\sim 3\,\mathrm{mm}$. These shifts are also observed by optical survey measurements which determined the z positions of the six C-frames on side C. The survey measurements are given in Figure 6.17 together with the software results. For comparison, half layers $(0, 1)$ and $(8, 9)$ are constrained to $\Delta z = 0\,\mathrm{mm}$ which is the value the survey has measured [88]. The uncertainties of the parameters determined with the alignment algorithm are too small to be visible in the plot. The misalignment parameters determined with the alignment algorithm agree very well with the parameters obtained by the optical survey measurements. This result explicitly confirms the reliable performance of the algorithm.

The determined differences of the relative z positions of neighbouring layers is explained by the fact that a half layer is not a rigid body. It is composed out of nine individual

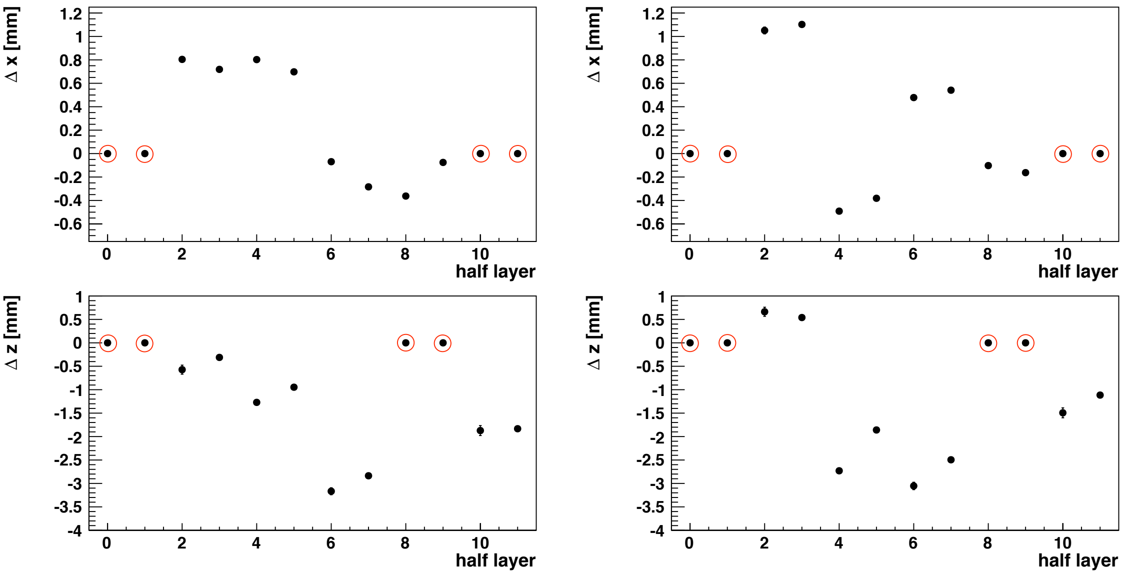

Figure 6.15: The misalignment parameters for the translational degrees of freedom, the results for the half layers on the A-side are shown in the left column, C-side results in the right column. The parameters values equal to zero represent the applied constraints. Most of the error bars are covered by the drawn points.

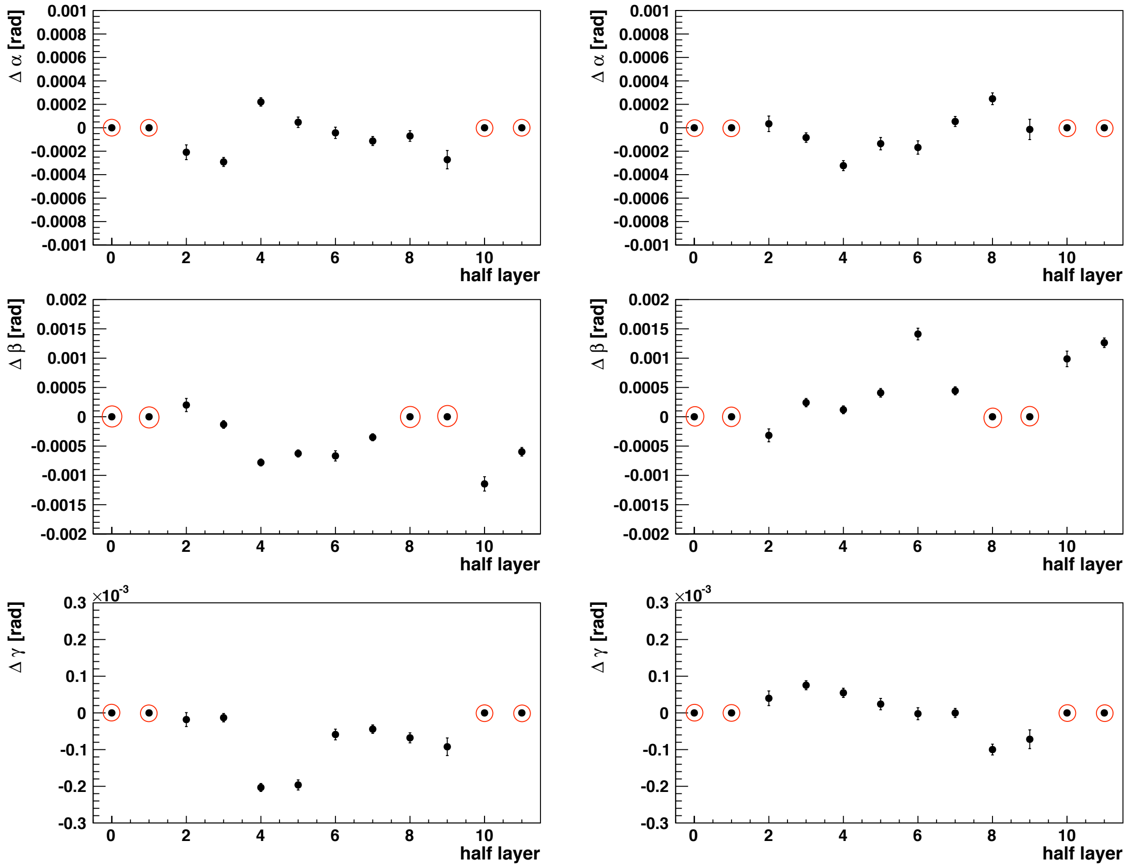

Figure 6.16: The misalignment parameters for the rotational degrees of freedom, the results for the half layers on the A-side are shown in the left column, C-side results in the right column. The parameter values equal to zero represent the applied constraints. Most of the error bars are covered by the drawn points.

modules. As these modules are very long, they possibly can bent in the middle as they are attached only at the upper and lower end to the C-frame. This effect can influence the determination of the misalignment parameters for the half layer.
The results for the rotational degrees of freedom are illustrated in Figure 6.16. The rotations $\Delta\alpha$ and $\Delta\gamma$ are negligible as they are well below 0.5 mrad. The rotation around the y axis are up to 1.5 mrad on the C-side. This rather large rotation leads to a difference of the z positions of the inner- and outermost modules of the layer of about 4.5 mm. This significant module shifts are confirmed by the module alignment in section Section 6.5.2. The impact of the alignment on the track reconstruction is presented in the following section.

Improvement of track quality

The alignment procedure corrects for shifts and rotations of the half layers in order to minimize any deterioration of the track reconstruction. Therefore the track properties, e. g., mean and width of residual or χ^2 of the track, are important quantities to validate the alignment. Figure 6.18 (a) shows the number of hits on the track used for the alignment. In average 20 hits are associated to a track, as expected from simulation.

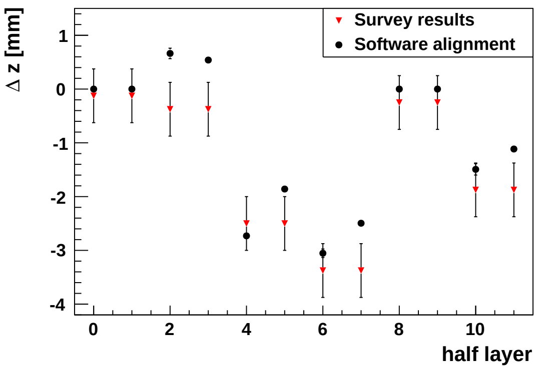

Figure 6.17: Correction parameter Δz for the half layers on the C-side. The triangles depict the z positions of the frames, determined by survey measurements. The points are the positions of the half layers found by the software alignment.

The mean of the reduced χ^2 improves after the alignment from 1.36 to 1.24 as shown in Figure 6.18 (b).

The alignment is further validated by the study of track residual distributions. Figure 6.18 (c) shows the mean of track residual for each of the 24 half layers. The presented distribution is obtained by the following procedure: 1) The half layers are aligned in all degrees of freedom and the detector geometry is corrected according to the determined misalignment parameters. 2) The track reconstruction is processed again with the same track sample and the mean of the track residual is determined. The broad distribution (dashed lines) with $RMS = 0.374 \pm 0.054$ indicates the misalignment of the detector. After alignment, the distribution peaks at zero with

$$RMS = 0.010 \pm 0.002\,\mathrm{mm}\ , \tag{6.2}$$

showing that the alignment algorithm is working as expected.

It is important to note, that this result reflects the mean of the track distribution in the half layers. It does not account for the fact that a half layer is a unity composed of modules. Individual shifts or rotations of the modules are not resolved by an alignment of the half layers. This effect of the substructure is presented in Figure 6.18 (d). It shows the mean of the residual for each of the 216 modules, before (dashed lines) and after (solid lines) the alignment of the half layers positions. Though, the width of the distribution improves from $RMS = 0.396 \pm 0.019\,\mathrm{mm}$ to $RMS = 0.129 \pm 0.006\,\mathrm{mm}$, it is significant larger compared to the mean of residuals measured for each half layer, Equation 6.2. Remaining misalignments on the module level are still to be determined. The determination of this remaining displacements is presented in the next section.

6.5 Alignment of module positions

This section described the alignment procedure for modules. The results obtained by the alignment of module positions will be compared to the results of the half layer alignment. This requires that the misalignment parameters are determined in identical reference systems. Therefore, the constraints applied to the alignment procedure for

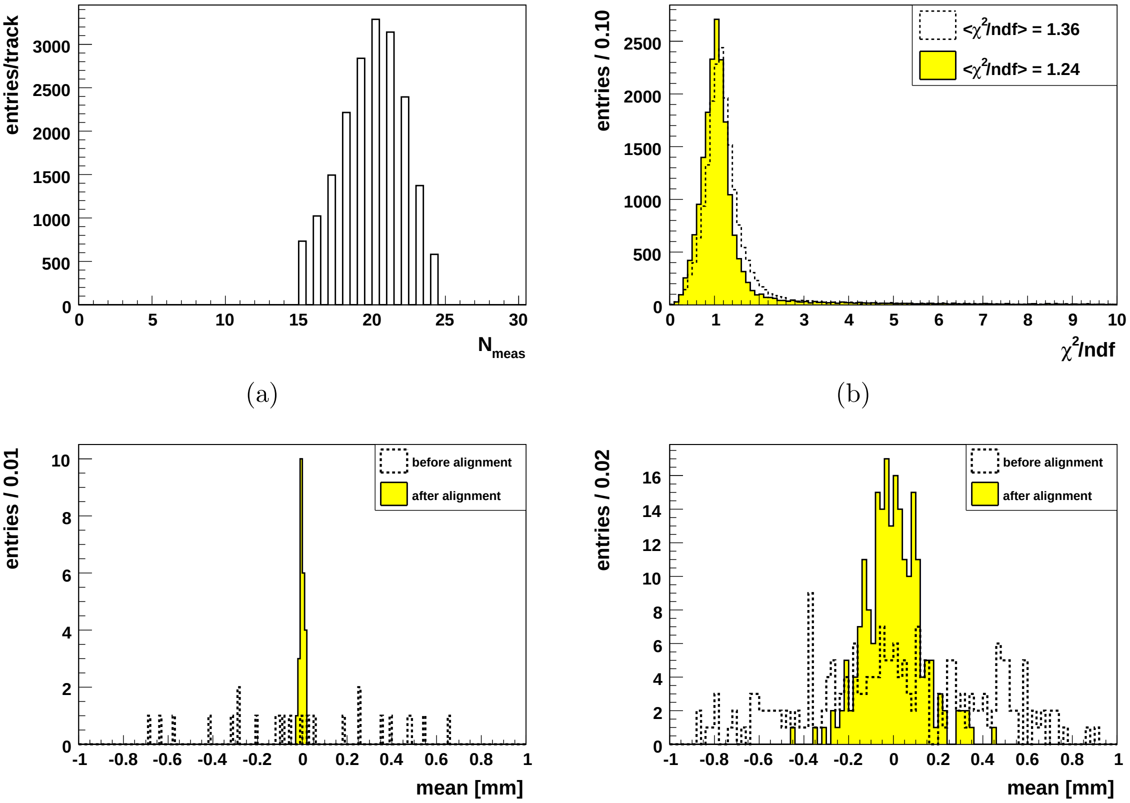

(a)

(b)

(c) Half layer

(d) Module

Figure 6.18: Improvement of the track parameters after half layer alignment. (a) The number of measurements per track. Plot (b) shows the reduced χ^2/ndf before and after alignment. The track residual mean of the half layers is presented in (c), after alignment, the achieved width is $RMS = 0.010 \pm 0.0015$ mm. The residual mean for modules is shown in (d), the improvement is less pronounced due to remaining misalignments of individual modules, see Section 6.5.2.

modules are identical to the constraints used in the half layer alignment procedure (Table 6.3): All modules in the first and last two layers are fixed to their nominal positions, except for the determination of Δz, where the modules in station T3 are fixed in the first x and in the u layer. This implies that 72 out of the 216 modules are fixed to their nominal positions.

Due to the narrow width of the modules, the alignment procedure is not sensitive to a module rotation around the y axis. This leaves in total $4 \cdot 144 = 576$ misalignment parameters for the four degrees of freedom.

6.5.1 Correlation of module misalignment parameters

To study the misalignment parameters on the module level, it is important to consider the impact of correlations between the modules on the parameters. Evidently, these correlations are imposed by the interconnecting tracks. But these tracks also propagate the constraint information of the fixed modules to the 'free' ones and thus minimize

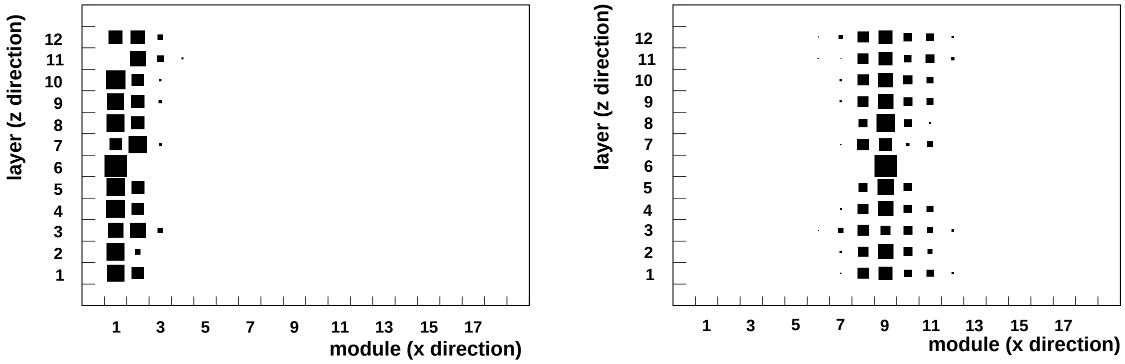

(a) (b)

Figure 6.19: Modules that are connected by tracks through module 1 of layer 6 (a) and module 9 of layer 6 (b). The size of the squares denotes the number of hits in the module: The larger the square, the more hits are measured.

the misalignment parameter uncertainty for the modules. This effect is also reflected in the correlation coefficient $\rho_i = \sqrt{1 - 1/(C^{-1}_{ii} \cdot C_{ii})}$ that defines the correlation of parameter i to all other parameters. In case parameter i is determined for a module that is traversed by many tracks that contain constraint information, ρ_i will be significantly smaller than 1 ($\rho_i = 1$ indicates a 100 % correlation between the parameters).

Modules that are interconnected by cosmic muon tracks are illustrated in Figure 6.19. The 18 bins on the horizontal axis of the figures indicate the 9 modules on the A-side (module 1-9) and the nine modules on the C-side, numbered 10-18. The twelve layers are positioned along the z direction that is given by the vertical axis. The bin (M_i, L_j) of the two dimensional histograms depicts module M_i in layer L_j, with $i = 1 - 18$ and $j = 1 - 12$. The size of the drawn squares indicates the number of hits measured in the corresponding module. The more hits detected, the larger the square.
Figure (a) shows all modules, that are connected by tracks going through module (M_1, L_6), i. e., module 1 of the second layer in station T2. The tracks have a small slope t_x in the xz plane and most tracks traverse the modules (M_1, L_j), where $j = 1 - 12$. Tracks with a larger slope also traverse modules M_2, an insignificant number of tracks travers modules M_3. This track distribution implies that the outermost module is hardly additionally constrained by interconnecting tracks.

Figure (b) shows all modules that are connected via tracks to (M_9, L_6), the module of the A-side which is closest to the beam line. Many tracks with rather large slopes t_x

Table 6.5: Hit distribution for the modules of the second layer in T2. The uncertainty on Δx depends on N_{hit} and the correlation between the modules.

Module	1	2	3	4	5	6	7	8	9
N_{hit}	3332	6012	9144	10268	9392	9868	9328	8536	7424
Correlation ρ	0.94	0.78	0.58	0.52	0.48	0.48	0.51	0.52	0.48
$\sigma_{\Delta x}$ [mm]	0.183	0.072	0.044	0.039	0.040	0.039	0.042	0.044	0.046

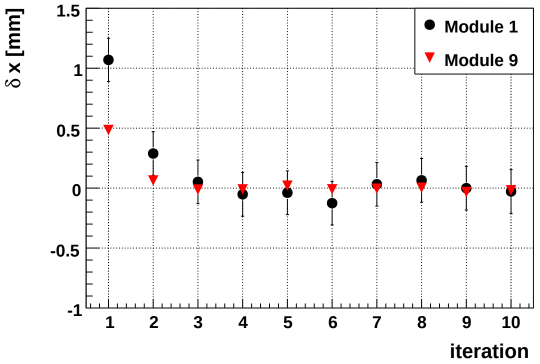

Figure 6.20: An example for the convergence of Δx on the module level. The circles represent module 1, the triangles module 9 of the second layer in T station 2. Error bars for module 9 are inside the drawn points. The different errors are due to a) variations in the number of hits and b) the correlation ρ of the parameters.

traverse this module. This track distribution applies additional constraints to parameters determined in module M_9, reducing the uncertainty and the correlation value ρ_{M_9} of the parameters for this module.

In Table 6.5, the uncertainty and correlation of the misalignment parameters Δx of the nine modules $M_1 - M_9$ of layer L_6 are listed, together with the number of hits N_{hit} measured in the corresponding module. It is evident, that the correlation $\rho_1 - \rho_9$, reduces from module 1 to module 9. The uncertainty σ_i of the misalignment parameter depends on both, the correlation and the number of hits, as the statistical uncertainty is $\propto (N_{hit})^{-\frac{1}{2}}$.

Further, the convergence of the alignment procedure on module level is studied. Figure 6.20 depicts the misalignment parameters Δx_k of module $M_1 - M_9$ of layer L_6 that are determined in an alignment procedure with $k = 10$ iterations. Within the uncertainties, the parameters are stable after the first iteration, as is expected for this degree of freedom. The uncertainties on the parameters for module 9 are much smaller compared to the parameters uncertainties for module 1 and are not visible in the Figure. This is a result of the distribution of interconnecting tracks in the detector, as discussed above.

6.5.2 Module alignment constants

The alignment procedure on module level determines in total 576 misalignment parameters. All 576 misalignment parameters are presented in Appendix D. The results are discussed in detail in the next section in which the misalignment parameters obtained for modules and for half layers are compared.

Figure 6.21 illustrates a subset of all misalignment parameters. It depicts the $8 \cdot 9 = 72$ parameters Δx for the modules in the 8 half layers on the C-side (4 of the 12 half layers on this side are used for the constraints). Each figure comprises 18 parameters for the modules that are mounted on the same C-frame. These modules show a similar pattern and this dependence is observed for all frames. It underlines the result obtained for the alignment of half layers for which an equal shift of neighbouring layers are detected.

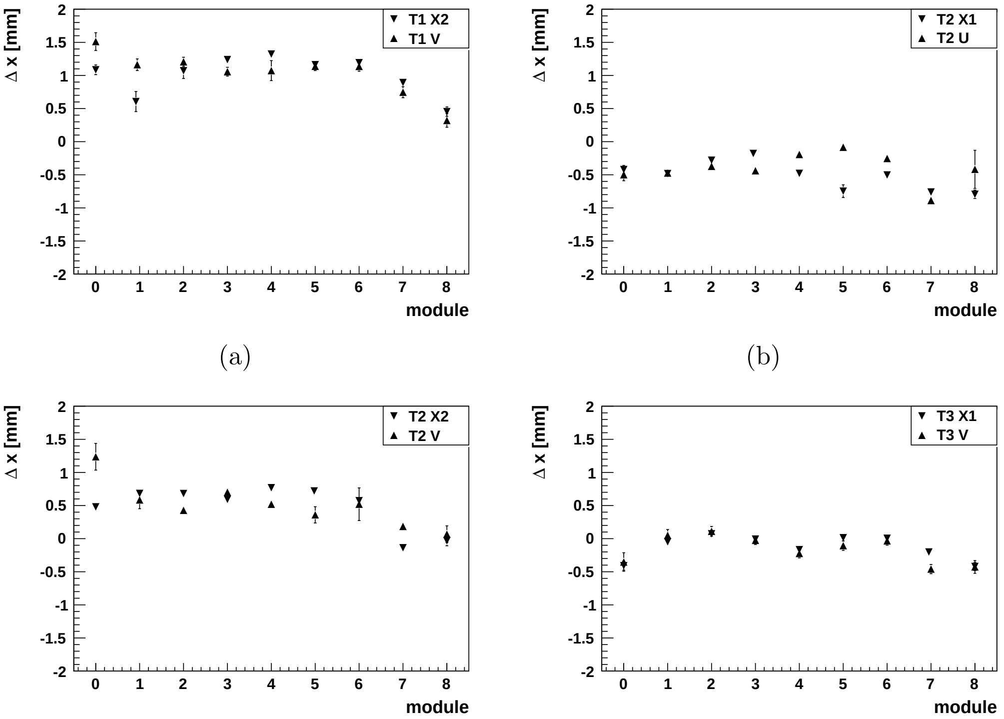

(a) (b)

(c) (d)

Figure 6.21: Corrections Δx on the module level. For each layer, the nine alignment parameters of the corresponding modules are drawn. For layers mounted on the same frame, i. e., the layer combination *vx* and *xu*, the modules parameters show similar pattern.

6.5.3 Comparison of misalignment parameters obtained for modules and for half layers

In this section, the results obtained for the alignment of modules positions are cross ckecked with the results obtained for the alignment of the half layers positions. The mean of the nine module misalignment parameters should be consistent with the parameter of the corresponding half layer. A first order polynomial function is fitted to the misalignment parameters determined for the nine modules of a layer.

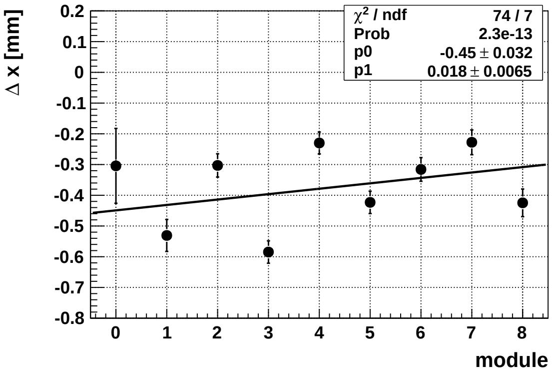

Figure 6.22: Determination of the mean of the module misalignments in one half layer. The fit function value taken at module 4 defines the mean misalignment.

Table 6.6: Comparison between half layer alignment and module alignment, the given values are obtained for the layers and modules on the A-side. The results in column 'module' are gained by a first order polynomial fit to the nine module alignment parameters of a half layer. The alignment results are consistent with each other.

half layer	Δx [mm]		Δz [mm]	
	half layer	module	half layer	module
T1X1	-	-	-	-
T1U	-	-	-	-
T1V	0.8 ± 0.03	$0.78(\pm 0.08)$	-0.57 ± 0.10	$-0.35(\pm 0.26)$
T1X2	0.72 ± 0.02	$0.72(\pm 0.06)$	-0.31 ± 0.06	$-0.10(\pm 0.19)$
T2X1	0.8 ± 0.01	$0.8(\pm 0.04)$	-1.27 ± 0.05	$-1.22(\pm 0.14)$
T2U	0.7 ± 0.02	$0.65(\pm 0.05)$	-0.95 ± 0.05	$-0.83(\pm 0.16)$
T2V	-0.7 ± 0.02	$-0.09(\pm 0.05)$	-3.17 ± 0.08	$-3.11(\pm 0.18)$
T2X2	-0.28 ± 0.01	$-0.28(\pm 0.04)$	-2.84 ± 0.05	$-2.92(\pm 0.14)$
T3X1	-0.36 ± 0.02	$-0.4(\pm 0.04)$	-	-
T3U	-0.08 ± 0.03	$-0.11(\pm 0.07)$	-	-
T3V	-	-	-1.87 ± 0.11	$-1.65(\pm 0.28)$
T3X2	-	-	-1.83 ± 0.06	$-1.73(\pm 0.16)$

Figure 6.22 shows a first order polynomial fit to the Δx shifts of the nine modules of a half layer. The fit function value at module 4 is taken as the mean value. The deviations of the parameters Δx with respect to the fit function indicate the systematic shifts of the module positions.

In Table 6.6, the misalignment parameters Δx and Δz determined for the half layers are listed together with the values determined by a fit to the shifts of the corresponding modules. The uncertainties quoted for the parameters in the column 'half layer' are given by the covariance matrix $\boldsymbol{C}'^{-1}$, Equation 4.19, and represent the statistical uncertainties of the parameters. The uncertainties in column 'module' represent the statistical uncertainty of the fit. They are set in parentheses as the deviations of the parameters from the fit function are caused by systematic effects. A comparison of the values show that the alignment results are fully consistent with each other.

In Table 6.7, the results of the rotational degrees of freedom are compared. The determined parameters $\Delta\alpha$ and $\Delta\gamma$ are in the order of 10^{-4} mrad and 10^{-5} mrad, respectively. Again, comparing the results of the two alignment procedures shows excellent agreement.

A direct comparison between half layer and module results for a rotation around the y axis is excluded: With the module width of just $x \approx 300$ mm, a rotation around y hardly affects the measured track χ^2. However, $\Delta\beta$ of the half layers is verified by a study of the module shifts in z direction. This is possible because the rotation of the whole half layer results in z shifts of the modules, illustrated in Figure 6.23 (a). Once the

Table 6.7: Comparison between half layer alignment and module alignment. Given are the results for the rotational degrees of freedom.
*The determination of $\Delta\beta$ on the module level is not possible, the given numbers are deduced from the modules z shifts, see text.

Half layer	$\Delta\alpha\ 10^{-4}$[rad]		$\Delta\gamma\ 10^{-5}$[rad]		$\Delta\beta\ 10^{-4}$[rad]	
	half layer	module	half layer	module	half layer	module*
T1X1	-	-	-	-	-	-
T1U	-	-	-	-	-	-
T1V	−2.1±0.6	−1.2(±1.7)	−1.82±1.9	1.05(±5)	2.0±1.1	1.7(±1.5)
T1X2	−2.9±0.4	−2.7(±1.3)	−1.3±1.15	2.3(±4)	-1.3±0.7	-3.2(±1.1)
T2X1	2.2±0.4	2.9(±1.1)	−20.3±1.1	−19(±3)	-7.8±0.6	-6.6(±0.8)
T2U	0.5±0.4	−0.01(±1.4)	−19.6±1.4	−17.7(±3.9)	-6.2±0.6	-9.7(±1.0)
T2V	−0.4±0.5	0.7(±1.4)	−5.9±1.5	−4.1(±3.8)	-6.7±0.9	-4.2(±1.0)
T2X2	1.1±0.4	0.1(±1.2)	−4.4±1.2	−3.3(±3.1)	-3.5±0.6	-3(±0.8)
T3X1	−0.7±0.5	−0.6(±1.4)	−6.8±1.4	−7.0(±3.8)	-	-
T3U	−2.7±0.8	−2.9(±2.3)	−9.2±2.4	−8.1(±6.5)	-	-
T3V	-	-	-	-	-11.5±1.2	-8.7(±1.5)
T3X2	-	-	-	-	-6.0±0.7	-4.5(±0.9)

misalignment Δz for the modules are determined, the y rotation of the corresponding half layer is calculated by $\sin\beta = \frac{\delta z}{L}$. Here, δz is the difference of the z positions of module 1 and module 9 and L the half layer width. For comparison, the calculated and the measured y rotations are shown in Figure 6.23 (b). The good match between the values confirms the reliability of the algorithm on the module level. Furthermore, the agreement demonstrates the robustness of the alignment algorithm, i. e., misalignments also in the z direction in the order of $\mathcal{O}(\,\mathrm{mm})$ can be resolved directly on the module level.

Improvement of track parameters

The successful alignment improves the track reconstruction, best seen by the mean of the track residuals. Figure 6.24 (a) shows the mean of the residuals for each of the 216 modules before (dashed lines) and after (solid lines) the alignment of the modules positions. The alignment improves the RMS of the distribution to

$$RMS = 0.042 \pm 0.002\,\mathrm{mm} \tag{6.3}$$

and thus enhances the result of the half layer alignment of $RMS = 129 \pm 0.006\,\mathrm{mm}$ significantly. Figure (b) shows the mean of residuals in every module with respect to

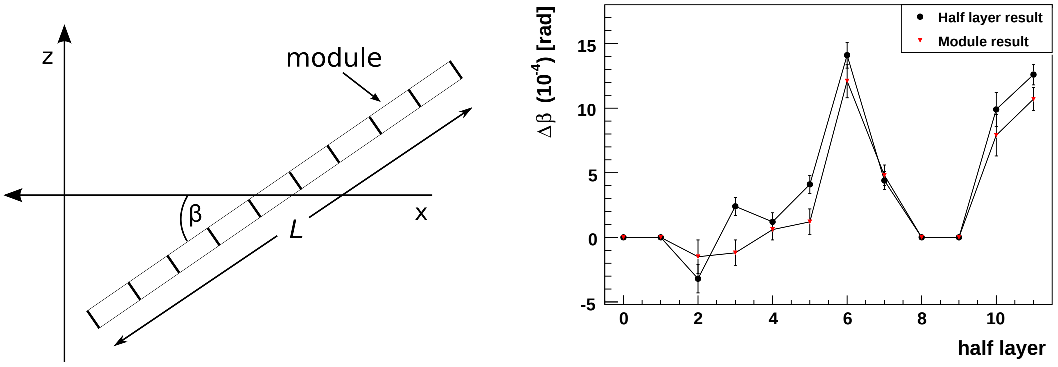

(a) (b)

Figure 6.23: (a) Sketched is a half layer rotation around y. This leads to Δz shifts of the modules of the half layer. (b) Parameter $\Delta\beta$ for the half layers on the C-side, obtained by half layer alignment (points) and calculated by the Δz shifts of the modules obtained by module alignment (triangles).

the module number[5]. The modules are numbered from $0 - 216$ beginning from the outermost module of the first layer in the first station on the C-side. The error bars indicate the RMS of the corresponding residual distribution. Their size is related to the number of hits measured in the module. A scattering is evident for module number $0 - 36$ and $179 - 215$. These modules are fixed in the alignment procedure in order to constrain the system of equation, hence for them no corrections $\mathbf{\Delta a}$ are determined. An improvement of the measured mean of residuals for these modules is solely induced by the correction of the remaining modules. Therefore a larger scattering at the fixed

---

[5] The module number n is determined by $n = T * 72 + L * 18 + S * 9 + M$, where $T = 0, 1, 2$ indicates the T station of the module, $L = 0, 1, 2, 3$ the layer, $S = 0, 1$ the C-side (0) or A-side (1) and $M = 0 - 8$ the module.

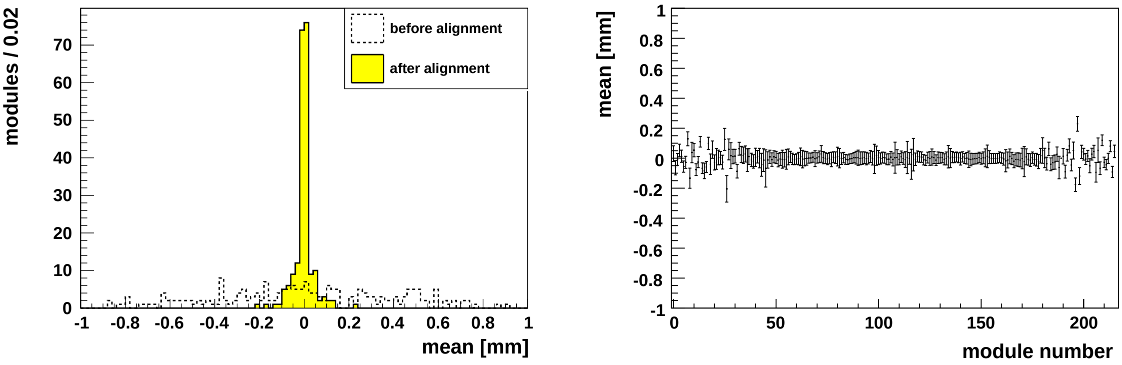

(a) (b)

Figure 6.24: (a) The mean of the track residuals for each of the 216 modules before (dashed) and after (alignment). (b) Mean of the rack residual versus the module number. The scattering at module number 0-36 and 179-215 are due to constraints applied to the modules.

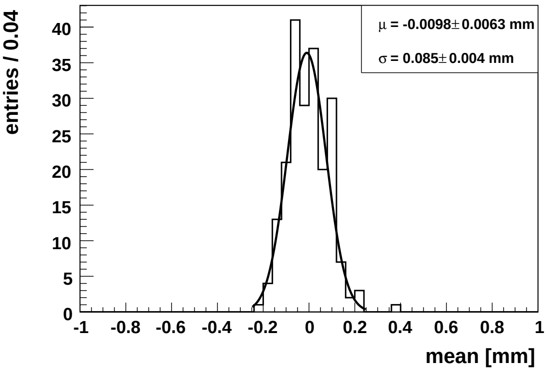

Figure 6.25: The means of the track residuals measured for every modul. The width $\Delta = 90\,\mu$m of the distribution indicates the reproducibility of the misalignment parameters, see text.

positions is expected.

The mean of the residuals for the fixed modules could be improved if these modules are now left floating, while a conveniently chosen subset of the already aligned modules can be fixed to constrain the problem. Misalignment parameters for the previously fixed modules can be obtained. Possible correlations must are taken into account by iterating this procedure.

6.5.4 Reproducibility of misalignment parameters

In order to measure the alignment accuracy, the used muon track sample is split into two, to get statistically uncorrelated samples. One half is used for the determination of the alignment constants on module level. Then, the tracks of the second sample are reconstructed considering the corrections of the determined misalignments. The so gained alignment accuracy, defined as the width of the distribution of the mean of residuals measured for each module (Figure 6.25), is

$$\Delta = 0.085 \pm 0.004\,\text{mm}\ . \tag{6.4}$$

This is well below the hit resolution of 0.2 mm per cell. With only 10000 tracks, the developed algorithm is capable of determining the misalignment constants with very high precision.

Systematic effects in the alignment procedure

The track based alignment algorithm exploits that misalignments change the residual between a hit and the reconstructed track. Misalignment parameters $\mathbf{\Delta a}$ of a detector element are determined from the hit residuals of many tracks in the element. The finally obtained parameters reflect a mean value of the measured residuals and indicate shifts and rotations of the element which is considered as a rigid body.

The approach does not allow to resolve systematic effects in the alignment procedure that can occur due to deformations of the detector elements. In case of the Outer Tracker, a deformation could be a twist of a module around its y axis, a bending of the

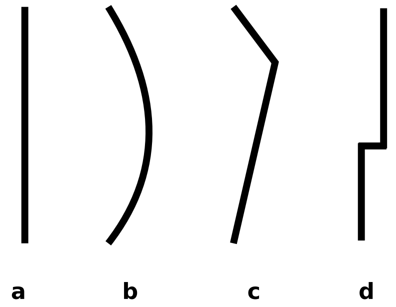

Figure 6.26: Sketch of internal deformations. Line **a** represents the ideal form of the element. Deformations of this line are shown in **b,c,d**. A detection of such deformations depends on the detector element level on which the alignment is processed, see text.

module and many other effects that are incompatible with the assumption of a stiff element, Figure 6.26.

Some deformations, like the bending of a module (b in the Figure) can be estimated by splitting the available track sample into tracks, that traverse only certain areas of the module. In case the misalignment parameters determined for the various areas differ significantly, this can be an indication of a deformation. A possible influence of the track selection on the alignment results must be considered, as the determination of parameters depend among others on the track slopes.

Such studies require a large number of tracks that are homogeneous distributed over the detector elements.

6.6 Conclusion

The collected cosmic muon sample is used for the first alignment of the LHC*b* Outer Tracker. It is the very first data triggered and measured with the large area detectors, i. e., ECal, Muon stations and T stations. The trajectories of cosmic muons differ significantly from tracks emerging in proton-proton collisions. The pattern recognition has been modified for the cosmic muon measurements, the track fit results are as expected from simulations. However, large hit cluster sizes are observed in the Outer Tracker. The impact of the hit cluster size on the alignment results has been discussed, it is prevented by refining track selection criteria for the alignment algorithm.

Results for the Outer Tracker alignment with 20 000 cosmic muon tracks have been presented for all degrees of freedom. The reliability of the algorithm is demonstrated by the consistent outcome of alignment procedures for half layers and modules. Determined alignment parameters are consistent with survey measurements and improve the track parameters significantly. After alignment of the module positions, the means of residuals measured for every module are centered at zero. Additional, with only 10 000 tracks the misalignment parameters can be reproduced with an accuracy of about 90 μm.

With the first measured data, the reliability of the developed alignment algorithm is demonstrated successfully.

Chapter 7

Summary and conclusion

A software alignment algorithm to determine the precise position of the LHC*b* Outer Tracker detector elements has been developed and is described in this thesis. The algorithm is based on the reconstruction of tracks and exploits that detector misalignments influence the residual between a measured hit and the reconstructed track. Different granularities of the detector components are considered by the algorithm and correlations between all detector elements are taken into account.
The presented Outer Tracker alignment procedure is an *internal* alignment procedure: All information used are contained in the residuals of tracks that are reconstructed in the Outer Tracker stations. Geometrical transformations like an overall shift or rotation of the detector leave the track residuals unchanged and have to be constrained. Two different methods to constrain these transformations have been implemented in the algorithm. A comparison of the methods shows equivalent results in the determined position of the detector elements.

In a detailed validation procedure, the algorithm has been tested with simulated data for different levels of detector segmentation. Several misaligned detector geometries have been generated and used as input to the track reconstruction and alignment procedure. Simulated translations and rotations of the half layers have been reconstructed with high statistical precision by using about 260 000 tracks for the alignment process:

$$\begin{aligned} \sigma_{\Delta x} &\approx 0.02\,\mathrm{mm}\,, & \sigma_{\Delta\alpha} &\approx 0.07\,\mathrm{mrad}\,, \\ \sigma_{\Delta z} &\approx 0.20\,\mathrm{mm}\,, & \sigma_{\Delta\beta} &\approx 0.11\,\mathrm{mrad}\,, \\ & & \sigma_{\Delta\gamma} &\approx 0.02\,\mathrm{mrad}\,. \end{aligned}$$

It has been shown that residual misalignments of the Outer Tracker half layers of $\sigma_x < 150\,\mu\mathrm{m}$ and $\sigma_z < 300\,\mu\mathrm{m}$ in x and z direction and rotations $\sigma_{rot} < 0.45\,\mathrm{mrad}$ do not decrease the track reconstruction performance in a significant way. The statistical precision achieved with the presented alignment procedure is well below this limit.

Cosmic ray events have been collected during the commissioning of the detector. The events have been analysed and used for the spatial alignment of the Outer Tracker half layers and modules. The data sample has been split into two statistically independent samples to study the reproducibility of the determined misalignment parameters for

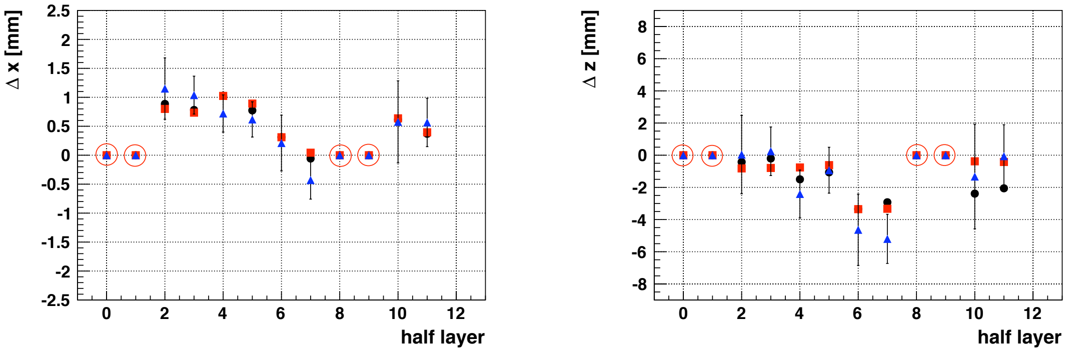

(a) (b)

Figure 7.1: Half layer misalignment parameters determined with three different data sets. Black points: Cosmic ray events measured in 2008. Red squares: Cosmic ray events collected in 2009. Blue triangles: First proton-proton collisions at $\sqrt{s} = 900\,\mathrm{MeV}$. Open circles indicate the parameters used to constrain the undefined degrees of freedom.

the 216 modules. The reproducibility is expressed in the width Δ of the distribution of the mean of track residuals obtained for the individual modules. With only 10 000 tracks the module positions have been determined within

$$\Delta = 0.085 \pm 0.004\,\mathrm{mm}\ . \tag{7.1}$$

The presented results of the alignment procedure are the first results for the spatial alignment of the Outer Tracker.

In November 2009, a commissioning run of the LHC provided proton-proton collisions at a center-of-mass energy of $\sqrt{s} = 900\,\mathrm{MeV}$. Figure 7.1 shows the determined misalignment parameters Δx and Δz for the Outer Tracker half layers of the A-side (the results for the C-side look similar). Depicted are parameters obtained with three different data sets: Cosmic ray events measured in 2008 (black points) and 2009 (red squares) and the collision data from 2009 (blue triangles). All data have been taken without magnetic field in the detector. The uncertainties of the parameters determined with tracks from the collision data are dominated by statistical uncertainties - the corresponding track sample was very small. The parameters uncertainties from the alignment with cosmic ray muons are too small to be visible in the figures. The distribution of tracks from cosmic ray events and from collision data differ significantly. For a comparison of the determined misalignment constants, the track distributions have to be similar to each other. The results show excellent agreement.
For the alignment of individual modules using proton-proton data, a larger track sample without magnetic field is necessary. Currently the usage of collision data taken with magnetic field is studied.

The track based alignment algorithm developed in the course of this thesis has demonstrated its functionality and stability. The algorithm is and will be used to determine the internal misalignment constants of the modules of the LHC*b* Outer Tracker detector.

Appendix A

Global derivatives

In the following the global derivatives are calculated [89]. The derivatives indicate the change of the residual $\boldsymbol{r}$ between a measurement $\boldsymbol{m} = (x, y)$ and the reconstructed track $\boldsymbol{t}$ with respect to the geometry parameters $\mathbf{a} = \mathbf{a_{nom}} + \boldsymbol{\Delta}\mathbf{a}$, where $\mathbf{a_{nom}}$ indicates the nominal detector position and $\boldsymbol{\Delta}\mathbf{a}$ are misalignments. As only misalignments $\boldsymbol{\Delta}\mathbf{a}$ influence this residual, the derivative can be written as

$$\frac{\partial \boldsymbol{r}}{\partial \boldsymbol{\Delta}\mathbf{a}} = \frac{\partial \boldsymbol{r}}{\partial \mathbf{a}} = \frac{\partial \boldsymbol{t}(\mathbf{a})}{\partial \mathbf{a}} - \frac{\partial \boldsymbol{m}(\mathbf{a})}{\partial \mathbf{a}}\,, \tag{A.1}$$

where $\boldsymbol{m}(\mathbf{a})$ indicates a measurement in the global coordinate system. These measurements are influenced by shifts and rotations of the local measurement $\boldsymbol{m}'$ according to

$$\boldsymbol{\Delta m} = \boldsymbol{\Delta \Omega m}' + \boldsymbol{\Delta T}\,, \tag{A.2}$$

where $\boldsymbol{\Delta T}$ are translations and $\boldsymbol{\Delta \Omega}$ are rotations according to Equation 4.26 and Equation **??** with the substitution $\alpha \to \Delta\alpha$, $\beta \to \Delta\beta$ and $\gamma \to \Delta\gamma$. The misalignments are assumed to be very small, thus the approximation $\sin a \to a$ and $\cos a \to 1$ are valid and the the derivatives of the rotation matrix are

$$\frac{\partial \boldsymbol{\Delta \Omega}}{\partial \Delta\alpha} = \begin{pmatrix} 0 & 0 & 0 \\ 0 & 0 & -1 \\ 0 & 1 & 0 \end{pmatrix}, \frac{\partial \boldsymbol{\Delta \Omega}}{\partial \Delta\beta} = \begin{pmatrix} 0 & 0 & 1 \\ 0 & 0 & 0 \\ -1 & 0 & 0 \end{pmatrix}, \frac{\partial \boldsymbol{\Delta \Omega}}{\partial \Delta\gamma} = \begin{pmatrix} 0 & -1 & 0 \\ 1 & 0 & 0 \\ 0 & 0 & 0 \end{pmatrix}. \tag{A.3}$$

The derivatives for $\boldsymbol{\Delta m}$ with respect to the parameters $\boldsymbol{\Delta}\mathbf{a}$ are

$$\frac{\partial \boldsymbol{\Delta m}}{\partial \boldsymbol{\Delta}\mathbf{a}} = (1 \quad \frac{\partial \boldsymbol{\Delta \Omega}}{\partial \Delta\alpha}\boldsymbol{m}' \quad \frac{\partial \boldsymbol{\Delta \Omega}}{\partial \Delta\beta}\boldsymbol{m}' \quad \frac{\partial \boldsymbol{\Delta \Omega}}{\partial \Delta\gamma}\boldsymbol{m}') = \begin{pmatrix} 1 & 0 & 0 & 0 & 0 & -y \\ 0 & 1 & 0 & 0 & 0 & x \\ 0 & 0 & 1 & y & -x & 0 \end{pmatrix}. \tag{A.4}$$

Further it is necessary to calculate the derivative of the predicted hit $\partial \boldsymbol{t}/\partial \mathbf{a} = \partial \boldsymbol{t}/\partial \boldsymbol{\Delta}\mathbf{a}$ with respect to the parameters $\boldsymbol{\Delta}\mathbf{a}$. The predicted hit is the propagation of the track to the sensor surface. Only a shift of the sensor in Δz will change the penetration point of the track on the sensor plane. The movement of the sensor plane is equivalent to the movement of the hit. Therefore $\partial\boldsymbol{t}/\partial\boldsymbol{\Delta}\mathbf{a}$ can be written as

$$\frac{\partial\boldsymbol{t}}{\partial\boldsymbol{\Delta}\mathbf{a}} = \frac{\partial\boldsymbol{t}}{\partial\boldsymbol{\Delta m}}\frac{\partial\boldsymbol{\Delta m}}{\partial\boldsymbol{\Delta}\mathbf{a}} = \begin{pmatrix} 0 & 0 & t_x \\ 0 & 0 & t_y \\ 0 & 0 & 1 \end{pmatrix} \frac{\partial\boldsymbol{\Delta m}}{\partial\boldsymbol{\Delta}\mathbf{a}} = \begin{pmatrix} 0 & 0 & t_x & yt_x & -xt_x & 0 \\ 0 & 0 & t_y & yt_y & -xt_y & 0 \\ 0 & 0 & 1 & y & -x & 0 \end{pmatrix} \tag{A.5}$$

where t_x and t_y are the tangents of the trajetory at the penetration point. Thus the derivative of the difference between predicted and measured position becomes

$$\frac{\partial\boldsymbol{r}}{\partial\boldsymbol{\Delta}\mathbf{a}} = \frac{\partial\boldsymbol{t}}{\partial\boldsymbol{\Delta}\mathbf{a}} - \frac{\partial\boldsymbol{\Delta m}}{\partial\boldsymbol{\Delta}\mathbf{a}} = \begin{pmatrix} -1 & 0 & t_x & yt_x & -xt_y & y \\ 0 & -1 & t_y & yt_y & -xt_y & -x \\ 0 & 0 & 0 & 0 & 0 & 0 \end{pmatrix} . \tag{A.6}$$

In Equation 4.13, only the prediction function $h(\mathbf{a}, \boldsymbol{\Delta}\mathbf{a})$ depends on the geometry parameters and the measurement is assumed to be in the local frame of the sensor. Therefore the residual is

$$\boldsymbol{r} = \boldsymbol{t}(\mathbf{a}) - \boldsymbol{m}(\mathbf{a}) = \mathbf{h}(\mathbf{a}, \boldsymbol{\Delta}\mathbf{a}) - \boldsymbol{m}' , \tag{A.7}$$

and thus

$$\frac{\partial\boldsymbol{r}}{\partial\boldsymbol{\Delta}\mathbf{a}} = \frac{\partial\mathbf{h}(\mathbf{a}, \boldsymbol{\Delta}\mathbf{a})}{\partial\boldsymbol{\Delta}\mathbf{a}} = \frac{\partial\mathbf{h}(\mathbf{a}, \boldsymbol{\Delta}\mathbf{a})}{\partial\mathbf{a}} . \tag{A.8}$$

Appendix B

Parameters transformation for Lagrange Multiplier method

Presented are parameters transformations for applied misalignments δx and δz. A detailed description for the transformations of all degrees of freedom can be found at [90].

Examining shifts in the x and z direction the net translation of the input misalignment are calculated to

$$\begin{aligned} D_x^{net} &= <\delta x_i> \;, & \text{(B.1)} \\ D_z^{net} &= <\delta z_i> \;, & \text{(B.2)} \end{aligned}$$

where δx_i and δz_i are the shifts of layer i. The net shearing for x is

$$S_{xz}^{net} = \frac{<\delta x_i(z_i - \overline{z})>}{<(z_i - \overline{z})^2>} \;, \tag{B.3}$$

with the coordinate z_i of layer i and the mean z position of all layers given by $\overline{z}$. The net rescaling in z gives

$$C_z^{net} = \frac{<\delta z_i(z_i - \overline{z})>}{<(z_i - \overline{z})^2>} \;. \tag{B.4}$$

The applied displacements are transformed according to the net translation, shearing and scaling as follows:

$$\begin{aligned} \delta x_i' &= \delta x_i - <\delta x_i> - S_{xz}^{net}(z_i - \overline{z}) \;, & \text{(B.5)} \\ \delta z_i' &= \delta z_i - <\delta z_i> - C_z^{net}(z_i - \overline{z}) \;. & \text{(B.6)} \\ & & \text{(B.7)} \end{aligned}$$

The transformed parameters $\delta x_i'$ and $\delta z_i'$ are then comparable with the determined misalignment parameters Δx and Δz.

Appendix C

Pattern recognition for cosmic muon tracks

Cosmic muon tracks are reconstructed using PatSeeding [83] pattern recognition algorithm. The pattern recognition algorithm configured for cosmic muon tracks accounts neither for a magnetic field nor for possible constraints imposed by the proton-proton interaction point. The fit method and the hit search in the xz and yz planes are outlined.

The fit method

The fit of a track is separated into two distinct fits regarding for tracks in the xz and in the yz plane. The particle trajectory is described by a straight line in x and y direction as the data are collected without magnetic field

$$x(z) = a + b(z - z_{ref}) \,, \tag{C.1}$$

$$y(z) = a_y + b_y(z - z_{ref}) \,, \tag{C.2}$$

with the track parameters a, b, a_y and b_y to be determined. To numerically stabilize the fit, z is shifted by z_{ref} which, by default, is set to the center of the T stations. Each track is fitted up to ten times in x and y direction, after each iteration step the hit coordinates are updated. This is due to the fact that the T stations are rotated: A change of track parameters results in shifts in x because of the stereo angles and in z due to the tilt of the T station coordinate system with respect to the LHCb one. The χ^2 to minimize is

$$\chi^2 = \sum_i \frac{1}{\sigma_i^2} \left(\frac{x_i - x_{track}(z_i)}{\cos(\alpha)} \right)^2 \,, \tag{C.3}$$

where i denotes the i^{th} hit of the track and $x_i(z_i)$ its x coordinate at $y(z_i)$, σ_i is the hit uncertainty. Dividing the distance in x between wire and track by a factor $\cos\alpha = (1 + b^2)^{-\frac{1}{2}}$, the distance of closest approach d between track and wire is determined. The expression is similar for the fit in the yz plane, the residual $x_i - x_{track}$ is divided by an additional factor $-\tan(\gamma_i)$ necessary to project the x into a y distance (γ_i is the stereo angle of the i^{th} layer). The iteration is finalized before the tenth iteration if the change of the track parameters is smaller than

$$\begin{aligned} |\Delta a| &< 5 \cdot 10^{-3} & \qquad |\Delta a_y| &< 5 \cdot 10^{-2} \\ |\Delta b| &< 5 \cdot 10^{-6} & \qquad |\Delta b_y| &< 5 \cdot 10^{-5} \ , \end{aligned}$$

which shows that the fit has converged. Since no drift time information is used for the fit, solving for the left-right ambiguity is precluded. The χ^2 is calculated again after the iterative fit and in case a fitted hit contributes to the χ^2 with a value greater than a specified threshold, it is removed as an outlier and the fitting procedure for the track is repeated.

Track search in two projection planes

In the xz plane, two hits in the x layers of station T1 and T3 are selected and connected to a straight line, the remaining hits in the x layers lying inside a window around the line are counted. Every combination of two hits forming a line is tried and the combination giving the largest number of hits inside the window is taken as a track candidate.

To fit the candidate as discussed above, each hit is assigned a weight $w = \frac{1}{\sigma}$ with the hit uncertainty $\sigma = \frac{5\text{mm}}{\sqrt{12}}$, defined by the pitch of the straw tubes, neglecting drift time information. The track is stored if the fit has converged and fulfills requirements to the track quality, e.g. the χ^2 is below a selected maximum χ^2_{max}.

The collected track in the xz plane is then used to search for hits in y by first projecting the stereo hits into the xz plane. Hits are collected inside a window around the track candidate if they fulfill the following requirement

$$y_{min} \tan(\gamma) - d < x_{hit} - x_{track} < y_{max} \tan(\gamma) + d \ , \tag{C.4}$$

with d the size of the search window. In this relation, γ denotes the stereo angle, y_{min} and y_{max} are the terminations of the straw in y, x_{hit} is the coordinate of the hit in the stereo layer at $y = 0$ and x_{track} is the calculated coordinate of the track candidate at z of the stereo layer. Second, the collected hits are combined to pairs defining a straight line and stereo hits inside a window around this line are counted. Again, the pair with the largest number of hits around the line is supposed to give the best track candidate in y which is then fitted to remove possible outliers.

All hits forming a seed for the possible track are solely searched for in the OT and not in the IT. This is because it is unlikely that more than one IT station will be hit by a cosmic particle because of their steep incident angle.

Appendix D

Module misalignment parameters determined with cosmic ray data

The following figures show the 576 module misalignment parameters determined with data from cosmic ray events.

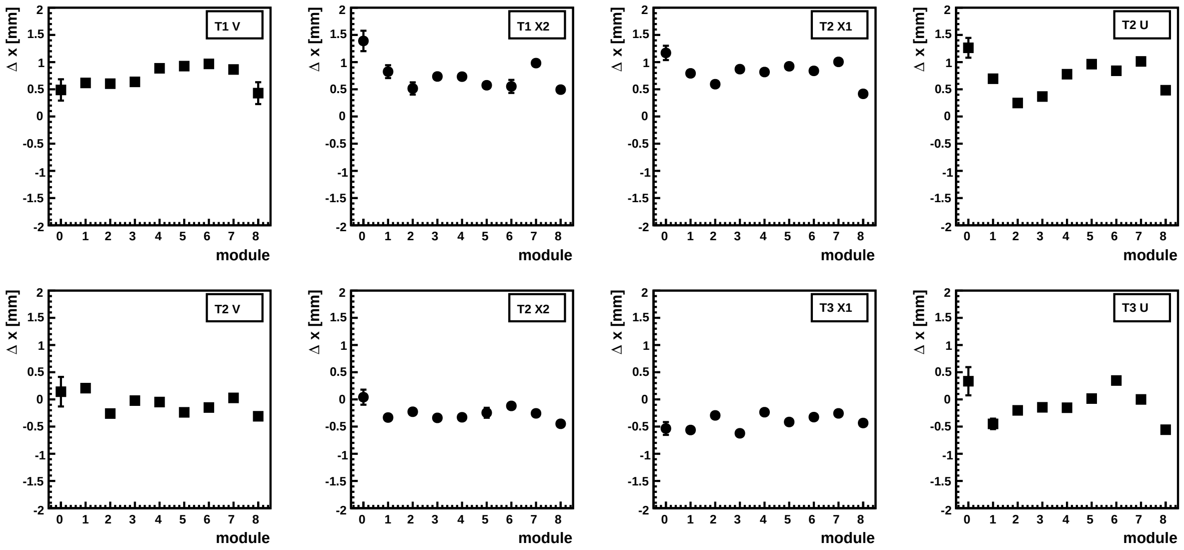

Figure D.1: Misalignment parameter Δx for the A-side

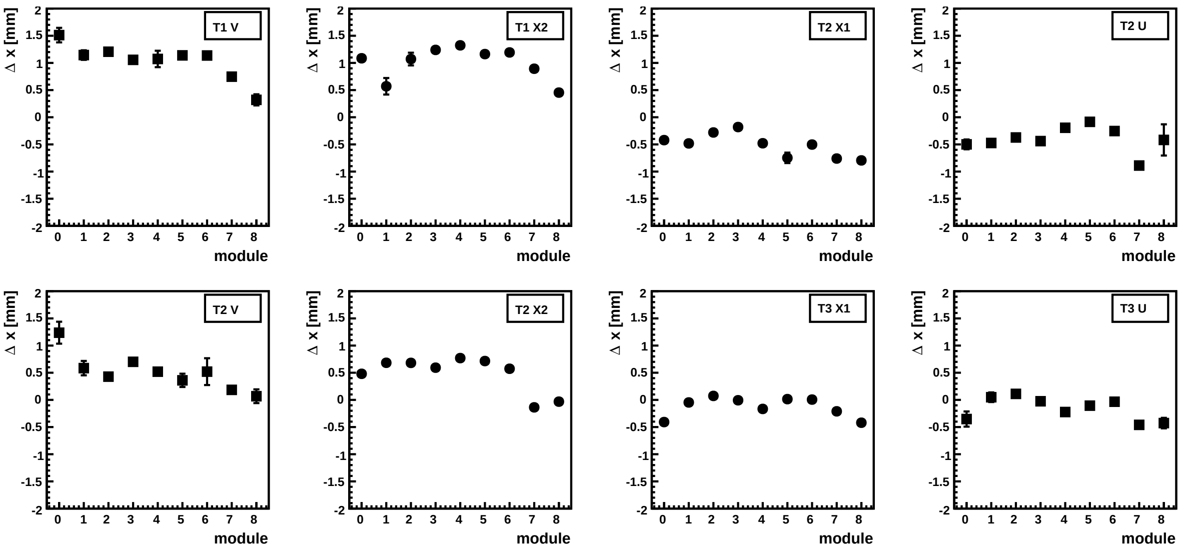

Figure D.2: Misalignment parameter Δx for C-side

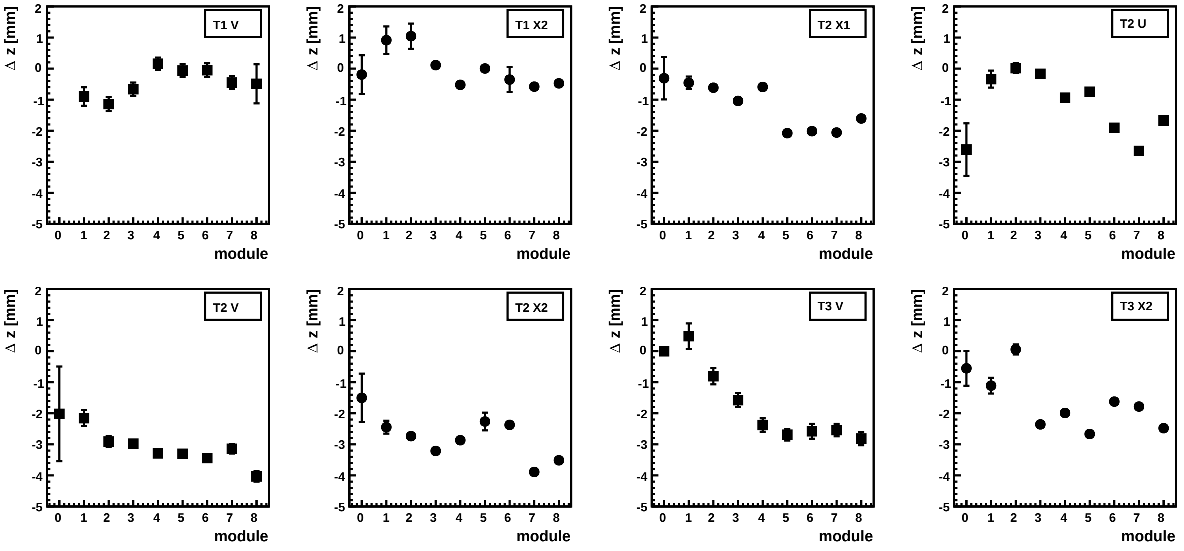

Figure D.3: Misalignment parameter Δz for the A-side

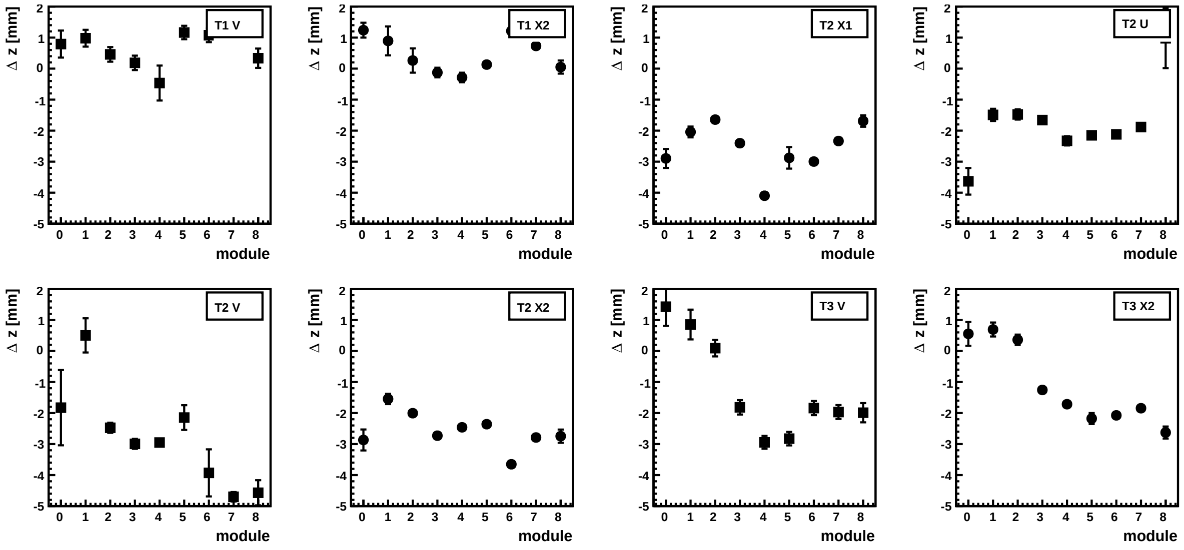

Figure D.4: Misalignment parameter Δz for C-side

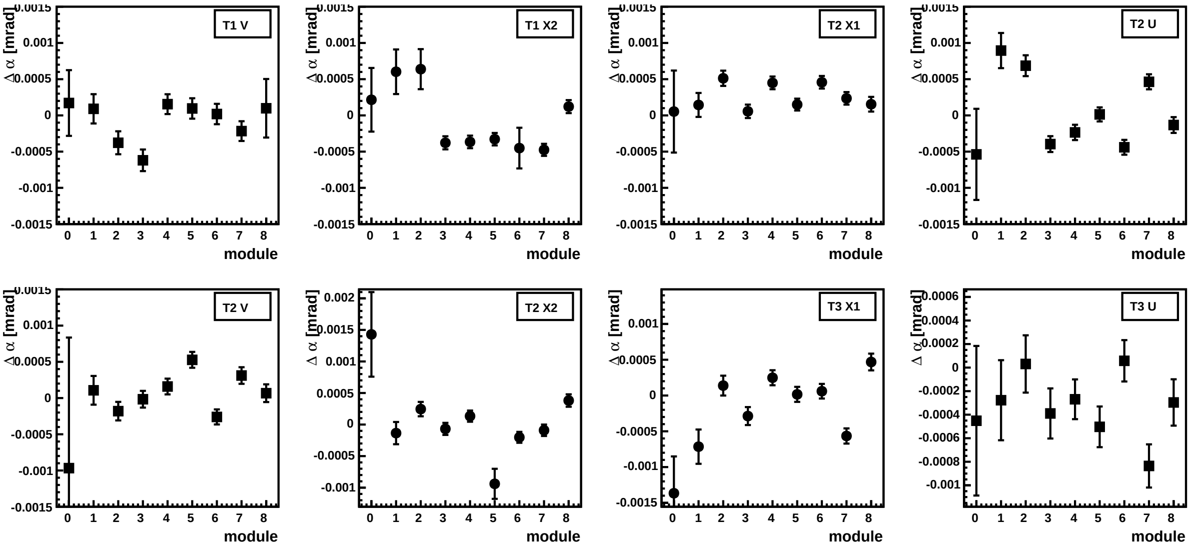

Figure D.5: Misalignment parameter $\Delta\alpha$ for the A-side

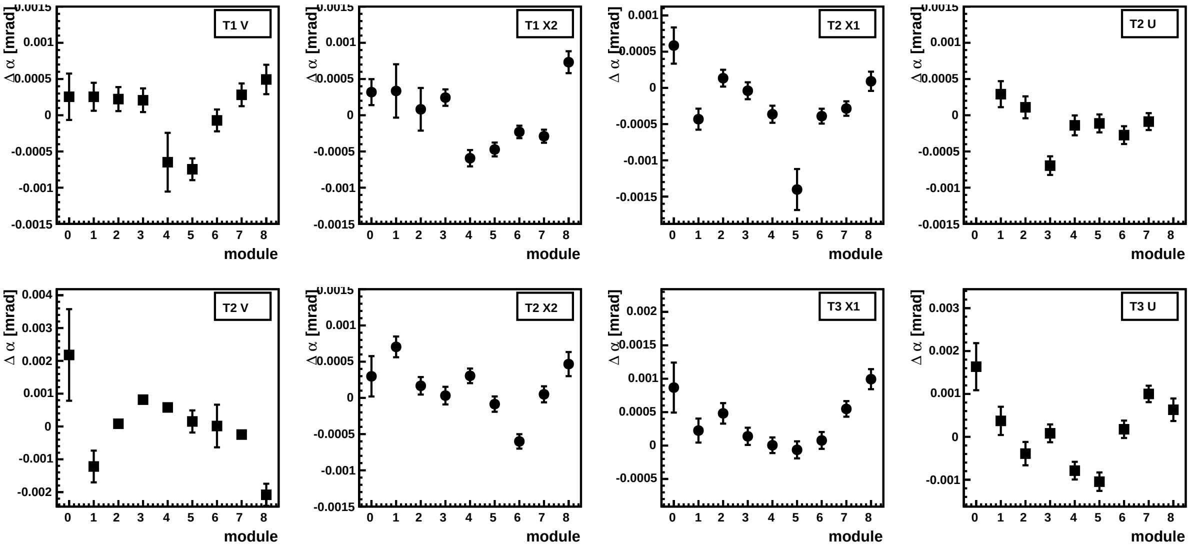
T1 V
T1 X2
T2 X1
T2 U
T2 V
T2 X2
T3 X1
T3 U

Figure D.6: Misalignment parameter $\Delta\alpha$ for C-side

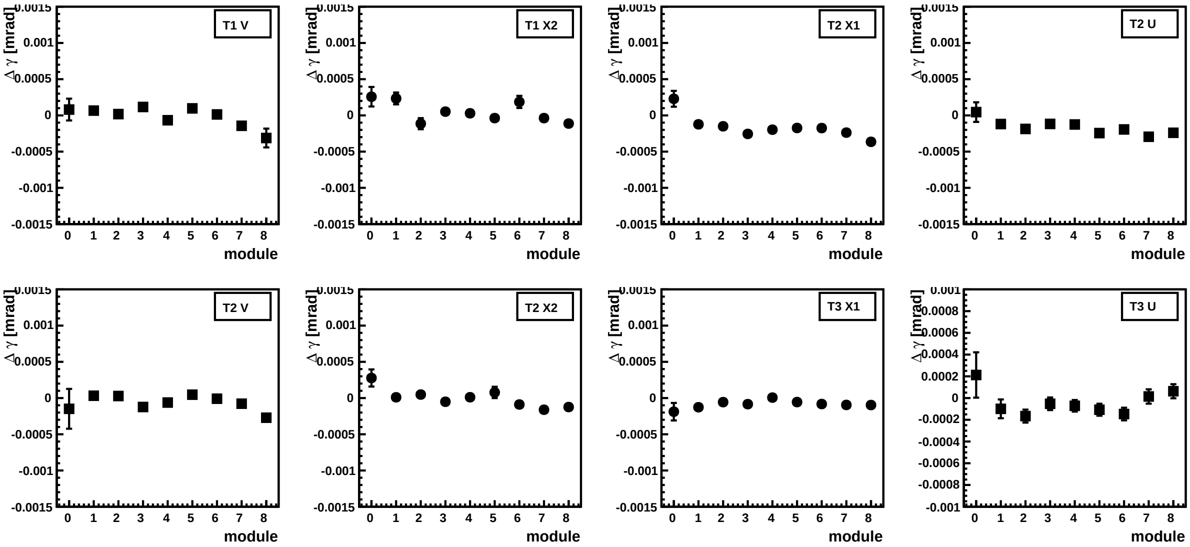
T1 V
T1 X2
T2 X1
T2 U
T2 V
T2 X2
T3 X1
T3 U

Figure D.7: Misalignment parameter $\Delta\gamma$ for the A-side

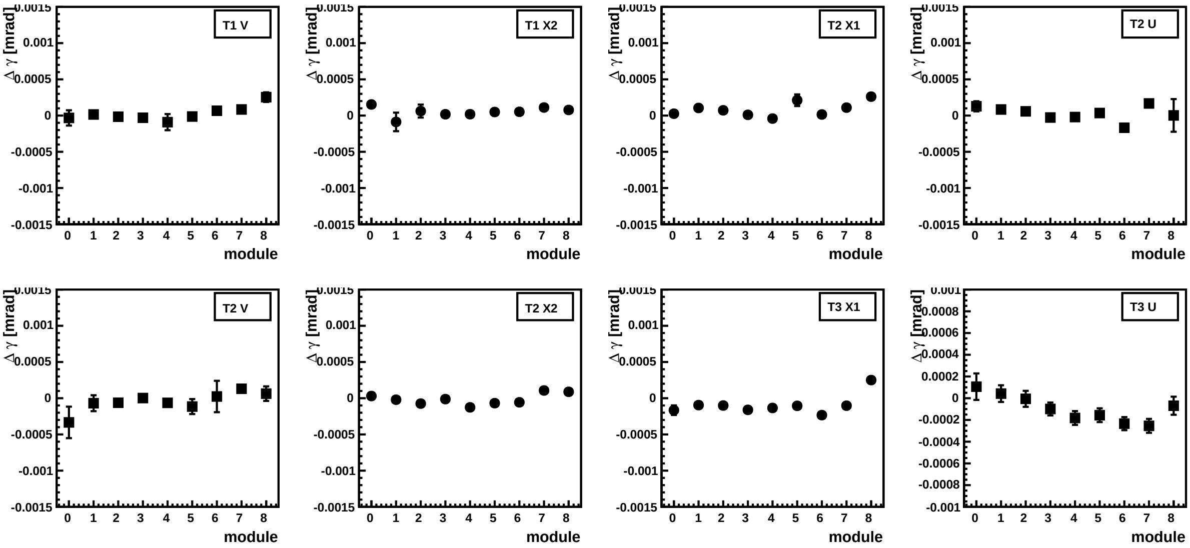

Figure D.8: Misalignment parameter $\Delta\gamma$ for C-side

List of Figures

List of Tables

Bibliography

[1] Glashow, S. *Nucl. Phys.* **22** , 579 (1961).

[2] Salam, A. and Ward, J. C. *Phys. Lett.* **13** , 168 (1964).

[3] Weinberg, S. *Phys. Rev. Lett.* **19** , 1264 (1967).

[4] Lyndon Evans and Philip Bryant (editors). *LHC Machine.* 2008 JINST **3** S08001.

[5] The LHCb Collaboration, A. Augusto Alves Jr et al. *The LHCb Detector at the LHC.* 2008 JINST **3** S08005.

[6] Yosef Nir. *CP Violation in Meson Decays.* arXiv:hep-ph/0510413v1, (2005).

[7] Yosef Nir. *Probing new physics with flavor physics (and probing flavor physics with new physics).* arXiv:hep-ph/0708.1872, (2007).

[8] V. Blobel, C. K. *A new method for high-precision alignment of track detectors.* hep-ex/0208021, (2002).

[9] Halzen, F. and Martin, A. D. *Quarks and Leptons: An Introductory Course in Modern Particle Physics.* John Wiley & Sons Inc., (1984).

[10] Nachtmann, O. *Phänomene und Konzepte der Elementarteilchenphysik.* Friedr. Vieweg & Sohn, (1986).

[11] Perkins, D. H. *Introduction to High Energy Physics.* Cambridge University Press, 4th edition, (2000).

[12] Yao, W.-M. et al. *J. Phys.* **G33** , 1–1232 (2006).

[13] Amsler, C. et al. *Physics Letters B 667* , 1–1232 (2008).

[14] J. Van Tilburg. *Track simulation and reconstruction in LHCb.* CERN-THESIS-2005-020, (2005).

[15] CKMfitter group, J. Charles et al. *updated results and plots available at: http://ckmfitter.in2p3.fr.* Eur. Phys. J. C41, 1-131, hep-ph/0406184, (2009).

[16] Jarlskog, C. *Commutator of the quark mass matices in hte standard electroweak model and a measure of maximal CP violation.* Phys.Rev.Lett. **55** 1039, (1985).

[17] ARGUS collaboration, H. Albrecht et al. *Observation of B^0 - $\overline{B}^0$ mixing.* Phys.Lett **B192** 245, (1987).

[18] S.L. Glashow, J. I. and Maiani, L. *Phys. Rev.* ***D2*** , 1285 (1970).

[19] A. Lenz. *Theoretical status of B_s-mixing and lifetimes of heavy hadrons.* arXiv:0705.3802v2 [hep-ph], (2007).

[20] Christenson, J. H. et al. *Phys. Rev. Lett.* **13**, 138 (1964).

[21] Belle collaboration, K. A. e. *Improved measurement of direct CP violation in $B \to K^+\pi^-$.* Belle-Conf-0523, (2005).

[22] BaBar collaboration, B. A. e. *Direct CP violation asymmetry in $B \to K^+\pi^-$.* Phys.Rev.Lett. **93, 131801**, (2004).

[23] Albrecht, J. et al. *Road map for the measurement of mixing induced CP violation in* $\mathrm{B_s} \to \mathrm{J}/\psi\phi$ *at LHCb.* LHCb/ROADMAP3-001, (March 2009).

[24] The CDF collaboration. *First Flavor-Tagged Determination of Bounds on Mixing-Induced CP Violation in* $\mathrm{B_s} \to \mathrm{J}/\psi\phi$ *Decays.* Phys. Rev. Lett. 100, 161802, (2008).

[25] The CDF collaboration. *An updated measurement of the CP violating phase $\Phi_{\mathrm{J}/\psi\phi}$.* CDF/ANAL/BOTTOM/PUBLIC/9458, (2009).

[26] The D0 collaboration. *Measurement of Bs mixing parameters from the flavor-tagged decay* $\mathrm{B_s} \to \mathrm{J}/\psi\phi$. hep-ex, arXiv:0802.2255v1, (2008).

[27] CDF/D0 Δ Γ_s, β_s Combination Working Group. *Combination of D0 and CDF Results on $\Delta\Gamma_s$ and the CP-Violating Phase $\beta_s^{J/\psi\phi}$.* CDF/PHYS/BOTTOM/CDFR/9787 and D Note 5928-CONF, (2009).

[28] O. Deschamps et al. *The Two Higgs Doublet of Type II facing flavor physics data.* arXiv:0907.5135v1 [hep-ph], (2009).

[29] S. Cohen, M. Merk, E. Rodrigues. *$\gamma + \phi_s$ sensitivity studies from combined $B_s^0 \to D_s^-\pi^+$ and $B_s^0 \to D_s^\pm K^\pm$ samples at LHCb.* LHCb/PUB-2007-041, (2007).

[30] M.-O. Bettler. *The LHCb analysis for $B_s^0 \to \mu^+\mu^-$.* LHCb-CONF-2009-022, (2009).

[31] G. Buchalla et al. *B, D and K decays, report on the CERN workshop: Flavor in the era of the LHC.* arXiv:0801.1833, (2008).

[32] D. Martinez et al. *Analysis of the decay* $\mathrm{B_s} \to \mu^+\mu^-$ *at LHCb.* LHCb/ROADMAP1-002, (March 2009).

[33] H.E. Logan, U. Nierste. *$B_{s,d} \to \ell^+\ell^-$ in a Two-Higgs-Doublet Model.* arXiv:hep-ph/0004139, (2000).

[34] J.F. Gunion, H.E. Haber, G.L. Kane and S Dawson. *Errata for The Higgs Hunter's Guide.* arXiv:hep-ph/9302272, (1993).

[35] J. Nardulli. *Reconstruction of two-body B decays in LHCb.* CERN-THESIS-2007-063, (2007).

[36] P. Nason et al. *Bottom Production.* arXiv:hep-ph/0003142v2, (2001).

[37] Altarelli, G. and (editors), M. M. *Standard model physics (and more) at the LHC.* CERN-2000-004, (2000).

[38] The LHCb Collaboration. *LHCb Technical proposal.* CERN-LHCC/98-4, 1998.

[39] The LHCb Collaboration. *LHCb Technical proposal.* CERN-LHCC/2000-007, 1999.

[40] The LHCb collaborationy. *LHCb Velo technical design report.* CERN-LHCC/2001-011, (2001).

[41] M. Needham. *Silicon Tracker simulation performance.* CERN/LHCb-2003-015, (2003).

[42] The LHCb collaboration. *LHCb Inner Tracker design report.* CERN-LHCC/2002-029, (2003).

[43] The LHCb Collaboration. *LHCb Outer Tracker Technical Design Report.* CERN/LHCC-2001-024, (2001).

[44] S. Bachmann, T. Haas, M. Walter, U. Uwer, D. Wiedner. *Construction of module boxes for the Outer Tracker straw tube modules.* CERN/LHCb-2003-051, (2003).

[45] G.W. van Apeldoorn et al. *Beam Tests of Final Modules and Electronics of the LHCb Outer Tracker in 2005.* CERN/LHCb-2005-076, (2005).

[46] S. Berni, A. Froton, J.C. Gayde. *Outer Tracker T2-Q02 (C frame B2 position).* EDMS document (URL: `http://edms.cern.ch/document/771336`), (2006).

[47] H. Dekker, H. van der Graaf, et al. *The RASNIK/CCD 3-Dimensional alignment system.* 3rd International Workshop On Accelerator Alignment (IWAA 93) (URL: `www.slac.stanford.edu./econf/C930928/papers/017.pdf`), (2003).

[48] O. Callot. *Improved robustness of the VELO tracking.* LHCb/2003-17, (2003).

[49] M. Benayoun, O. Callot. *The forward tracking, an optical model method.* LHCb-2002-008, (2002).

[50] S. Hansmann-Menzemer, O. Callot. *The Forward Tracking : Algorithm and Performance Studies.* CERN-LHCb-2007-015, (2007).

[51] Forty, R. *Track seeding.* LHCb-2001-0109, (2001).

[52] M. Schiller. *LHCb tracking Twiki page.* `https://twiki.cern.ch/twiki/bin/view/LHCb/LHCbTrackingStrategies`, (2008).

[53] The LHCb collaboration. *LHCb RICH Technical Design Report.* CERN-LHCC/2000-037, (2000).

[54] The LHCb Collaboration. *LHCb Calorimeters Technical Design Report.* CERN/LHCC-2000-036, (2000).

[55] The LHCb Collaboration. *LHCb Muon Technical Design Report.* CERN/LHCC-2000-037, (2000).

[56] Charpak, G. e. a. *Nucl. Instr. and Meth.* **62**, 235 (1968).

[57] The LHCb Collaboration. *Addendum to the Muon Technical Design Report.* CERN/LHCC-2003-002, (2003).

[58] The LHCb Collaboration. *LHCb Trigger System Technical Design Report.* CERN/LHCC-2003-031, (2003).

[59] J. Albrecht. *Fast Track Reconstruction for the High Level Trigger of the LHCb Experiment.* CERN-THESIS-2009-120, (2009).

[60] G. Barrand et al. *GAUDI - A software architecture and framework for building HEP data processing applications.* Comput. Phys. Commun. **140** 45, (2001).

[61] I. Belyaev et al. *Simulation application for the LHCb experiment.* arXiv:physics/0306035v1 [physics.comp-ph], (2003).

[62] T. Sjöstrand et al. *High-Energy-Physics Event Generation with PYTHIA 6.1.* Computer Physics Commun.**135** 238, (2001).

[63] A. Ryd et al. *EvtGen A Monte Carlo Generator for B-Physics.* BAD 522 v6., (2005).

[64] GEANT 4 collaboration. *Geant4: A Simulation toolkit.* Nucl. Inst. and Methods **A 506** (2003), 250., (2003).

[65] The LHCb collaboration. *Boole: The LHCb digitization program.* `http://lhcb-release-area.web.cern.ch/LHCb-release-area/DOC/boole/`, (2004).

[66] The LHCb collaboration. *Boole: The LHCb digitization program.* `http://lhcb-release-area.web.cern.ch/LHCb-release-area/DOC/moore`, (2004).

[67] The LHCb collaboration. *Brunel: The LHCb reconstruction program.* `http://lhcb-release-area.web.cern.ch/LHCb-release-area/DOC/brunel`, (2004).

[68] The LHCb collaboration. *Escher: The LHCb software alignment program.* `http://lhcb-release-area.web.cern.ch/LHCb-release-area/DOC/alignment`, (2005).

[69] The LHCb collaboration. *Davinci: The LHCb physics analysis program.* `http://lhcb-release-area.web.cern.ch/LHCb-release-area/DOC/davicni`, (2004).

[70] The LHCb collaboration. *Panoramix: The LHCb event display program.* `http://lhcb-release-area.web.cern.ch/LHCb-release-area/DOC/panoramix`.

[71] S. Ponce et al. *Detector Description Framework in LHCb.* physics/0306089, (2003).

[72] S. Ponce. *The LHCb Detector Description DTD.* `http://lhcb-comp.web.cern.ch/lhcb-comp/Frameworks/DetDesc/Documents/lhcbDtd.pdf`, (2001).

[73] SQLite. *SQLite.* `http://http://www.sqlite.org/index.html`.

[74] A. Perieanu. *A Fast Algorithm to Identify and Remove Clone Tracks.* CERN-LHCb-2008-020, (2008).

[75] Kalman, R.E. *A new approach to linear filtering and prediction problems.* Trans. ASME J. Bas. Eng. **D82** (1960) 35.

[76] R. Van der Eijk. *Track reconstruction in the LHCb experiment.* CERN-THESIS-2002-032, (2005).

[77] S. Blusk et al. *Proceedings of the first LHC Detector Alignment Workshop.* CERN-2007-04, (2007).

[78] V. Blobel, E. L. *Statistische und numerische Methoden der Datenanalyse.* Teubner Studienbücher, (1998).

[79] A. Bocci, W. Hulsbergen. *TRT alignment for SR1 cosmics and beyond.* ATL-INDET-PUB-2007-009.

[80] Paige, C. C. and Saunders, M. A. *SIAM J. Numerical Analysis* **12**, 617–629 (1975).

[81] Saad, Y. and Schultz, M. *SIAM J. Sci. Statist. Comput.* **7**, 856–869 (1986).

[82] Bronstein, Semendjajew, M. and Muehlig. *Taschenbuch der Mathematik.* Verlag Harry Deutsch, (1999).

[83] Callot, O., Schiller, M. *Pat Seeding: A Standalone Track Reconstruction Algorithm.* CERN-LHCb-2008-042, (2008).

[84] G. v. Apeldoorn et al. *Beam Tests of Final Modules and Electronics of the LHCb Outer Tracker in 2005.* LHCb/PUB-2005-076, (2005).

[85] Cowan, G. *Statistical Data Analysis.* Oxford University Press, (1998).

[86] Dolgoshein, B. *Nucl. Instr. and Meth. A* **326**, 434–469 (1993).

[87] Bachmann, S. *private communication* .

[88] Pellegrino, A. *private communication* .

[89] M. Stoye. *Calibration and Alignment of the CMS Silicon Tracking Detector.* CERN-THESIS-2007-049 DESY-THESIS-2007-026, (2007).

[90] R. Mankel. *A 'Canonical' Procedure to Fix External Degrees of Freedom in the Internal Alignment of a Tracking System.* Hera-B 99-087 (1999).